

Surface functionalization and analysis thereof by ambient mass spectrometry

Radostina K. Manova

Thesis committee

Promotor

Prof. Dr H. Zuilhof

Professor of Organic Chemistry

Wageningen University

Co-promotor

Dr T.A. van Beek

Assistant professor, Laboratory of Organic Chemistry

Wageningen University

Other members

Prof. Dr A.H. Velders, Wageningen University

Prof. Dr F.P.J.T. Rutjes, Radboud University Nijmegen, the Netherlands

Prof. Dr C.G. de Koster, University of Amsterdam, the Netherlands

Prof. Dr-ing. H. Vogt, Universität Duisburg-Essen and Fraunhofer-IMS, Germany

This research was conducted under the auspices of the Graduate School VLAG (Advanced studies in Food Technology, Agrobiotechnology, Nutrition and Health Sciences).

Surface functionalization and analysis thereof by ambient mass spectrometry

Radostina Koleva Manova

Thesis

submitted in fulfilment of the requirements for the degree of doctor

at Wageningen University

by the authority of the Rector Magnificus

Prof. Dr M.J. Kropff,

in the presence of the

Thesis Committee appointed by the Academic Board

to be defended in public

on Wednesday 17 December 2014

at 1.30 p.m. in the Aula.

Radostina K. Manova

Surface functionalization and analysis thereof by ambient mass spectrometry, 224 pages.

PhD thesis, Wageningen University, Wageningen, NL (2014)

With references, with summaries in Dutch and English

ISBN 978-94-6257-157-0

To my son Angie

“Alles van waarde is weerloos”

Table of Contents

Chapter 1	Introduction	1
Chapter 2	Surface functionalization by strain-promoted azide-alkyne click reactions: a highlight.....	11
Chapter 3	Copper-free click biofunctionalization of silicon nitride surfaces via strain-promoted azide-alkyne cycloaddition reactions	25
Chapter 4	Ambient mass spectrometry of covalently bound organic monolayers	65
Chapter 5	Ambient surface analysis of organic monolayers using DART and Orbitrap mass spectrometry.....	81
Chapter 6	General discussion and outlook	105
Appendix 1	Information supplementing Chapter 3	121
Appendix 2	Information supplementing Chapter 4	145
Appendix 3	Information supplementing Chapter 5 (XPS spectra).....	155
Appendix 4	Information supplementing Chapter 5 (MS spectra)	177
Summary	201
Samenvatting	203
Acknowledgment	205
About the author	209
List of publications	213
Completed training activities	214

Chapter 1

Introduction

1.1 General introduction

Over the past decades, almost all types of analytical systems underwent a significant degree of miniaturization. The overall driver for this development was typically a combination of an increased rate of analysis and increased sensitivity. Such improvements have also characterized the research and design of biosensor devices. The need for such compact and more user-friendly devices is uncontroversial and indisputable: easy, fast, reliable and cost-effective responses facilitate the decision-making process in clinical, medical and veterinary diagnostics, food safety, environmental monitoring, and in emergency applications.

Point-of-care tests (POC) allow, for instance, early diagnosis and rapid initiation of treatment. In a POC test, a drop of blood from a finger prick or a fresh urine sample is analyzed on a biosensing test strip engineered to detect a single (such as glucose to detect diabetes) or multiple biomarkers (such as high and low density cholesterol and triacylglycerols as markers for cardiovascular diseases). Based on the test result, the clinician takes a decision for an appropriate treatment, or an additional thorough investigation is undertaken. Moreover, POC tests provide continuous monitoring of clinical biomarkers, guiding the treatment in real-time with a flexibility to change the therapy with an alternative one. The early diagnosis is brought, in this manner, at the site of patient care. The POC tests have evolved in biosensors for direct tissue measurements¹ that further shorten the analysis time and the diagnosis timescale. Such POC tests are even more beneficial in emergency rooms.²

Typical POC rapid tests are blood glucose monitoring systems, rapid HIV tests, drug and alcohol analysis systems, cholesterol measurement systems, diagnosis of cancer and cardiovascular diseases (Figure 1.1).

Besides the reduced analysis time, the POC tests can be produced at a low cost: this is an additional advantage especially “in a world in which cost is everything.”³ In developing countries, monitoring and controlling diseases and food or environmental contaminations remain major healthcare issues. The shortage of diagnostics equipment in poverty-related conditions has led to the use of ineffective and outdated medical diagnostics, often based solely on systematic guidelines, e.g. sign and symptoms. WHO’s Integrated Management of Childhood Illness⁴ is an example of such a diagnostic procedure: an approach that is not exhaustive and often time-consuming, but the only zero-cost and practiced diagnostics in poverty-related conditions. Similarly, the detection of foodborne illness and waterborne diseases due to inadequate sanitation requires affordable technologies that could enable the local rural communities to improve the healthcare and food quality.⁵



Figure 1.1: Point-of care tests commercially available; (a) OneTouch® Verio®IQ Blood Glucose Monitoring System from © Universal biosensor; (b) Clearview® Strep A Exact II cassette direct detection of Group A Streptococcal antigen from throat swabs to aid in the diagnosis of Group A pharyngitis. © 2013 Alere (c) Digital strip reader © Bio-alternative medical devices.

Despite the urgent need, there is little interest from industrial companies to invest in such affordable technologies mainly because of the limited market and low-profit margins. For instance, the POC market experienced a slower

growth than expected in 2012.⁶ Forecasters predict that the global POC diagnostics market will reach \$ 30 billion in 2019, with a compound annual growth rate (CAGR) of 3.5% between 2014 and 2020 due to the commercialization of microfluidics devices.⁷ Fortunately, product development in this sector is substantially supported by grants from governmental and non-governmental organizations.

In the context of food safety, analysis of food contaminants needs a selective, high-throughput, multi-analyte screening technology that limits the use of time-consuming sample pretreatment and sophisticated analytical tools only for non-compliant or positive samples. In this respect, a significant problem is the analysis of food allergens and other harmful constituents of a protein nature, triggering food intolerance. Food allergy and food intolerance are conditions that require life-long treatment and avoidance of the responsible food. Although worldwide legislation mandates labeling of any foods containing allergenic or otherwise harmful proteins, a possible cross-contamination of the food or the presence of hidden allergens puts the consumer at risk. The analytical methods for identification of harmful proteins are laborious, tedious and expensive. Thus, fast detection of allergens in food would be of benefit to the consumer protection.

Regardless of the application, all the aforementioned technologies are based on biosensor platforms. A biosensor platform relies on biomolecular interactions between an analyte (e.g. disease biomarker, allergen, toxin, or pathogen) and a ligand immobilized on the sensor surface. The ligand plays a role as a recognition element that specifically binds the analyte in the sample. The binding event triggers changes in the mass or in optical, thermal or electric properties of the sensor. The change of these parameters is finally transduced into a signal that relates to the concentration of the analyte in the sample. For such bioassays, the quality and selectivity of the recognition elements and the choice of the assay types are evidently crucial. For instance, the choice of ligand determines the specificity of the binding. Analogously, a high specificity avoids nonspecific interactions and then no or only a limited sample preparation is necessary. The simplest assay types provide yes-or-no readouts. For more information on advances and recent development in the field of biosensors, please refer to two books.^{8,9}

The current research has been carried out under the framework of the Unihealth project funded by the INTERREG IV A Germany-Netherlands program and the European Regional Development Fund. This is an interdisciplinary project with a close collaboration between IMS Fraunhofer (Duisburg, Germany), Laboratory of Organic Chemistry, Wageningen University (The Netherlands) and Radboud University Nijmegen (Nijmegen, The Netherlands). A micromechanical biosensing device was designed at IMS Fraunhofer (Figure 1.2). This biosensing device is a mass sensor constructed with Complementary Metal–Oxide–Semiconductor compatible pressure technology (CMOS). The core elements in this mass-sensing device are the circular membrane structures made of silicon nitride (Si_3N_4) with a diameter of 60-100 μm . Such a membrane oscillates with a natural resonance frequency, dependent on the mass of the membrane, its diameter and other factors. Once a sample is introduced on the ligand-coated membrane, any targeted analytes would interact specifically with immobilized ligands and any matrix molecules could be removed by a washing step. The binding event would lead to an increase of the mass of the membrane. Subsequently, the resonance frequency shifts to lower values, and the difference in the resonance frequency is transduced in an analytical signal. This specific mass sensor device is aimed to detect analytes with a molecular weight above 20 kDa, and the sensor could open up new perspectives for detection of biomolecules at low concentrations.

The ultimate goal of the Unihealth project is to implement the membrane mass sensor technology in a biosensor for detection of biomolecules like allergens and biomarkers (proteins with MW above 20 kDa). The biosensors, thus, could be used as either a POC test in medical diagnostics, or in food safety applications for the detection of allergens.

However, implementing biosensor technology into final analytical devices is not a trivial issue.¹⁰ Apart from an appropriate choice of ligand molecules, especially the immobilization of such ligands within the device constitutes a crucial development step. The optimal immobilization protocol will determine the spatial arrangement, density and accessibility of the ligand molecules for the analytes. Hence, parameters as stability of the sensor, reusability and sensitivity should be optimized. An appropriate immobilization strategy will impact not only the development of biosensors, but also their implementation

in practice. This is the background of the research reported in this thesis, for which the goals are summarized below.

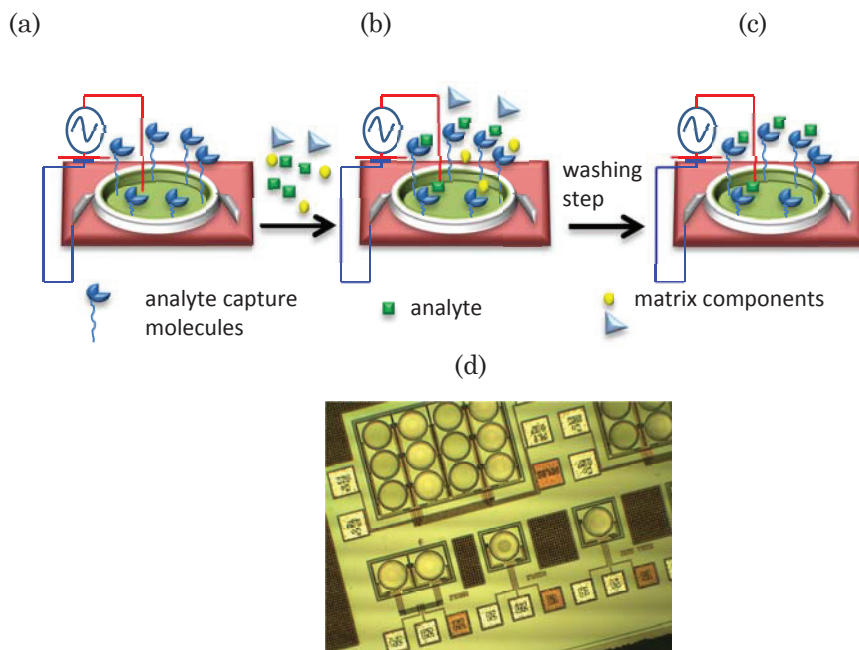


Figure 1.2: Schematic representation of membrane sensor device developed by IMS Fraunhofer, Duisberg; (a) a circular membrane of the sensor before application of the sample; (b) the circular membrane after application of the sample; \blacksquare analytes; \blacktriangle and \bullet are matrix components; (c) the circular membrane after washing the matrix components; (d) optical image of the mass sensor with a set of circular membranes each with $65\ \mu\text{m}$ diameter.

1.2 Aim of this research

To facilitate the wide application of the biosensing device designed at IMS Fraunhofer, a versatile approach for tailoring the sensor surface is needed to obtain, from the same sensing device, a biosensor selectively targeting a range of biomolecules. The versatile approach should be applicable for silicon nitride – the material used to construct the sensor and the circular membranes – and should result in a stable covalent bond to ensure performance of the sensor over time. One of the potentially useful surface modification approaches for biosensor surfaces could be the use of nanometer-thick covalently bound monolayers with terminal functional groups that allow facile and smooth covalent attachment of ligand molecules. The surface chemistry applied in this manner should preserve the biological function of the ligands, without interfering with their role as recognition elements in the binding event. Finally, the surface modification strategy should afford a sufficient yield of the attached ligands on the surface, resulting in a high resonance frequency shift, and thus high sensitivity.

Taking into account the area of the sensing surface (μm scale) for modification, a proper characterization technique should be selected, which is able to control the manufacturing process. In terms of surface characterization, the widely used X-ray Photoelectron Spectroscopy (XPS) analysis might be a first choice, but this technique is expensive and provides minimal structural information. Infrared microscopy provides functional group information, but yields problems with sensitivity and the reproducibility of quantitation. Finally, scanning probe microscopies typically display insufficient chemical specificity. Therefore new analytical methods in surface characterization are a top priority.

In this respect, the goals of the current research thesis were the development of a) a reliable generic surface modification method, capable of attaching different ligands targeting specific biomolecules, and b) an analytical surface characterization method that can gather rapid and structure-specific information from the modified surface, and that can be applied for quality control.

1.3 Outline of this thesis

The research carried out in this thesis is targeted towards the aforementioned goals and thus can be classified into two parts. The first part deals with developing a surface modification approach for silicon nitride and its use in growing a nm-thick (ultra-thin) layer tailoring the sensor surface. The second part is dedicated to the development of a new analytical approach for characterization of these nm-thick layers applied in the manufacturing of biosensing platforms, microarray and sensing chips. The content of the thesis Chapters is briefly summarized below.

In **Chapter 2** we provide an overview of the current literature related to strain-promoted Cu-free click reactions (SPAAC). This type of reactions can play a major role in the development of biosensors and bioassays. In this chapter we focus only on several distinctive applications of this prominent bioorthogonal reaction for smooth attachment of biomolecules on the surface. The chapter shows the capability of the SPAAC reaction, not only in immobilizing biomolecules, cells, and labile modelling systems, but also in triggering a specific behavior on the surface.

Chapter 3 experimentally underpins the potential of these reactions for attachment of biomolecules onto a surface while preserving their biological function. The chapter describes in detail a versatile, step-wise surface modification method that can transform the inorganic Si_3N_4 surface into a biosensing platform. Utilizing consecutive reactions on the surface, a monolayer with a range of end-groups can be grafted. Using this approach, the surface coating can be customized with desirable functional groups. The chapter demonstrates that via SPAAC reactions biological molecules can be easily tethered onto the surface and used in the screening of biomolecular interactions.

Chapter 4 provides the foundation of a novel analytical approach for analysis and characterization of monolayers. Ambient ionization (Direct Analysis in Real Time – DART) combined with High-Resolution Mass Spectrometry (HRMS, Orbitrap mass spectrometer) was tested for the identification of covalently bound monolayers on silicon nitride surfaces. Two types of monolayers, e.g. ester-terminated and amide-terminated layers were

subjected to analysis with DART-HRMS and the potential of this method was briefly compared with XPS methods for the analysis of monolayers.

Chapter 5 provides further insights into the potential of DART-HRMS for the analysis and characterization of a large set of different monolayers grafted on a variety of substrates. The study deepens our understanding of the monolayer fragmentation upon DART ionization, and formulates general MS interpretation rules. The studied monolayers are widely used in engineered surfaces, and in the preparation of biosensor platforms and bioassays. Therefore, we applied these rules in the investigation of relevant and commercially available coatings. The results underline the usefulness of DART-HRMS, not only for identification of coatings but also for quality control purposes.

At the end of the thesis, **Chapter 6** provides a general discussion reflecting on the major achievements of the thesis, giving further perspectives and potential applications.

References

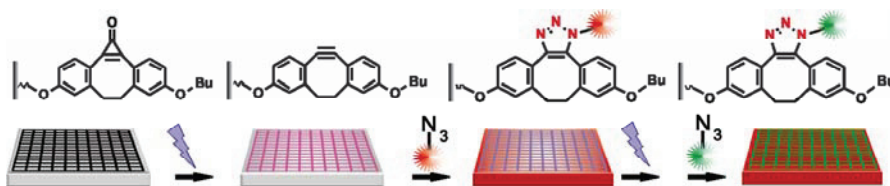
1. Rogers, M. L.; Boutelle, M. G. Real-Time Clinical Monitoring of Biomolecules. *Annu. Rev. Anal. Chem.* **2013**, *6* (1), 427-453.
2. Chan, C. P. Y.; Mak, W. C.; Cheung, K. Y.; Sin, K. K.; Yu, C. M.; Rainer, T. H.; Renneberg, R. Evidence-Based Point-of-Care Diagnostics: Current Status and Emerging Technologies. *Annu. Rev. Anal. Chem.* **2013**, *6* (1), 191-211.
3. Whitesides, G. M. A lab the size of a postage stamp. *TEDX Boston*. **2009**, *TED talk* (http://www.ted.com/talks/george_whitesides_a_lab_the_size_of_a_postage_stamp.html).
4. Integrated Management of Childhood Illness. MOPH&P,WHO/CHD, UNICEF, HCMC/CDP. *World Health Organization* **2008**, Accessed 2012 May 16 http://whqlibdoc.who.int/publications/2008/9789241597289_eng.pdf.
5. Yetisen, A. K.; Akram, M. S.; Lowe, C. R. Paper-based microfluidic point-of-care diagnostic devices. *Lab Chip* **2013**, *13* (12), 2210-2251.
6. Roussel, B. Point of Care Testing 2014: Applications for Microfluidic Technologies. *Yole Développement* **2014**.
7. Shields, D.; Sale, A. Global In Vitro Diagnostics (IVD) Market (Technique, Product, Usability, Application, End User, and Geography) - Size, Share, Global Trends, Company Profiles, Demand, Insights, Analysis, Research, Report, Opportunities,

Segmentation and Forecast, 2013 – 2020. *Allied Market Research* **2014**, Report Code: *ME 14336*.

8. Marinesco, S.; Dale, N. *Microelectrode Biosensors*; Humana Press 2013.
9. Evtugyn, G. *Biosensors: Essentials*; Springer Berlin Heidelberg 2014. p 265.
10. Whitesides, G. M. Cool, or simple and cheap? Why not both? *Lab Chip* **2013**, *13* (1), 11-13.

Chapter 2

Surface functionalization by strain-promoted azide-alkyne click reactions: a highlight



“Clickable” surface without Cu. There is a growing demand for reproducible site-specific attachment of biomolecules on functional surfaces without introduction of unwanted groups or catalysts, as they may interfere with later applications. Strain-promoted alkyne-azide (SPAAC) click reactions can fulfill these requirements to a high degree, and recent applications are discussed.



Part of this chapter was published as:

Manova, R. K.; van Beek, T. A.; and Zuilhof, H. *Angew. Chem. Int. Ed.* **2011**, *50*, 5428-5430.

2.1 Introduction

Functionalization of surfaces becomes increasingly important given the ever-decreasing size of active devices, with the concomitant increase in surface-to-volume ratios. As a result, efficient routes for such functionalizations via the attachment of functional monolayers or multilayers have become the focus of much research in the last decade, both for hard (typically inorganic) and soft (polymeric, dendritic) surfaces. Specific features of desirable surface modifications include the combination of high efficiency with mild, non-corrosive reaction conditions. This avoids work-up to remove (surface-bound) by-products or excess reactants, as this is typically not trivial or practically impossible. Therefore click reactions, such as the Cu(I)-catalyzed alkyne-azide cycloaddition (CuAAC) with surface-bound alkynes or azides,¹ have been used to functionalize a wide range of surfaces. However, the presence of Cu(I) can be problematic: Cu ions are cytotoxic, disrupt ds-DNA, alter the structure of 'protein-repelling' ethylene oxide moieties, and can change the intrinsic functional properties of the surfaces, such as the through-monolayer conductivity on semiconductor surfaces and the fluorescence of quantum dots. As a result, alternative approaches have been developed over the last five years, which include metal-free ligation chemistry that either requires no further activation (e.g. NHS-based amide formations)² or activated but traceless chemistry (e.g. photoinduced thiol-ene addition reactions).^{3,4,5} Recently several examples have been published that aim to combine traceless reactions with room-temperature conditions via application of strain-promoted alkyne-azide cycloadditions (SPAAC or Huisgen-Bertozzi-type cycloadditions)^{6,7} to surfaces. The current chapter focuses on a few of these (arranged by the type of surface that is modified, §2.1-2.7, or specific features to be highlighted, §2.8-2.9), to indicate the high potential of this type of surface functionalization, and discusses the current state of affairs and goals for the years to come.

2.2 SPAAC on organomicelles

Boons and co-workers have modified the surface of organomicelles that were constructed from tailor-made block copolymers.⁸ By appending amphiphilic copolymers of poly(ethylene oxide) and poly(ϵ -caprolactone) with amines, these could be reacted with a dibenzocyclooctyne that was functionalized with an activated ester (Figure 2.1a). This led to the formation of micelles with a cyclooctyne-containing surface (Figure 2.1b), which could be readily reacted with a range of azides, including fluorescent dyes, peptides, and azide-linked mannosides. The latter bound specifically to surfaces onto which Concanavalin A had been deposited. Similarly, functionalized micelles could potentially also be used for drug delivery, and initial steps were made to show this potential.

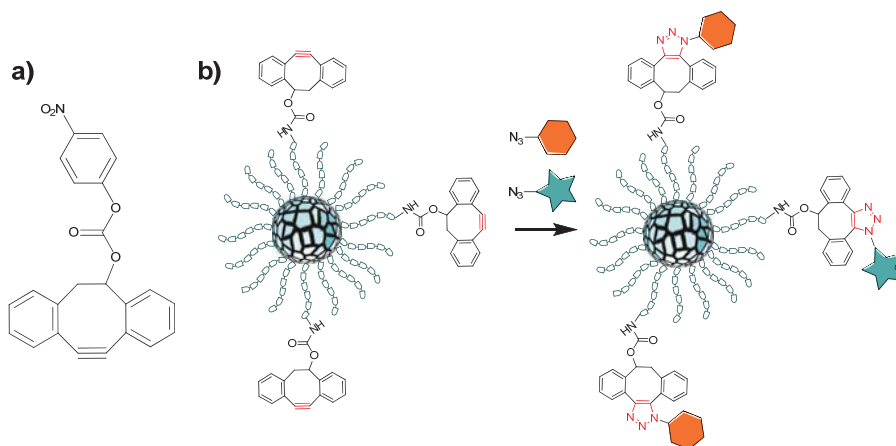


Figure 2.1: (a) Structure of dibenzocyclooctyne with activated ester; (b) Micelle with cyclooctyne-functionalized surface.

2.3 SPAAC on quantum dots

Quantum dots (QDs) are an attractive tool in fluorescence imaging techniques. Functionalization of QD surfaces has been carried out using a metal-free click reaction by Texier and co-workers.⁹ Cyclooctyne-modified QDs have been functionalized with azido-tagged mannosamine and have been compared with mannosamine conjugates prepared by CuAAC. Interestingly, the QDs – which were used for labeling cell membrane epitopes – that were prepared in the presence of Cu showed only 50% of the initial quantum yield,

while the QDs prepared via SPAAC actually displayed a 30% increase of the quantum yield.

2.4 SPAAC on glass surfaces

An application of cyclooctyne-based click reactions on glass surfaces has recently been developed by Popik and co-workers.¹⁰ An epoxide-functionalized glass surface was reacted with an amine-linked aza-dibenzocyclooctyne (ADIBO) to yield a highly reactive cyclooctyne-functionalized surface (Figure 2.2a). This reactivity was studied with azides bearing a fluorescence probe. Since inclusion of the amide functionality in the cyclooctyne speeds up the SPAAC reaction relative to that of dibenzocyclooctyne, with just 0.1 mM of azide, the click reaction reached surface saturation levels after only 100 min at room temperature. This high efficiency at low concentrations is of significance, as the amount of tailor-made azides may be limited by either the availability of (naturally derived-) materials or by the synthetic complexity. In addition, the authors also studied the inverse reaction, in which azide-functionalized surfaces were reacted with ADIBO (Figure 2.2b). Use of routinely available azide-functionalized surfaces in combination with ADIBO allowed a versatile entry to surface bioconjugation e.g. biotinylation of the surface, immobilization of proteins, as well as patterning of the surface with fluorescent probes.

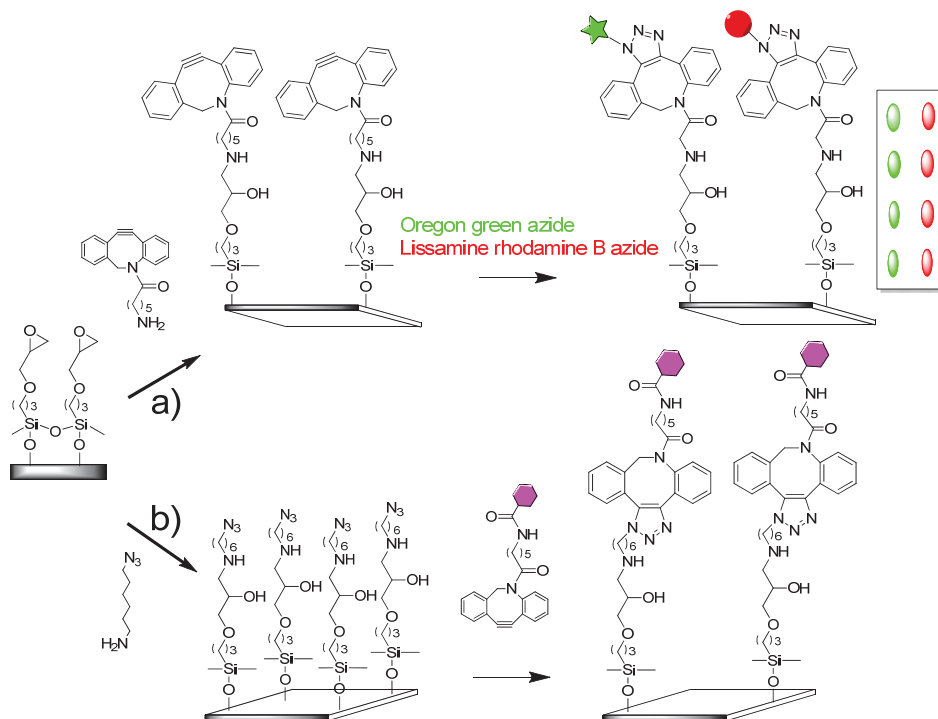


Figure 2.2: (a) Aza-dibenzocyclooctyne-functionalized glass surface, which was subsequently reacted with fluorescent moieties; (b) Inverse copper-free click reaction, starting from azide-terminated surfaces, and subsequent local immobilization of fluorescent label.

2.5 SPAAC for labelling of liposomes

Another relevant application of SPAAC reactions on surfaces is the labeling and immobilization of synthetic membranes, such as liposomes, supported lipid monolayers and bilayers. These are frequently exploited as model systems, for instance, in drug delivery, imaging of biological systems, and modeling signaling pathways through binding interactions at membrane surfaces. The decoration of membrane surfaces enables their widespread application, but at the same time requires bioorthogonal labeling. Typical bioorthogonal labeling is achieved via the Cu(I)-catalyzed azide–alkyne cycloaddition (CuAAC). However, the reaction conditions of CuAAC can be detrimental for liposomes¹¹ and membrane bilayers, thus the SPAAC is an ideal alternative. For instance,

Best and co-workers¹² gave an example of such a strategy by incorporating an azido-lipid in fluorescently labeled liposomes. Subsequently, the fluorescent liposomes were reacted with ADIBO-biotin conjugates to decorate the liposome surfaces with biotin. Afterwards, the biotinylated liposomes were immobilized on streptavidin coated 96-well microplates, and the immobilization was monitored via the fluorescence intensity measured with a microplate reader.

2.6 Spatial control and tuneable surface density of attached molecules (ligands) with SPAAC

The most valuable advantage of SPAAC reaction is its biocompatibility. But a relevant question is, then, whether this bioorthogonal reaction is just simple alternative to the toxic Cu-mediated reactions, or whether it can additionally give control over the final density of the attached biomolecules (ligands) on the surface. A control over the density of ligands would allow tuning of the surfaces according to the envisaged application. Such a study was carried out on ADIBO-functionalized supermagnetic iron oxide nanoparticles.¹³ A fixed concentration of ADIBO-labeled particles were clicked with increasing concentrations of azido fluorescent ligands (e.g. targeting peptide and affibodies), and the final density was assessed based on the resulting fluorescent signal. The effect of ligand density was evaluated in cell-binding studies by employing conjugates with different peptide ligands for targeting cells having diverse receptors. For these nano-platforms an optimal ligand density was found that led to significant improvement in cell binding and contrast in the associated cell imaging. Several factors contributed to the observed optimal ligand-density effect: packing density, ligand orientations, steric interference originated from the ligand size and density.

2.7 SPAAC for biorepellent and functional coatings

The versatility of SPAAC was elegantly demonstrated for the attachment of small molecules up to whole cells onto biorepellent surface coatings.¹⁴ To this aim, bicyclo[6.1.0]nonyne (BCN) was selected for its high reactivity and low lipophilicity. An azido-terminated poly-(L-lysine)-*graft*-poly(ethylene glycol) (PLL-g-PEG) was used to obtain a biorepellent and at the same time functional surface coating (Figure 2.3a). The spontaneous and catalyst-free cycloaddition of the BCN with the terminal azide group of the coating eases the surface functionalization, and allows facile application of the procedure in aqueous solutions at physiological pH, salt concentrations, and at ambient temperature. In this way, different BCN-conjugates can be easily attached on the coating, enhancing its application in ELISA format, cell adhesion, proliferation and cell migration studies. The degree of functionalization can be controlled simply by diluting the azido-terminated PLL-g-PEG with methoxy-terminated PLL-g-PEG. For instance, mixtures of azido and methoxy-terminated PLL-g-PEG at different dilutions were used to coat standard ELISA 96-well plates. The wells of a 96-well plate were subsequently filled with 100 μ M BCN-biotin solution in PBS buffer and left to react for 1 hour. After washing the wells only with buffer and water, the HRP-based enzyme-linked assay was performed with streptavidin-HRP solution. The bio-repellent coating allowed for omitting the traditional detergents and serum albumins as a measure against nonspecific adsorption.

Similarly, an RGD-BCN conjugate (RGD is an amino acid sequence promoting cell adhesion) was immobilized onto the bio-repellent clickable coating, and this platform was used to stimulate cells adhesion and proliferation (Figure 2.3b). Since the reaction of RGD-BCN conjugate with the azide-terminated coating could be carried out at physiological conditions and without copper, the RGD peptide could be attached in the presence of cells. HeLa cells, for instance, were seeded onto fibronectin disks surrounded by the azido-terminated PLL-g-PEG coating. Once the cells had adhered to the surface, the RGD-BCN conjugate was applied to immobilize RGD onto the coating. The attached RGD triggered the cells to migrate and leave their confinement. Furthermore, the biocompatibility of the SPAAC reaction and the limited number of steps required (amongst which only single pipetting of

aqueous stock solution) allowed both specialists and non-specialists to engineer the surface properties in order to carry out more complex cell dynamics studies: switching on/off cell migration, enabling cell shape co-culture, etc.¹⁵ This straightforward approach might offer a new strategy for development of responsive materials in stem cell stimulation.¹⁶

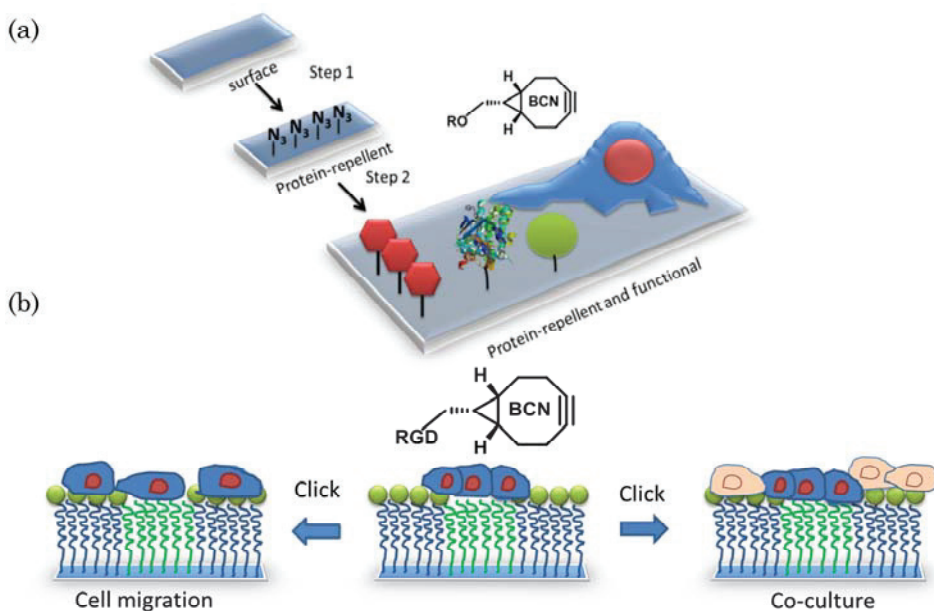


Figure 2.3: (a) The versatility of SPAAC demonstrated for the attachment of small molecules up to whole cells onto biorepellent surface coatings of PLL-g-PEG; (b) an RGD-BCN conjugate (RGD promotes cell adhesion) was immobilized onto the biorepellent clickable coating via SPAAC, and this platform was used to stimulate cells adhesion and proliferation, and co-culture.

2.8 SPAAC for biosensing applications

Another interesting application of SPAAC is the site-specific attachment of biomolecules in biosensor platforms. In this respect, the advantage of SPAAC over other coupling reactions was recently illustrated for peptide and protein immobilization on Surface Plasmon Resonance (SPR) chips.¹⁷ In the SPR applications, the amide coupling is the prevalent approach for

biofunctionalization: the SPR chips are tailored with active NHS (*N*-hydroxy succinimide) ester groups, which are reactive towards amino groups of the biomolecules. The presence of multiple NH₂ groups with different accessibility in proteins and peptides affects the modes of attachment, and a random immobilization is usually obtained. In order to achieve site-specific attachment, the SPR chips were first functionalized with BCN moieties, and azide-terminated proteins (*i.e.* azido-GFP) or azide-terminated peptides were clicked on the chip *via* a strain-promoted cycloaddition. Although the binding interactions on the SPR chip occurred with a similar binding constant regardless of the route of attachment (SPAAC or amide coupling), the SPR chips obtained *via* SPAAC demonstrated a better robustness, and thus were used for multiple experiments without significant loss of sensitivity. Despite the accessibility of the BCN derivative, obtaining azide-functionalized peptides and proteins is still not a trivial issue and limits this approach to some extent.

2.9 Kinetics of surface-bound click reactions

To widen the application of SPAAC on the surface, several studies were carried out to determine the rate constant and surface yield. On the one hand, the cyclooctyne derivatives display different reactivity based on the substituent present,¹⁸ and this might account for different rates of SPAAC reactions carried out on surfaces. The rate of SPAAC on surfaces would depend also on the density of the reactive surface-bound species (either alkyne or azide terminal groups). For instance, the reaction rates of SPAAC on polymer brushes with pending dibenzocyclooctyne (DIBO), ADIBO or propargyl were compared.¹⁹ These alkyl-terminated polymer brushes were reacted with 4-(*N*-3-Azidopropyl)sulfonylamido lissamine rhodamine (azido-rhodamine) and the resultant fluorescent signal was used to describe the kinetics of the surface-bound reactions. Since the azido-rhodamine was applied in a large excess (40 mM) relative to the immobilized alkyl groups on the surface (\approx nM) a pseudo-first order reaction rate was assumed. The kinetic study showed that azido-lissamine rhodamine attachment proceeded at a higher rate on ADIBO polymer brushes (4.4 ± 0.8) $\times 10^{-3}$ s⁻¹ than on DIBO-polymer brushes (7.7 ± 1.2) $\times 10^{-4}$ s⁻¹. This corroborates the relative reactivity of these strained cyclooctynes.¹⁸ Notably, the CuAAC reaction on propargyl polymer brushes was at least 5-fold faster than the strain-promoted cycloaddition.

On the other hand, in some applications the final surface yield might be more valuable than the actual reaction rate. For instance, Becker *et al.* clearly indicated in a comparative study²⁰ of three click reactions – thiol-ene, SPAAC, and CuAAC – that the attachment of biological relevant peptides (e.g. RGD) proceeded with the highest surface yield (70%) when thiol-ene click reactions were used. The metal-free and copper-catalyzed azide–alkyne cycloaddition resulted in only 30% peptide surface coverage, most probably due to the steric hindrance introduced by the formation of the triazole ring.²⁰ In this particular example, the peptides were bearing alkyl groups, whilst the glass/silicon surfaces were functionalized with terminal azide groups. Nevertheless, the authors elegantly demonstrated the use of sequential click reactions for creating peptide concentration gradients on the surface.

2.10 Lighten up and click

The aforementioned reactions proceeded in a facile manner: the method of localization is basically determined by locally dropping a reactive solution on a surface. Although dropping is doable with micro-addition systems, a combination with other localization methods would be desirable. Such a technique has recently been developed by Oski *et al.*, who coupled a protected dibenzocyclooctyne via an amine linker to a polymer brush onto silicon oxide.²¹ The dibenzocyclooctyne is protected by a photoremovable cyclopropanone moiety, that is, on the one hand, fully thermally stable, but on the other hand, can be rapidly activated by irradiation with UV light (350 nm, only 3 min; Figure 2.4). This photochemical step leads to a quantitative loss of CO, and yields at the irradiated spots reactive C≡C bonds. The authors demonstrated this via a process of local irradiation of the surface through a photomask, reaction with azido-linked dye 1, subsequent deprotection of all remaining cyclopropanone moieties and reaction of all newly formed alkynes with azido-linked dye 2, which led in a highly elegant way to a patterned surface.

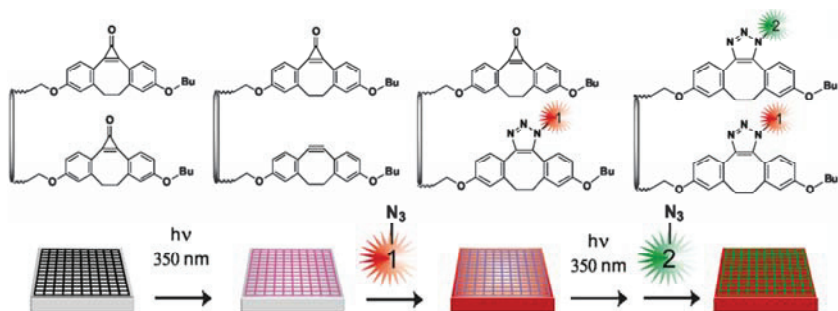


Figure 2.4: Photopatternable clickable surfaces using sequential light-induced, local deprotection and cycloaddition reactions.²¹

2.11 Conclusion

Like for polymer science,²² on surfaces purification by non-chromatographic methods is essential and drives the development of highly efficient, true ‘click’ reactions. After an incomplete reaction, surfaces can behave slightly to significantly different from surfaces with quantitatively modified end groups, yet typically cannot be converted to a fully substituted surface. At best a generic passivation method (surface blocking) can be used to minimize the problems.

The chemistry displayed above therefore also points to further developments that will be required. First of all, the reaction efficiency needs to be quantitative. The difficulty of this is seen in the elegant work by Boons⁸ who reported yields of 58-76% for cycloaddition reactions. Second, given the size of e.g. the dibenzocyclooctyne moieties it is unlikely that all azides on an azide-terminated surfaces or in the abovementioned polymer brush will react. Since these surfaces are of specific interest for biodiagnostic purposes, cross-contamination should be zero or at least as low as possible, requiring the development of quantitative blocking procedures in case the cycloaddition chemistry cannot be performed quantitatively. Finally, highly reactive cycloalkyne moieties tend to react also with other groups than just azides, thus reducing the lifetime of cycloalkyne-terminated surfaces. Azido-terminated surfaces are expected to have a longer shelf life. Depending on the application, a tunable reactivity of these moieties is necessary, requiring further comparative kinetic studies. The work presented above displays both the

potential and challenges in further work, and is thus highly illustrative for future developments in this exciting branch of organic surface chemistry.

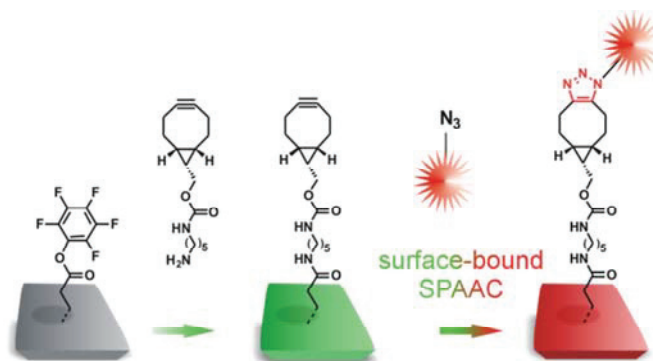
References

1. Collman, J. P.; Devaraj, N. K.; Chidsey, C. E. D. "Clicking" Functionality onto Electrode Surfaces. *Langmuir* **2004**, *20* (4), 1051-1053.
2. Yang, M.; Teeuwen, R. L. M.; Giesbers, M.; Baggerman, J.; Arafat, A.; de Wolf, F. A.; van Hest, J. C. M.; Zuilhof, H. One-Step Photochemical Attachment of NHS-Terminated Monolayers onto Silicon Surfaces and Subsequent Functionalization. *Langmuir* **2008**, *24* (15), 7931-7938.
3. Weinrich, D.; Lin, P.-C.; Jonkheijm, P.; Nguyen, U. T. T.; Schröder, H.; Niemeyer, C. M.; Alexandrov, K.; Goody, R.; Waldmann, H. Oriented Immobilization of Farnesylated Proteins by the Thiol-Ene Reaction. *Angew. Chem. Int. Ed.* **2010**, *49* (7), 1252-1257.
4. Campos, M. A. C.; Paulusse, J. M. J.; Zuilhof, H. Functional monolayers on oxide-free silicon surfaces via thiol-ene click chemistry. *Chem. Commun.* **2010**, *46* (30), 5512-5514.
5. Hoyle, C. E.; Bowman, C. N. Thiol-Ene Click Chemistry. *Angew. Chem. Int. Ed.* **2010**, *49* (9), 1540-1573.
6. Jewett, J. C.; Bertozzi, C. R. Cu-free click cycloaddition reactions in chemical biology. *Chem. Soc. Rev.* **2010**, *39* (4), 1272-1279.
7. Sletten, E. M.; Bertozzi, C. R. Bioorthogonal Chemistry: Fishing for Selectivity in a Sea of Functionality. *Angew. Chem. Int. Ed.* **2009**, *48* (38), 6974-6998.
8. Guo, J.; Chen, G.; Ning, X.; Wolfert, M. A.; Li, X.; Xu, B.; Boons, G.-J. Surface Modification of Polymeric Micelles by Strain-Promoted Alkyne-Azide Cycloadditions. *Chem. Eur. J.* **2010**, *16* (45), 13360-13366.
9. Bernardin, A.; Cazet, A. I.; Guyon, L.; Delannoy, P.; Vinet, F. o.; Bonnaffé, D.; Texier, I. Copper-Free Click Chemistry for Highly Luminescent Quantum Dot Conjugates: Application to in Vivo Metabolic Imaging. *Bioconjugate Chem.* **2010**, *21* (4), 583-588.
10. Kuzmin, A.; Poloukhine, A.; Wolfert, M. A.; Popik, V. V. Surface Functionalization Using Catalyst-Free Azide-Alkyne Cycloaddition. *Bioconjugate Chem.* **2010**, *21* (11), 2076-2085.
11. Said Hassane, F.; Frisch, B.; Schuber, F. Targeted Liposomes: Convenient Coupling of Ligands to Preformed Vesicles Using "Click Chemistry". *Bioconjugate Chem.* **2006**, *17* (3), 849-854.

12. Bostic, H. E.; Smith, M. D.; Poloukhine, A. A.; Popik, V. V.; Best, M. D. Membrane labeling and immobilization via copper-free click chemistry. *Chem. Commun.* **2012**, *48* (10), 1431-1433.
13. Elias, D. R.; Poloukhine, A.; Popik, V.; Tsourkas, A. Effect of ligand density, receptor density, and nanoparticle size on cell targeting. *Nanomedicine (N. Y., NY, U. S.)* **2013**, *9* (2), 194-201.
14. van Dongen, S. F. M.; Janvore, J.; van Berkel, S. S.; Marie, E.; Piel, M.; Tribet, C. Reactive protein-repellent surfaces for the straightforward attachment of small molecules up to whole cells. *Chem. Sci.* **2012**, *3* (10), 3000-3006.
15. van Dongen, S. F. M.; Maiuri, P.; Marie, E.; Tribet, C.; Piel, M. Triggering Cell Adhesion, Migration or Shape Change with a Dynamic Surface Coating. *Adv. Mater.* **2013**, *25* (12), 1687-1691.
16. Skorb, E. V.; Möhwald, H. 25th Anniversary Article: Dynamic Interfaces for Responsive Encapsulation Systems. *Adv. Mater.* **2013**, *25* (36), 5029-5043.
17. Wammes, A. E. M.; Fischer, M. J. E.; de Mol, N. J.; van Eldijk, M. B.; Rutjes, F. P. J. T.; van Hest, J. C. M.; van Delft, F. L. Site-specific peptide and protein immobilization on surface plasmon resonance chips via strain-promoted cycloaddition. *Lab Chip* **2013**, *13* (10), 1863-1867.
18. Debets, M. F.; van Berkel, S. S.; Dommerholt, J.; Dirks, A. J.; Rutjes, F. P. J. T.; van Delft, F. L. Bioconjugation with Strained Alkenes and Alkynes. *Acc. Chem. Res* **2011**, *44* (9), 805-815.
19. Orski, S. V.; Sheppard, G. R.; Arumugam, S.; Arnold, R. M.; Popik, V. V.; Locklin, J. Rate Determination of Azide Click Reactions onto Alkyne Polymer Brush Scaffolds: A Comparison of Conventional and Catalyst-Free Cycloadditions for Tunable Surface Modification. *Langmuir* **2012**, *28* (41), 14693-14702.
20. Ma, Y.; Zheng, J.; Amond, E. F.; Stafford, C. M.; Becker, M. L. Facile Fabrication of "Dual Click" One- and Two-Dimensional Orthogonal Peptide Concentration Gradients. *Biomacromolecules* **2013**, *14* (3), 665-671.
21. Orski, S. V.; Poloukhine, A. A.; Arumugam, S.; Mao, L.; Popik, V. V.; Locklin, J. High Density Orthogonal Surface Immobilization via Photoactivated Copper-Free Click Chemistry. *J. Am. Chem. Soc.* **2010**, *132* (32), 11024-11026.
22. Barner-Kowollik, C.; Du Prez, F. E.; Espeel, P.; Hawker, C. J.; Junkers, T.; Schlaad, H.; Van Camp, W. "Clicking" Polymers or Just Efficient Linking: What Is the Difference? *Angew. Chem. Int. Ed.* **2011**, *50* (1), 60-62.

Chapter 3

Copper-free click biofunctionalization of silicon nitride surfaces *via* strain-promoted azide-alkyne cycloaddition reactions



Cu-free “click” chemistry is explored on silicon nitride surfaces as an effective way for site-specific oriented immobilization of biomolecules.

—————

This chapter has been published as:

Manova, R. K.; Pujari S. P.; Weijers, C. A. G. M.; Zuilhof, H.; and van Beek, T. A. *Langmuir*. **2012**, *28*, 8651-8663.

ABSTRACT

Cu-free “click” chemistry is explored on silicon nitride (Si_3N_4) surfaces as an effective way for site-specific oriented immobilization of biomolecules. An ω -unsaturated ester was grafted onto Si_3N_4 using UV irradiation. Hydrolysis followed by carbodiimide-mediated activation yielded surface-bound active succinimidyl and pentafluorophenyl ester groups. These reactive surfaces were employed for the attachment of bicyclononyne with an amine spacer, which subsequently enabled room-temperature strain-promoted azide-alkyne cycloaddition (SPAAC). This stepwise approach was characterized by means of static water contact angle, X-ray photoelectron spectroscopy and fluorescence microscopy.

The surface-bound SPAAC reaction was studied with both a fluorine-tagged azide and an azide-linked lactose, yielding hydrophobic and bioactive surfaces for which the presence of trace amounts of Cu ions would have been problematic. Additionally, patterning of the Si_3N_4 surface using this metal-free click reaction with a fluorescent azide is shown. These results demonstrate the ability of the SPAAC, as a generic tool for anchoring complex molecules onto a surface under extremely mild, namely ambient and metal-free, conditions in a clean and relatively fast manner.

3.1 Introduction

Silicon nitride (Si_3N_4) is an important non-oxide ceramic material with numerous applications.¹ Due to its outstanding tribological and mechanical properties, silicon nitride films are widely applied to improve mechanical characteristics and wear resistance of polymeric materials and electronic devices.^{2, 3} Silicon nitride coatings are also a resistant barrier to diffusion of sodium ions and moisture.⁴ Therefore, this ceramic is commonly deposited in the microelectronic industry as a passivation layer in, for instance, integrated circuits and solar cells.^{5, 6, 7} On the other hand, being not only an insulator, but also a material with excellent biocompatibility, Si_3N_4 has received considerable attention in biosensing^{8, 9} and medical applications.^{10, 11} Combined with silicon or silicon oxide, Si_3N_4 is the preferred material for microcantilever-based biosensors,^{12, 13} for integrated optical waveguides,¹⁴ and for functionalized AFM

cantilevers.¹⁵ Thus, it has potential application in bio-micro and nano electro-mechanical systems (bio-MEMS/NEMS).

When used as the final passivation layer in biosensing devices, a functionalization scheme for this insulator is of paramount importance. Up to date, only a few strategies for surface modification of Si₃N₄ have been reported. Silanization of the native SiO₂ layer on the Si₃N₄ film, is the prevalently used method for immobilization of biomolecules.^{14, 16, 17} However, a major problem is that the resulting Si-O-Si-C linkage is prone to hydrolysis. Thus, organosilane monolayers are somewhat difficult to reproduce, and are known to have a somewhat lower stability than e.g. Si-C based layers.^{18, 19} Less explored alternative for covalent bond formation onto oxide-free Si₃N₄ films is the use of alkyl halides towards the surface NH₂ / =NH moieties is an option.²⁰ The reactivity of the Si-N-H moieties was employed for selectively functionalizing silicon nitride in the presence of silicon oxide for biosensor platforms.²¹ However, the obtained density of attached molecules was well below²² that of a densely packed monolayer, which will likely hamper the long-term stability. A more promising approach involves the Si-H bonds for the formation of stable covalently bonded monolayers through interfacial Si-C bonds. Due to their extremely high stability (e.g. stable under heating at pH = 11),^{23, 24} reproducibility and higher density, these monolayers are superior and therefore the method of choice. Nevertheless, the relatively harsh reaction conditions necessary for modifying Si₃N₄ (prolonged heating at 165 °C or overnight irradiation with UV 254 nm) are not compatible with direct anchoring of labile molecules. Biofunctionalization of monolayers onto Si₃N₄ thus requires a stepwise grafting approach yielding a tailored monolayer, which is highly reactive towards the final biosensing component.^{25, 26}

A variety of catalyst-free reactions proceeding at ambient temperature has been explored for surface modification.²⁷ For example, a Diels-Alder reaction has been used for attaching cells to SAMs,²⁸ while a Wolff rearrangement of pending diazoketo groups of polymer material was demonstrated to be useful not only for attaching cells but also for the covalent attachment of DNA and proteins.²⁹ Also “photo-click” reactions like a Diels-Alder photo-click reaction,³⁰ and thiol-ene click reactions have been applied.^{31, 32, 33, 34} The thiol-ene click

reactions can proceed under solvent-free conditions and they allow a facile photopatterning for making 2D or even 3D structures.³⁵

The copper(I)-catalyzed azide-alkyne cycloaddition (CuAAC)^{36, 37} is the most eminent “click” reaction and extensively used for conjugate preparation of proteins,³⁸ glycans,³⁹ lipids,⁴⁰ and for functionalization of polymers.^{41, 42} Additionally, this “click” chemistry provides very attractive opportunities for bioconjugation of the surfaces. Furthermore it can be performed under ambient conditions, with readily available starting materials, affording a triazole linker with an excellent chemical stability. Therefore, the CuAAC is widely used on surfaces, for instance, on graphene,⁴³ nanoparticles,⁴⁴ silicon,^{45, 46, 47} gold,⁴⁸ diamond,⁴⁹ and silica surfaces.⁵⁰ While the reaction efficiency of such surface attachments onto alkyne-terminated surfaces is sometimes low (*ca.* 7%)⁴⁶ to satisfactory (40%),⁵¹ optimization of the reaction conditions can even lead to quantitative surface attachment.⁵² Additionally, such “clickable platforms” were applied as an efficient strategy for PEGylation of the surfaces⁵³ and for immobilization of biomolecules like peptides,⁵⁴ oligonucleotides,⁵² and mannose moieties.^{47, 55}

Although a robust, orthogonal and efficient reaction, CuAAC on a surface is sometimes carried out under conditions that are incompatible with the group to be attached or the envisioned application. For example, microwave irradiation,⁵⁶ heating for prolonged time,⁵¹ and high concentrations of copper ions may be detrimental for the attached moieties. Moreover, the use of Cu ions is incompatible with certain applications,⁵⁷ as, for instance, copper can quench the fluorescence of quantum dots.⁵⁸ In addition, Cu ions may disrupt the monolayer conductivity,⁵⁹ are cytotoxic,^{38, 60} can cause denaturation of proteins,⁶¹ degradation of oligonucleotides⁶² and polysaccharides,⁶³ all of which may be disadvantageous for biosensor platforms. Finally, to carry out the reaction and to remove any remaining metal ions from the surface, a polar solvent is required. The use thereof may alter the surface properties, while in addition trace amounts of entrapped copper ions may be hard to remove.⁶⁴ As a consequence, Cu-free click reactions have recently received considerable attention.

An elegant approach to circumvent the metal catalysis in surface modification is reactive microcontact printing (μ CP). With this technique an acetylene-bearing molecular ink is brought into close contact to an azide-terminated SAM on a surface using an elastomeric stamp. The subsequent Huisgen 1,3-dipolar cycloaddition is accelerated due to the local high concentration of the reagents on the stamp. Although this approach was successfully applied for deposition of alkyne-modified DNA,^{65, 66} μ CP of alkyne-modified carbohydrates without Cu turned out to be inefficient.^{67, 68, 69}

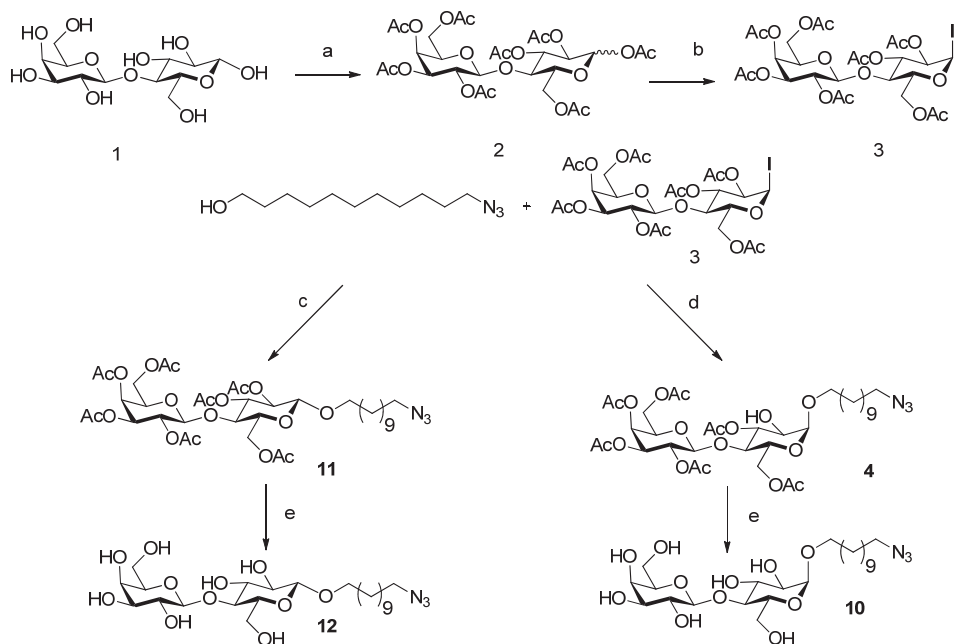
Alternatively, the strain-promoted azide-alkyne cycloaddition reaction (SPAAC) introduced by Bertozzi and co-workers,⁷⁰ opens up a new perspective for metal-free click reactions. Derivatives of cyclooctyne^{71, 72} were designed and SPAAC reactions have found a wide application in cell labeling,^{73, 74, 75} bioconjugation,⁷⁶ and polymer functionalization.⁷⁷ However, there are only few applications of strain-promoted “click” reactions reported on inorganic surfaces.^{78, 79} So far, no research has been found that surveyed “click” chemistry on silicon nitride films.

Owing to the wide scope of applications of strain-promoted “click” reactions and accessibility of such activated alkynes, the aim of this study was to evaluate the potential of this type of “click” chemistry on a surface. Here we describe a versatile, simple and reliable stepwise method for the functionalization of Si_3N_4 with covalently attached organic monolayers. These monolayers are built-up via a four-step consecutive surface-bound organic reaction sequence, with as a final step a SPAAC reaction with a commercially available ring strain-activated cyclooctyne derivative and a series of azides (a fluorescent dye, a perfluorinated compound and oligosaccharides). The resulting surfaces are investigated in detail by contact angle measurements, extensive XPS analysis and fluorescence microscopy, and the obtained variety of surface properties is used to indicate the potential of this approach towards surface functionalization.

3.2 Materials and methods

3.2.1 Chemicals and materials

All chemicals and solvents were purchased from Sigma-Aldrich and used as received unless stated otherwise. Dichloromethane (DCM, Fisher) and petroleum ether 40/60 were distilled prior to use. Other used solvents were, hydrochloric acid (p.a. 37%, Riedel de Haën), acetone (semiconductor grade, Riedel de Haën) and ultrapure water (18.2 M Ω .cm). The wafers with stoichiometric LPCVD Si₃N₄ coating (135 nm thickness, 4 nm roughness) were generous gifts by The Fraunhofer Institute for Microelectronic Circuits and Systems, Duisburg, Germany. The Si₃N₄ was deposited on a polycrystalline silicon film, coated onto SiO₂/Si p-type(100) wafers. The cyclooctyne derivative N-(1R,8S,9s)-bicyclo[6.1.0]non-4-yn-9-ylmethoxycarbonyl 1,5-diaminopentane (**7**) was purchased from SynAffix, B.V., The Netherlands and was kept at -20 °C before use. 2,2,2-Trifluoroethyl undec-10-enoate (TFE)²⁴ and N-hydroxysuccinimidyl undec-10-enoate⁸⁰ were prepared as described elsewhere. 11-Azido-1-undecanol was synthesized from 11-bromo-1-undecanol and sodium azide according to a literature procedure.⁸¹ 4,4,5,5,6,6,7,7,8,8,9,9,9-Tridecafluorononyl azide (**8**) was purchased from Sigma-Aldrich. Alexa Fluor® 555 azide (**9**) and the fluorescent labeled lectin Alexa Fluor® 647 conjugate of PNA from *Arachis hypogaea* (peanut) were supplied by Invitrogen.



Scheme 3.1: Synthesis of 11-azido-undecyl-lactoside (α or β). (a) Ac₂O, I₂, 35 °C, 6 h; (b) I₂, HMDS in CH₂Cl₂, RT, 16 h; (c) I₂, MeCN (β), RT, 0 °C → RT; (d) I₂, CH₂Cl₂ (α), RT, 0 °C → RT, 16 h; (e) NaOMe in MeOH, RT, 16 h.

3.2.2 Synthesis of 2,3,4,6-tetra-*O*-acetyl- β -D-galactopyranosyl-(1→4)-2,3,6-tri-*O*-acetyl- α -D-glucopyranosyl iodide (3) (Scheme 3.1).

The per-*O*-acetylation of lactosyl iodide (3) was carried out as described elsewhere⁸² with some modifications. Briefly, to a suspension of lactose (1) (3.40 g, 10 mmol) and acetic anhydride (7.8 ml, 82 mmol), iodine (50 mg, 0.20 mmol) was added, and the mixture was stirred under N₂ for 6 h at 35 °C, yielding the D-lactose octaacetate. After the complete conversion to the per-*O*-acetylated derivative (2), dry DCM (10 ml) was added, followed by iodine (2.53 g, 10 mmol) and hexamethyldisilane (2.08 ml, 10 mmol). The reaction mixture was stirred for 20 h at room temperature. After completion, the mixture was diluted with DCM and quenched with a 10% aqueous solution of Na₂S₂O₃. The organic layer was further washed with saturated NaHCO₃ and saturated NaCl solution, and dried over Na₂SO₄. Subsequently, the organic phase was filtered and

concentrated under reduced pressure to yield a white solid. Purification of this crude product by column chromatography (eluent: petroleum ether / ethyl acetate 1:1) yielded 2,3,4,6-tetra-*O*-acetyl- β -D-galactopyranosyl-(1 \rightarrow 4)-2,3,6-tri-*O*-acetyl- α -D-glucopyranosyl iodide (**3**) (5.66 g, 7.6 mmol, 76%).

3.2.3 Synthesis of β -D-galactopyranosyl-(1 \rightarrow 4)-1-(11-azido-undecanyl)- α -D-glucopyranoside (**10**)

The lactosides **10**, **11**, **12** were synthesized according to a literature procedure.⁸³ Briefly, a solution of **3** (3.00 g, 4.0 mmol), 11-azido-1-undecanol (1.70 g, 8 mmol) and mol sieves (2.0 g, 4 Å) in dry dichloromethane (10 ml) was cooled to 0 °C under nitrogen. After adding iodine (2.03 g, 8 mmol) the mixture was allowed to stir overnight, and to warm up to room temperature. The reaction mixture was diluted with ethyl acetate (120 ml) and filtered. The filtrate was subsequently washed with 1 M Na₂S₂O₃ solution (2 \times 75 ml). The ethyl acetate layer was further washed with brine (1 \times 75 ml), dried (Na₂SO₄), filtered and finally concentrated under reduced pressure. Purification of this crude product by column chromatography (eluent: petroleum ether / ethyl acetate 1:1) yielded 2,3,4,6-tetra-*O*-acetyl- β -D-galactopyranosyl-(1 \rightarrow 4)-1-(11-azidoundecanyl)-3,6-di-*O*-acetyl- α -D-glucopyranoside (**4**) as a colorless syrup (1.32 g, 2.5 mmol, 61%). This hexa-*O*-acetylated derivative (1.10 g, 1.32 mmol) was dissolved in dry methanol (10 ml) and a solution of sodium methoxide in methanol (1.0 M, 0.12 ml) was added. The mixture was allowed to stir overnight during which a white suspension formed. After complete conversion, as shown by TLC on silica (eluent: ethyl acetate), the mixture was quenched by adding Amberlite 120 H, until the pH reached 7. The reaction mixture was filtered over celite and the filtrate was concentrated under reduced pressure to afford the β -D-galactopyranosyl-(1 \rightarrow 4)-1-(11-azido-undecanyl)- α -D-glucopyranoside (**10**) as a cream-colored solid (0.70 g, 1.3 mmol, 98%).

3.2.4 Synthesis of 2,3,4,6-tetra-*O*-acetyl- β -D-galactopyranosyl-(1 \rightarrow 4)-1-(11-azidoundecanyl)-2,3,6-tri-*O*-acetyl- β -D-glucopyranoside (**11**)

Performing the 11-azido-1-undecanol (1.70 g, 8 mmol) glycosylation with **3** (3.0 g, 4 mmol) in acetonitrile changes the stereospecificity. The glycosylation reaction resulted in the formation of a colorless syrup of 2,3,4,6-tetra-*O*-acetyl-

β -D-galactopyranosyl-(1 \rightarrow 4)-1-(11-azidoundecanyl)-2,3,6-tri-O-acetyl- β -D-glucopyranoside (**11**) (32%, 1.05 g, 1.32 mmol).

3.2.5 Synthesis of β -D-galactopyranosyl-(1 \rightarrow 4)-1-(11-azidoundecanyl)- β -D-glucopyranoside (**12**)

After deprotection of **11**, performed in a similar fashion as described above, β -D-galactopyranosyl-(1 \rightarrow 4)-1-(11-azidoundecanyl)- β -D-glucopyranoside (**12**) was obtained in quantitative yield. The spectroscopic characterization of **10**, **11** and **12** is provided in the Appendix 1.

3.3 Monolayer formation

Primary modification. Preceding the modification, silicon nitride substrates were cleaned and etched as follows. After rinsing with acetone, the substrates were cleaned by sonication in acetone for 10 min, dried with argon, and treated with air-based plasma for 15 min. Immediately afterwards, the oxidized surfaces were etched for 2.5 min in 2.5% HF solution. Subsequently, the etched Si₃N₄ surfaces were dried with argon and transferred to a custom-made quartz flask for surface modification.

The photochemical modification of Si₃N₄ was performed as previously described.²⁴ Neat alkene was transferred to the quartz reactor connected to a Schlenk line with a vacuum line and an argon inlet. The alkene (TFE) was deoxygenated by three consecutive freeze-pump-thaw cycles, after which the liquid was frozen again under argon atmosphere. The freshly etched Si₃N₄ substrate was introduced in the reactor during the last cycle, when the alkene was still frozen. Immediately afterwards, the reactor was closed and vacuum was applied and maintained until the alkene had molten completely. After 30 min under an argon flow, two UV pen low-pressure mercury lamps (254 nm, 9.0 mW/cm², Jelight, USA) were placed in front of the Si₃N₄ specimen at approximately 0.5 cm distance. The reactor was enclosed in aluminum foil, and the sample was irradiated for 9 h. After irradiation, the sample was removed, cleaned by rinsing thoroughly with dichloromethane, sonicated in the same solvent for 10 min and dried under argon.

Secondary modification: basic hydrolysis. TFE-terminated surfaces were exposed to a solution of 250 mM potassium *tert*-butoxide and 60 mM water in dry dimethyl sulfoxide (DMSO) for 10 - 12 min at room temperature. The samples were rinsed with DMSO, 1 M HCl, and acetone, then sonicated for 10 min in the same solvents and finally dried under argon.

Tertiary modification: (A) N-hydroxysuccinimide ester (NHS) formation. Acid-terminated samples were modified in 1.5 ml of a solution of *N,N'*-dicyclohexylcarbodiimide (DCC, 0.4 M) and *N*-hydroxysuccinimide (NHS, 0.4 M) in anhydrous DMSO for 4 h at room temperature. The solution was stirred using a magnetic stirring bar encompassed in a wider glass ring, above which the acid-terminated specimen was placed. In this way, the sample was protected from mechanical damage. Afterwards, the samples were rinsed with DMSO, acetone and sonicated in the same solvents prior to drying with argon.

Tertiary modification: (B) pentafluorophenyl ester (PFP) formation. Acid-terminated samples were placed in 1.5 ml of a solution of 2,3,4,5,6-pentafluorophenol (PFP, 0.4 M) and DCC (0.4 M) in dichloromethane. The reaction mixture was stirred for 4 h at room temperature. The PFP-terminated samples were rinsed with copious amounts of dichloromethane, sonicated in this solvent and dried under argon.

Quaternary modification: amide formation. The reactivity of NHS-terminated surfaces was tested with a 0.1 M solution of 4-(trifluoromethyl)benzylamine (*p*-CF₃-PhCH₂NH₂, 97%) in DMSO as described previously.²⁴ Additionally, the NHS-functionalized specimens were tested with trifluoroethylamine (CF₃CH₂NH₂, 0.7 M in DMSO) in a similar way. The samples were rinsed and sonicated subsequently in DMSO and acetone prior to the surface analysis.

Quaternary modification: alkyne functionalization and SPAAC reaction on surface. The attachment of cyclooctyne **7** onto the surface was performed by dipping NHS-terminated or PFP-terminated samples in a solution of **7** (20 mM) in dichloromethane, under argon at room temperature for 4 h. Immediately afterwards, the specimens were rinsed with copious amounts of dichloromethane and immersed in a 10 mM azide solution for azides **8**, **10-12** (see Figure 3.6) and 8.8 mM for azide **9**. The reactions were carried out at room

temperature, without excluding the air from reaction vials and stopped after 24 h. The duration of the SPAAC reaction with the azide **8** was varied from 0.3 to 24 h.

Patterning. Patterning experiments were performed according to the literature.⁸⁴ Briefly, patterning experiments were performed in a glovebox (MBraun MB200G with a gas purification unit MBraun MB20G) under an argon atmosphere and a content of H₂O and O₂ each below 0.1 ppm. Degassed TFE was added to freshly etched surface till a thin liquid layer formed, afterwards an electron microscopy grid (SEM F1, Au, Gilder Grids) with various mesh numbers was placed on top, followed by a fused quartz cover. The specimen was thus locally irradiated with two UV pen lamps ($\lambda = 254$ nm) for 9 h. Black paper was used to cover the setup and to minimize light scattering and reflection. After irradiation, the samples were cleaned with dichloromethane and sonicated in the same solvent. Next, the sample was treated as described above to carry out the hydrolysis step (secondary modification), formation of the PFP ester (tertiary modification), attachment of **7** and subsequent SPAAC reaction with azide **9** (Figure 3.6).

3.4 Surface characterization

3.4.1 Water contact angle measurements.

Static water contact angle measurements were carried out using a Krüss DSA-100 goniometer. Drops of 3 μ L of deionized water were automatically dispensed on a surface and the water contact angles were determined numerous times for each drop with a CCD camera using a tangential method. The error in the contact angles is less than 2°.

3.4.2 X-ray Photoelectron Spectroscopy (XPS)

XPS analyses were performed using a JPS-9200 photoelectron spectrometer (JEOL). The spectra were obtained under ultrahigh vacuum (UHV) conditions using monochromatic Al K α X-ray radiation at 12 kV and 20 mA, using an analyzer pass energy of 10 eV. The X-ray incidence angle and the electron

acceptance angle were 80° and 10° to the surface normal, respectively. Due to the electrostatic charging in the positive direction on the surface, a charge compensation was used during the XPS scans with an accelerating voltage of 2.8 eV and a filament current of 5.00 A. Afterwards the spectra were reprocessed with the CASA XPS peak fit program (version 2.3.15) using the alkyl C 1s component calibrated at 285.0 eV. For the curve fitting of C 1s spectra, linear background subtraction and a Gaussian/Lorentzian peak shape model G(30) were used. The full widths at half maximum (FWHM) were constrained to be equal for all peaks within one spectrum, resulting in FWHM values ranging from 0.9 to 1.4 eV. Following the approach of Yang et al.⁸⁰ the yield of the surface reaction was calculated by comparing the experimental peak intensity ratios with the theoretically expected ratios, i.e. by comparing the peak intensity of a distinguishable C 1s emission versus the intensity of the CH₂ peak in the high-resolution C 1s spectrum or by using the C/F atomic ratio derived from the XPS survey spectrum. All approximate yields are relative setting the surface **S1** (Figure 3.1) as 100%. Following the stepwise approach of surface modification, the resulting mixture of different adlayers on the surface complicates the correction of the peak intensity due to the XPS signal attenuation. Therefore no correction was applied, and the reported yields are uncorrected upper limits, which likely deviate up to a few percent from the real values.

3.4.3 XPS thickness calculation

For the purpose of thickness calculations of the organic adlayers after each consecutive reaction, we used the average attenuation length for organic films according to Eqn (1),⁸⁵

$$L = 0.00837 \cdot E^{0.842} \quad (1)$$

where L is the attenuation length in nm and E is the electron kinetic energy in eV. The film thickness was determined using an uniform overlay model according to Eqn (2):

$$I = I^0 \cdot \exp\left[\frac{-t}{L \times \cos\theta}\right] \quad (2)$$

where I = measured intensity of Si 2p with a carbon overlayer with a thickness t , I^0 = intensity of Si 2p of an unmodified, cleaned substrate, t = thickness of the adsorbed layer in nm, L = attenuation length of Si 2p electrons in the hydrocarbon layer, derived from equation (1), and θ = photoelectron emission takeoff angle relative to the surface normal ($\theta = 10^\circ$).

3.4.4 Density Functional Theory (DFT)

Electronic Core Level Calculations (ECC) were used to simulate core levels of C 1s XPS spectra. All ECC were done with the GAUSSIAN09 program.¹³ The effect of the bulk substrate on Si-C bound monolayers was mimicked by attaching the organic species to a $(\text{NH}_2)_3\text{Si}$ - moiety. The geometries of the different systems were optimized at the B3LYP/6-311G(d,p) level of theory. Natural bond orbital (NBO) analysis⁸⁶ was employed to obtain the core orbital energies. Assuming that the core orbital energy levels are directly related to the binding energies (BE) of the core electrons, the DFT calculations can be compared with the XPS spectrum. Due to the difference in reference energy between theory and experiment,⁸⁷ absolute values of calculated BE were referenced to the measured BE of CH_2 moieties in the aliphatic hydrocarbon chain by multiplying with a scaling factor (1.0438) and the energy differences ΔBE were used to simulate XPS spectra.⁸³ An assumption for equal contribution by each carbon atom was made and for every carbon atom a Gaussian centered at the corresponding BE was used with an FWHM of 0.94 eV. The simulated XPS spectra were used to facilitate the peak fitting procedure for overlapping contributions in the experimental XPS data.

3.4.5 Confocal Laser Scanning Microscopy

Laser scanning microscopy or FCS data were obtained using a Zeiss Axiovert 200M inverted microscope and an AxioCam MRm camera. The following settings were kept constant for all measurements, unless stated otherwise: 10.0 \times objective magnification (EC Plan-Neofluor 10 \times /0.30 M27), laser intensity (10 - 15%), photomultiplier (700 V), image size (512 \times 512 pixels), pixel dwell 25.61 μsec , scan time 11.33 scans/ μsec , averaging of four measurements, and no zoom factor. The argon laser HeNe543 (1.2 mW) and HeNe633 (5.0 mW) were utilized to excite the labeled PNA lectin and Alexa Fluor® 555 azide on the

surface at 543 nm and 633 nm, with the emission scanned above 560 and 650 nm, respectively.

3.5 Results and discussion

The UV (254 nm) photochemical attachment method²⁴ was employed to attach covalently grafted monolayers onto silicon nitride. In order to avoid possible side-reactions and due to the limited thermal stability of the angle-strained cycloalkyne,⁷⁴ a tailor-made monolayer was grafted in several steps, to allow facile anchoring of **7** on a surface.

3.5.1 Formation of the NHS ester on silicon nitride surface using a one-step modification

As a first attempt, NHS-terminated monolayers were prepared by linking an NHS-terminated-1-alkene (N-hydroxysuccinimidyl undec-10-enoate) photochemically to HF-etched Si₃N₄. A similar one-step method was successfully employed on hydrogen-terminated silicon⁸⁰ and glass,⁸⁸ and can yield a surface that reacts efficiently with amines, typically clean and straightforward at room temperature. In this manner, the commercially available cyclooctyne *N*-(1R,8S,9s)-bicyclo[6.1.0]non-4-yn-9-ylmethoxycarbonyl 1,5-diaminopentane (**7**) with a terminal amine group can be attached in a facile and mild manner, preserving the highly reactive and strained cyclooctyne ring of **7** for subsequent copper-free click reactions (Figure 3.1).

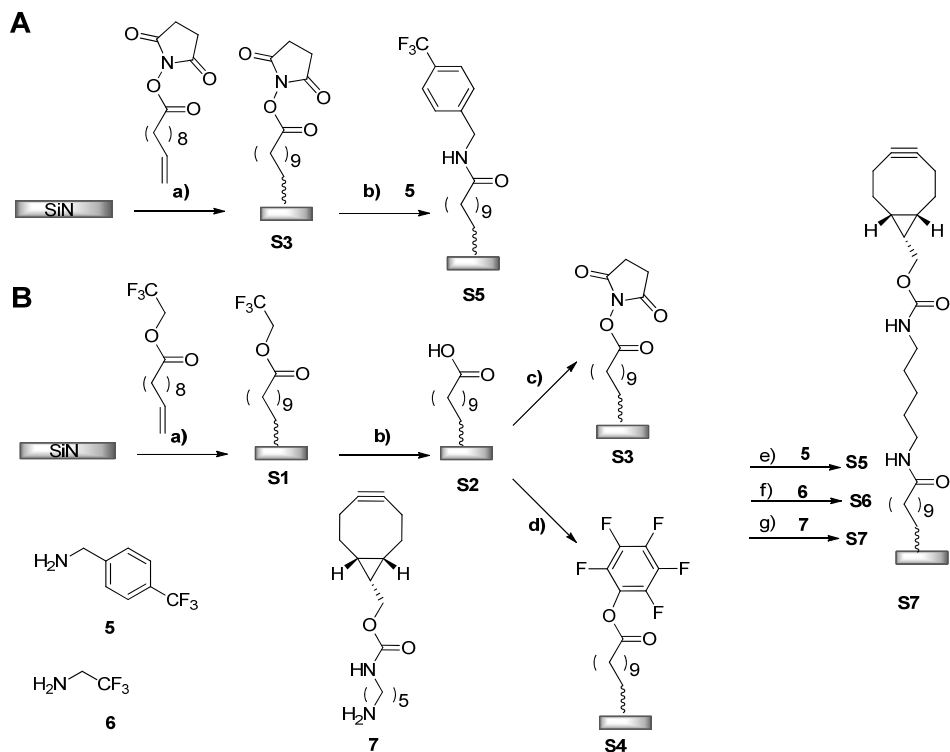


Figure 3.1: **A.** Preparation of an NHS-terminated monolayer on Si_3N_4 using (a) one-step photochemical modification with *N*-hydroxysuccinimidyl decanoate (9 h, 254 nm) and (b) subsequent testing of the surface with amine **5**, 100 mM in DMSO, giving an (incomplete) surface **S5**. **B.** Preparation of an NHS-terminated monolayer on Si_3N_4 using a multiple reaction approach; (a) UV-assisted grafting of TFE on a Si_3N_4 surface affording surface **S1**, (9 h, 254 nm); (b) hydrolytic deprotection giving an undecanoic acid-terminated monolayer **S2**, 10 min, 250 mM *t*-BuOK in DMSO; (c) activation through an NHS active ester (surface **S3**), 400 mM NHS, 400 mM DCC in DMSO; (d) activation through a PFP active ester (surface **S4**), 400 mM PFP and 400 mM DCC in DCM; (e) attachment of **5**, 100 mM in DMSO, giving a (complete) surface **S5**; (f) attachment of **6**, 700 mM in DMSO, yielding the corresponding surface **S6**; (g) attachment of bicyclononyne **7**, 20 mM in DCM, giving a clickable surface **S7**.

However, in case of the Si_3N_4 surface, the UV grafting of this NHS-terminated-1-alkene turned out to be inefficient. The surface analysis with XPS, showed lack of consistency with the previously reported data.^{80, 89} The C 1s high-resolution spectrum revealed broad peaks from overlapping emissions, mainly from $\underline{\text{C}}\text{-N}$ and amides ($\text{-}\underline{\text{C}}(\text{=O})\text{-NH}$) (Figure 3.2b).

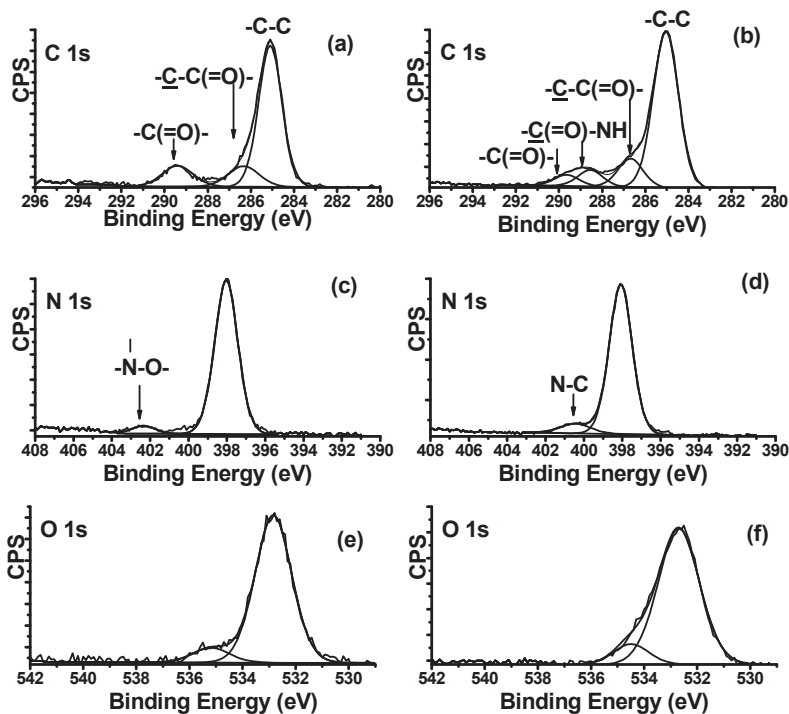


Figure 3.2: XPS characterization of NHS ester on Si_3N_4 surfaces. High resolution spectra of (a) C 1s, (c) N 1s and (e) O 1s after stepwise formation of NHS and (b) C 1s, (d) N 1s and (f) O 1s after direct attachment of NHS-UA on the surface.

The O 1s narrow scan showed negligible emission of an ester functionality on the surface (Figure 3.2f). In addition, the N 1s emission with a BE of 402.3 eV, which is a chemical shift typical for an NHS moiety, was not detected. Instead, amide bond formation was revealed by the emission at 400.2 eV (Figure 3.2d). The resulting spectrum suggested significant upside-down attachment and

possible reaction with surface groups such as NH or NH₂ formed after the etching of the substrates.⁹⁰ To confirm the ineffective attachment of the alkene, the NHS-terminated monolayer was reacted with a fluorine-tagged amine **5** (*p*-CF₃PhCH₂NH₂). Since only 14% successful attachment was demonstrated, a stepwise reaction approach was developed to produce a surface with active ester groups.

3.5.2 Formation of a trifluoroethyl ester-terminated monolayer on Si₃N₄

The stepwise procedure started with the photochemical formation of a trifluoroethyl ester (TFE) monolayer. This ester can be grafted onto silicon nitride substrates in an intact manner,²⁴ affording a stable monolayer, which after deprotection and active ester formation on a surface, can be used for the covalent attachment of amines.⁹¹

Once introduced onto the surface the trifluoroethyl group facilitated the surface characterization by means of XPS, and optimization of the reaction time could be easily achieved. Figure 3.3 shows the XPS C 1s narrow scan of the TFE monolayer on Si₃N₄ after 9 h of UV irradiation. The spectrum was deconvoluted in five main peaks and each was assigned to the different carbons present in the attached TFE monolayer (Figure 3.3).

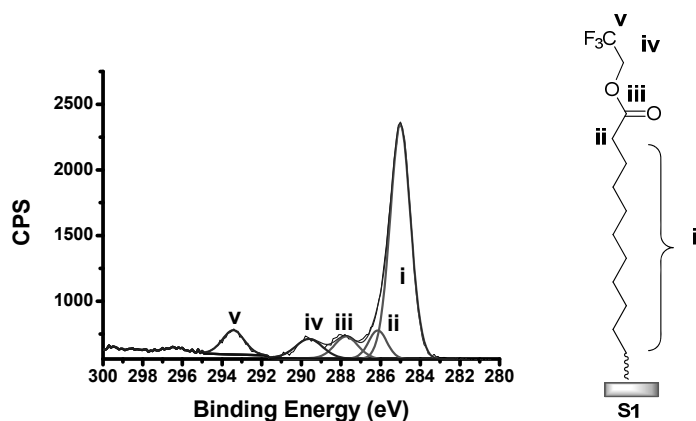


Figure 3.3: C 1s narrow scan XPS spectrum of film **S1** with deconvolution. (i) aliphatic carbons with a BE 285.0 eV, (ii) α -carbon adjacent to the carbonyl (286.2 eV), (iii) methylene group next to the trifluoro carbon (287.8 eV), (iv) carbonyl (289.6 eV) and (v) trifluoro carbon (293.4 eV).

The relative areas of those signals are in good agreement with the expected 1 : 1 : 1 : 1 : 9 molar ratio. The survey spectrum revealed a C/F ratio of 4.5, which agrees well with the expected theoretical value of $13/3 = 4.33$. For this monolayer a C/Si ratio of 1.2 was found. In a former study²⁴ the optimal reaction time for the grafting of this alkene on silicon-rich silicon nitride was found to be 24 h. In our work, 24 h for the grafting of TFE onto stoichiometric Si_3N_4 was too long, since the resulting C 1s narrow scan demonstrated an unexpectedly high peak for the alkyl C-C contribution (ratio of 1 : 1 : 1 : 1 : 14), combined with both higher C/F (7.3) and C/Si (5.9) ratios, which suggested overlayer formation. While the water contact angle θ remained 87° – in good agreement with previously reported TFE monolayers on silicon^{91, 92} – the XPS-calculated thickness of 5.1 nm indeed confirmed overlay formation after such extended irradiation.

After optimization, the optimal time of irradiation was found to be 9 h and was chosen for all consecutive experiments. The water contact angle of the thus optimized TFE-terminated surface was 88° , i.e. in good agreement with previously reported values.^{91, 92}

Based on these data the bonding after photochemical grafting of TFE onto Si_3N_4 substrates can only be described tentatively to occur via Si-C bonds. Rosso et al. have reported photochemical attachment of an alkene via both N and Si sites, and presumed a preference for C-N bond formation.²⁴ That conclusion was based on the higher contribution of C-N bonds (286.2 eV) in the C 1s spectra over the C-Si contribution (283.5 eV). In the current case of TFE attachment it was not feasible to fit the partially overlapping C-Si, C-C, C-N, C-O and C-C=O contributions unequivocally, so as to distinguish between C-Si and/or C-N bonding to the Si_3N_4 surface. We did not observe a N-C bond emission in the N 1s narrow scan spectra of these monolayers as was observed for Si-C-N films,⁹³ and which would be expected in the case of predominantly hydroamination of the alkene with surface NH_2 sites. Therefore we think attachment here is predominantly via Si-C bonds. However, the formation of some N-C bonds cannot be excluded. Although the bond energy of N-H (93.4 kcal/mol) is higher than of Si-H (70.4 kcal/mol), a selective breaking of N-H over Si-H under vacuum-ultraviolet irradiation on Si_3N_4 films has previously been observed.⁹⁴ In fact, the 254 nm irradiation has enough energy per photon

(4.88 eV) to break a wide variety of bonds including N-H (4.05 eV) and Si-H bonds (3.05 eV). Under these conditions, a surface coverage of TFE chains onto Si₃N₄ was estimated, by comparing the XPS C/Si signal in this system, with that of well-studied hexadecenyl monolayers on Si(111).⁹⁵ For TFE-surface **S1**, we observed that the C/Si ratio per carbon atom is 1.8 times higher as the C/Si ratio for these C₁₆ monolayers on Si. Taking into account that for Si₃N₄ only $\sim 3/7 = 43\%$ of the surface sites is a Si atom, and compensating for the difference in chain lengths (C₁₃ vs C₁₆) we estimate that monolayer **S1** has a density of 4.4×10^{14} molecules per cm² (57% surface coverage). This is in the same order of magnitude as the monolayers on Si(111) (4.6×10^{14} or 60% surface coverage), although the actual density may be slightly less, since the surface roughness of Si₃N₄ is higher than that of Si(111).

Table 3.1: Water Contact Angles θ of Films **S1–S4**, **S7**, **S8** and **S10–S12**

Films	S1	S2	S3	S4	S7	S8	S10	S11	S12
θ	88°	71°	72°	88°	74°	82°	61°	72°	53°
	±1.0°	±1.0°	±1.0°	±1.0°	±1.0°	±2.0°	±1.0°	±2.0°	±1.0°

3.5.3 Stepwise deprotection and active NHS ester formation on Si₃N₄

The TFE-terminated monolayer was deprotected by basic hydrolysis (250 mM *t*-BuOK in DMSO, 10 min). This deprotection step and the subsequent formation of the NHS-terminated monolayer were followed by XPS and static water contact angle measurements in order to evaluate the overall efficiency of these consecutive reactions prior to the final attachment of an amine. The hydrolytic step was continued until there was no longer any CF₃ emission peak in the XPS spectrum. Under these conditions the remaining monolayer showed a decrease in the C/Si ratio of only 15%, which is mainly due to the removal of the CF₃CH₂- moiety. The water contact angle after hydrolysis was 71° (Table 3.1, entry **S2**) which was consistent with a carboxylic acid-terminated monolayer of undecanoic acid grafted with a one-step photochemical attachment onto diamond,⁹⁶ but exceeded the reported values for attachment onto silicon.⁹¹ The C 1s spectra after hydrolysis showed complete removal of

organic F, but a total disappearance of the F signal in the survey spectra was not achievable, mainly due to the Si-F bonds formed during the etching of the substrate. This fluorine contribution was subtracted when calculations based on an elemental composition were made. On silicon substrates, organic monolayers display some instability under basic conditions, thereby lowering the density of the carboxylic acid groups.⁹⁷ A monolayer on silicon nitride displays a significantly higher stability under basic conditions,²⁵ as confirmed here by the insignificant reduction of the total CH₂ contribution.

Despite the near-quantitative deprotection step, reaction of the acid-terminated surface with NHS did not afford a densely packed NHS-terminated surface. Similar observations have been reported for silicon.⁹⁸ The incomplete coverage with NHS esters is probably due to the complex carbodiimide-mediated mechanism of the reaction, which leads to the formation of byproducts during the activation step (*N*-acylurea) or side products (anhydrides between two adjacent COOH groups), which in both cases could interfere with the formation of new active sites on the surface.⁹⁸ However, the presence of NHS functionalities was confirmed by the C 1s, N 1s and O 1s XPS narrow scans (Figure 3.2 a, c, and e). The two O 1s peaks at 532.8 (oxygen in carbonyl group) and 535.5 eV (oxygen in C-O-N bonds) are characteristic for ester formation.⁸⁰ The experimental ratio of these two oxygen peaks of 6 : 1 exceeded the theoretically expected 3 : 1 ratio, which suggests an incomplete formation of the active ester. In the N 1s signal, characteristic emissions of nitrogen from the NHS moiety at 402.3 eV and the typical N 1s emission of the substrate at 398.1 eV (BE) were observed. The C 1s narrow scan revealed the same contributions as previously reported for well-defined monolayers obtained by direct UV-assisted grafting of the NHS ester of undecanoic acid onto silicon.⁸⁰ The spectrum was deconvoluted in three main contributions, as reported earlier.⁸⁰ However, the comparison of simulated XPS spectra by DFT calculations with the experimental spectrum revealed a too large contribution by the C-C bonds in the alkyl chain and confirmed once again incomplete coverage. The C 1s spectrum was fitted with three peaks centered at 285.0 (aliphatic carbons), 286.3 eV (α -CH₂) and 289.3 eV (carbonyl carbons), where the overlapping emissions from -COOH and ester moieties were summed

together. Based on this fitting model the percentage formation of NHS moieties on the surface was estimated at 40 - 60% (cf., surface **S1** = 100%).

In the next step, we aimed to determine to what extent the final NHS ester functionalities were available for amide formation, via the amidation with two fluorine-tagged amines, *p*-CF₃PhCH₂NH₂ and CF₃CH₂NH₂, followed by XPS. The final surface coverage based on the C/F atomic ratio derived from the survey spectra was 51 ± 6% (n=3) for *p*-CF₃PhCH₂NH₂, and 30 ± 6% (n=3) for the less reactive CF₃CH₂NH₂, calculated from the F/C ratio in the survey spectra. Furthermore, the introduced CF₃ group at BE 293.2 eV in the narrow scan of C 1s had an intensity which corresponded well with the surface coverage as determined from the elemental composition in the XPS survey scan.

3.5.4 Formation of the PFP ester on Si₃N₄ using stepwise modification

As an alternative to the commonly used NHS ester, pentafluorophenyl esters (PFP) can be used. Their formation has been little studied on inorganic substrates. As PFP esters have a reactivity that is ~10 times greater than that of NHS esters,^{99, 100} they could benefit from a decreased hydrolysis rate¹⁰¹ and additionally, PFP esters have the advantage of being easily analyzable by XPS.

The formation of PFP esters on carboxylic-acid terminated Si₃N₄ surfaces restored the hydrophobicity of the surface (Table 3.1, entry **S4**). Figure 3.4 depicts the C 1s and O 1s XPS narrow scans of **S4** films, following the stepwise functionalization. The oxygen emission demonstrated significant ester formation on the surface (Figure 3.4d). By comparison with the simulated C 1s XPS spectrum (Figure 3.4c), the experimental C 1s signal (Figure 3.4a) was deconvoluted into five components with binding energies corresponding to the alkyl C-C (285.0 eV; **i**), α-carbonyl carbon (286.1 eV; **ii**), the ipso aromatic carbon adjacent to the O atom (287.3 eV; **iii**), the five C-F atoms (288.5 eV; **iv**) and finally the carbonyl carbon (289.7 eV; **v**). The experimental ratio found for these peaks is 11.6 (**i**) : 1.3 (**ii**) : 1.0 (**iii**) : 3.7 (**iv**) : 1.0 (**v**), where the theoretical ratios would have been 9 : 1 : 1 : 5 : 1 in case of a 100% PFP ester surface coverage. Both the (**i**)/(**iv**) and (**v**)/(**iv**) ratios can be used to estimate the reaction yield, and give percentages of 58% and 74%, respectively (relative to

the original TFE monolayer $S1 = 100\%$). Analogously, the elemental composition of F and C derived from the survey spectrum yields a $67 \pm 5\%$ ($n=4$) surface coverage. In XPS measurements the alkyl peaks at 285 eV (i) are typically slightly too high, due to adventitious contamination, which has as an effect that the calculated yield is slightly underestimated. Therefore we estimate the reaction yield for the $S4$ surface is in the range of 67 - 74 %.

Using the thus formed PFP ester, a higher reactivity of this activated surface towards amines was observed. The reaction with $p\text{-CF}_3\text{PhCH}_2\text{NH}_2$, restored the CF_3 emission peak (293.0 eV) in the C 1s narrow scan and based on its area, a surface coverage of $67 \pm 12\%$ was calculated with respect to the total number of alkyl chains.

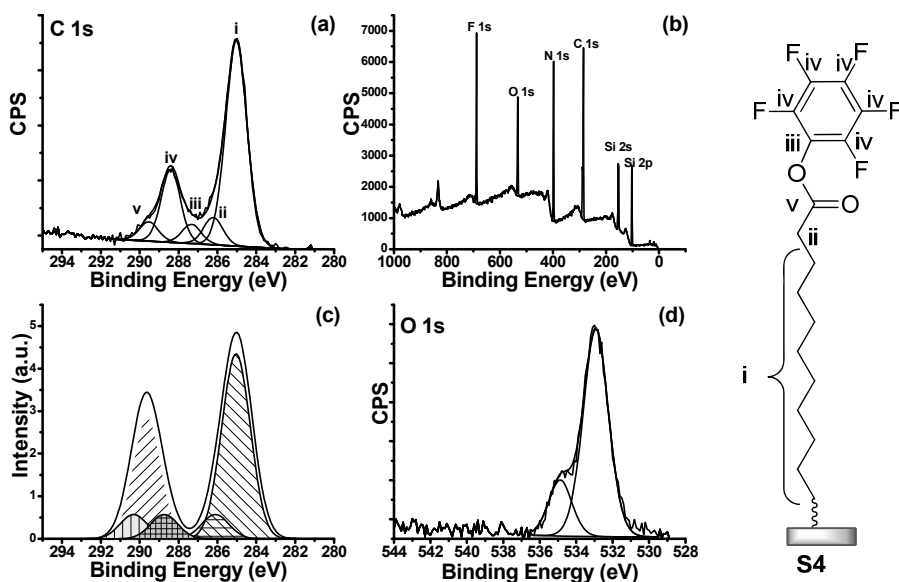


Figure 3.4: XPS data of PFP ester-functionalized Si_3N_4 (films $S4$); (a) C 1s XPS spectrum of films $S4$; (b) survey spectrum; (c) DFT-simulated C 1s spectrum and (d) O 1s spectrum.

3.5.5 Quaternary modification - alkyne functionalization and surface-bound SPAAC reactions.

The active ester platform was employed for reaction with an amine-linked cyclooctyne (**7**). Using a PFP-activated surface, the amidation with **7** reduced

the contact angle from 88° to 74° (Table 3.1, entries **S4** and **S7**) and reduced the F 1s signal intensity in the survey XPS spectrum to 1.5 At %. Based on the F/C ratio from the survey spectrum about 9% PFP ester functionalities remained of the original 69% PFP moieties (**S1** = 100%). This means that approximately 87% of the available PFP moieties were converted to cyclooctyne moieties (single step conversion), i.e. the approximate overall surface coverage of the cyclooctyne moieties (**S1** = 100%) is $0.87 \times 69\% = 60\%$ under the assumption that no significant hydrolysis took place under these reaction conditions. Supported by theoretical calculations (Figure 3.5b and Appendix 1), the C 1s spectrum **S7** was deconvoluted into four components (Figure 3.5a): a predominant C-C peak at 285.0 eV, a carbamate carbon ($-\text{O}-\underline{\text{C}}(=\text{O})-\text{NH}-$; 289.6 eV), a new peak due to an amide carbonyl atom ($-\text{NH}-\underline{\text{C}}(=\text{O})-$; 288.1 eV) and low binding energy contributions at 286.4 eV, assigned to the two nitrogen-bonded ($\underline{\text{C}}-\text{N}$) carbon atoms and one $-\underline{\text{C}}-\text{O}-\text{C}(=\text{O})-$ carbon. The C-N and C-O contributions are too close to allow resolution, thus they were summed together. Likewise the contributions of C-C, C-Si and carbons from the acetylene groups were summed together.

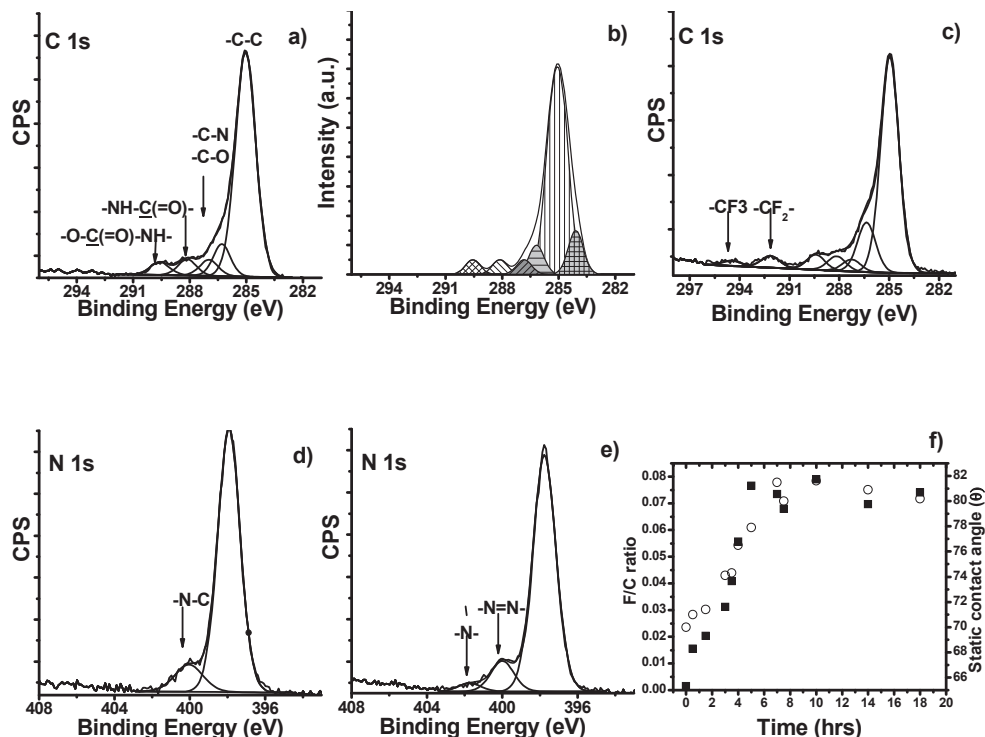


Figure 3.5: (a) C 1s XPS high resolution spectrum of **S7** and (b) simulated core level C 1s XPS spectra for **S7**; (c) C 1s of **S7** after “click” reaction with **8**; (d) N 1s of **S7** before and (e) after the SPAAC reaction with **8** to form **S8**; (f) progress of the SPAAC reaction with **8**, monitored with F/C elemental composition (squares; left scale), and static water contact angles (circles; right scale).

3.5.6 Cu free click functionalization on alkyne-terminated surface

To illustrate the utility of the strain-promoted click approach for anchoring functionalities onto a surface in an oriented fashion, four representative azides were selected to react with cyclooctyne-terminated substrates (**8-12**) (see Figure 3.6).

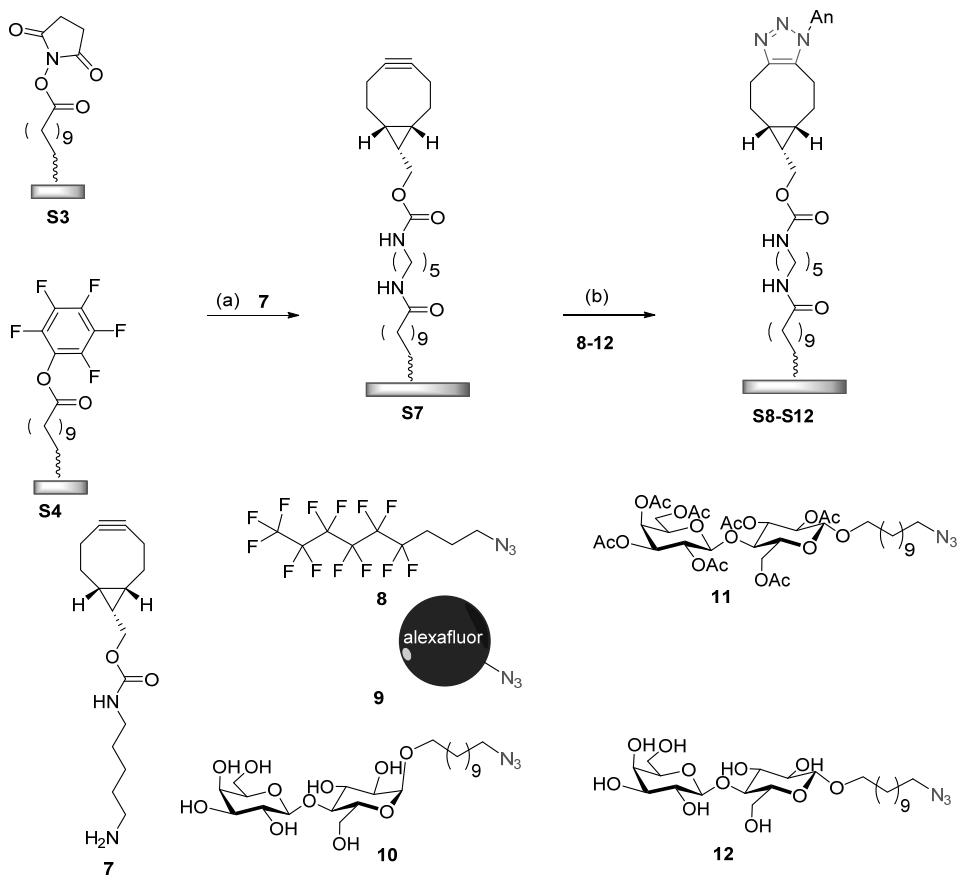


Figure 3.6: Strain-promoted azide-alkyne cycloaddition (SPAAC) reaction on a Si_3N_4 surface; (a) Attachment of a bicyclononyne **7** (20 mM in DCM) using films **S3** or **S4** with NHS or PFP active ester groups, respectively; (b) SPAAC reaction of a clickable film (**S7**) with azides **8-12**, resulting in the corresponding films **S8 - S12** (10 mM for **8**, **10** and **12**, and 8.8 mM for **9** in MeCN).

The cycloaddition of polyfluorinated azide **8** onto the cyclooctyne-terminated surface facilitated the characterization of the SPAAC reaction by XPS. To avoid ambiguous interpretation of the spectra after the click reaction with **8**, the attachment of **7** was performed using the cyclooctyne-surface that was derived from NHS moieties **S3** (rather than pentafluorophenyl moieties), in spite of the lower surface coverage. Deconvolution of the C 1s narrow scan (Figure 3.5c) revealed newly introduced CF_2 and CF_3 groups with emissions centered at 292.5 eV and 294.5 eV, respectively. The peak intensity of the CF_3 contribution

was rather low, but a distinguishable CF_2 peak was observed. The C/F atomic ratio derived from the survey elemental analysis suggested a 20% overall yield for the triazole product based on TFE films **S1**. Moreover, the N 1s narrow scan showed unequivocally the formation of the triazole ring. Apart from the N 1s emission of the Si_3N_4 substrate, two additional contributions of N atoms with different chemical environments were observed after the SPAAC reaction (Figure 3.5d and e). The fitting procedure yielded two peaks at 400.2 eV ($\underline{\text{N}}-\underline{\text{N}}=\underline{\text{N}}$ and $\underline{\text{N}}-\text{C}$ amide) and 401.7 eV ($\underline{\text{N}}-\text{N}=\text{N}$), respectively, while no physically adsorbed azide **8** was detected at 403 eV). Due to the intensive peak of N 1s electrons from the inorganic surface, the peak at 400.2 eV (BE) should be interpreted as an overlapping contribution from N 1s electrons of the N atoms in the triazole ring and the N-C amide bonds present in the spacer (Figure 3.5d). The data are in good agreement with an XPS study of heterocycles introduced after a Cu-assisted azide-alkyne cycloaddition reaction.⁴⁷

To study in more detail the reactivity of the cyclooctyne on the surface, the progress of the SPAAC reaction was followed by means of XPS and static water contact angle measurements. The reaction time for grafting azide **8** on films **S7** was varied. In Figure 3.5f the atomic concentration ratio F/C, derived from the survey elemental analysis, and the contact angles are plotted versus the reaction time. The rise of the F/C ratio correlates with the increase of hydrophobicity of the substrates. The cycloaddition reaction was complete after 5-6 h. This is somewhat slower than observed for clicking fluorescent azides onto cycloalkyne (ADIBO) terminated glass slides (fluorescence saturation after ~2 h),⁷⁸ which we attribute to differences in steric effects.

The final surface coverage after SPAAC reaction with **8** was $20 \pm 4\%$ for the triazole product and the water contact angle was 82° (Table 3.1, entry **S8**). The relative small standard deviation illustrates the reaction reproducibility in terms of yield. This allows us to estimate the efficiency of the surface-bound SPAAC reaction. Taking into account that the surface coverage of the NHS ester was within the range of 40 - 60%, and that the attachment of BCN onto PFP ester surfaces was 87% (no data were obtained for the NHS surface used, to minimize the competing hydrolysis) the yield of the SPAAC reaction with **7** is thus 38 - 57%. We attribute this moderate yield to the very high reactivity of **7**. While such high reactivity is frequently essential for biological studies, for

surface modifications, we think it is likely that higher yields of surface-bound SPAAC reactions will actually be obtainable with less reactive/more selective cyclooctyne derivatives.

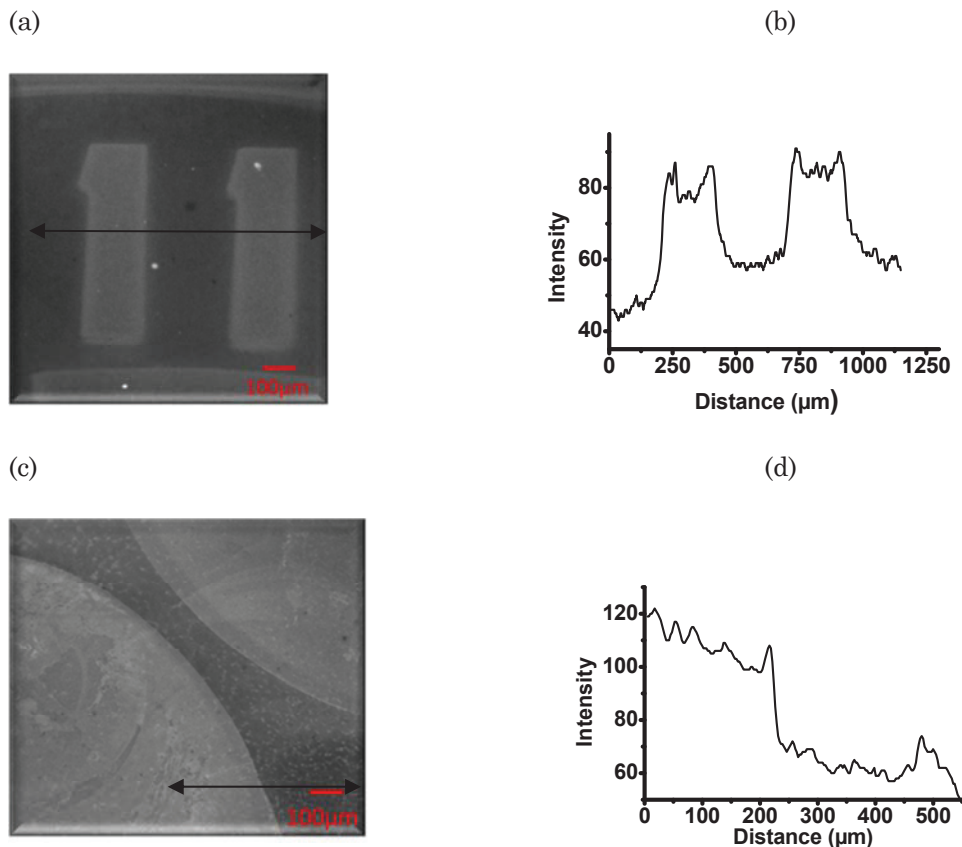


Figure 3.7: (a) Fluorescent microscopy image of photopatterning of Si_3N_4 followed by consecutive reactions with finally a SPAAC reaction with fluorescent azide **9**; (b) Profile histogram: plot of fluorescence intensity versus distance after photopatterning and visualization with **9**; (c) Binding of fluorescent PNA lectin on a β -lactosyl-terminated Si_3N_4 surface and (d) the corresponding intensity profile.

Furthermore to demonstrate the versatility of the clickable platform, a fluorescent azide was added to react with **S7**. To facilitate the read-out of the reaction, the initial TFE monolayer on the surface was grafted by photopatterning through a gold electron microscope mask with specific mesh numbers and features. Afterwards, the consecutive reactions were carried out

with an extensive washing and sonication of the specimen after each step. The obtained pattern corresponds to the mesh numbers (Figure 3.7a) and features of the mask. As seen from the intensity profile (Figure 3.7b), the fluorescent signals emanating from the surface area exposed to UV light have a twice higher intensity relative to the covered surface. The high background intensity is most probably due to internal reflection scattering of UV light during the first monolayer formation.⁸⁴

To study the potential of this metal-free click reaction on the surface in biosensing applications, a particular example from receptor-ligand interactions was chosen, namely carbohydrate-lectin interactions. Carbohydrates are involved in signaling processes and their specific recognition by lectins is important in a large number of diseases. Therefore, the construction of carbohydrate microarrays with an oriented arrangement of the carbohydrates moieties is of vital importance for many biosensing applications. The cyclooctyne-terminated surfaces were therefore clicked with lactosides with an azide terminal group (**10**, **11**, **12**).

The presence of the carbohydrates was clearly indicated by significant changes in the wettability of the substrates. The contact angle of the α - (**10**) and β -lactoside (**12**) tethered specimens decreased from 74° for the alkyne-terminated surface to 61° and 53° , respectively. In comparison, the SPAAC reaction with protected lactoside **11** on film **S7** resulted only in an insignificant change (from 74° to 72°). Despite the enhanced surface hydrophilicity upon the introduction of interfacial -OH groups of the lactosides, the water contact angles are higher as compared to self-assembled dimannoside thiol molecules on gold.¹⁰² Relatively higher water contact angles suggest exposition of aliphatic carbon moieties and a surface not fully covered with saccharide moieties.

To further address these issues, XPS was used to characterize the clicked sugars on the specimens. The XPS spectrum after the SPAAC reaction with **12** was compared with the spectrum of the protected sugar **11** (Figure 3.8).

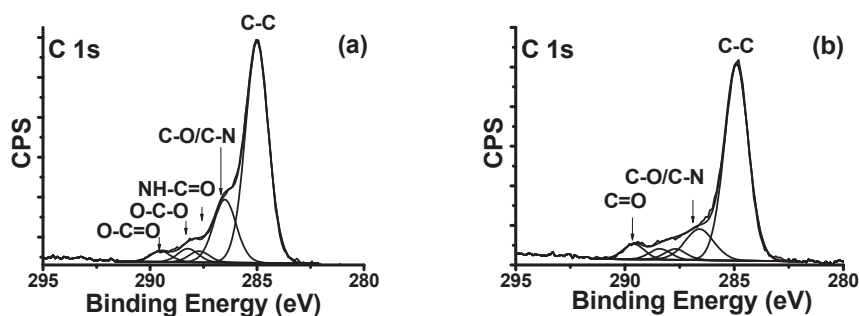


Figure 3.8: C 1s XPS narrow scans for cyclooctyne terminated Si_3N_4 surfaces after the SPAAC reaction with (a) 11-azidoundecyl-lactoside (**S12**) and (b) an acetyl-protected derivative of 11-azidoundecyl-lactoside (**S11**).

Deconvolution of the peaks, in combination with DFT calculation of models representing films **S11** and **S12**, elucidated in more detail the binding shifts resulting after the SPAAC reaction with lactosides (Figure 3.8). The reaction with the acetyl-protected analog rendered the surface not only more hydrophobic, but introduced in the XPS spectrum a significant contribution of carbon atoms from the acetyl-protected groups (288.0 eV), while the intensity of C-O peaks was insignificant and resulted in rather multiple overlapping contributions. The C 1s spectrum of films **S10** and **S12** showed strong emissions at 286.5 eV, characteristic of $\underline{\text{C}}\text{-O}$ peaks, which were summed together with the contribution for the $\underline{\text{C}}\text{-N}$ emissions. Another new characteristic contribution, centered at 288.6 eV, was assigned to $\text{O}\underline{\text{C}}\text{-O}$. In addition to the contributions introduced only after the SPAAC reaction, the emissions assigned already in the C 1s spectrum of film **S7** to carbamate and amide $\underline{\text{C}}\text{=O}$ atoms in the linker, were included in the peak fitting model. To estimate the approximate surface coverage for these new triazole products, the ratio of atomic percentage areas of $\underline{\text{C}}\text{-O}$ and $\underline{\text{C}}\text{-N}$ emissions (summed together as described above) versus the alkyl chain was used. The intensity of the $\underline{\text{C}}\text{-O/N}$ peak of the α -lactosyl films was somewhat lower than that of the β -lactosyl layers. Thus, the surface coverage for the triazole products in **S10** was found slightly inferior relative to that of **S12**, 51% and 57%, respectively (**S1** = 100%). These values are upper limits, as they were calculated without taking into

account the increasing attenuation of the alkyl carbon signal upon construction of the finally clicked monolayers.

3.5.7 Binding of PNA lectin by β -lactosyl-terminated Si_3N_4 surface

To confirm bioactivity of the lactose-tethered surfaces, they were treated with fluorescently labeled PNA lectin and studied with fluorescence microscopy.^{83, 103} Prior to the spotting procedure, the surfaces were washed and incubated in BSA solution to block any non-specific binding. After subsequently dropping 3 μl of PNA solution onto the lactose-terminated surface, the specimens were left for 2 h in a humid chamber at 4 °C to allow specific interactions with carbohydrates on the surface. Prior to the fluorescence imaging, the specimens were washed extensively with buffer (pH = 7.5, 3% BSA, 0.1% SDS) and ultrapure water. The fluorescent image in Figure 3.7c revealed the high fluorescence intensity from the area exposed to the PNA and confirmed the selective immobilization of the protein. Despite the blocking step with BSA and extensive washing of the surface, there was still some background intensity. We speculate that this might be due to the residual interaction of the PNA lectin molecules during the washing step. A control sample of a well cleaned silicon nitride surface was alongside treated in the same manner. The fluorescent imaging showed the lack of strongly bound proteins on the surface and no fluorescent drop shape was formed.

3.6 Conclusions

A surface functionalization method was developed to anchor a wide range of functional groups (oligosaccharides, a dye, a perfluorinated compound) onto silicon nitride surfaces. There are three key features of the consecutive four-step organic reaction sequence that was developed: 1) the covalently attached monolayers are really strongly bound, which favors their stability under a wide range of reaction conditions typically employed in organic synthesis, including strong base and prolonged heating, 2) the development of an improved, efficient route for the attachment and reactivity of activated esters, and 3) the use of an surface-bound strain-promoted alkyne-azide cycloaddition (SPAAC) reaction. This generic approach allows the site-specific immobilization of biocomponents (e.g. oligosaccharides, proteins), dyes or other functional groups (e.g.

perfluorinated materials) without a need for any metal catalyst, that may be toxic or difficult to remove. Such generically tunable “clickable” platform can thus be used for a wide range of applications, including e.g. biosensor surfaces and/or AFM tips.

References

1. Riley, F. L. Silicon Nitride and Related Materials. *J. Am. Ceram. Soc.* **2000**, *83* (2), 245-265.
2. Patil, L. S.; Pandey, R. K.; Bange, J. P.; Gaikwad, S. A.; Gautam, D. K. Effect of deposition temperature on the chemical properties of thermally deposited silicon nitride films. *Opt. Mater.* **2005**, *27* (4), 663-670.
3. Belmonte, M.; Miranzo, P.; Osendi, M. I.; Gomes, J. R. Wear of Aligned Silicon Nitride under Dry Sliding Conditions. *Wear* **2009**, *266* (1-2), 6-12.
4. Minamikawa, T.; Heya, A.; Niki, T.; Takano, M.; Yonezawa, Y.; Muroi, S.; Minami, S.; Masuda, A.; Umemoto, H.; Matsumura, H. Formation of Highly Moisture-Resistive SiN_x Films on Si Substrate by Cat-CVD at Room Temperature. *Thin Solid Films* **2006**, *501* (1-2), 154-156.
5. Benoit, D.; Regolini, J.; Morin, P. Hydrogen Desorption and Diffusion in PECVD Silicon Nitride. Application to Passivation of CMOS Active Pixel Sensors. *Microelectron. Eng.* **2007**, *84* (9-10), 2169-2172.
6. Yoo, J.; Kumar Dhungel, S.; Yi, J. Annealing Optimization of Silicon Nitride Film for Solar Cell Application. *Thin Solid Films* **2007**, *515* (19), 7611-7614.
7. Kafrouni, W.; Rouessac, V.; Julbe, A.; Durand, J. Synthesis of PECVD a-SiC_xN_y:H Membranes as Molecular Sieves for Small Gas Separation. *J. Membr. Sci.* **2009**, *329* (1-2), 130-137.
8. Misiakos, K.; Petrou, P. S.; Kakabakos, S. E.; Yannoukakos, D.; Contopanagos, H.; Knoll, T.; Velten, T.; DeFazio, M.; Schiavo, L.; Passamano, M.; Stamou, D.; Nounesis, G. Fully Integrated Monolithic Optoelectronic Transducer for Real-Time Protein and DNA Detection: The NEMOSLAB Approach. *Biosens. Bioelectron.* **2010**, *26* (4), 1528-1535.
9. Tlili, A.; Jarbou, M. A.; Abdelghani, A.; Fathallah, D. M.; Maaref, M. A. A Novel Silicon Nitride Biosensor for Specific Antibody-Antigen Interaction. *Mater. Sci. Eng., C* **2005**, *25* (4), 490-495.
10. Cappi, B.; Neuss, S.; Salber, J.; Telle, R.; Knüchel, R.; Fischer, H. Cytocompatibility of High Strength Non-Oxide Ceramics. *J. Biomed. Mater. Res., Part A* **2010**, *93A* (1), 67-76.

11. Mazzocchi, M.; Gardini, D.; Traverso, P.; Faga, M.; Belloso, A. On the Possibility of Silicon Nitride as a Ceramic for Structural Orthopaedic Implants. Part II: Chemical Stability and Wear Resistance in Body Environment. *J. Mater. Sci. Mater. Med.* **2008**, *19* (8), 2889-2901.
12. Kwon, H.-S.; Han, K.-C.; Hwang, K. S.; Lee, J. H.; Kim, T. S.; Yoon, D. S.; Yang, E. G. Development of A Peptide Inhibitor-Based Cantilever Sensor Assay for Cyclic Adenosine Monophosphate-Dependent Protein Kinase. *Anal. Chim. Acta* **2007**, *585* (2), 344-349.
13. Frisch, M. J. T., G. W.; Schlegel, H. B.; Scuseria, G. E.; Robb, M. A.; Cheeseman, J. R.; Scalmani, G.; Barone, V.; Mennucci, B.; Petersson, G. A.; Nakatsuji, H.; Caricato, M.; Li, X.; Hratchian, H. P.; Izmaylov, A. F.; Bloino, J.; Zheng, G.; Sonnenberg, J. L.; Hada, M.; Ehara, M.; Toyota, K.; Fukuda, R.; Hasegawa, J.; Ishida, M.; Nakajima, T.; Honda, Y.; Kitao, O.; Nakai, H.; Vreven, T.; Montgomery, Jr., J. A.; Peralta, J. E.; Ogliaro, F.; Bearpark, M.; Heyd, J. J.; Brothers, E.; Kudin, K. N.; Staroverov, V. N.; Kobayashi, R.; Normand, J.; Raghavachari, K.; Rendell, A.; Burant, J. C.; Iyengar, S. S.; Tomasi, J.; Cossi, M.; Rega, N.; Millam, N. J.; Klene, M.; Knox, J. E.; Cross, J. B.; Bakken, V.; Adamo, C.; Jaramillo, J.; Gomperts, R.; Stratmann, R. E.; Yazyev, O.; Austin, A. J.; Cammi, R.; Pomelli, C.; Ochterski, J. W.; Martin, R. L.; Morokuma, K.; Zakrzewski, V. G.; Voth, G. A.; Salvador, P.; Dannenberg, J. J.; Dapprich, S.; Daniels, A. D.; Farkas, Ö.; Foresman, J. B.; Ortiz, J. V.; Cioslowski, J.; Fox, D. J. *Gaussian 09, Revision A.1*, Gaussian, Inc., Wallingford CT: 2009.
14. Wu, P.; Högberg, P.; Grainger, D. W. DNA and Protein Microarray Printing on Silicon Nitride Waveguide Surfaces. *Biosens. Bioelectron.* **2006**, *21* (7), 1252-1263.
15. Cherian, S.; Mehta, A.; Thundat, T. Investigating the Mechanical Effects of Adsorption of Ca²⁺ Ions on a Silicon Nitride Microcantilever Surface. *Langmuir* **2002**, *18* (18), 6935-6939.
16. Diao, J.; Ren, D.; Engstrom, J. R.; Lee, K. H. A Surface Modification Strategy on Silicon Nitride for Developing Biosensors. *Anal. Biochem.* **2005**, *343* (2), 322-328.
17. Terry, J. G.; Campbell, C. J.; Ross, A. J.; Livingston, A. D.; Buck, A. H.; Dickinson, P.; Mountford, C. P.; Evans, S. A. G.; Mount, A. R.; Beattie, J. S.; Crain, J.; Ghazal, P.; Walton, A. J. Improved Silicon Nitride Surfaces for Next-Generation Microarrays. *Langmuir* **2006**, *22* (26), 11400-11404.
18. Sano, H.; Maeda, H.; Ichii, T.; Murase, K.; Noda, K.; Matsushige, K.; Sugimura, H. Alkyl and Alkoxy Monolayers Directly Attached to Silicon: Chemical Durability in Aqueous Solutions. *Langmuir* **2009**, *25* (10), 5516-5525.
19. Wasserman, S. R.; Tao, Y. T.; Whitesides, G. M. Structure and reactivity of alkylsiloxane monolayers formed by reaction of alkyltrichlorosilanes on silicon substrates. *Langmuir* **1989**, *5* (4), 1074-1087.

20. Cattaruzza, F.; Cricenti, A.; Flamini, A.; Girasole, M.; Longo, G.; Mezzi, A.; Prospero, T. Carboxylic acid terminated monolayer formation on crystalline silicon and silicon nitride surfaces. A surface coverage determination with a fluorescent probe in solution. *J. Mater. Chem.* **2004**, *14* (9), 1461-1468.
21. Bañuls, M.-J.; González-Pedro, V.; Barrios, C. A.; Puchades, R.; Maquieira, Á. Selective Chemical Modification of Silicon Nitride/Silicon Oxide Nanostructures to Develop Label-free Biosensors. *Biosens. Bioelectron.* **2010**, *25* (6), 1460-1466.
22. Stine, R.; Cole, C. L.; Ainslie, K. M.; Mulvaney, S. P.; Whitman, L. J. Formation of Primary Amines on Silicon Nitride Surfaces: a Direct, Plasma-Based Pathway to Functionalization. *Langmuir* **2007**, *23* (8), 4400-4404.
23. Arafat, A.; Schroën, K.; de Smet, L. C. P. M.; Sudhölter, E. J. R.; Zuilhof, H. Tailor-Made Functionalization of Silicon Nitride Surfaces. *J. Am. Chem. Soc.* **2004**, *126* (28), 8600-8601.
24. Rosso, M.; Giesbers, M.; Arafat, A.; Schroen, K.; Zuilhof, H. Covalently Attached Organic Monolayers on SiC and Si_xN₄ Surfaces: Formation Using UV Light at Room Temperature. *Langmuir* **2009**, *25* (4), 2172-2180.
25. Arafat, A.; Giesbers, M.; Rosso, M.; Sudhölter, E. J. R.; Schroën, K.; White, R. G.; Yang, L.; Linford, M. R.; Zuilhof, H. Covalent Biofunctionalization of Silicon Nitride Surfaces. *Langmuir* **2007**, *23* (11), 6233-6244.
26. Coffinier, Y.; Boukherroub, R.; Wallart, X.; Nys, J.-P.; Durand, J.-O.; Stiévenard, D.; Grandidier, B. Covalent Functionalization of Silicon Nitride Surfaces by Semicarbazide Group. *Surf. Sci.* **2007**, *601* (23), 5492-5498.
27. Rusmini, F.; Zhong, Z.; Feijen, J. Protein Immobilization Strategies for Protein Biochips. *Biomacromolecules* **2007**, *8* (6), 1775-1789.
28. Dillmore, W. S.; Yousaf, M. N.; Mrksich, M. A Photochemical Method for Patterning the Immobilization of Ligands and Cells to Self-Assembled Monolayers. *Langmuir* **2004**, *20* (17), 7223-7231.
29. Ganesan, R.; Yoo, S. Y.; Choi, J.-H.; Lee, S. Y.; Kim, J.-B. Simple micropatterning of biomolecules on a diazoketo-functionalized photoresist. *J. Mater. Chem.* **2008**, *18* (6), 703-709.
30. Arumugam, S.; Orski, S. V.; Locklin, J.; Popik, V. V. Photoreactive Polymer Brushes for High-Density Patterned Surface Derivatization Using a Diels–Alder Photoclick Reaction. *J. Am. Chem. Soc.* **2011**, *134* (1), 179-182.
31. Chan, J. W.; Yu, B.; Hoyle, C. E.; Lowe, A. B. Convergent synthesis of 3-arm star polymers from RAFT-prepared poly(*N,N*-diethylacrylamide) *via* a thiol-ene click reaction. *Chem. Commun.* **2008**, (40), 4959-4961.
32. Campos, L. M.; Killops, K. L.; Sakai, R.; Paulusse, J. M. J.; Damiron, D.; Drockenmuller, E.; Messmore, B. W.; Hawker, C. J. Development of Thermal and

Photochemical Strategies for Thiol–Ene Click Polymer Functionalization. *Macromolecules* **2008**, *41* (19), 7063-7070.

33. Campos, M. A. C.; Paulusse, J. M. J.; Zuilhof, H. Functional monolayers on oxide-free silicon surfaces via thiol-ene click chemistry. *Chem. Commun.* **2010**, *46* (30), 5512-5514.

34. Ruizendaal, L.; Pujari, S. P.; Gevaerts, V.; Paulusse, J. M. J.; Zuilhof, H. Biofunctional Silicon Nanoparticles by Means of Thiol-Ene Click Chemistry. *Chem. Asian J.* **2011**, *6* (10), 2776-2786.

35. DeForest, C. A.; Polizzotti, B. D.; Anseth, K. S. Sequential click reactions for synthesizing and patterning three-dimensional cell microenvironments. **2009**, *8* (8), 659-664.

36. Rostovtsev, V. V.; Green, L. G.; Fokin, V. V.; Sharpless, K. B. A Stepwise Huisgen Cycloaddition Process: Copper(I)-Catalyzed Regioselective “Ligation” of Azides and Terminal Alkynes. *Angew. Chem.* **2002**, *114* (14), 2708-2711.

37. Tornøe, C. W.; Christensen, C.; Meldal, M. Peptidotriazoles on Solid Phase: [1,2,3]-Triazoles by Regiospecific Copper(I)-Catalyzed 1,3-Dipolar Cycloadditions of Terminal Alkynes to Azides. *J. Org. Chem.* **2002**, *67* (9), 3057-3064.

38. Speers, A. E.; Adam, G. C.; Cravatt, B. F. Activity-Based Protein Profiling in Vivo Using a Copper(I)-Catalyzed Azide-Alkyne [3 + 2] Cycloaddition. *J. Am. Chem. Soc.* **2003**, *125* (16), 4686-4687.

39. Rabuka, D.; Hubbard, S. C.; Laughlin, S. T.; Argade, S. P.; Bertozzi, C. R. A Chemical Reporter Strategy to Probe Glycoprotein Fucosylation. *J. Am. Chem. Soc.* **2006**, *128* (37), 12078-12079.

40. Charron, G.; Zhang, M. M.; Yount, J. S.; Wilson, J.; Raghavan, A. S.; Shamir, E.; Hang, H. C. Robust Fluorescent Detection of Protein Fatty-Acylation with Chemical Reporters. *J. Am. Chem. Soc.* **2009**, *131* (13), 4967-4975.

41. Fournier, D.; Hoogenboom, R.; Schubert, U. S. Clicking Polymers: A Straightforward Approach to Novel Macromolecular Architectures. *Chem. Soc. Rev.* **2007**, *36* (8), 1369-1380.

42. Iha, R. K.; Wooley, K. L.; Nyström, A. M.; Burke, D. J.; Kade, M. J.; Hawker, C. J. Applications of Orthogonal “Click” Chemistries in the Synthesis of Functional Soft Materials. *Chem. Rev.* **2009**, *109* (11), 5620-5686.

43. Devadoss, A.; Chidsey, C. E. D. Azide-Modified Graphitic Surfaces for Covalent Attachment of Alkyne-Terminated Molecules by “Click” Chemistry. *J. Am. Chem. Soc.* **2007**, *129* (17), 5370-5371.

44. Kinge, S.; Gang, T.; Naber, W. J. M.; van der Wiel, W. G.; Reinhoudt, D. N. Magnetic Nanoparticle Assembly on Surfaces Using Click Chemistry. *Langmuir* **2010**, *27* (2), 570-574.

45. Ciampi, S.; Eggers, P. K.; Le Saux, G.; James, M.; Harper, J. B.; Gooding, J. J. Silicon (100) Electrodes Resistant to Oxidation in Aqueous Solutions: An Unexpected Benefit of Surface Acetylene Moieties. *Langmuir* **2009**, *25* (4), 2530-2539.
46. Rohde, R. D.; Agnew, H. D.; Yeo, W.-S.; Bailey, R. C.; Heath, J. R. A Non-Oxidative Approach toward Chemically and Electrochemically Functionalizing Si(111). *J. Am. Chem. Soc.* **2006**, *128* (29), 9518-9525.
47. Qin, G.; Santos, C.; Zhang, W.; Li, Y.; Kumar, A.; Erasquin, U. J.; Liu, K.; Muradov, P.; Trautner, B. W.; Cai, C. Biofunctionalization on Alkylated Silicon Substrate Surfaces via “Click” Chemistry. *J. Am. Chem. Soc.* **2010**, *132* (46), 16432-16441.
48. Collman, J. P.; Devaraj, N. K.; Eberspacher, T. P. A.; Chidsey, C. E. D. Mixed Azide-Terminated Monolayers: A Platform for Modifying Electrode Surfaces. *Langmuir* **2006**, *22* (6), 2457-2464.
49. Nichols, B. M.; Butler, J. E.; Russell, J. N.; Hamers, R. J. Photochemical Functionalization of Hydrogen-Terminated Diamond Surfaces: A Structural and Mechanistic Study. *J. Phys. Chem. B* **2005**, *109* (44), 20938-20947.
50. Lummerstorfer, T.; Hoffmann, H. Click Chemistry on Surfaces: 1,3-Dipolar Cycloaddition Reactions of Azide-Terminated Monolayers on Silica. *J. Phys. Chem. B* **2004**, *108* (13), 3963-3966.
51. Ciampi, S.; Böcking, T.; Kilian, K. A.; James, M.; Harper, J. B.; Gooding, J. J. Functionalization of Acetylene-Terminated Monolayers on Si(100) Surfaces: A Click Chemistry Approach. *Langmuir* **2007**, *23* (18), 9320-9329.
52. Ciampi, S.; James, M.; Michaels, P.; Gooding, J. J. Tandem “Click” Reactions at Acetylene-Terminated Si(100) Monolayers. *Langmuir* **2011**, *27* (11), 6940-6949.
53. Britcher, L.; Barnes, T. J.; Griesser, H. J.; Prestidge, C. A. PEGylation of Porous Silicon Using Click Chemistry. *Langmuir* **2008**, *24* (15), 7625-7627.
54. Li, Y.; Zhao, M.; Wang, J.; Liu, K.; Cai, C. Biofunctionalization of a “Clickable” Organic Layer Photochemically Grafted on Titanium Substrates. *Langmuir* **2011**, *27* (8), 4848-4856.
55. Li, Y.; Zuilhof, H. Photochemical Grafting and Patterning of Organic Monolayers on Indium Tin Oxide Substrates. *Langmuir* **2012**, *28* (12), 5350-5359.
56. Li, Y.; Wang, J.; Cai, C. Rapid Grafting of Azido-Labeled Oligo(ethylene glycol)s onto an Alkynyl-Terminated Monolayer on Nonoxidized Silicon via Microwave-Assisted “Click” Reaction. *Langmuir* **2011**, *27* (6), 2437-2445.
57. Manova, R.; van Beek, T. A.; Zuilhof, H. Surface Functionalization by Strain-Promoted Alkyne–Azide Click Reactions. *Angew. Chem. Int. Ed.* **2011**, *50* (24), 5428-5430.
58. Bernardin, A.; Cazet, A. I.; Guyon, L.; Delannoy, P.; Vinet, F. o.; Bonnaffé, D.; Texier, I. Copper-Free Click Chemistry for Highly Luminescent Quantum Dot

Conjugates: Application to in Vivo Metabolic Imaging. *Bioconjugate Chem.* **2010**, *21* (4), 583-588.

59. McCarty, G. S. Molecular Lithography for Wafer-Scale Fabrication of Molecular Junctions. *Nano Lett.* **2004**, *4* (8), 1391-1394.

60. Link, A. J.; Tirrell, D. A. Cell Surface Labeling of Escherichia coli via Copper(I)-Catalyzed [3+2] Cycloaddition. *J. Am. Chem. Soc.* **2003**, *125* (37), 11164-11165.

61. Wang, Q.; Chan, T. R.; Hilgraf, R.; Fokin, V. V.; Sharpless, K. B.; Finn, M. G. Bioconjugation by Copper(I)-Catalyzed Azide-Alkyne [3 + 2] Cycloaddition. *J. Am. Chem. Soc.* **2003**, *125* (11), 3192-3193.

62. Gierlich, J.; Burley, G. A.; Gramlich, P. M. E.; Hammond, D. M.; Carell, T. Click Chemistry as a Reliable Method for the High-Density Postsynthetic Functionalization of Alkyne-Modified DNA. *Org. Lett.* **2006**, *8* (17), 3639-3642.

63. Lallana, E.; Fernandez-Megia, E.; Riguera, R. Surpassing the Use of Copper in the Click Functionalization of Polymeric Nanostructures: A Strain-Promoted Approach. *J. Am. Chem. Soc.* **2009**, *131* (16), 5748-5750.

64. Zhou, C.; Walker, A. V. Formation of Multilayer Ultrathin Assemblies Using Chemical Lithography. *Langmuir* **2010**, *26* (11), 8441-8449.

65. Rozkiewicz, D. I.; Jańczewski, D.; Verboom, W.; Ravoo, B. J.; Reinhoudt, D. N. "Click" Chemistry by Microcontact Printing. *Angew. Chem.* **2006**, *118* (32), 5418-5422.

66. Rozkiewicz, D. I.; Gierlich, J.; Burley, G. A.; Gutmiedl, K.; Carell, T.; Ravoo, B. J.; Reinhoudt, D. N. Transfer Printing of DNA by "Click" Chemistry. *ChemBioChem* **2007**, *8* (16), 1997-2002.

67. Michel, O.; Ravoo, B. J. Carbohydrate Microarrays by Microcontact "Click" Chemistry. *Langmuir* **2008**, *24* (21), 12116-12118.

68. Mehlich, J.; Ravoo, B. J. Click Chemistry by Microcontact Printing on Self-Assembled Monolayers: A Structure-Reactivity Study by Fluorescence Microscopy. *Org. Biomol. Chem.* **2011**, *9* (11), 4108-4115.

69. Godula, K.; Rabuka, D.; Nam, K. T.; Bertozzi, C. R. Synthesis and Microcontact Printing of Dual End-Functionalized Mucin-like Glycopolymers for Microarray Applications. *Angew. Chem. Int. Ed.* **2009**, *48* (27), 4973-4976.

70. Agard, N. J.; Prescher, J. A.; Bertozzi, C. R. A Strain-Promoted [3 + 2] Azide-Alkyne Cycloaddition for Covalent Modification of Biomolecules in Living Systems. *J. Am. Chem. Soc.* **2004**, *126* (46), 15046-15047.

71. Jewett, J. C.; Bertozzi, C. R. Cu-Free Click Cycloaddition Reactions in Chemical Biology. *Chem. Soc. Rev.* **2010**, *39* (4), 1272-1279.

72. Debets, M. F.; van Berkel, S. S.; Dommerholt, J.; Dirks, A. J.; Rutjes, F. P. J. T.; van Delft, F. L. Bioconjugation with Strained Alkenes and Alkynes. *Acc. Chem. Res* **2011**, *44* (9) (9), 805-815.

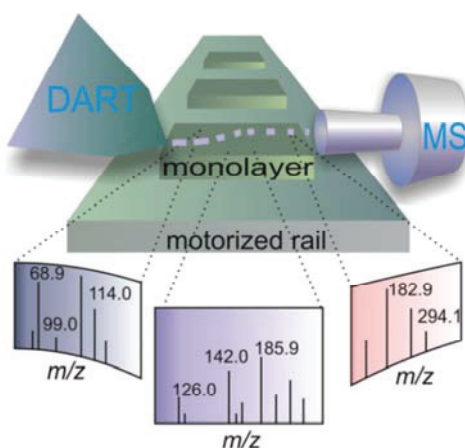
73. Poloukhine, A. A.; Mbua, N. E.; Wolfert, M. A.; Boons, G.-J.; Popik, V. V. Selective Labeling of Living Cells by a Photo-Triggered Click Reaction. *J. Am. Chem. Soc.* **2009**, *131* (43), 15769-15776.
74. Dommerholt, J.; Schmidt, S.; Temming, R.; Hendriks, L. J. A.; Rutjes, F. P. J. T.; van Hest, J. C. M.; Lefeber, D. J.; Friedl, P.; van Delft, F. L. Readily Accessible Bicyclononynes for Bioorthogonal Labeling and Three-Dimensional Imaging of Living Cells. *Angew. Chem. Int. Ed.* **2010**, *49* (49), 9422-9425.
75. Stockmann, H.; Neves, A. A.; Stairs, S.; Ireland-Zecchini, H.; Brindle, K. M.; Leeper, F. J. Development and Evaluation of New Cyclooctynes for Cell Surface Glycan Imaging in Cancer Cells. *Chem. Sci.* **2011**, *2* (5), 932-936.
76. Kii, I.; Shiraishi, A.; Hiramatsu, T.; Matsushita, T.; Uekusa, H.; Yoshida, S.; Yamamoto, M.; Kudo, A.; Hagiwara, M.; Hosoya, T. Strain-promoted double-click reaction for chemical modification of azido-biomolecules. *Org. Biomol. Chem.* **2010**, *8* (18), 4051-4055.
77. Xu, J.; Prifti, F.; Song, J. A Versatile Monomer for Preparing Well-Defined Functional Polycarbonates and Poly(ester-carbonates). *Macromolecules* **2011**, *44* (8), 2660-2667.
78. Kuzmin, A.; Poloukhine, A.; Wolfert, M. A.; Popik, V. V. Surface Functionalization Using Catalyst-Free Azide-Alkyne Cycloaddition. *Bioconjugate Chem.* **2010**, *21* (11), 2076-2085.
79. Orski, S. V.; Poloukhine, A. A.; Arumugam, S.; Mao, L. D.; Popik, V. V.; Locklin, J. High Density Orthogonal Surface Immobilization via Photoactivated Copper-Free Click Chemistry. *J. Am. Chem. Soc.* **2010**, *132* (32), 11024-11026.
80. Yang, M.; Teeuwen, R. L. M.; Giesbers, M.; Baggerman, J.; Arafat, A.; de Wolf, F. A.; van Hest, J. C. M.; Zuilhof, H. One-Step Photochemical Attachment of NHS-Terminated Monolayers onto Silicon Surfaces and Subsequent Functionalization. *Langmuir* **2008**, *24* (15), 7931-7938.
81. Yang, J.; Wang, Y.; Rassat, A.; Zhang, Y.; Sinay, P. Synthesis of novel highly water-soluble 2:1 cyclodextrin/fullerene conjugates involving the secondary rim of β -cyclodextrin. *Tetrahedron* **2004**, *60* (52), 12163-12168.
82. Mukhopadhyay, B.; Kartha, K. P. R.; Russell, D. A.; Field, R. A. Streamlined Synthesis of Per-O-acetylated Sugars, Glycosyl Iodides, or Thioglycosides from Unprotected Reducing Sugars. *J. Org. Chem.* **2004**, *69* (22), 7758-7760.
83. ter Maat, J.; Regeling, R.; Ingham, C. J.; Weijers, C. A. G. M.; Giesbers, M.; de Vos, W. M.; Zuilhof, H. Organic Modification and Subsequent Biofunctionalization of Porous Anodic Alumina Using Terminal Alkynes. *Langmuir* **2011**, *27* (22), 13606-13617.
84. Vong, T.; ter Maat, J.; van Beek, T. A.; van Lagen, B.; Giesbers, M.; van Hest, J. C. M.; Zuilhof, H. Site-Specific Immobilization of DNA in Glass Microchannels via Photolithography†. *Langmuir* **2009**, *25* (24), 13952-13958.

85. Seah, M. P.; Spencer, S. J. Attenuation lengths in organic materials. *Surf. Interface Anal.* **2011**, *43* (3), 744-751.
86. Glendening, E. D., Reed, A. E., Carpenter, J. E., and Weinhold, F. *NBO, version 3.1*.
87. Tielens, F.; Costa, D.; Humblot, V.; Pradier, C.-M. Characterization of ω -Functionalized Undecanethiol Mixed Self-Assembled Monolayers on Au(111): A Combined Polarization Modulation Infrared Reflection–Absorption Spectroscopy/X-ray Photoelectron Spectroscopy/Periodic Density Functional Theory Study. *J. Phys. Chem. C* **2007**, *112* (1), 182-190.
88. Park, S.; Pai, J.; Han, E.-H.; Jun, C.-H.; Shin, I. One-Step, Acid-Mediated Method for Modification of Glass Surfaces with N-Hydroxysuccinimide Esters and Its Application to the Construction of Microarrays for Studies of Biomolecular Interactions. *Bioconjugate Chem.* **2010**, *21* (7), 1246-1253.
89. Böcking, T.; James, M.; Coster, H. G. L.; Chilcott, T. C.; Barrow, K. D. Structural Characterization of Organic Multilayers on Silicon(111) Formed by Immobilization of Molecular Films on Functionalized Si–C Linked Monolayers. *Langmuir* **2004**, *20* (21), 9227-9235.
90. Mezzasalma, S.; Baldovino, D. Characterization of Silicon Nitride Surface in Water and Acid Environment: A General Approach to the Colloidal Suspensions. *J. Colloid Interface Sci.* **1996**, *180* (2), 413-420.
91. Strother, T.; Cai, W.; Zhao, X.; Hamers, R. J.; Smith, L. M. Synthesis and Characterization of DNA-Modified Silicon (111) Surfaces. *J. Am. Chem. Soc.* **2000**, *122* (6), 1205-1209.
92. Scheres, L.; Klingebiel, B.; Maat, J. t.; Giesbers, M.; de Jong, H.; Hartmann, N.; Zuilhof, H. Micro- and Nanopatterning of Functional Organic Monolayers on Oxide-Free Silicon by Laser-Induced Photothermal Desorption. *Small* **2010**, *6* (17), 1918-1926.
93. Shi, Z.; Wang, Y.; Du, C.; Huang, N.; Wang, L.; Ning, C. The structure, surface topography and mechanical properties of Si–C–N films fabricated by RF and DC magnetron sputtering. *Applied Surface Science* **2011**, *258* (4), 1328-1336.
94. Akazawa, H. Radiation effects in vacuum-ultraviolet-irradiated SiN_x:H films. *Nuclear Instruments and Methods in Physical Research Section B* **1996**, *116* (1–4), 355-359.
95. Rijkssen, B.; Pujari, S. P.; Scheres, L.; van Rijn, C. J. M.; Baio, J. E.; Weidner, T.; Zuilhof, H. Hexadecadienyl Monolayers on Hydrogen-Terminated Si(111): Faster Monolayer Formation and Improved Surface Coverage Using the Enyne Moiety. *Langmuir* **2012**.
96. Zhong, Y. L.; Chong, K. F.; May, P. W.; Chen, Z.-K.; Loh, K. P. Optimizing Biosensing Properties on Undecylenic Acid-Functionalized Diamond. *Langmuir* **2007**, *23* (10), 5824-5830.

97. Liu, Y.-J.; Navasero, N. M.; Yu, H.-Z. Structure and Reactivity of Mixed ω -Carboxyalkyl/Alkyl Monolayers on Silicon: ATR-FTIR Spectroscopy and Contact Angle Titration. *Langmuir* **2004**, *20* (10), 4039-4050.
98. Touahir, L.; Chazalviel, J. N.; Sam, S.; Moraillon, A.; Henry de Villeneuve, C.; Allongue, P.; Ozanam, F.; Gouget-Laemmel, A. C. Kinetics of Activation of Carboxyls to Succinimidyl Ester Groups in Monolayers Grafted on Silicon: An in Situ Real-Time Infrared Spectroscopy Study. *J. Phys. Chem. C* **2011**, *115* (14), 6782-6787.
99. Sullivan, T. P.; Huck, W. T. S. Reactions on Monolayers: Organic Synthesis in Two Dimensions. *Eur. J. Org. Chem.* **2003**, *2003* (1), 17-29.
100. Kovacs, J.; Mayers, G. L.; Johnson, R. H.; Cover, R. E.; Ghatak, U. R. Racemization of amino acid derivatives. III. Rate of racemization and peptide bond formation of cysteine active esters. *J. Org. Chem.* **1970**, *35* (6), 1810-1815.
101. Lockett, M. R.; Phillips, M. F.; Jarecki, J. L.; Peelen, D.; Smith, L. M. A Tetrafluorophenyl Activated Ester Self-Assembled Monolayer for the Immobilization of Amine-Modified Oligonucleotides. *Langmuir* **2007**, *24* (1), 69-75.
102. Dietrich, P. M.; Horlacher, T.; Girard-Lauriault, P.-L.; Gross, T.; Lippitz, A.; Min, H.; Wirth, T.; Castelli, R.; Seeberger, P. H.; Unger, W. E. S. Adlayers of Dimannoside Thiols on Gold: Surface Chemical Analysis. *Langmuir* **2011**, *27* (8), 4808-4815.
103. Wendeln, C.; Heile, A.; Arlinghaus, H. F.; Ravoo, B. J. Carbohydrate Microarrays by Microcontact Printing. *Langmuir* **2010**, *26* (7), 4933-4940.

Chapter 4

Ambient mass spectrometry of covalently bound organic monolayers



Detailed molecular analysis by Direct Analysis in Real Time High Resolution Mass Spectrometry (DART-HRMS) of ester and amide-terminated monolayers is demonstrated. The structural information obtained allowed monitoring of the progress of a 4-step surface modification.

This chapter was published as:

Manova, R. K.; Claassen, F. W.; Nielen, M. W. F.; Zuilhof, H.; and van Beek, T. A. Ambient Mass Spectrometry of Covalently Bound Organic Monolayers. *Chem. Commun.* **2013**, *49*, 922-924.

4.1 Introduction

The emergence of new functional nanostructures is the driving force towards nanoscale miniaturization and the fast development of nanoscience and technology. Among the various nanostructures, organic monolayers are highly useful to tailor surface properties,¹ which makes them attractive elements in miniaturized micro- and nanoelectronic devices. However, for detailed characterization still only a limited number of techniques is available. While a wide range of analytical methods (XPS, SEM, STM, AFM, etc.) is employed to describe the mechanical properties of nanostructures, their elemental composition and identification of some functional groups, it is still hard to obtain any structural information or to characterize surfaces with a heterogeneous surface composition. In this paper we propose the use of surface-sensitive ambient mass spectrometry (MS) to fill this gap in the analysis of covalently bound organic monolayers.

The use of MS to obtain structural information is still limited in this field of research. Secondary-ion mass spectrometry (SIMS) allows analysis of molecular surface structures, but is relatively expensive, and suffers from too much fragmentation.² MALDI-TOF-MS of self-assembled monolayers (SAMs), introduced by Mrksich,³ opened up new perspectives in surface science for molecular characterization of SAMs. With all its advantages for the analysis of surface-bound biomolecules, its main limitation is the prerequisite of a matrix, which hampers its use for low-molecular weight (< ~400 Da) compounds.³ Moreover, the choice of the matrix is complicated, since the optimal matrix varies with the structure of the monolayer.⁴ Additionally, sampling by both MALDI-TOF-MS and SIMS is performed under vacuum.

DART (Direct Analysis in Real Time) is an alternative ambient ionization technique that circumvents these limitations.⁵ DART-MS allows for direct analysis of untreated samples in the open air, and has been mainly employed in food and pharmaceutical applications for fast analysis without tedious and expensive sample preparation.⁶ The ionization process relies on the formation of metastable gas species (He^*) formed in the DART glow discharge compartment. The metastable species are heated to facilitate thermodesorption of the analytes from the sample surface, and directed to the sampling region,

located between the DART outlet and the MS inlet. The metastables can directly ionize the analyte molecules, but since the sampling takes place in the open air, atmospheric water and oxygen molecules can also be involved in the ionization process. For instance, in (+)-mode, formation of ionized water clusters is detected, and subsequent proton transfer to the analyte molecule produces $[M+H]^+$ ions,⁷ whilst in (-)-mode, $O_2^{\bullet-}$ ions could play a role in forming anions.⁸

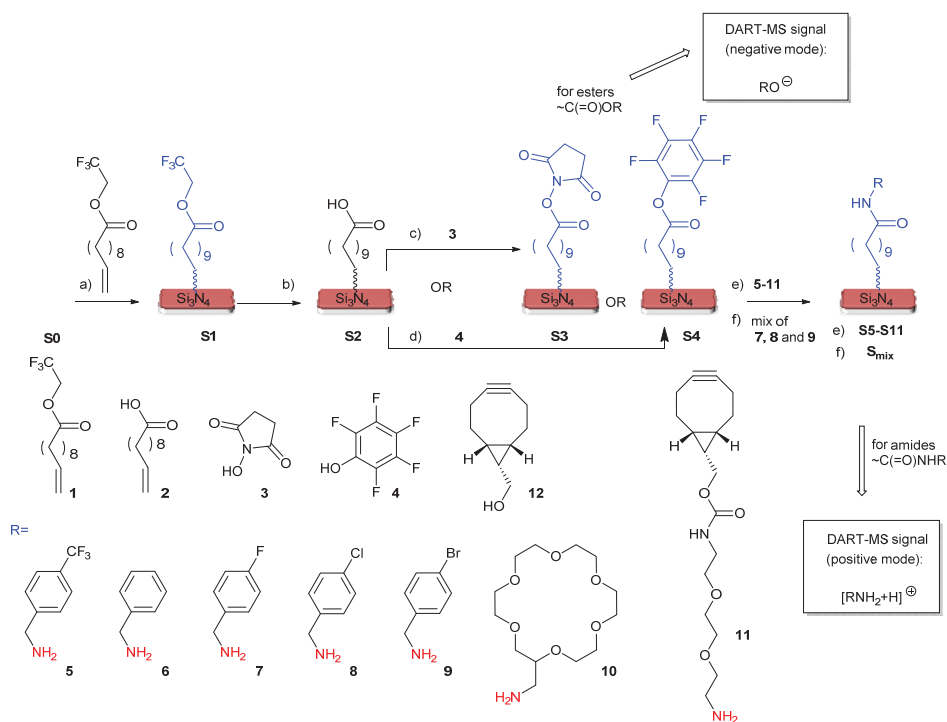


Figure 4.1: Step-wise surface modification reaction, used to afford a variety of ester and amide-terminated monolayers for DART-MS analysis

So far, DART-MS was explored for the analysis of SAMs on gold beads⁹ and on Cu surfaces.¹⁰ SAMs on noble metal surfaces are relatively easy to remove,¹¹ thus the desorption and direct ionization of the thiolates on these surfaces allow facile identification of the intact molecule forming the monolayer. However, DART-MS analyses of monolayers with a strong covalent interfacial bond have not yet been reported.

To evaluate its potential for surface analysis, DART-MS was applied to several stable functionalized alkyl chains on silicon nitride (Si_3N_4), which were prepared using UV-assisted grafting of an ω -1-alkene, **1** (Figure 4.1). The alkene moieties react with the surface through Si-C and/or N-C covalent bond formation and yield a surface terminated with trifluoroethanol ester moieties (**S1**), which has been characterized in detail before.¹² Due to the high stability of the monolayer,¹³ sequential reactions can be employed to tailor the surface properties and to afford different ester or amide-terminated monolayers. For instance, after basic hydrolysis of the trifluoroethanol ester moieties, the resulting COOH-terminated monolayers (**S2**) were converted to N-hydroxysuccinimide (NHS, **3**) (**S3**) or pentafluorophenyl (PFP, **4**) esters (**S4**) using carbodiimide coupling chemistry. The monolayers **S3** and **S4** were then used for the covalent attachment of a variety of amines, providing amide monolayers **S5** - **S11**,¹² which all contain one type of amide, and surface **S_{mix}** that is composed of three different halogen-containing amides. The step-wise functionalization was followed by XPS analysis to confirm the successful conversion of the different monolayers and afterward the obtained monolayers were scrutinized via DART-MS.

4.2 Material and methods

All chemicals and solvents were purchased from Sigma-Aldrich and used as received unless stated otherwise. The cyclooctyne derivative (**11**) was purchased from SynAffix, B.V., The Netherlands. The synthesis of **1** and surface chemistry reactions on Si_3N_4 were described in Chapter 3.¹²

4.3 XPS analysis

The analysis with XPS was carried out according to a previously described procedure in Chapter 3.¹²

4.4 Analysis with DART mass spectrometry

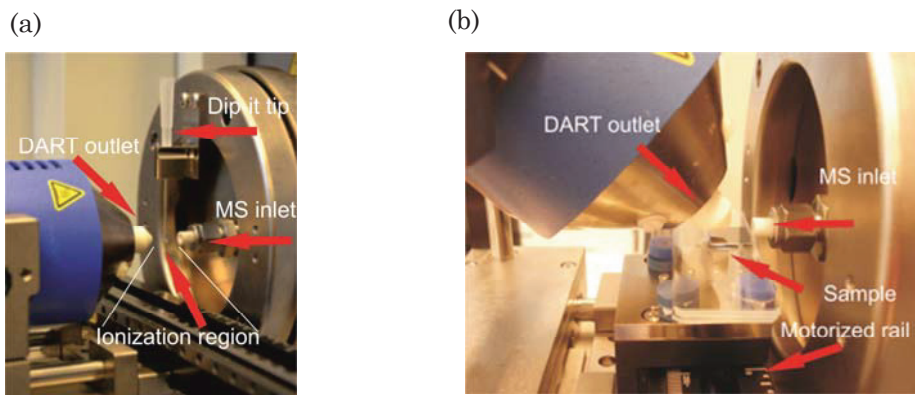


Figure 4.2: Experimental set-up of DART-HRMS: (a) measurement of liquids: a Dip-it® glass tip was immersed in a solution of the compound and introduced in the ionization region; (b) measurement for solid samples: DART outlet (at 45°); ceramic tube, which guides the ions to the MS inlet; sample, immobilized on a glass slide; motorized rail moving the sample between DART outlet and MS inlet.

The DART mass spectrometry set-up consisted of a DART ion source (model DART-SVP, IonSense, Saugus, USA) coupled with an Exactive high-resolution mass spectrometer (Thermo Fisher Scientific, San Jose, CA, USA) and is here indicated as DART High Resolution Mass Spectrometry (DART-HRMS). The mass spectrometer was calibrated at the beginning of each day. XCALIBUR software (v. 2.1) was used for instrument control, data acquisition and data processing. The distance between mass inlet and the DART outlet was kept at ~1 cm. For identification purposes, only ions with a mass accuracy of 1 mmu or less were considered. In few cases, a mass shift higher than 1 mmu was observed. This was due to their low relative abundance and the presence of adjacent intense isobaric peaks. Under these conditions, a mass shift can occur due to phenomena described elsewhere.¹⁴

DART settings in (+)-mode were: He as ionizing gas, fixed flow of ~3.5 L/min; gas beam temperature set at 450 °C; grid electrode voltage +350 V. MS: capillary voltage +80 V; tube lens voltage +185 V; skimmer voltage +42 V; capillary temperature: 275 °C. The resolution was set at “ultra high” (100,000

FWHM at m/z 200) and a scan rate of 1 Hz was used. The mass range was m/z 50-500.

DART settings in (-)-mode were: He as ionizing gas, fixed flow of ~ 3.5 L/min; gas beam temperature set at 450 °C; grid electrode voltage -350 V. MS: capillary voltage -50 V; tube lens voltage -100 V; skimmer voltage -20 V; capillary temperature: 275 °C. The resolution was set at “ultra high” and a scan rate of 1 Hz was used. The mass range was m/z 50-300.

DART settings in (+)-mode were additionally optimized for the simultaneous analysis of all six ions in monolayer S_{mix} : He as ionizing gas, fixed flow of ~ 3.5 L/min; gas beam temperature set at 450 °C; grid electrode voltage $+350$ V. MS: capillary voltage $+25$ V; tube lens voltage $+50$ V; skimmer voltage $+18$ V; capillary temperature: 275 °C. The resolution was set at “ultra high” and a scan rate of 1 Hz was used. The mass range was m/z 100-300.

For the analysis of liquid samples a glass tip, further indicated as Dip-it tip, from Ionsense was used. The compounds were first dissolved in MeOH and then the Dip-it® tip was immersed in the solution. The wet Dip-it tip was introduced in the ionization region and left on a holder for a few seconds until the appearance of a sharp and intense signal. Afterwards, the Dip-it tip was removed from the holder and the background noise was recorded for 30 s. This procedure was repeated several times in order to perform several consecutive measurements.

For the analysis of monolayers, different geometrical conditions were used with DART. Firstly, all samples were cleaned by exhaustive sonication in appropriate solvents for at least 15 min and afterwards dried under argon. The samples were then analyzed with XPS to confirm the successful formation of the monolayers (Appendix 2, Figure S10 and S11). After XPS analysis, the specimens were stored till analysis with DART-HRMS in a glove box (MBraun MB200G & MBraun MB20G) under an argon atmosphere with a H_2O and O_2 content each below 0.1 ppm. Prior to the analysis with DART-HRMS, specimens (0.7×1.5 cm) that had been extensively cleaned by sonication were placed together with a reference sample – bare Si_3N_4 , freshly etched with 2.5% HF – on a glass slide using double-sided tape. The distance between the specimens was kept at ~ 1 cm (spatial resolution of DART: 2-3 mm¹⁵). The glass

slide with the specimens was positioned in the ionization region (the space between the DART outlet and the MS inlet) in such a way that the specimens were as close as possible to the ceramic transfer tube leading the ions towards the MS inlet. The DART outlet, pointed at 45 °C (Figure 4.2), was adjusted vertically as close as possible to the surface of the flat specimens while avoiding direct contact and, thus contamination of the outlet. After setting the position, the glass slide with the specimens was moved away via the motorized rail and the temperature of the DART was set to 450 °C. Once the set temperature was reached, the acquisition was started and the glass slide was moved backwards, i.e. towards the ionization region at a speed of 0.2 mm/s. The ionization mode of DART was chosen based on one criterion: sufficient ionization to produce ions that are clearly characteristic of the esters or amides under study.

4.5 Results and discussion

First, surfaces **S1** were analyzed by DART-HRMS and the spectra were compared with those of neat **1** and unbound **1** spiked onto the uncoated silicon nitride surface **S0**. In (+)-mode, DART-MS analysis of **1** gave a high signal intensity for $[1+H]^+$ at m/z 267.1560, while in (-)-mode, the most intense ion was $[CH_2=CH(CH_2)_8CO_2]^-$ at m/z 183.1379; the ions for the trifluoroethanol part, e.g. $[CF_3]^-$ at m/z 68.9948 and $[CF_3CH_2O]^-$ at m/z 99.0053, were observed at a lower abundance (Figure 4.3 and Table 4.1).

The specimens with surface **S1** were analyzed in both (+) and (-)-mode. Given the stability of these monolayers and the strength of the surface linkage, it was expected that bond cleavage would occur around the ester functionality. Indeed, we observed in the spectrum of **S1** in (-)-mode that anions derived from trifluoroethanol were cleaved off, and both $[CF_3]^-$ (m/z 68.9949) and $[CF_3CH_2O]^-$ (m/z 99.0054) were detected (Figure 4.3, time interval 4-4.5 min; mass spectra are given in Appendix 2. Figure S1 and S2).

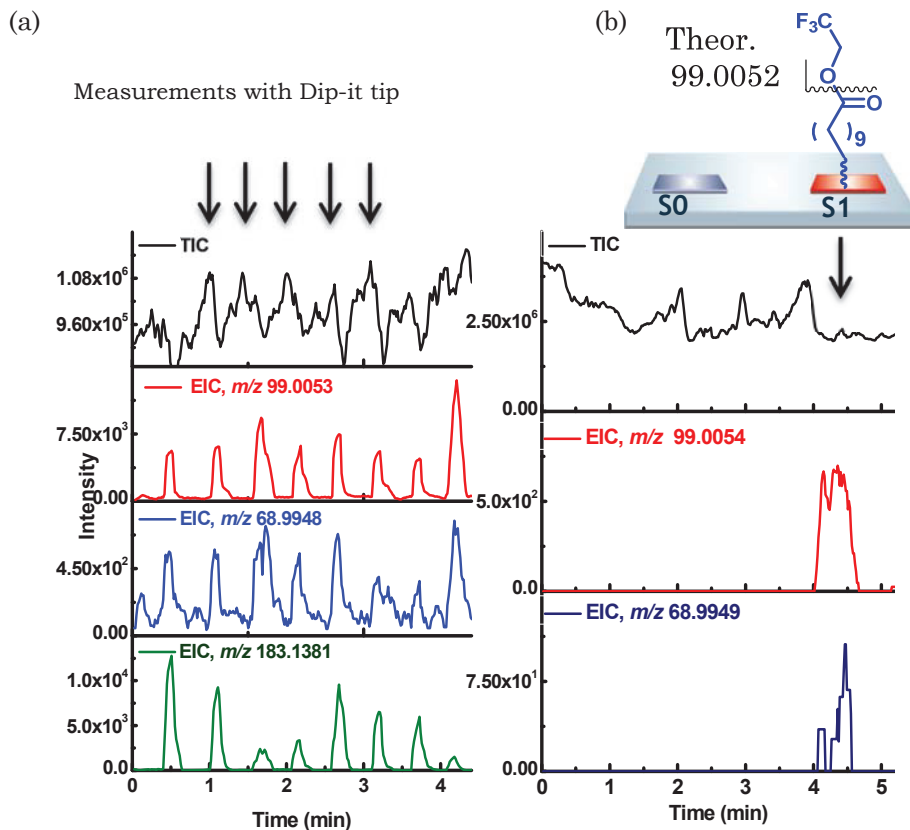


Figure 4.3: DART-HRMS analysis of **1** neat and after its covalent attachment onto Si_3N_4 . (a) Multiple measurements of **1** with Dip-it tip; from top to bottom: total ion current (TIC); extracted ion current (EIC) of ion at m/z 99.0053 [$\text{CF}_3\text{CH}_2\text{O}$] $^-$, EIC for ion at m/z 68.9948 ($[\text{CF}_3]$ $^-$), EIC for ion at m/z 183.1381, assigned for $[\text{CH}_2=\text{CH}(\text{CH}_2)_8\text{CO}_2]$ $^-$. (b) Measurement of monolayer **S1** and blank sample **S0** in (-)-mode, from top to bottom: TIC, EIC of ion at m/z 99.0053 [$\text{CF}_3\text{CH}_2\text{O}$] $^-$ and EIC of ion at m/z 68.9948 ($[\text{CF}_3]$ $^-$). Monolayer **S1** was measured between 4.0 and 4.5 min.

As the free alkene was no longer present after covalently binding to the surface, neither a $[\mathbf{1}+\text{H}]^+$ for **S1** nor the characteristic ion for **2** ($[\text{CH}_2=\text{CH}(\text{CH}_2)_8\text{CO}_2]$ $^-$) at m/z 183.1379 for **S1** or **S2** was found. This showed the absence of physically adsorbed molecules. In addition, no characteristic peaks were observed that resulted from cleavage of the surface links (Si-C/N-C)

or the linking chain (C-C) including **S2**, as no hydrolysable functional group was present. Based on these findings, we, thus, conclude that the high bond strength of Si-C/N-C bonds (~ 75 kcal/mol),¹³ (higher than that of Au-S; ~ 50 kcal/mol),¹¹ yields in DART-MS analyses of these ester monolayers, and more specifically: their *in situ* hydrolysis products, and not the intact molecule forming the monolayer.

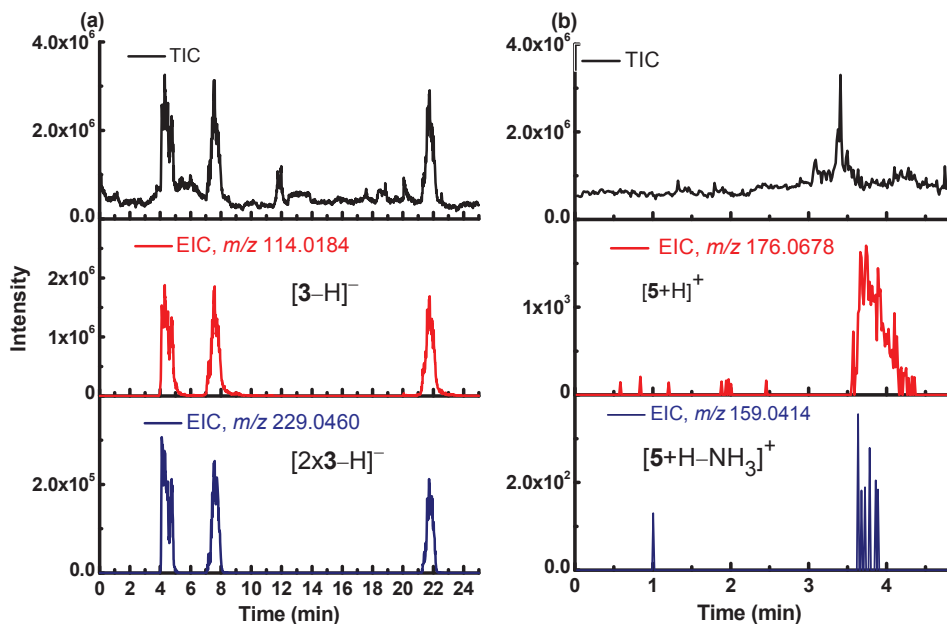


Figure 4.4: Chronograms for monolayers (a) **S3** and (b) **S5**. (a) Top: total ion current (TIC) in (-)-mode of **S3**; center: extracted ion current (EIC) of m/z 114.0184; bottom: EIC of m/z 229.0460; (b) Top: TIC in (+)-mode of **S5**; center: EIC of m/z 176.0678; bottom: EIC of m/z 159.0414

Several other monolayers having ester and amide functionalities (**S3-S11**) were analyzed to further evaluate the general usefulness of DART-HRMS. In each case, mass spectrometric analysis was compared with the free alcohol or amine in solution. For instance, the sample **S3** was passed between the DART and MS inlet thrice at 4.1-4.8 min, at 7.0-7.8 min and at 21.3-22.0 min (Figure 4.4a). Only during these intervals, ions related to the free NHS alcohol were observed, *i.e.* $[M-H]^-$ at m/z 114.0184 and $[2M-H]^-$ at m/z 229.0460 (Appendix 2, Figure S3). In parallel, uncoated Si₃N₄ samples (**S0**) were treated as the

modified surfaces, *e.g.* they were immersed for 24 h in the same reaction solution as used for the modified specimens. Afterwards, samples **S0** were cleaned as described above and subjected to DART-MS analysis. In all cases, no signal was found for the ions at either m/z 114.0184 or m/z 229.0460. This confirmed that the ions observed for **S3** were produced from the covalently bound monolayer rather than from molecules left from the reaction mixture. Similarly, the PFP ester monolayer **S4** was investigated in (-)-mode and the spectrum was compared with that of free PFP (**4**). The main ion in the spectrum of unbound **4** was $[M-H]^-$ at m/z 182.9860. The extracted ion current (EIC) of m/z 182.9860 in the mass spectrum of surface **S4** confirmed that this $C_6F_5O^-$ ion was observed in the spectrum of **S4** and was the most abundant one (Figure 4.5 and Appendix 2, Figure S4).

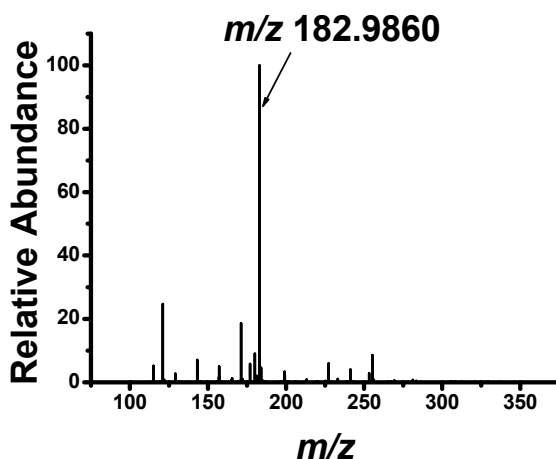


Figure 4.5: Negative mode DART-Orbitrap mass spectrum from m/z 50-450 of **S4**. The ion at m/z 182.9860 is $[M-H]^-$, where M is **4** (pentafluorophenol, PFP).

The DART-HRMS analysis was successfully extended to covalently bound amides. Using either the activated ester platform **S3** or **S4** and the amine **5**, the final pending group was exchanged for a trifluoromethylbenzylamide group (**S5**). Both (+) and (-)-modes were investigated. The spectra of **5** in (+)-mode showed not only the ion $[5+H]^+$ at m/z 176.0684, but also $[5+H-NH_3]^+$ at m/z 159.0418. In (-)-mode, no ion corresponding to $[5-H]^-$ was observed. Instead ions at m/z 188.0307 and m/z 189.0162 ($C_8H_4F_3O_2$, $[5+2O-NH_3-H]^-$) were present. Although its formation is yet unclear, for the latter ion an isotopic ion

at m/z 190.0194 ($C_7^{13}C_1H_4F_3O_2$) of correct intensity and an additional ion at m/z 161.0212 corresponding to $[C_8H_4F_3O_2-CO]^-$ were also detected. The formation of weak ions as $[M+O-H]^-$, $[M+2O-H]^-$ and $[M+3O-H]^-$ were also observed in (-)-mode for amines **6** and **10**. Even though, ionization in (-)-mode has not been studied in detail, most probably these ions are produced by electron capture and dissociative electron capture mechanisms, involving $O_2^{\bullet-}$ formed in the DART sampling zone.^{8, 16}

Analysis of surface **S5** in (+)-mode revealed the expected hydrolysis ions at m/z 176.0678 ($[5+H]^+$) and m/z 159.0414 ($[5+H-NH_3]^+$) (Figure 4.4b, and Appendix 2, Figure S5); in (-)-mode, the ions characteristic for compound **5** mentioned above were also present, which confirmed the identity of the monolayer (Figure 4.6a). DART-MS analysis in (-)-mode of surface **S5** did reveal an additional interesting feature. If surface **S5** was prepared from **S3**, it also demonstrated the presence of remnant NHS moieties (m/z 114.0184) (Figure 4.6a the second panel from top to bottom). This fits well with our previous, XPS-based finding that the attachment of trifluoromethylbenzylamine onto this active ester platform is not quantitative.¹²

That observation was based on the C/F ratio after the reaction, but the XPS spectrum did not resolve the ester functionality left on the surface. In this respect, DART-HRMS analysis complements XPS. Additionally, it illustrated that a simultaneous and fast analysis (≤ 1 min) of a mixture of ester and amide-terminated monolayers can be carried out without optimizing the MS settings, and clearly points to a broad applicability of DART-HRMS in surface analysis.

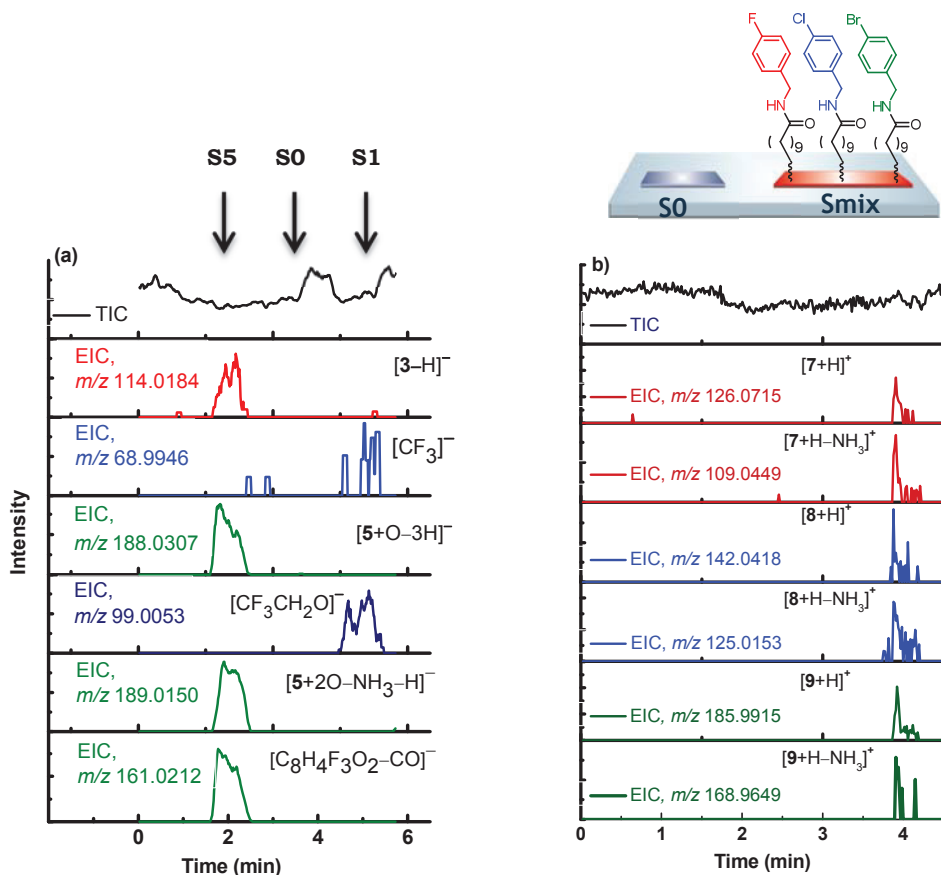


Figure 4.6: DART-HRMS analysis in (a) (-)-mode of surfaces **S5** (1.7-2.3 min), **S0** (2.8-3.6 min) and **S1** (4.4-5.3 min); (b) (+)-mode of **S_{mix}**.

The ionization of the covalently attached amides produced the same ions as the corresponding free amines in solution. To check if this is a general pattern, we synthesized additional amide monolayers, employing **6**, which differs only by one substituent from **5**, and **10**, which is an aliphatic amine containing also ether groups. We also selected an additional aliphatic amine (**11**), a derivative of strained cyclooctyne **12**. The application of such strained cyclooctynes in Cu-free reactions on a surface has previously been shown.^{12, 17} Moreover, the amines **7**, **8**, and **9** were also anchored onto the surface. For the attachment of all these amines the surfaces **S4** were employed, and the DART-HRMS analysis was carried out under the same conditions for as **S6** - **S11**.

As expected, for monolayers **S6** - **S9**, DART-HRMS in (+)-mode unambiguously identified the $[M+H]^+$ ions for each of the amide monolayers and the corresponding fragments for the loss of NH_3 , e.g. $[M+H-NH_3]^+$ (M being the free amine) (Table 4.1; Appendix 2 Figure S6). Monolayer **S10** was identified by the $[10+H]^+$ ion (m/z 294.1906), corresponding to the cleaved amine-crown ether **10** from the surface (Appendix 2, Figure S7). For monolayer **S11**, in (-)-mode two ions were observed corresponding to $[M-H]^-$ (m/z 149.0961) and $[M+2O-H]^-$ (m/z 181.0861), where M is alcohol **12** (Appendix 2, Figure S8). Apparently, the carbamate function is preferentially hydrolyzed, as in (+)-mode no ion corresponding to protonated **11** was observed.

In parallel, a separate **S4** sample was immersed in an equimolar mixture of amines **7**, **8** and **9**, affording mixed monolayer **S_{mix}**. DART-MS in (+)-mode of **S_{mix}**, demonstrated that all of the six expected ions were produced from the surface **S_{mix}**. All three protonated amine ions were observed at m/z 126.0714, 142.0418 and 185.9915 ($[M+H]^+$ for **7**, **8** and **9**), while also all three $[M+H-NH_3]^+$ fragments were clearly seen (m/z = 109.0449, 125.0153 and 168.9649, respectively) (Figure 4.6b; Appendix 2, Figure S9). Amines **8** and **9** were additionally identified by the presence of isotopic ions. Despite the fact that XPS also confirmed the formation of amides onto **S_{mix}** (clear signal in the N 1s narrow spectra assigned to the amide bond formation), their identification by means of XPS was not possible. The main reasons are: the lack of distinctive contributions in the C1s narrow spectra and a very low intensity for the fluorine, chlorine and bromine peaks, practically close to the signal to noise ratio. These results clearly point out the capability of DART-HRMS to outperform XPS for the structural analysis in cases of surface-bound monolayers of even only intermediate complexity. With a further increase of structural complexity, DART-HRMS may in fact be the only tool yet available to analyze organic monolayers.

Table 4.1: Detected ions on monolayers **S1-S11** and **S_{mix}**.

Compound	Selected fragments	Monolayer	Observed m/z on surface	Calculated m/z ^[b]
1 C ₁₃ H ₂₁ F ₃ O ₂	[M+H] ⁺	n.d.	n.d. ^[a]	267.1566
	[C ₂ H ₃ OF ₃ -H] ⁻	S1	99.0054	99.0058
	[CF ₃] ⁻	S1	68.9949	68.9946
2 C ₁₁ H ₂₀ O ₂	[M-H] ⁻	n.d.	n.d.	183.1385
3 C ₄ H ₅ NO ₃	[M-H] ⁻	S3	114.0184	114.0185
	[2M-H] ⁻	S3	229.0460	229.0455
4 C ₆ HF ₅ O	[M-H] ⁻	S4	182.9860	182.9863
5 C ₈ H ₈ F ₃ N	[M+H] ⁺	S5	176.0678	176.0681
	[M+H-NH ₃] ⁺	S5	159.0414	159.0416
	[M+O-3H] ⁻	S5	188.0307	188.0322
6 C ₇ H ₉ N	[M+H] ⁺	S6	108.0805	108.0802
	[M+H-NH ₃] ⁺	S6	91.0544	91.0542
10 C ₁₃ H ₂₈ NO ₆	[M+H] ⁺	S10	294.1906	294.1911
12 C ₁₀ H ₁₄ O	[M-H] ⁻	S11	149.0961	149.0960
	[M+2O-H] ⁻	S11	181.0861	181.0859
7 C ₇ H ₈ FN	[M+H] ⁺	S_{mix}; S7	126.0714	126.0714
	[M+H-NH ₃] ⁺	S_{mix}; S7	109.0449	109.0448
8 C ₇ H ₈ ClN	[M+H] ⁺	S_{mix}; S8	142.0418	142.0418
	[M+H-NH ₃] ⁺	S_{mix}; S8	125.0153	125.0153
9 C ₇ H ₈ BrN	[M+H] ⁺	S_{mix}; S9	185.9915	185.9913
	[M+H-NH ₃] ⁺	S_{mix}; S9	168.9649	168.9647

[a] n.d. – not detected; [b] calculated with XCALIBUR software (v. 2.1)

As the reaction of pure amine with **S4** proceeded with 67% yield (**S1** = 100%; surface density for **S1** $\sim 4 \times 10^{14}$ molecules/cm²),¹² the reaction with a mixture of three amines, having similar reactivity, should lead to a $\sim 22\%$ final surface density for each amide. Given the analogous substituent effects of *para*-Cl, -Br

and -I on the ionization efficiency, one could qualitatively argue that the intensities of the observed ions agree with an approximate 1 : 1 : 1 ratio for the attachment of all three amines. This would mean that for S_{mix} the density of **7**, **8** or **9** separately would be $\sim 9 \times 10^{13}$ molecules/cm². As the absolute intensity of each ion was ~ 20 times higher than the lowest detectable signal, the limit of detection of DART-MS with a spot size of ~ 5 mm² is about 5×10^{12} molecules/cm², i.e. around just 1% of a monolayer, i.e. in the pmol range.

4.6 Conclusion

In summary, DART-HRMS was shown to be a new highly effective tool for surface analysis of covalently bound monolayers, containing esters, amides or mixtures thereof. Due to the high stability of the covalent bonds (Si-N or Si-C) that anchor the monolayer to the surface, identification proceeds through hydrolysis products formed *in situ*. Surface-bound esters yield in (-)-mode alcohol anions RO⁻, while surface-bound amides yield in (+)-mode RNH₃⁺ ions. In addition, the progress of a 4-step surface-bound synthesis could be followed in detail. DART-MS provides fast analyses (≤ 1 min) and yields detailed molecular information in the low-mass range (as low as m/z 69) that is inaccessible to *e.g.* MALDI. The sensitivity is in the pmol range, which allows for the probing of even low-density monolayers. These characteristics plus the fact that no labels are required make DART-HRMS a highly promising surface analysis technique.

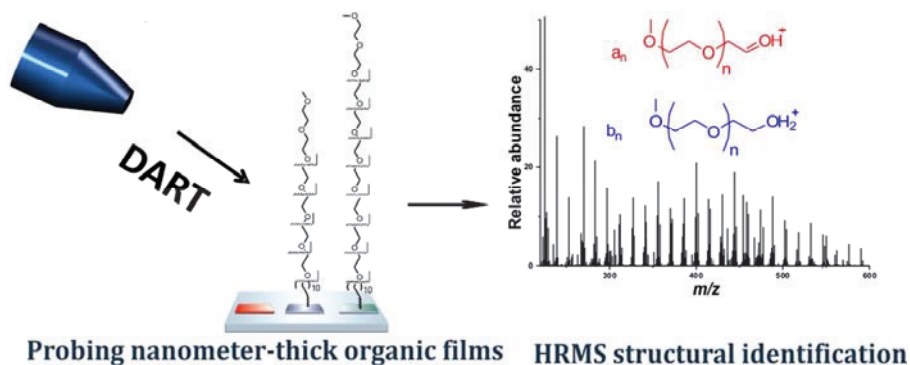
References

1. Whitesides, G. M. Nanoscience, Nanotechnology, and Chemistry. *Small* **2005**, *1* (2), 172-179.
2. Van Vaeck, L.; Adriaens, A.; Gijbels, R. Static secondary ion mass spectrometry (S-SIMS) Part 1: methodology and structural interpretation. *Mass Spectrom. Rev.* **1999**, *18* (1), 1-47.
3. Su, J.; Mrksich, M. Using MALDI-TOF Mass Spectrometry to Characterize Interfacial Reactions on Self-Assembled Monolayers. *Langmuir* **2003**, *19* (12), 4867-4870.
4. Mrksich, M. Mass Spectrometry of Self-Assembled Monolayers: A New Tool for Molecular Surface Science. *ACS Nano* **2008**, *2* (1), 7-18.

5. Cody, R. B.; Laramée, J. A.; Durst, H. D. Versatile New Ion Source for the Analysis of Materials in Open Air under Ambient Conditions. *Anal. Chem.* **2005**, *77* (8), 2297-2302.
6. Hajslova, J.; Cajka, T.; Vaclavik, L. Challenging applications offered by direct analysis in real time (DART) in food-quality and safety analysis. *TrAC, Trends Anal. Chem.* **2011**, *30* (2), 204-218.
7. Song, L.; Gibson, S. C.; Bhandari, D.; Cook, K. D.; Bartmess, J. E. Ionization Mechanism of Positive-Ion Direct Analysis in Real Time: A Transient Microenvironment Concept. *Anal. Chem.* **2009**, *81* (24), 10080-10088.
8. Song, L.; Dykstra, A.; Yao, H.; Bartmess, J. Ionization mechanism of negative ion-direct analysis in real time: A comparative study with negative ion-atmospheric pressure photoionization. *J. Am. Soc. Mass Spectrom.* **2009**, *20* (1), 42-50.
9. Kpegba, K.; Spadaro, T.; Cody, R. B.; Nesnas, N.; Olson, J. A. Analysis of Self-Assembled Monolayers on Gold Surfaces Using Direct Analysis in Real Time Mass Spectrometry. *Anal. Chem.* **2007**, *79* (14), 5479-5483.
10. Ma, L.; Jia, M.; Hu, J.; Ouyang, J.; Na, N. The Characterization of Self-Assembled Monolayers on Copper Surfaces by Low-Temperature Plasma Mass Spectrometry. *J. Am. Soc. Mass Spectrom.* **2012**, *23* (7), 1271-1278.
11. Love, J. C.; Estroff, L. A.; Kriebel, J. K.; Nuzzo, R. G.; Whitesides, G. M. Self-Assembled Monolayers of Thiolates on Metals as a Form of Nanotechnology. *Chem. Rev.* **2005**, *105* (4), 1103-1170.
12. Manova, R. K.; Pujari, S. P.; Weijers, C. A. G. M.; Zuilhof, H.; van Beek, T. A. Copper-Free Click Biofunctionalization of Silicon Nitride Surfaces via Strain-Promoted Alkyne–Azide Cycloaddition Reactions. *Langmuir* **2012**, *28* (23), 8651-8663.
13. Rosso, M.; Giesbers, M.; Arafat, A.; Schroën, K.; Zuilhof, H. Covalently Attached Organic Monolayers on SiC and SixN4 Surfaces: Formation Using UV Light at Room Temperature. *Langmuir* **2009**, *25* (4), 2172-2180.
14. Kaufmann, A.; Walker, S. Accuracy of relative isotopic abundance and mass measurements in a single-stage orbitrap mass spectrometer. *Rapid Commun. Mass Spectrom.* **2012**, *26* (9), 1081-1090.
15. Morlock, G.; Ueda, Y. New coupling of planar chromatography with direct analysis in real time mass spectrometry. *J. Chromatogr. A* **2007**, *1143* (1–2), 243-251.
16. McEwen, C. N.; Larsen, B. S. Ionization Mechanisms Related to Negative Ion APPI, APCI, and DART. *J. Am. Soc. Mass Spectrom.* **2009**, *20* (8), 1518-1521.
17. Manova, R. K.; van Beek, T. A.; Zuilhof, H. Surface Functionalization by Strain-Promoted Alkyne–Azide Click Reactions. *Angew. Chem. Int. Ed.* **2011**, *50* (24), 5428-5430.

Chapter 5

Ambient surface analysis of organic monolayers using DART and Orbitrap mass spectrometry



This chapter was published as:

Manova, R. K.; Joshi, S.; Debrassi, A.; Bhairamadgi, N. S.; Roeven, E.; Gagnon, J.; Tahir, M. N.; Claassen, F. W.; Scheres, L. M. W.; Wennekes, T.; Schroën, K.; van Beek, T. A.; Zuilhof, H.; and Nielen, M. W. F. *Anal. Chem.* **2014**, *86*, 2403-2411.

ABSTRACT

A better characterization of nanometer-thick organic layers (monolayers) as used for engineering surface properties, biosensing, nanomedicine and smart materials will widen their application. The aim of this study was to develop direct analysis in real time high-resolution mass spectrometry (DART-HRMS) into a new and complementary analytical tool for characterizing organic monolayers. To assess the scope and formulate general interpretation rules, DART-HRMS was used to analyze a diverse set of monolayers having different chemistries (amides, esters, amines, acids, alcohols, alkanes, ethers, thioethers, polymers, sugars) on five different substrates (Si, Si₃N₄, glass, Al₂O₃, Au). The substrate did not play a major role except in the case of gold, for which breaking of the weak Au-S bond that tethers the monolayer to the surface, was observed. For monolayers with stronger covalent interfacial bonds, fragmentation around terminal groups was found. For ester and amide-terminated monolayers, *in-situ* hydrolysis during DART resulted in the detection of ions characteristic of the terminal groups (alcohol, amine, carboxylic acid). For ether and thioether-terminated layers, scission of C-O or C-S bonds also led to the release of the terminal part of the monolayer in a predictable manner. Only the spectra of alkane monolayers could not be interpreted. DART-HRMS allowed for the analysis of and distinction between monolayers containing biologically relevant mono or disaccharides. Overall, DART-HRMS is a promising surface analysis technique that combines detailed structural information on nanomaterials and ultrathin films with fast analyses under ambient conditions.

5.1 Introduction

Nanomaterials – for example monolayers, nanoparticles, quantum dots, stimuli-responsive polymers and smart materials – are rapidly commercialized, e.g. in nanomedicine, electronics, biosensors, and over 60 nanomaterials are currently on the market.¹ Thus, nanomaterial characterization is needed for proper quality control, process efficiency² and environmental health risk assessment.^{3, 4, 5, 6} Nanofabrication of biosensors, often involves multiple surface modification steps⁷ of monolayers grafted on the sensor surface. A proper

surface characterization of each modification step would assist the desired control at a molecular level.

The most frequently used technique for surface analysis is X-ray photoelectron spectroscopy (XPS). XPS provides qualitative and quantitative information, yet suffers from a lack of chemical resolution. Surface mass spectrometry (MS) has, gained considerable attention as a complementary surface analysis technique.⁸ Secondary ion MS (TOF-SIMS) is the most common MS method for MS imaging of surfaces.^{9, 10, 11} The TOF-SIMS analysis of self-assembled monolayers (SAMs)^{10, 12} on gold revealed, however, extensive fragmentation. This led to low secondary ion yields and a poor signal-to-noise ratio. Alternative MS analytical techniques for SAMs are laser desorption MS (LDMS),¹³ thermodesorption high-resolution MS (TD-HRMS)¹⁴, two-laser MS (L2MS)^{10, 15} and matrix-assisted laser desorption/ionization mass spectrometry MS (MALDI-MS).¹⁶ The latter is able to probe different surfaces, which recently opened up new perspectives in the molecular identification of SAMs,¹⁷ nanoparticles,^{18, 19} biosensors²⁰ and biochips.²¹ Actually, the combination of surface MALDI-MS and SAMs on gold evolved in a technique termed by Mrksich as SAMDI.²² Upon MALDI, the interfacial Au-S bond breaks and the resultant intact modified thiolate is released. So far, the SAMDI approach was not only applied to subsequent surface reactions, but also to study biochemical reactions on the interface of tailor-made monolayers,²³ to perform immunoassays²⁴ or enzyme assays,²⁵ and to screen novel multicomponent reactions.²⁶ Unfortunately, the use of MALDI-MS is limited to the analysis of higher molecular weight (>300 Da) compounds due to MALDI matrix interferences and signal suppression.¹⁷ Moreover, the inhomogeneous distribution of matrix and the resulting poor shoot-to-shoot reproducibility,²⁷ as well as the choice of a suitable matrix for monolayer analysis²² are additional complicating factors.

To circumvent the aforementioned shortcomings, ambient MS has been considered as an alternative,²⁸ because it provides fast analysis and direct ionization of the sample without the need of sample preparation, addition of matrix, highly energetic ion beams, high vacuum or laser irradiation. Moreover, the ambient ionization sources can be hyphenated with most types of atmospheric pressure ionization mass spectrometers.²⁸ So far ambient MS has

been applied for SAMs on noble metal surfaces as gold²⁹ or copper.³⁰ In all cases, upon ambient plasma ionization, either with Direct Analysis in Real Time (DART)²⁹ or with Low Temperature Plasma (LTP),³⁰ the desorption of monomeric and dimeric thiolate molecules from the gold surfaces was observed, which is consistent with previous surface MS studies.^{10, 14, 15, 17} However, little is known about the fragmentation of monolayers with stronger interfacial bonds tethering the monolayer i.e. covalently bound monolayers on glass,^{31, 32} silicon nitride (Si₃N₄),³³ silicon (Si),^{34, 35} alumina (Al₂O₃),³⁶ etc.

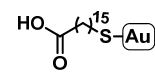
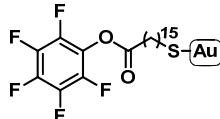
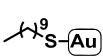
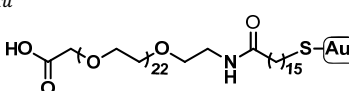
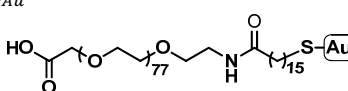
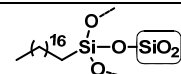
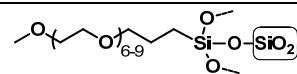
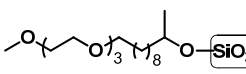
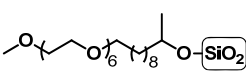
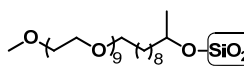
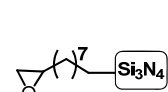
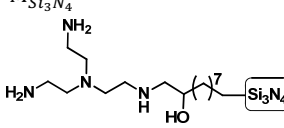
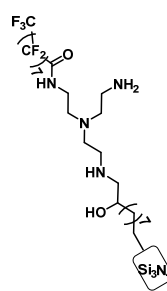
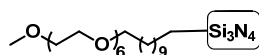
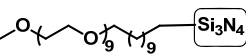
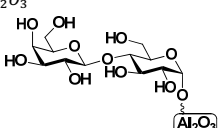
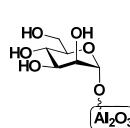
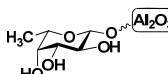
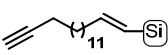
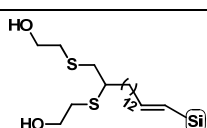
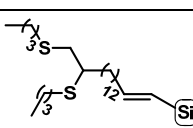
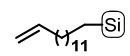
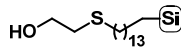
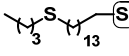
We showed previously that several ester and amide-terminated monolayers on Si₃N₄ could be analyzed by means of DART-HRMS.³⁷ The sensitivity was in the pmol range, and the high selectivity of the mass spectrometer even allowed the structure elucidation of mixed monolayers, differing only by the type of halogen present, which was not possible with e.g. XPS. Although this seemed promising, only one substrate and only two functional groups were investigated. Thus, the general usefulness of DART-MS as a surface analysis tool was not assessed.

Here we aim to develop DART-HRMS into a widely applicable analytical surface tool. To this end, a wide variety of monolayers, with different head and tail groups, were grafted onto gold, silicon nitride, silicon, glass, and alumina surfaces. The monolayers were, modified employing various surface reactions: click reactions (i.e. thiol-ene, thiol-yne, and copper-catalyzed cycloaddition reactions), esterification and amidation. The resulting modified surfaces were investigated by XPS and DART-HRMS, and their mass spectra were analyzed to arrive at a set of interpretation rules to deduce the surface chemistry present. Finally, three commercially available monolayers were studied to evaluate the usefulness for quality control.

5.2 Experimental section

All chemicals, solvents, inorganic substrates, commercially available coatings, the synthesis of azidoundecanyl carbohydrates (**1**, **4**, **7**) and the preparation of the monolayers are described in Appendix 3). Monolayers, investigated in this study, are depicted in Table 1.

Table 5.1: Overview of organic monolayers studied with DART-HRMS

Symbol	Monolayer structure			
Au	M_{Au}^1 	M_{Au}^2 	M_{Au}^5 	
	M_{Au}^3 	M_{Au}^4 		
SiO ₂	$M_{SiO_2}^1$ 	$M_{SiO_2}^2$ 		
	$M_{SiO_2}^{EO3}$ 	$M_{SiO_2}^{EO6}$ 	$M_{SiO_2}^{EO9}$ 	
Si ₃ N ₄	$M_{Si_3N_4}^1$ 	$M_{Si_3N_4}^2$ 	$M_{Si_3N_4}^3$ 	
	$M_{Si_3N_4}^{EO6}$ 	$M_{Si_3N_4}^{EO9}$ 		
Al ₂ O ₃	$M_{Al_2O_3}^{lac}$ 	$M_{Al_2O_3}^{man}$ 	$M_{Al_2O_3}^{fuc}$ 	
Si	M_{Si}^1 	M_{Si}^2 	M_{Si}^3 	
	M_{Si}^4 	M_{Si}^5 	M_{Si}^6 	

5.2.1 X-ray photoelectron spectroscopy (XPS).

Each monolayer formation was first confirmed by XPS. Prior to analysis, all substrates were extensively cleaned by sonication in appropriate solvents and dried under a stream of argon (for details see Appendix 3). XPS analyses were performed as described elsewhere.³⁸

5.2.2 Direct analysis in real time high-resolution mass spectrometry (DART-HRMS)

The DART-HRMS system consisted of a DART-SVP (IonSense, Saugus, USA) coupled to an Exactive Orbitrap high-resolution mass spectrometer (HRMS) (Thermo Fisher Scientific, San Jose, CA, USA). The MS was daily calibrated. The resolution was set at “ultra high” (100,000 FWHM at m/z 200 at a scan rate of 1 Hz). The mass range was either m/z 50-300 or m/z 100-2000. Xcalibur software (v. 2.1) was used for instrument control, data acquisition and data processing. Ions with values within ± 1.5 mDa of the theoretical values were considered in the structural elucidation of organic monolayers. The ionizing gas in the DART was He with a fixed flow of ~ 3.5 L/min and the temperature was set at 450 °C. DART settings in positive-ion mode and in negative-ion mode were as described previously.³⁷ The actual temperature of 199 °C in the ionization region at the surface of the specimen was measured with a Testo surface temperature sensor (Distrelec B.V, Utrecht, Netherlands) in static mode.

Specimens: modified monolayer samples (0.7 x 1.5 cm or 1 x 1 cm) together with a non-modified, freshly cleaned sample, were immobilized on a glass slide (Figure 5.1a). The glass slide with the specimens was carefully positioned on top of the motorized rail. The motorized rail moves horizontally and was used to introduce samples in and out of the ionization region (region between DART outlet and MS inlet). The DART outlet was pointed at an angle 45° to the sample and the height adjusted to minimize the DART outlet – sample distance, while still avoiding direct contact (typically ~ 1 cm). After optimization of the sample stage, the samples were removed from the ionization region via the rail and the DART heating was started. When the DART temperature

reached the set value, the samples were moved slowly (0.2 mm/s) towards the ionization region. Meanwhile the acquisition of data was started and in this way, ions from the ambient atmosphere, from the glass slide, and the non-modified sample were also collected and used for comparison and background subtraction. For collecting spectra in positive and negative-ion mode individual specimens were used. The obtained mass spectra and video material of a measurement can be found in Appendix 4 and on <http://pubs.acs.org/doi/suppl/10.1021/ac4031626>.

5.3 Results and discussion

5.3.1 DART-HRMS of amide and ester-terminated monolayers

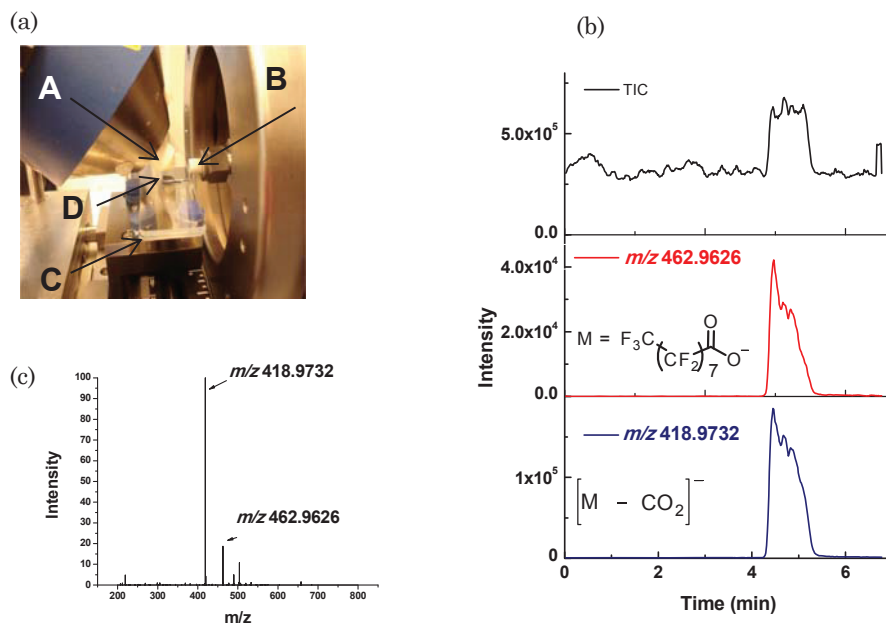


Figure 5.1: (a) DART-HRMS experimental set-up used for the characterization of organic monolayers. A) DART source pointed at 45° towards the sample. B) MS inlet. C) motorized rail. D) a 1×1 cm Si_3N_4 sample; (b) DART-HRMS of the reversed amide monolayer $M^3_{Si_3N_4}$ in negative-ion mode, measured between 4.2 min and 5.3 min; from top to bottom: total ion current (TIC), the extracted ion current (EIC) of $CF_3(CF_2)_7COO^-$ at m/z 462.9626 and EIC of $CF_3(CF_2)_7^-$ at m/z 418.9732; (c) mass spectrum of monolayer $M^3_{Si_3N_4}$.

First, samples were analyzed that could clarify the role of hydrolysis in ester and amide-functionalized monolayers. We reported previously³⁷ that ester-containing monolayers on Si₃N₄ could be identified in negative-ion mode by ions related to the free alcohol. Similarly, in positive-ion mode, amide monolayers were characterized by ions associated with the free amine. In both cases, the alcohol or amine had reacted with the activated terminal carboxylic acid moiety of an already present monolayer on Si₃N₄ (ROC(=O)(CH₂)₁₀–Si₃N₄ and RNHC(=O)(CH₂)₁₀–Si₃N₄ respectively). Based on these findings, we hypothesized that *in-situ* hydrolysis occurred during DART ionization with (protonated) water molecules, involved in the ionization process,³⁹ giving rise to the release of the free alcohol or amine. To test this hypothesis, the reversed amide $M_{Si_3N_4}^3(CF_3(CF_2)_7C(=O)NH-R-Si_3N_4)$ was constructed by reacting a carboxylic acid with a terminal amine group of a monolayer on Si₃N₄. If *in-situ* hydrolysis with or without simultaneous ionization proceeds during DART, then reverse amide monolayer $M_{Si_3N_4}^3$ (Table 1) should yield ions of the corresponding carboxylate component.

In the top panel of Figure 5.1b, the total ion current of $M_{Si_3N_4}^3$ shows when the sample is moved under the DART beam (between 4.2 min and 5.3 min). The spectrum in this interval revealed the ions CF₃(CF₂)₇COO⁻ at m/z 462.9626 (Figure 5.1b, middle panel) and CF₃(CF₂)₇⁻ at m/z 418.9732 (Figure 5.1, bottom panel) – as base peak. The spectrum is presented in Figure 5.1 c. This indicates that amide hydrolysis is indeed the dominant process.

To confirm that hydrolysis is not influenced by the substrate, we compared the negative-ion mode spectrum of the previously reported³⁷ pentafluorophenyl ester-terminated monolayer on Si₃N₄: C₆F₅OC(=O)(CH₂)₁₀–Si₃N₄, with that of a pentafluorophenyl ester-terminated monolayer on Au: C₆F₅OC(=O)(CH₂)₁₄CH₂S–Au (Table 1, M_{Au}^2). For both monolayers, the ion [C₆F₅O]⁻ that results from ester hydrolysis, was observed at m/z 182.9860. Therefore, the substrate linkage appears of only minor importance in effecting the formation of hydrolysis products.

5.3.2 DART-HRMS of monolayers having S-Au bonds

DART-MS should be able to reveal information on the strength of the interfacial bond tethering the monolayer. To this aim, we continued to investigate ester-terminated monolayers, but now in positive-ion mode. No fragments associated with the carboxylate function of the $C_6F_5OC(=O)(CH_2)_{10}-Si_3N_4$ were detected, whilst the analysis of $C_6F_5OC(=O)(CH_2)_{15}S-Au$ (M_{Au}^2) revealed the presence of $[C_6F_5OC(=O)(CH_2)_{15}S]^+$ at m/z 453.1870 (see Appendix 4, Figure S5). Apparently, while the Si-C and N-C bonds do not easily break under these conditions, the weak Met-S bond (Met = Au, Cu) is preferentially cleaved, resulting in the formation of positive ions containing the whole monomer of the SAMs, a finding that corroborates other surface MS studies on S-Au monolayers.^{29, 30} In this regard, the substrate plays a role in the fragmentation of the monolayer, especially when the interfacial bond is weak enough to break and yields stable ions of sufficient volatility.

Next monolayers lacking hydrolyzable bonds, e.g. the SAMs $HOOC(CH_2)_{14}CH_2S-Au$ (Table 1, M_{Au}^1), and $CH_3(CH_2)_9S-Au$, (Table 1, M_{Au}^5) were studied. They were first analyzed in positive-ion mode, because under these conditions desorption of intact ions from the noble metal surface is most likely to be observed.^{15, 29, 30} In positive-ion mode $CH_3(CH_2)_9S-Au$, did not show the ions $[CH_3(CH_2)_9S]^+$ and the corresponding dimers $[CH_3(CH_2)_9S-SH-(CH_2)_9CH_3]^+$. Instead, many oxidation products were observed: $[M + 2O - H]^+$, $[M + O - 3H]^+$, $[M + O - H]^+$, $[M + 3O - H]^+$, and $[M + 2O - 3H]^+$ for the monomeric molecules (Figure 5.2, upper panel), and $[2M - SH + 2O]^+$, $[2M - SH + 2O - H_2O]^+$, and $[2M - H_2S + 5O]^+$ for the dimers (Figure 5.2, middle panel), where M is $CH_3(CH_2)_9SH$. Combined, the ions provide proof for the presence of decanethiol. In the m/z 170-220 mass range several ions unrelated to the monolayer were observed, which shows the necessity of carrying out scans of non-modified substrate, i.e. in this case gold. The ions at m/z 206, 207, 328 and 380 were related to the monolayer but could not be assigned.

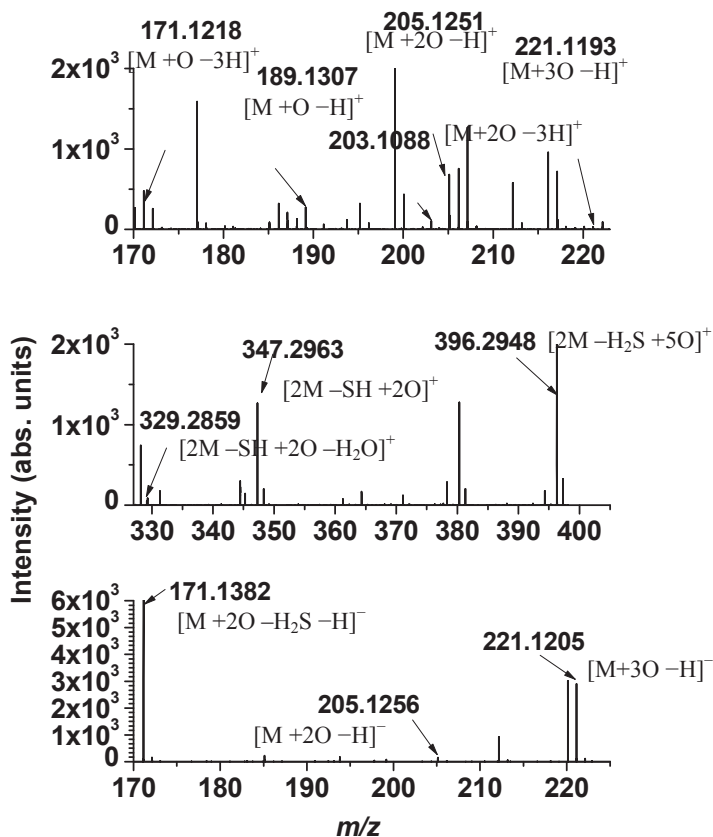


Figure 5.2: DART-HRMS of M_{Au}^5 (decanethiol on gold) in positive (m/z 170-220, upper; m/z 325-405, middle) and negative-ion mode (m/z 170-225, lower), providing similar information. The ions at m/z 177, 199, 212, 216 and 217 in positive-ion mode are due to background.

In negative-ion mode, the spectrum of $CH_3(CH_2)_9S-Au$ (M_{Au}^5) revealed two oxidation products of decanethiol also present in positive-ion mode but now negatively charged, i.e. $[M+3O-H]^-$ and $[M+2O-H]^-$, as well as $[M+2O-H_2S-H]^-$ at m/z 171.1382 (Figure 5.2, lower panel). Thus the positive-ion mode measurements corroborated the negative-ion conclusions. The presence of extensive oxidation in both negative and positive-ion modes can be explained by the close proximity of the DART outlet to the MS inlet and the specimen. Under such geometric conditions, the presence of a relative high abundance of

reactive O_2^{+} species has been reported.³⁹ Alkylsulfonate anions are also prominently present in negative ion spectra obtained with TOF-SIMS¹² or LDMS¹³ of different sulfur-containing monolayers. However, other thiol molecular species such as $[M-H]^+$, $[M-H]^-$ and dimeric molecular species such as $Met[M-H]_x^-$ (Met = Au, Ag, Cu, Pt; M = thiol; x=2-4) are the most characteristic ions in TOF-SIMS spectra,^{11, 40, 41} while DART ionization mainly produced oxidation products. Positive secondary ion mass spectra obtained with TOF-SIMS¹¹ are, on the other hand, dominated by ions characteristic of long-chain hydrocarbons, namely C_xH_y and a variety of fragments originating from the alkyl chain. These ions were absent in the DART-HRMS spectra of M_{Au}^5 , i.e. such extensive fragmentation was not observed.

The SAM M_{Au}^1 demonstrated the formation of ions $[HOOC-(CH_2)_{15}-S]^+$ at m/z 287.2034. In its spectrum, the ions corresponding to the loss of water at m/z 269.1931 and to the loss of H_2 at m/z 285.1878 were even more intense (Appendix 4, Figure S4). Additionally, the ion related to the loss of H_2S at m/z 253.2159 was detected. Interestingly, the above mentioned cations were scarcely present in the spectrum of the solution of the free thiol $HS-(CH_2)_{15}-COOH$ or when present on a glass surface. Instead, the ammonia adduct $[HS-(CH_2)_{15}-COOH + NH_4]^+$ was predominantly formed together with the ion for $[HS-(CH_2)_{15}-COOH + NH_4 + H_2O - NH_3]^+$. In other words, DART-HRMS analysis was able to discriminate between covalently bound thiolates on flat gold surfaces and unbound thiol molecules on glass.

5.3.3 DART-HRMS of monolayers having C-S bonds

Considering this, monolayers with C-S bonds were also probed in order to test whether stronger covalent bonds could be cleaved, giving rise to characteristic fragments. To this aim, two different thiols, i.e. mercaptoethanol and butanethiol, were covalently attached to an alkyne (Table 1, M_{Si}^1) and an alkene (Table 1, M_{Si}^4) monolayer on Si via thiol-yne or thiol-ene click reactions, respectively.⁴² Thus, four different monolayers were obtained. Dithioether-terminated monolayer M_{Si}^2 and monothioether-terminated monolayer M_{Si}^5 , obtained via attachment of mercaptoethanol, have the same terminal groups but differ by their surface coverage of the attached mercaptoethanol in favor of M_{Si}^2 ($M_{Si}^2 > M_{Si}^5$; Table 1)⁴². Similarly, monolayers M_{Si}^3 and M_{Si}^6 , obtained by

attachment of butanethiol, have the same terminal groups but differ by their coverage ($M_{Si}^3 > M_{Si}^6$; Table 1). In contrast to the S-Au monolayers, DART-HRMS analysis of M_{Si}^2 , M_{Si}^3 , M_{Si}^5 and M_{Si}^6 , in positive-ion mode gave no characteristic peaks, confirming the results obtained on Si_3N_4 that intact monolayers cannot be analyzed due to the strong interfacial bond. Negative-ion analysis, however, revealed ions related to oxidized mercaptoethanol. The monolayers M_{Si}^2 and M_{Si}^5 , for instance, were identified by the ions $[HO(CH_2)_2SO_2]^-$ at m/z 108.9954 and $[HO(CH_2)_2SO_3]^-$ at m/z 124.9903 (Appendix 4, Figure S8 and S9). Likewise, monolayers M_{Si}^3 and M_{Si}^6 released the ion $[CH_3(CH_2)_3SO_3]^-$ at m/z 137.0268 (Appendix 4, Figure S10 and S11). The ion for $[CH_3(CH_2)_3SO_2]^-$ could not be detected due to the presence of interfering background ions at m/z 121.0286. These results suggest that upon DART ionization C-S bonds were cleaved, which broadens the scope of the application of this surface MS technique. Furthermore, two specimens of equal size, having the same thioether groups but with a different density (M_{Si}^3 and M_{Si}^5) were measured consecutively, and the intensity of the ions $[HO(CH_2)_2SO_2]^-$ and $[HO(CH_2)_2SO_3]^-$ on both monolayers was compared. Due to the different relative surface coverage,⁴² it was observed that these ions were of approximately one order of magnitude higher intensity for M_{Si}^2 (dithioether-terminated monolayer) than for monolayer M_{Si}^5 (monothioether-terminated). Thus, on a relative basis, DART-MS can yield information on the surface coverage of similar monolayers.

5.3.4 DART-HRMS of alkyl-terminated monolayers

Monolayers having a hydrocarbon chain e.g. the alkyne (C16) M_{Si}^1 and alkene (C14)-terminated monolayer M_{Si}^4 on Si, and the epoxy-terminated monolayer $M_{Si_3N_4}^1$ on Si_3N_4 , showed neither in positive nor in negative-ion mode distinguishable fragmentation upon DART ionization. For instance, no peaks representing ions reported for n-alkanes³⁹ as $[C_nH_{2n+2}-H]^+$, $[C_nH_{2n-1}]^+$ or their oxidation products were detected in positive-ion mode. The monolayer $M_{SiO_2}^1$, prepared via silane modification of glass and yielding a C_{18} -terminated monolayer, demonstrated in negative-ion mode several distinguishable but unexplainable ions besides ions that were also detected on a clean non-modified substrate. Recently, it was shown that only alkanes, significantly larger than

C₁₈, can be ionized by DART in negative-ion mode, albeit with relatively poor sensitivity.⁴³ In addition, those alkanes were analyzable as [M +O₂]⁻, and no extensive fragmentation was observed. Taking this into consideration, it is not surprising that the aforementioned alkyl-terminated monolayers were not identifiable with DART. In this respect, TOF-SIMS outperformed DART-HRMS with the ability to characterize alkyl-terminated monolayers due to the extensive formation of both organic and mixed organic/inorganic fragments from a variety of substrates including glass, silicon and gold.^{40, 44, 45}

5.3.5 DART-HRMS of oligo(ethylene glycol)-terminated monolayers

Whether DART-HRMS is applicable for identification of polyether monolayers, which are frequently applied to minimize biofouling, was addressed by analysis of monolayers $M_{SiO_2}^{EO3}$, $M_{SiO_2}^{EO6}$, $M_{SiO_2}^{EO9}$, and $M_{Si_3N_4}^{EO6}$, $M_{Si_3N_4}^{EO9}$. These methoxy-oligo(ethylene oxide) (EO)-terminated monolayers were prepared on two different substrates: Si₃N₄ and SiO₂, resulting in strong covalent C-N/C-Si and C-O-Si interfacial bonds, respectively. Additionally, 2-[[methoxy-oligo(EO)₆₋₉]-propyl]trimethoxysilane on glass provided the mixed monolayer $M_{SiO_2}^2$, containing oligo-EO tails with six to nine EO units.

The monolayers were studied in positive-ion mode by analyzing several adjacently positioned samples in one run (Figure 5.3). For all oligo(EO)-terminated monolayers we observed C-O scission at different positions in the EO tail and subsequent formation of two homologous series of protonated fragments. The first series was composed of truncated oligomers with methoxy/carbonyl chain ends: [CH₃O(CH₂CH₂O)_nCH₂CHO +H]⁺ (Figure 5.3a and 5.3b; marked as a_n) while the second series had methoxy/hydroxyl chain ends [CH₃O(CH₂CH₂O)_nCH₂CH₂OH +H]⁺ (Figure 5.3a and 5.3b; marked as b_n). The *m/z* of the observed ions was directly related to the length of the EO chain. The reconstructed ion chronogram of $M_{SiO_2}^{EO3}$, for instance, demonstrated peaks of relatively high abundance but only with n=1-2 (data not shown). Likewise, monolayers with six EO units, e.g. $M_{SiO_2}^{EO6}$ and $M_{Si_3N_4}^{EO6}$, gave rise to the oligomers with n=1-5, while monolayers with nine EO units, e.g. $M_{SiO_2}^{EO9}$ and $M_{Si_3N_4}^{EO9}$, produced not only the aforementioned oligomers but also longer fragments (n=1-8). Thus, by DART-HRMS analysis, it is possible to break down the EO

chain unit by unit, and to determine the longest oligo-EO linker present on the surface. Consequently in the case of the mixed monolayer $M_{SiO_2}^2$, all fragments with n between 1 and 8 were found. Apart from the said oligomers, their corresponding NH_4^+ -cationized species were also detected but with lower abundance.

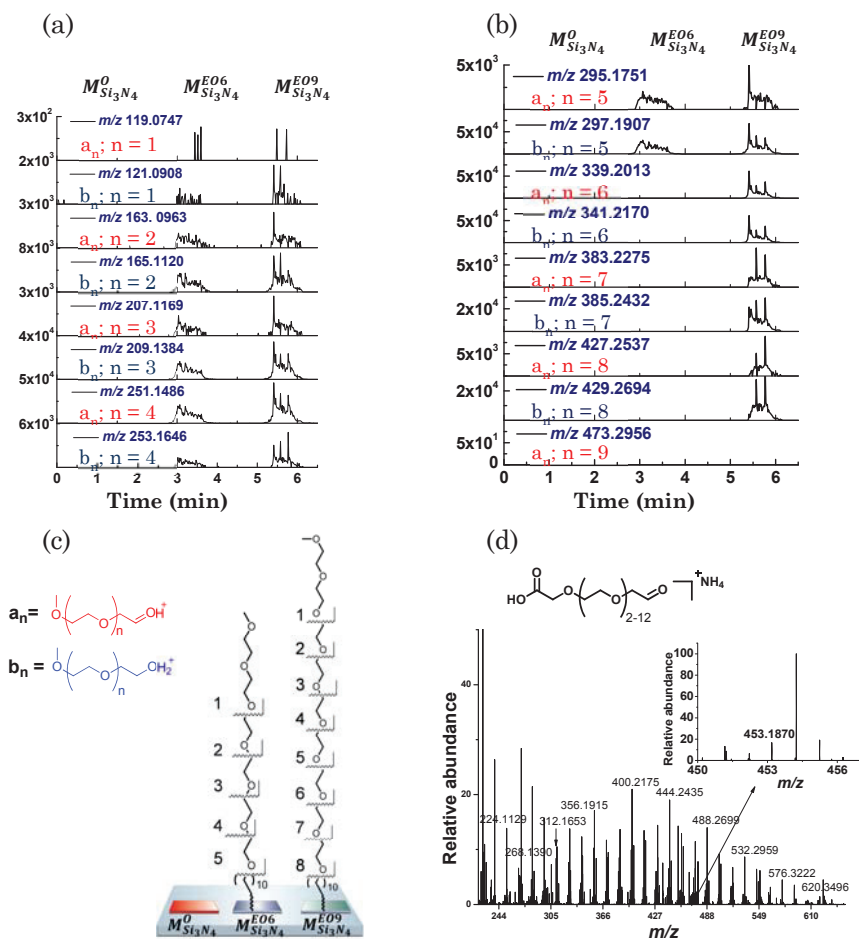


Figure 5.3: Reconstructed ion chromatograms (a and b) in positive-ion mode of $M_{Si_3N_4}^O$ (a non-modified Si_3N_4 substrate, measured between 1.0 min and 2.0 min), and methoxy-oligo(EO) monolayers $M_{Si_3N_4}^{EO6}$ (3.0-4.0 min) and $M_{Si_3N_4}^{EO9}$ (5.2-6.2 min); (a) ions from homologous series a_n and b_n with $n=1-4$ and (b) ions from homologous series a_n and b_n with $n=5-9$; (c) schematic representations of $M_{Si_3N_4}^O$, $M_{Si_3N_4}^{EO6}$, $M_{Si_3N_4}^{EO9}$, and structure of ions from homologous series a_n and b_n ; (d) positive-ion DART mass spectrum of carboxymethyl-PEG monolayer on gold (M_{Au}^3). The insert shows the ion at m/z 453.1870

$[\text{C}_6\text{F}_5\text{OC}(=\text{O})(\text{CH}_2)_{15}\text{-S}]^+$ in positive-ion mode corresponding with remaining unreacted PFP moieties.

5.3.6 DART-HRMS of poly(ethylene glycol)-terminated layers

Having shown that short monolayers with ether bonds can be analyzed by DART-HRMS, the question arose whether analysis of high-molecular weight polyether layers was also feasible. To this aim, the reactive ester-terminated monolayer M_{Au}^2 was used for the covalent attachment of a bifunctional poly(ethylene glycol) (PEG) with NH_2 and COOH as terminal groups. The attachment thus proceeded via amide bond formation on the surface. In this fashion two different PEGs were attached, mainly a 22-mer (PEG, 1 kDa), yielding the carboxymethyl-PEG-terminated layer M_{Au}^3 , and a 77-mer (PEG, 3.5 kDa) for obtaining the carboxymethyl-PEG-terminated layer M_{Au}^4 . The DART-HRMS analysis of these layers in positive-ion mode, showed series of homologous fragments each differing 44.0260 ($\text{C}_2\text{H}_4\text{O}$) following C-O and C-C scission of the polymer chain.⁴⁶ In contrast to the oligo-EO monolayers discussed above, all these ions were NH_4^+ adducts, and the most intense ions were assigned to truncated fragments bearing the carboxymethyl chain end of the polymer: $[\text{HOOC-CH}_2\text{O}(\text{CH}_2\text{CH}_2\text{O})_n\text{CH}_2\text{CHO} + \text{NH}_4]^+$ (Figure 5.3d). The highest MW fragment observed for these monolayers was the 12-mer because ions with higher mass and higher polarity most probably cannot be desorbed by DART. Ions bearing the amino chain end of the polymers were clearly discerned only in solution, while on the surface after amide bond formation and covalent attachment, ions with the free amino chain end of the polymer were not observed in positive-ion mode of DART. Measurement of M_{Au}^3 in positive-ion mode showed that not all of the original PFP groups of M_{Au}^2 had reacted with the amino-terminated PEG (Figure 5.3d insert). This could be more sensitively confirmed by scanning the same surfaces in negative-ion mode (PFP anion). This shows that DART-HRMS can be used in a semi-quantitative fashion to follow monolayer synthesis.

5.3.7 DART-HRMS of sugar-terminated monolayers

The potential of DART-HRMS to analyze thermally labile biomolecules attached on a surface was evaluated with lactose, mannose and fucose-functionalized monolayers on Al_2O_3 : $M_{\text{Al}_2\text{O}_3}^{\text{lac}}$, $M_{\text{Al}_2\text{O}_3}^{\text{man}}$, and $M_{\text{Al}_2\text{O}_3}^{\text{fuc}}$. Sugar-terminated monolayers find wide applications in biosensors,⁴⁷ molecular diagnostics,³⁶ and drug delivery.⁴⁸ The DART-HRMS analysis of these specimens in positive-ion mode did not show ions related to the original azidoundecanyl carbohydrates **1**, **4** or **7** (see SI) used in their synthesis confirming XPS analyses. Given the previously observed efficient cleavage of ether linkages in e.g. oligoethylene oxide monolayers, we expected C-O bond cleavage and ions for the corresponding monosaccharides. Indeed, these ions were detected, which implies C-O scission and ionization of the carbohydrate fragments. On monolayers $M_{\text{Al}_2\text{O}_3}^{\text{man}}$ and $M_{\text{Al}_2\text{O}_3}^{\text{lac}}$, for example, several adducts, described previously as being characteristic for a monosaccharide in solution $\text{C}_6\text{H}_{12}\text{O}_6$,^{49,47} were identified: $[\text{C}_6\text{H}_{12}\text{O}_6 + \text{NH}_4]^+$ at m/z 198.0969, $[\text{C}_6\text{H}_{12}\text{O}_6 + \text{NH}_4 - \text{H}_2\text{O}]^+$ at m/z 180.0863, $[\text{C}_6\text{H}_{12}\text{O}_6 + \text{NH}_4 - \text{H}_2\text{O} - \text{NH}_3]^+$ at m/z 163.0597, and $[\text{C}_6\text{H}_{12}\text{O}_6 + \text{NH}_4 - 2\text{H}_2\text{O} - \text{NH}_3]^+$ at m/z 145.0492. In addition to the aforementioned ions, on monolayer $M_{\text{Al}_2\text{O}_3}^{\text{lac}}$ ions related to a disaccharide $\text{C}_{12}\text{H}_{22}\text{O}_{11}$ were found: $[\text{C}_{12}\text{H}_{22}\text{O}_{11} + \text{NH}_4 - \text{NH}_3]^+$ at m/z 343.1229 and $[\text{C}_{12}\text{H}_{22}\text{O}_{11} + \text{NH}_4 - \text{H}_2\text{O}]^+$ at m/z 342.1387 (see Mass spectral library). The latter ion but not the former ion was reported by Wang et al. in their recent DART-MS study on dissolved sugars⁵⁰. Instead they reported an $[\text{M} + \text{NH}_4]^+$ for lactose, which was not observed in our surface analysis. Similarly the fucose-terminated monolayer $M_{\text{Al}_2\text{O}_3}^{\text{fuc}}$ demonstrated two ions for fucose $\text{C}_6\text{H}_{12}\text{O}_5$, namely $[\text{C}_6\text{H}_{12}\text{O}_5 + \text{NH}_4 - \text{H}_2\text{O}]^+$ at m/z 164.0915 and $[\text{C}_6\text{H}_{12}\text{O}_5 + \text{NH}_4 - 2\text{H}_2\text{O} - \text{NH}_3]^+$ at m/z 147.0649. Thus, DART-HRMS has the ability to discriminate between covalently immobilized monosaccharides and disaccharides, i.e. it could play a role in surface MS analysis of carbohydrate-based biosensors. It also shows that even monolayers incorporating very polar, non-volatile, thermally labile molecules, are amenable to analysis by DART-HRMS.

5.3.8 Application to commercially available samples

Based on all collected mass spectra of in-house prepared monolayers, specific ions characteristic for these monolayers are summarized in Table 2. Using this table, the surface chemistry of unknown samples can be easily evaluated. To demonstrate this for quality control of commercially available surfaces, several glass slides for microarrays (PolyAn GmbH, and Schott) and gold SPR chips (XanTec biodiagnostics) with different covalently attached monolayers (syn. coatings) were analyzed. Such engineered surfaces, used for bioassays and diagnostic purposes, are often supplied with limited information about the surface chemistry present. Therefore, a fast and reliable surface analysis tool could provide proper characterization and aid in the manufacturing process.

SPR chips (XanTec biodiagnostics) with the coating CMPGx are stated to be modified gold surfaces with a carboxymethyl-PEG (6 kDa) thin film. According to the manufacturer, this coating is suitable for further attachment of NH₂-terminated compounds, suggesting that the COOH terminal groups are free and available on the surface for further functionalization. Carboxymethyl-PEG coatings are best analyzed with DART-HRMS in positive-ion mode, and truncated fragments from homologous series [HOOC-CH₂O(CH₂CH₂O)_nCH₂CHO +NH₄]⁺ were expected (Table 2). In the positive-ion mass spectra of the SPR chip with CMPGx chip coating, the aforementioned set of ions were clearly observed, which confirmed the presence of terminal carboxymethyl-PEG groups. However, their intensity was one order of magnitude lower than that of the same ions detected in M_{Au}^3 and M_{Au}^4 (Appendix 3, Figure S22). This could be due to a lower surface coverage of carboxymethyl-PEG terminal groups on the SPR chip. This hypothesis is supported by the fact that fragments from this set of ions were detected only with n between 2 and 7, while ions with higher m/z values, as big as 12-mer could be detected from the in-house prepared monolayers.

Additionally, microarray glass slides with PEG coating (PolyAn) were also analyzed with DART-HRMS. On these PEG-ylated slides, very intense ions were observed differing by 44.0256 Da (C₂H₄O). In the mass spectrum, two homologous series of fragments could be clearly discerned: [C₈H₁₈O₄-(PEG)_n +NH₄]⁺ and [C₆H₁₀O₃-(PEG)_n +H]⁺.

Furthermore, PolyAn's microarray glass slides with terminal ester groups, namely N-hydroxysuccinimide (NHS), were also probed with DART-HRMS. The ester terminated glass slides were analyzed in negative-ion mode³⁷ (Table 2), and the presence of intense peaks at m/z 114.0188 for $[M-H]^-$ (Figure 5.4a) and at m/z 229.0454 for $[2M-H]^-$ (not shown), where M is NHS alcohol, confirmed the claimed surface functionality. In order to check on-slide reproducibility and batch-to-batch reproducibility of PolyAn's NHS (Figure 5.4a) and PEG slides, three specimens from one slide and two slides taken from two different batches (5 slides per batch) were subjected to DART-HRMS. The results were consistent and demonstrated good on-slide reproducibility and batch-to-batch reproducibility for both types of chemistries.

Glass slides with NHS terminal groups from another supplier (Schott) were also analyzed (Figure 5.4b). However, in this case the signal at m/z 114.0188 for $[M-H]^-$, where M is the NHS alcohol, was two orders of magnitude lower than for the PolyAn slides, and the ion for $[2M-H]^-$ was not detected at all. Additionally, the signal intensity of m/z 114.0187 varied (RSDs for PolyAn and Schott slides were 9% and 107% respectively) and suggested within-slide irreproducibility (Figure 5.4b). This evidently shows the usefulness of DART-HRMS for quality control of monolayers.

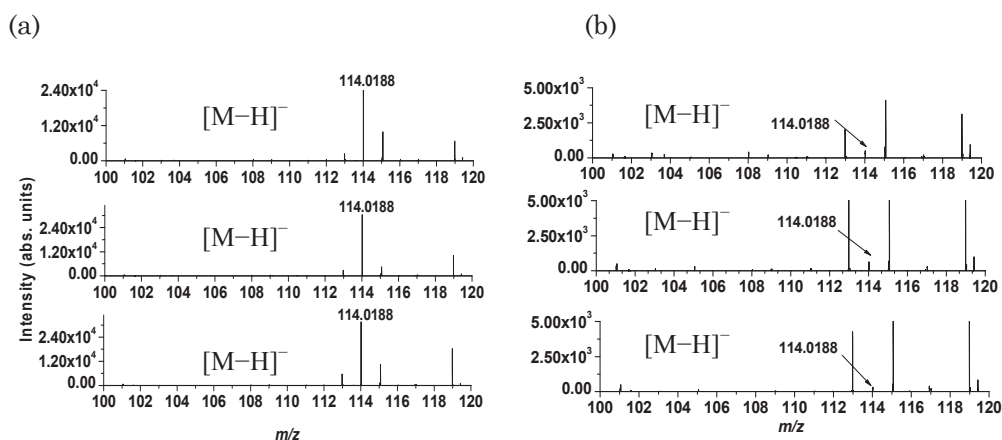


Figure 5.4: Negative-ion mode DART-HRMS of two types of commercial NHS glass slides; (a) 3 measurements of one slide of PolyAn; (b) 3 measurements of one slide of Schott. Please note difference in vertical axis values. The ions observed at m/z 113, 115 and 119 are due to background.

Table 5.2: Characteristic ions of monolayers observed with DART-HRMS.

Monolayer type	Characteristic ions observed in DART-HRMS	
	positive-ion mode	negative-ion mode
R-(C=O)O—surface	none	[R-(C=O)O] ⁻
R-O(C=O)—surface	none	[RO] ⁻
R-(C=O)NH—surface	none	[R-(C=O)O] ⁻
R-NH(C=O)—surface	[R-NH ₂ + H] ⁺	none
CH ₃ (CH ₂) ₉ S—Au	[M + 2O - H] ⁺ , [M + O - 3H] ⁺ , [M + O - H] ⁺ , [M + 3O - H] ⁺ , [M + 2O - 3H] ⁺ , [2M - SH + 2O] ⁺ , [2M - SH + 2O - H ₂ O] ⁺ , [2M - SH + 4O - H] ⁺ , M is CH ₃ (CH ₂) ₉ SH	[CH ₃ (CH ₂) ₉ SO ₃] ⁻ [CH ₃ (CH ₂) ₉ SO ₂] ⁻
HOOC-(CH ₂) ₁₅ -S—Au	[HOOC-(CH ₂) ₁₅ -S] ⁺ ; loss of H ₂ and H ₂ S	not measured
R-S-C _x H _y —surface	none	[RSO ₃] ⁻ , [RSO ₂] ⁻
C _x H _y —surface	none	none
CH ₃ O(EO) _n (CH ₂) _x —surface	[CH ₃ O(EO) _n CH ₂ CHO + H] ⁺ [CH ₃ O(EO) _n CH ₂ CH ₂ OH + H] ⁺	none
HOOCCH ₂ PEG—surface	[HOOCCH ₂ O(CH ₂ CH ₂ O) _n CH ₂ CHO NH ₄] ⁺	none
monosaccharide—surface	[C ₆ H ₁₂ O ₆ + NH ₄] ⁺ ; [C ₆ H ₁₂ O ₆ + NH ₄ - H ₂ O] ⁺ [C ₆ H ₁₂ O ₆ + NH ₄ - H ₂ O - NH ₃] ⁺ ; [C ₆ H ₁₂ O ₆ + NH ₄ - 2H ₂ O - NH ₃] ⁺	not measured
disaccharide—surface	[C ₆ H ₁₂ O ₆ + NH ₄] ⁺ ; [C ₆ H ₁₂ O ₆ + NH ₄ - H ₂ O] ⁺ ; [C ₆ H ₁₂ O ₆ + NH ₄ - H ₂ O - NH ₃] ⁺ ; [C ₆ H ₁₂ O ₆ + NH ₄ - 2H ₂ O - NH ₃] ⁺ ; [C ₁₂ H ₂₂ O ₁₁ + NH ₄ - NH ₃] ⁺ ; [C ₁₂ H ₂₂ O ₁₁ + NH ₄ - H ₂ O] ⁺	not measured

5.4 Conclusions

In 2009 Richman and Hutchison in their paper “The Nanomaterial Characterization Bottleneck” wrote “To reap the benefits of nanotechnology, improvements in characterization are needed to increase throughput as creativity outpaces our ability to confirm results.”² Current surface analysis tools such as SEM, fluorescence, and XPS cannot provide sufficiently detailed molecular information about the monolayer present. SIMS and MALDI-MS to some extent can but not under ambient conditions, and they suffer from fragmentation and background problems, respectively. Here we have shown, through a detailed analysis of a wide range of organic monolayers on five different substrates that DART-HRMS is able to provide such detailed chemical information for most monolayers. It does so in a simple, rapid, sensitive and reproducible manner under ambient conditions without any sample preparation and the fragmentation is in most cases predictable (Table 2). Thus DART-HRMS displays all the ingredients to become a valuable complimentary tool in the analysis of nm-thick layers leading to better characterization and thus removing bottlenecks on the way to improved engineered surfaces. Already we have shown that DART-MS is able to detect semi-quantitatively differences in the density of active groups of commercial nm-thick coatings. To facilitate further studies of organically modified surfaces by DART-HRMS, relevant spectra of all surfaces were compiled in a mass spectral library (Appendix 4).

References

1. *European Commission. Commission Staff Working Paper 2012*, available via <http://go.nature.com/Hebkwm>.
2. Richman, E. K.; Hutchison, J. E. The Nanomaterial Characterization Bottleneck. *ACS Nano* **2009**, *3* (9), 2441-2446.
3. Yu, T.; Greish, K.; McGill, L. D.; Ray, A.; Ghandehari, H. Influence of Geometry, Porosity, and Surface Characteristics of Silica Nanoparticles on Acute Toxicity: Their Vasculature Effect and Tolerance Threshold. *ACS Nano* **2012**, *6* (3), 2289-2301.

4. Riehemann, K. Nanotoxicity: How the Body Develops A Way to Reduce the Toxicity of Carbon Nanotubes. *Small* **2012**, *8* (13), 1970-1972.
5. Schrurs, F.; Lison, D. Focusing the research efforts. *Nat. Nanotechnol.* **2012**, *7* (9), 546-548.
6. Krug, H. F.; Wick, P. Nanotoxicology: An Interdisciplinary Challenge. *Angew. Chem. Int. Ed.* **2011**, *50* (6), 1260-1278.
7. Yang, W.; Zhang, R.; Willett, G. D.; Hibbert, D. B.; Gooding, J. J. Analysis of Self-Assembled Monolayer Interfaces by Electrospray Mass Spectrometry: A Gentle Approach. *Anal. Chem.* **2003**, *75* (23), 6741-6744.
8. Hanley, L.; Kornienko, O.; Ada, E. T.; Fuoco, E.; Trevor, J. L. Surface mass spectrometry of molecular species. *J. Mass Spectrom.* **1999**, *34* (7), 705-723.
9. Hutt, D. A.; Cooper, E.; Leggett, G. J. Structure and Mechanism of Photooxidation of Self-assembled Monolayers of Alkylthiols on Silver Studied by XPS and Static SIMS. *J. Phys. Chem. B* **1998**, *102* (1), 174-184.
10. Trevor, J. L.; Mencer, D. E.; Lykke, K. R.; Pellin, M. J.; Hanley, L. Surface Mass Spectrometry of Biotinylated Self-Assembled Monolayers. *Anal. Chem.* **1997**, *69* (21), 4331-4338.
11. Laiho, T.; Leiro, J. A. ToF-SIMS study of 1-dodecanethiol adsorption on Au, Ag, Cu and Pt surfaces. *Surf. Interface Anal.* **2008**, *40* (1), 51-59.
12. Offord, D. A.; John, C. M.; Griffin, J. H. Contact Angle Goniometry, Ellipsometry, XPS, and TOF-SIMS Analysis of Gold-Supported, Mixed Self-Assembled Monolayers Formed from Mixed Dialkyl Disulfides. *Langmuir* **1994**, *10* (3), 761-766.
13. Li, Y.; Huang, J.; McIver, R. T.; Hemminger, J. C. Characterization of thiol self-assembled films by laser desorption Fourier transform mass spectrometry. *J. Am. Chem. Soc.* **1992**, *114* (7), 2428-2432.
14. Shibue, T.; Nakanishi, T.; Matsuda, T.; Asahi, T.; Osaka, T. Thermal Desorption High-Resolution Mass Spectrometry of Mixed Self-Assembled Monolayers on Gold. *Langmuir* **2002**, *18* (5), 1528-1534.
15. Trevor, J. L.; Lykke, K. R.; Pellin, M. J.; Hanley, L. Two-Laser Mass Spectrometry of Thiolate, Disulfide, and Sulfide Self-Assembled Monolayers. *Langmuir* **1998**, *14* (7), 1664-1673.
16. Yan, B.; Zhu, Z.-J.; Miranda, O.; Chomposor, A.; Rotello, V.; Vachet, R. Laser desorption/ionization mass spectrometry analysis of monolayer-protected gold nanoparticles. *Anal. Bioanal. Chem.* **2010**, *396* (3), 1025-1035.
17. Su, J.; Mrksich, M. Using MALDI-TOF Mass Spectrometry to Characterize Interfacial Reactions on Self-Assembled Monolayers. *Langmuir* **2003**, *19* (12), 4867-4870.
18. Dass, A.; Stevenson, A.; Dubay, G. R.; Tracy, J. B.; Murray, R. W. Nanoparticle MALDI-TOF Mass Spectrometry without Fragmentation: Au₂₅(SCH₂CH₂Ph)₁₈ and

Mixed Monolayer Au₂₅(SCH₂CH₂Ph)_{18-x}(L)_x. *J. Am. Chem. Soc.* **2008**, *130* (18), 5940-5946.

19. Kim, B. H.; Shin, K.; Kwon, S. G.; Jang, Y.; Lee, H.-S.; Lee, H.; Jun, S. W.; Lee, J.; Han, S. Y.; Yim, Y.-H.; Kim, D.-H.; Hyeon, T. Sizing by Weighing: Characterizing Sizes of Ultrasmall-Sized Iron Oxide Nanocrystals Using MALDI-TOF Mass Spectrometry. *J. Am. Chem. Soc.* **2013**, *135* (7), 2407-2410.

20. Roth, M.; Kim, J.; Maresh, E.; Plymire, D.; Corbett, J.; Zhang, J.; Patrie, S. Thin-Layer Matrix Sublimation with Vapor-Sorption Induced Co-Crystallization for Sensitive and Reproducible SAMDI-TOF MS Analysis of Protein Biosensors. *J. Am. Soc. Mass Spectrom.* **2012**, *23* (10), 1661-1669.

21. Gurard-Levin, Z. A.; Mrksich, M. Combining Self-Assembled Monolayers and Mass Spectrometry for Applications in Biochips. *Annu. Rev. Anal. Chem.* **2008**, *1* (1), 767-800.

22. Mrksich, M. Mass Spectrometry of Self-Assembled Monolayers: A New Tool for Molecular Surface Science. *ACS Nano* **2008**, *2* (1), 7-18.

23. Li, S.; Liao, X.; Mrksich, M. Steady-State of an Enzymatic Reaction is Dependent on the Density of Reactant. *Langmuir* **2012**, *29* (1), 294-298.

24. Patrie, S. M.; Mrksich, M. Self-Assembled Monolayers for MALDI-TOF Mass Spectrometry for Immunoassays of Human Protein Antigens. *Anal. Chem.* **2007**, *79* (15), 5878-5887.

25. Ban, L.; Pettit, N.; Li, L.; Stuparu, A. D.; Cai, L.; Chen, W.; Guan, W.; Han, W.; Wang, P. G.; Mrksich, M. Discovery of glycosyltransferases using carbohydrate arrays and mass spectrometry. *Nat. Chem. Biol.* **2012**, *8* (9), 769-773.

26. Montavon, T. J.; Li, J.; Cabrera-Pardo, J. R.; Mrksich, M.; Kozmin, S. A. Three-component reaction discovery enabled by mass spectrometry of self-assembled monolayers. *Nat. Chem.* **2012**, *4* (1), 45-51.

27. Ocoy, I.; Gulbakan, B.; Shukoor, M. I.; Xiong, X.; Chen, T.; Powell, D. H.; Tan, W. Aptamer-Conjugated Multifunctional Nanoflowers as a Platform for Targeting, Capture, and Detection in Laser Desorption Ionization Mass Spectrometry. *ACS Nano* **2012**, *7* (1), 417-427.

28. Monge, M. E.; Harris, G. A.; Dwivedi, P.; Fernández, F. M. Mass Spectrometry: Recent Advances in Direct Open Air Surface Sampling/Ionization. *Chem. Rev.* **2013**.

29. Kpegba, K.; Spadaro, T.; Cody, R. B.; Nesnas, N.; Olson, J. A. Analysis of Self-Assembled Monolayers on Gold Surfaces Using Direct Analysis in Real Time Mass Spectrometry. *Anal. Chem.* **2007**, *79* (14), 5479-5483.

30. Ma, L.; Jia, M.; Hu, J.; Ouyang, J.; Na, N. The Characterization of Self-Assembled Monolayers on Copper Surfaces by Low-Temperature Plasma Mass Spectrometry. *J. Am. Soc. Mass Spectrom.* **2012**, *23* (7), 1271-1278.

31. Onclin, S.; Ravoo, B. J.; Reinhoudt, D. N. Engineering Silicon Oxide Surfaces Using Self-Assembled Monolayers. *Angew. Chem. Int. Ed.* **2005**, *44* (39), 6282-6304.

32. ter Maat, J.; Regeling, R.; Yang, M.; Mullings, M. N.; Bent, S. F.; Zuilhof, H. Photochemical Covalent Attachment of Alkene-Derived Monolayers onto Hydroxyl-Terminated Silica. *Langmuir* **2009**, *25* (19), 11592-11597.
33. Rosso, M.; Giesbers, M.; Arafat, A.; Schroën, K.; Zuilhof, H. Covalently Attached Organic Monolayers on SiC and Si_xN₄ Surfaces: Formation Using UV Light at Room Temperature. *Langmuir* **2009**, *25* (4), 2172-2180.
34. Li, Y.; Calder, S.; Yaffe, O.; Cahen, D.; Haick, H.; Kronik, L.; Zuilhof, H. Hybrids of Organic Molecules and Flat, Oxide-Free Silicon: High-Density Monolayers, Electronic Properties, and Functionalization. *Langmuir* **2012**, *28* (26), 9920-9929.
35. Ciampi, S.; Harper, J. B.; Gooding, J. J. Wet chemical routes to the assembly of organic monolayers on silicon surfaces via the formation of Si-C bonds: surface preparation, passivation and functionalization. *Chem. Soc. Rev.* **2010**, *39* (6), 2158-2183.
36. ter Maat, J.; Regeling, R.; Ingham, C. J.; Weijers, C. A. G. M.; Giesbers, M.; de Vos, W. M.; Zuilhof, H. Organic Modification and Subsequent Biofunctionalization of Porous Anodic Alumina Using Terminal Alkynes. *Langmuir* **2011**, *27* (22), 13606-13617.
37. Manova, R. K.; Claassen, F. W.; Nielen, M. W. F.; Zuilhof, H.; van Beek, T. A. Ambient mass spectrometry of covalently bound organic monolayers. *Chem. Commun.* **2013**, *49* (9), 922-924.
38. Manova, R. K.; Pujari, S. P.; Weijers, C. A. G. M.; Zuilhof, H.; van Beek, T. A. Copper-Free Click Biofunctionalization of Silicon Nitride Surfaces via Strain-Promoted Alkyne–Azide Cycloaddition Reactions. *Langmuir* **2012**, *28* (23), 8651-8663.
39. Cody, R. B. Observation of Molecular Ions and Analysis of Nonpolar Compounds with the Direct Analysis in Real Time Ion Source. *Anal. Chem.* **2008**, *81* (3), 1101-1107.
40. Tarlov, M. J.; Newman, J. G. Static secondary ion mass spectrometry of self-assembled alkanethiol monolayers on gold. *Langmuir* **1992**, *8* (5), 1398-1405.
41. Wong, S. C. C.; Lockyer, N. P.; Vickerman, J. C. Mechanisms of secondary ion emission from self-assembled monolayers and multilayers. *Surf. Interface Anal.* **2005**, *37* (9), 721-730.
42. Bhairamadgi, N. S.; Gangarapu, S.; Caipa Campos, M. A.; Paulusse, J. M. J.; van Rijn, C. J. M.; Zuilhof, H. Efficient Functionalization of Oxide-Free Silicon(111) Surfaces: Thiol–yne versus Thiol–ene Click Chemistry. *Langmuir* **2013**, *29* (14), 4535-4542.
43. Cody, R.; Dane, A. J. Soft Ionization of Saturated Hydrocarbons, Alcohols and Nonpolar Compounds by Negative-Ion Direct Analysis in Real-Time Mass Spectrometry. *J. Am. Soc. Mass Spectrom.* **2013**, 1-6.
44. Yang, L.; Lua, Y.-Y.; Jiang, G.; Tyler, B. J.; Linford, M. R. Multivariate Analysis of TOF-SIMS Spectra of Monolayers on Scribed Silicon. *Anal. Chem.* **2005**, *77* (14), 4654-4661.

45. Amalric, J.; Poleunis, C.; Delcorte, A.; Marchand-Brynaert, J. Static SIMS study on surfaces of chalcogenide glasses modified by an organic layer. *Surf. Sci.* **2012**, *606* (13–14), 1071-1077.
46. Wesdemiotis, C.; Solak, N.; Polce, M. J.; Dabney, D. E.; Chaicharoen, K.; Katzenmeyer, B. C. Fragmentation pathways of polymer ions. *Mass Spectrom. Rev.* **2011**, *30* (4), 523-559.
47. Cunningham, S.; Gerlach, J. Q.; Kane, M.; Joshi, L. Glyco-biosensors: Recent advances and applications for the detection of free and bound carbohydrates. *Analyst* **2010**, *135* (10), 2471-2480.
48. Gorityala, B. K.; Lu, Z.; Leow, M. L.; Ma, J.; Liu, X.-W. Design of a “Turn-Off/Turn-On” Biosensor: Understanding Carbohydrate-Lectin Interactions for Use in Noncovalent Drug Delivery. *J. Am. Chem. Soc.* **2012**, *134* (37), 15229-15232.
49. Saang'onryo, D. S.; Smith, D. L. Optimization of direct analysis in real time (DART) linear ion trap parameters for the detection and quantitation of glucose. *Rapid Commun. Mass Spectrom.* **2012**, *26* (3), 385-391.
50. Wang, Y.; Liu, L.; Ma, L.; Liu, S. Identification of saccharides by using direct analysis in real time (DART) mass spectrometry. *Int. J. Mass Spectrom.* **2014**, *357* (0), 51-57.

Chapter 6

General discussion and outlook



This final chapter summarizes the results of the thesis and points out the most important findings. Furthermore, we underline some interconnections between the outcomes obtained in the different chapters, and discuss how the results of this study could contribute to other areas of research. Finally, the chapter gives a broad perspective and further guidance towards achieving the ultimate goal of the project.

6.1 Introduction – development of universal sensor “Unihealth”

This work took part in the framework of the Euregio-funded project “UniHealth”. The ultimate goal of the “Unihealth” project is the development of a biosensor for detection of allergens and biomarkers. The biosensor must be cost-effective, label-free and capable of solving real-life problems. The intended applications are: 1) point-of-care tests for medical diagnoses, such as detection of biomarkers, and 2) rapid analysis of food allergens. The choice of these applications is motivated by the principle of detection of the sensor. The sensor system consists of a mass-sensitive sensor with micro- and nano-structures and its detection capability is well suited for analytes with a molecular mass above 20 kDa. Therefore, analytes of a protein nature, like biomarkers and allergens are obvious targets to explore.

The “Unihealth” project combines the scientific efforts of several research groups in order to arrive at a sensor, which is well usable in daily life situations. A research group at IMS Fraunhofer was responsible for the development of a micromechanical sensor system, while the other research groups focused on selecting specific ligands that could be attached to the sensor for recognizing targeted analytes. In the light of this, the objective of the current thesis was to bridge their scientific achievements and to steer the research towards a relevant application of the sensor. In this respect, the goals of the research described in this thesis were the development of: a) a reliable generic surface modification method for attachment of different ligands (developed by other research groups in the project) and b) an analytical surface characterization method that can gather information from the modified surface as part of quality control analyses.

6.2 Ligands to be attached onto the sensor

The attachment fashion must consider the type of ligand and their biological function. For example, the biomarkers in patients suffering from Guillain-Barré Syndrome (demyelination and axonal degeneration, resulting in acute, ascending and progressive neuropathy, characterized by weakness, paraesthesia, and hyporeflexia and ultimately death when untreated) are specific antibodies that bind the ganglioside GM1. Additionally, GM1 can bind specifically to various bacterial toxins, e.g. toxins from botulinum, tetanus and cholera (an enterotoxin produced by *Vibrio cholerae*), in this way mediating host-microbe interactions during infections. Such specific biointeractions can be used in the development of a biosensor for the diagnosis of either Guillain-Barré Syndrome or *Vibrio cholerae* infection.

In the framework of the “Unihealth” project, Garcia-Hartjes *et al.* have carried out an extensive investigation on novel selective ligands: GM1os-presenting compounds expressing strong binding capacity to cholera binding proteins and/or anti-GM1 antibodies.^{1, 2} All these new selective ligands are of an oligosaccharide nature and should be considered for chemical attachment onto the biosensor under development.

Other analytes of interest are allergens that trigger food allergies and food intolerance. In order to protect the allergic consumer from ambiguous food labelling practices, a fast sensing device that works in a non-professional setting, for instance at home, would be highly appreciated. Relevant allergens are, for example, gluten and peanut allergens. Again in the framework of the “Unihealth” project at Radboud University Nijmegen, Wammes *et al.* have conducted research towards finding selective ligands that bind peanut allergens and papain from papaya. All of these ligands are peptides or proteins,^{3, 4} and their immobilization onto the biosensor surface required a specific chemical attachment.

6.3 Versatile immobilization approach

Generally, the ligands that need to be attached are either oligosaccharides or proteins/peptides. On the one hand, the immobilization must lead to a very stable interfacial bond that allows long-term usage of the sensor, on the other hand the attachment should take place under mild conditions while preserving their capability to strongly bind the targeted analytes.

Bearing this in mind, we have selected a wet chemical approach to modify the Si_3N_4 -based sensor, i.e., UV-grafting of organic monolayers.⁵ As demonstrated by Rosso *et al.*,⁵ this method produces alkyl-monolayers with outstanding stabilities under both acidic (even in 2% HF) and basic conditions. Of course such methods cannot be implemented for the direct attachment of fragile biomolecules, so in this case a step-wise modification would be needed to produce a strongly bound – and at the same time – functional monolayer. The terminal group of this functional monolayer should be reactive towards NH_2 -terminated ligands because most of the ligands, that the “Unihealth” project anticipated to use, were proteins, peptides and antibodies.

Two different strategies can be applied in order to afford an amino-reactive covalently bound monolayer: direct attachment of 1-alkene monolayers bearing an amino-reactive functional group, and a step-wise surface modification tailoring the monolayer with a terminal amino-reactive functional group (Figure 6.1).

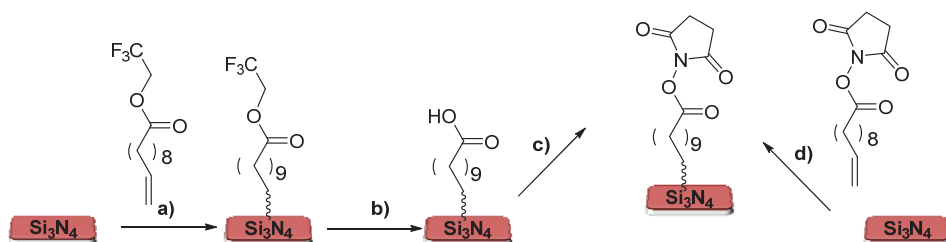


Figure 6.1: Stepwise surface modification (from a to c) yielding an NHS-terminal group, and direct attachment of N-hydroxysuccinimidyl undec-10-enoate (d) affording the same surface chemistry.

6.3.1 Direct or step-wise attachment of ligands onto Si₃N₄-based sensor

In this work, direct attachment of amino-reactive alkenes has been tested *via* either UV-grafting of an epoxy alkene or N-hydroxysuccinimidyl undec-10-enoate. While the interfacial bond, created by UV-grafting of all these terminal alkenes, is stable enough to withstand the working conditions of a biosensor, their terminal functionality did not always give a sufficient yield of the ligands to be attached. Chapter 3 deals with this problem, and examines in detail the introduction of an NHS-terminal group on monolayers bound to Si₃N₄ *via* either consecutive reactions or direct attachment of an ω -NHS-functionalized 1-alkene. The yield and reactivity of the resultant monolayers were compared, and suggested a possible upside-down attachment of the ω -NHS-functionalized 1-alkenes since NH- and NH₂-surface groups might be available on the Si₃N₄ surface. Thus, creating the NHS ester on the surface at a later stage rather than its direct introduction would lead to an overall high surface yield and quite possibly also a more reproducible process.

6.3.2 Surface analysis of a four-step reaction sequence

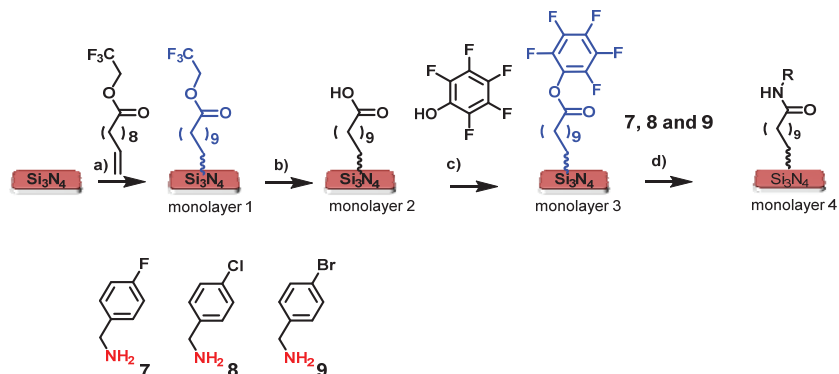
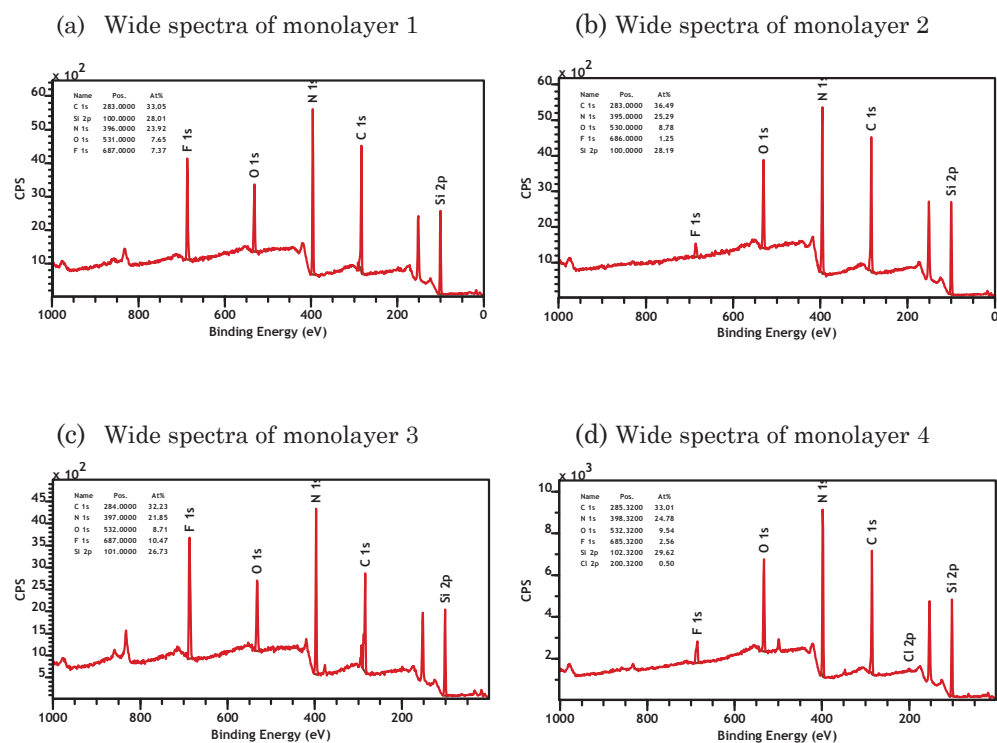
Figure 6.2: Consecutive reactions carried on Si_3N_4 -surface.

Figure 6.3: XPS spectra of monolayers depicted in scheme 6.1; (a) monolayer 1; (b) monolayer 2; (c) monolayer 3 and (d) monolayer 4. Each monolayer has its own characteristic ratio of the atomic percent fluorine/carbon on the surface, which facilitated the monitoring of the different reaction steps.

Another interesting result described in Chapter 3 is a surface analysis approach for characterization of monolayers on Si_3N_4 with XPS. A detailed surface analysis was carried out to characterize a step-wise approach and to quantify the yield of four-step synthesis. The surface analysis was especially facilitated by the replacement of the NHS-ester by a PFP-ester terminal group. A PFP-ester is a very reactive group towards amines and its hydrophobicity enhances monolayer stability under aqueous conditions (which is relevant in the context of biosensor applications). In addition, this group can be used as a XPS-label due to the high sensitivity for fluorine and higher binding energy shift for F-C chemical groups in the XPS analysis. In this manner, the PFP-terminal group not only introduces a useful function on the monolayer, but also plays a role as quantifier in the XPS analysis. For instance, the first introduction of fluorine on the surface is after UV-grafting of TFE (Figure 6.2, step a, and Figure 6.3a). Afterwards, a hydrolysis step is carried out (Figure 6.2b) that releases trifluoroethanol and consecutively a drop in the relative fluorine signal intensity is observed in the XPS spectrum (Figure 6.3b). In the next step, a PFP ester is formed, which results in an increase of the fluorine signal (Figure 6.2, step c, and Figure 6.3c). The latter is again reduced after reaction of the PFP-terminated ester monolayer with the NH_2 -functionalized ligand (Figure 6.2, step d and the corresponding spectrum in Figure 6.3d). Simply analyzing the fluorine signal on the surface, should ease the surface engineering quality control of the sensor. Moreover, as discussed in Chapter 3, the change in the hydrophobicity of the surface followed the same trend, so the expensive XPS analysis could to some degree be substituted by water contact angle measurements of the surface to follow the progress of the reactions.

6.3.3 Cu-free click reactions on the surface

Over the last few years, Cu-free click reactions gained a high popularity in biological settings, e.g., for cell-labelling, bioconjugation reactions, or drug discovery. Chapter 2 highlights the potential of this bioorthogonal reaction for surface functionalization, especially as an alternative for Cu-mediated reactions, as Cu ions can be detrimental for DNA, enzymes and other proteins, and can also influence the conductive properties of semiconductor surfaces and the fluorescent efficiency of quantum dots. In Chapter 3 we also make use of this reaction to build up a versatile immobilization platform for the attachment

of azido-terminated ligands. After step-wise surface modification of the Si_3N_4 surface, the PFP-activated monolayer reacted with an amino-terminated bicyclononyne (BCN). Immediately after that, the cyclooctyne-terminated surfaces reacted with azido-oligosaccharides similar to the GM1os compounds. Additionally, the reactivity of the surface-bound cyclooctyne was studied with a polyfluorinated azide and the progress of this Cu-free reaction was followed with XPS. This SPAAC reaction was not as fast as expected for “click” reactions and the yield of the final surface-bound triazole products was not quantitative either. Yet in spite of these shortcomings, this reaction has the advantages of: a) the omission of toxic Cu ions, and b) an attachment of biomolecules in an oriented fashion for biosensing application as later on was demonstrated by Trilling *et al.*⁶

6.4 Characterization of monolayers with surface-sensitive mass spectrometry

A versatile functionalization approach often leads to an increased complexity of surface bound-products. In this respect, even surface-sensitive techniques as XPS and secondary ion mass spectrometry (TOF-SIMS) face a challenge to unambiguously discriminate between a mixture of surface-bound products, especially when the surface yields are low. For instance, TOF-SIMS leads to too much fragmentation and generates too much data that are difficult to interpret. Additionally, the aforementioned techniques are only operational under vacuum, and expensive.

Therefore, in this work we have looked at a completely different approach to characterize thin layers covalently bound onto the surface, namely with a faster and more affordable type of mass spectrometry: DART-HRMS. The ambient ionization (DART) applied in this novel method is a good way to ionize organic monolayers present on flat solid surfaces, while the bench-top high resolution mass spectrometer (Orbitrap technology) actually provides sufficient resolution to detect and separate molecules present on the surface in the pmol range. In Chapter 4 we have described the foundation of the method, and its application for characterizing ester- and amide-terminated monolayers grafted on Si_3N_4 surfaces. During this study we found out that *in situ* hydrolysis of ester and amide-terminated monolayers on Si_3N_4 occurs upon DART ionization.

Since other observed ions were not assignable, we hypothesized that the covalent interfacial bond (that tethers the monolayers onto the surface) is strong enough to withstand the DART ionization process.

We investigated this in more detail in Chapter 5. First of all, we confirmed the *in situ* hydrolysis hypothesis. Afterwards, monolayers attached on other inorganic surfaces were also subjected to DART-HRMS analysis. The mode of attachment and the type of the surface actually lead to the formation of different interfacial bonds. In case of a thiolate monolayer on gold, the interfacial bond is weak enough to break and monomeric ions can be observed, whilst in case of strongly bound monolayers, only particular groups with sufficient volatility could be detected and assigned. For the same reason, alkyl-monolayers could not be identified, which is a limitation of this method. Nevertheless, we have also demonstrated that DART-HRMS is efficient in characterizing polymer coatings. Overall, we have built up a library of monolayers with different terminal groups, and based on it, we defined general interpretation rules for the mass spectra obtained thus enabling better analyses of monolayers. These rules are of practical importance, not only in the control of the Unihealth sensor under development but also in the quality control of coatings and other engineered surfaces outside of this project, e.g., microarrays glass slides, and SPR gold chips.

6.5 Practical Implications

6.5.1 “Unihealth” biosensor

The first positive outcome with a “Unihealth” sensor, following the surface modification approach described in this thesis, has been recently reported.⁷ The “Unihealth” sensor was modified with PFP-active groups onto the surface. Afterwards, a short amino-(PEG)₆-N₃ linker was attached to improve the antifouling capacity of the sensor and to introduce an azide group, and then, via Cu-click reactions, GM1-alkyne molecules were successfully attached on the sensor chip. In this case, the Cu-free click reaction was intentionally avoided due to the availability of pure GM1-alkyne, the low stability of the cyclooctynes, and the necessity to ship the chip sensor to another laboratory for the final testing (Fraunhofer Institute for Microelectronic Circuits and Systems, Duisburg, Germany).

As mentioned before, the sensor chip has a free standing membrane (60 μm), made of Si₃N₄ and electrostatically actuated to an oscillation with a resonance frequency of about 4 MHz. The mass sensitivity is in the picogram range. Using the generic surface modification approach (Chapter 3), the resonating micromechanical membrane structure was functionalized with GM1 to bind selectively cholera toxin B (Figure 6.4a). The analyte binding caused an increase of the effective mass of the membrane and therefore induced a decrease of the mechanical resonance frequency. The resonance measurements showed a non-linear behavior, which can be explained by a non-linear oscillator model (Figure 6.4b). Figure 6.4b shows the first derivative of a measurement showing a sharp peak due to the high frequency resolution.

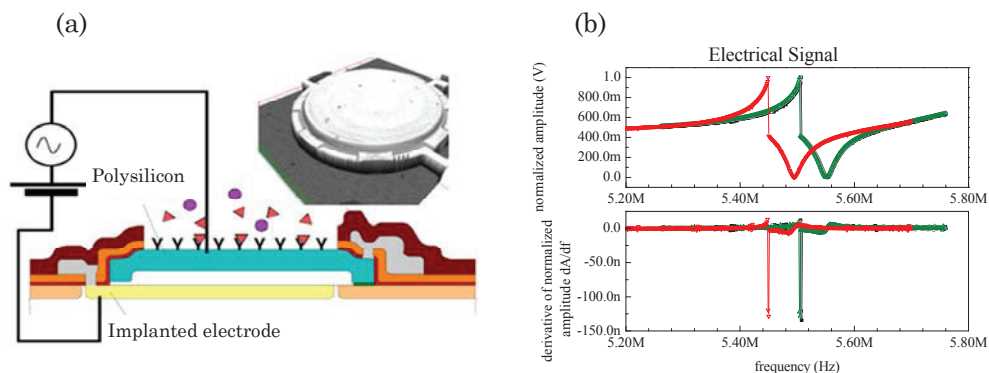


Figure 6.4: Cross section of the sensor element (a) and measured shift (b) of the resonance frequency due to the additional mass of bound analyte on a selectively functionalized sensor with a diameter of 60 μm .

6.5.2 Surface characterization

Microarray glass slides and SPR chips are widespread commercial engineered surfaces that are used in diagnostics and biomedical applications. The quality of the surface chemistry applied in these engineered surfaces is questionable due to the lack of affordable surface-sensitive techniques to control and prove the chemistry on the surface. For instance, a batch-to-bath reproducibility and sufficient surface yield of the terminal groups available on these engineered surfaces are crucial factors for successful applications. These characteristics can be easily followed by DART-HRMS as shown in Chapter 5. Taking into account that the high-resolution Orbitrap mass spectrometer is a bench-top instrument and the DART ion source is relatively cheap and easy to connect to a mass spectrometer, we recommend the use of this technique to realize an improved quality of the engineered products.

6.5.3 Policy implication

Finally, we would like to stress that the monolayers are somehow nanomaterials. According to the Regulation (EC) No 1223/2009 ‘nanomaterial’ means an insoluble or biopersistent and intentionally manufactured material with one or more external dimensions, or an internal structure, on the scale from 1 to 100 nm. Monolayers are the coatings that are often present on nanostructures, like nanoparticles, quantum dots, and nanotubes. Currently, the EU legislation is setting standards for risk assessments and is seeking to evaluate the toxicity of nanostructures.^{8, 9} Due to their complex nature and unpredictable behavior, the characterization of a nanomaterial is an analytical challenge. Hence, there are strong efforts to develop new analytical and toxicological methods fit for risk characterization of nanomaterials. In this respect, knowledge on the way in which the nanomaterials are synthesized and manufactured may prove helpful. The resultant surface chemistry on nanomaterials cannot only significantly affect the physico-chemical characteristics of nanomaterials, but may also influence their toxicological properties. In this context, the analytical tool DART-HRMS, developed in the current thesis, may be useful for the characterization of coatings of nanomaterials, and could shed light on the surface chemistry present and explain the resultant reactivity.

6.6 Future research

Additional elements that may be covered in future research are the following:

- An important aspect of the versatile immobilization approach was not considered: the control over nonspecific binding. Nonspecific binding can significantly impact the final performance of the sensor. However, at the outset we did not plan to cover this aspect of biosensor development, as this aspect can be readily incorporated as demonstrated by our group and other laboratories. Attaching or incorporating antifouling elements in the final surface chemistry for minimizing nonspecific binding of proteins and other matrix components in the sample is certainly worthwhile to investigate. Specifically the use of functionalized zwitterionic polymer coatings may be promising in this regard.

•An aspect to extend the development of the surface-sensitive analytical tool is the use of another type of ambient ionization, like AP- MALDI (atmospheric pressure matrix-assisted laser desorption ionization) or LAESI (Laser ablation electrospray ionization). These ionization techniques have up to now, as far as we know, not been used in the context of monolayer characterization, and potentially they could provide complementary information regarding the surface chemistry. Both AP-MALDI and LAESI rely on an ionization mechanism (UV or IR lasers) that is very different from the thermally assisted desorption mechanism of DART. The elevated temperatures needed during DART desorption and APCI-like ionization in the gas phase are incompatible with proteins and other polar high-MW biomolecules, thus somewhat limiting the application of DART. In addition to a more extended range of molecules in terms of MW and polarity, AP-MALDI and LAESI have the potential to probe (living) biological surfaces under physiological conditions. In terms of spatial resolution, these two ionization techniques definitely outperform the current DART methods with a spatial resolution as low as 7 μm for AP-MALDI and $\sim 100\text{-}200$ μm for LAESI. All these advantages make it worthwhile to evaluate them as alternative analytical tools for probing biosensing surfaces, including monolayers with immobilized ligands. This is especially true for sensors as small as the sensing membrane in the “Unihealth” biosensor (60 μm i.d.). Despite all these advantages, one should bear in mind that the higher spatial resolution may create sensitivity problems: smaller areas release fewer ions, requiring a high ionization efficiency and efficient ion transfer to the mass spectrometer – hurdles that have to be faced by AP-MALDI and LAESI too. Additional problems are the need of a matrix component for AP-MALDI and the presence of sufficient OH groups (e.g., water) for LAESI, factors that should be investigated too in the analysis of monolayers and thin coatings. Finally, aspects such as too little or too much fragmentation (including the informative *in situ* hydrolysis observed for DART) and ion suppression need to be looked into prior to a conclusion about the relative usefulness and best application areas of DART, AP-MALDI and LAESI.

•An additional immediate improvement of the DART-HRMS method is to couple the ion source to a high-resolution mass spectrometer that provides MS/MS data through further fragmentation of characteristic ions released from

the monolayer. During the monolayer investigations, numerous characteristic ions were found that were not assignable. Isolating these ions and fragmenting them in MS/MS mode could provide additional information and facilitate their identification. A reliable identification of the surface species might be crucial when complex research questions are addressed, e.g. identification of interfacial reactions, kinetics of surface reactions, and screening of potential ligands on biosensing surfaces.

• Finally, it is important to note that the current DART-HRMS method provides only qualitative, or at best semi-quantitative data, and extending the method to a quantitative surface analysis will be a plus.

6.7 Conclusion

The current thesis anticipated to make a contribution towards the development of a universal biosensor for detection of biomarkers and allergens. Two different aspects were regarded in this study: versatile surface modification that can facilitate a wide range of applications of the biosensor, and surface characterization that can improve the quality control and thus manufacturing of biosensors, biochips, nanomaterials and coatings. Although the ultimate goal of the project was partially achieved, the current research produced a fruitful and reproducible approach for functionalization of the “Unihealth” biosensor, and opened up new avenues in surface-bound analytical chemistry.

References

1. Garcia-Hartjes, J.; Bernardi, S.; Weijers, C. A. G. M.; Wennekes, T.; Gilbert, M.; Sansone, F.; Casnati, A.; Zuilhof, H. Picomolar inhibition of cholera toxin by a pentavalent ganglioside GM1os-calix[5]arene. *Org. Biomol. Chem.* 2013, 11 (26), 4340-4349.
2. Mattarella, M.; Garcia-Hartjes, J.; Wennekes, T.; Zuilhof, H.; Siegel, J. S. Nanomolar cholera toxin inhibitors based on symmetrical pentavalent ganglioside GM1os-sym-corannulenes. *Org. Biomol. Chem.* **2013**, 11 (26), 4333-4339.
3. Wammes, A. E. M.; Fischer, M. J. E.; de Mol, N. J.; van Eldijk, M. B.; Rutjes, F. P. J. T.; van Hest, J. C. M.; van Delft, F. L. Site-specific peptide and protein immobilization

on surface plasmon resonance chips via strain-promoted cycloaddition. *Lab Chip* **2013**, *13* (10), 1863-1867.

4. Wammes, A. E. M. Design, screening and orthogonal immobilization of peptide and protein ligands: towards a biosensor for food allergen detection. . PhD Doctoral dissertation, Radboud Univesrity, 2013.

5. Arafat, A.; Giesbers, M.; Rosso, M.; Sudhölter, E. J. R.; Schroën, K.; White, R. G.; Yang, L.; Linford, M. R.; Zuilhof, H. Covalent Biofunctionalization of Silicon Nitride Surfaces. *Langmuir* **2007**, *23* (11), 6233-6244.

6. Trilling, A. K.; Hesselink, T.; Houwelingen, A. v.; Cordewener, J. H. G.; Jongsma, M. A.; Schoffelen, S.; Hest, J. C. M. v.; Zuilhof, H.; Beekwilder, J. Orientation of llama antibodies strongly increases sensitivity of biosensors. *Biosens. Bioelectron.* **2014**, *60* (0), 130-136.

7. Burmester, K.; Goehlich, A.; Celik, Y.; Manova, R. K.; Scheres, L.; Roeven, E.; Trilling, A.; Schmidt, A.; Hutten, U.; Neureiter, K.; Pierrat, S.; Beek, T. v.; Vogt, H. CMOS integrated biosensor for the detection of biomarkers. *48th annual conference of the German Society for Biomedical Engineering - BMT, Hannover.* **2014**, 8-10 October, poster 65.

8. Scientific Committee on Emerging and Newly-Identified Health Risks, S. Opinion on the appropriateness of the risk assessment methodology in accordance with the technical guidance documents for new and existing substances for assessing the risks of nanomaterials. **2007**.

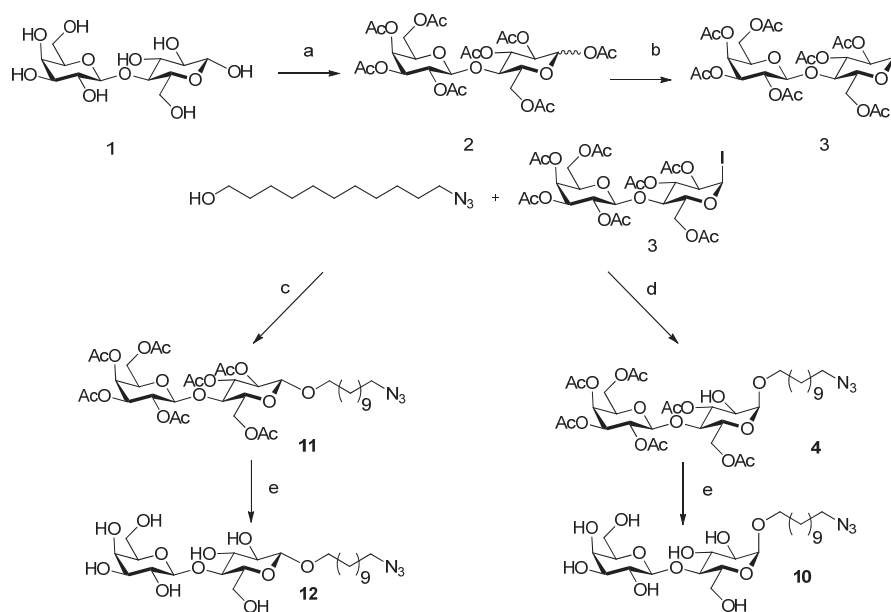
9. EFSA. Scientific opinion of the scientific committee on a request from the European commission on the potential risks arising from nanoscience and nanotechnologies on food and feed safety. *EFSA Journal* **2009**, *958*, 1–39.

Appendix 1

Information supplementing Chapter 3

Contents

1	Synthesis scheme S1 and ^1H and ^{13}C NMR data for of 3, 10, 11, 12	122
2	XPS spectra of NHS terminated monolayer S3 on Si_3N_4 surfaces	124
3	Thickness calculation by XPS	125
4	Electronic core level calculations for S1, TFE terminated monolayer	126
5	Electronic core level calculations for S2, undecanoic acid terminated surface	128
6	Electronic core level calculations for S3, NHS ester terminated surface	130
7	Electronic core level calculations for S4, PFP ester terminated surface	131
8	Electronic core level calculations for S7, cyclooctyne terminated surface	133
9	Electronic core level calculations for S8	135
10	Electronic core level calculations for S12	137
11	Atomic Force Microscopy (AFM)	140
12	References	143

1 Synthesis scheme S1 and ^1H and ^{13}C NMR data for of 3, 10, 11, 12

Scheme S1: Synthesis of 11-azido-undecyl-lactoside (α or β). (a) Ac_2O , I_2 , 35°C , 6 h; (b) I_2 , HMDS in CH_2Cl_2 , RT, 16 h; (c) I_2 , MeCN (β), RT, $0^\circ\text{C} \rightarrow \text{RT}$; (d) I_2 , CH_2Cl_2 (α), RT, $0^\circ\text{C} \rightarrow \text{RT}$, 16 h; (e) NaOMe in MeOH, RT, 16 h.

2,3,4,6-tetra-*O*-acetyl- β -D-galactopyranosyl-(1 \rightarrow 4)-2,3,6-tri-*O*-acetyl- α -D-glucopyranosyl iodide (3) $[\alpha]^{20}_{\text{D}} + 136.6^\circ$ (*c* 1.2, CHCl_3), *lit.* $[\alpha]^{23}_{\text{D}} + 137.0^\circ$ (*c* 1.0, CHCl_3).¹ ^1H NMR (400 MHz, CDCl_3): δ 6.91 (1H, d), 5.43 (1H, t), 5.33 (1H, d), 5.09 (1H, dd), 4.93 (1H, dd), 4.50 (1H, d), 4.46 (1H, dd), 4.04 – 4.19 (4H, m), 3.84 – 3.96 (3H, m), 2.13 (3H, s, OAc), 2.10 (3H, s, OAc), 2.06 (3H, s, OAc), 2.04 (3H, s, OAc), 2.03 (6H, s, OAc), 1.94 (3H, s, OAc). ^{13}C NMR (100 MHz, CDCl_3): δ 170.2, 170.0, 170.0, 169.9, 169.6, 169.1, 168.9 (7 \times C=O), 100.7 (CH), 75.6 (CH), 74.6 (CH), 72.6 (CH), 71.1 (CH), 70.9 (CH), 70.7 (CH), 70.5 (CH), 69.0 (CH), 66.6 (CH), 60.9 (CH_2), 60.8 (CH_2), 20.9, 20.7, 20.7, 20.7, 20.6, 20.5, 20.4 (7 \times $\text{CH}_3\text{-C(O)-}$, two peaks overlap). HRMS: *m/z* 745.0832, calculated for $\text{C}_{26}\text{H}_{34}\text{IO}_{17}$ ($[\text{M}-\text{H}]^-$): 745.0835.

β -D-galactopyranosyl-(1 \rightarrow 4)-1-(11-azido-undecanyl)- α -D-glucopyranoside (10). $[\alpha]^{20}_{\text{D}} + 61.6^\circ$ (*c* 1.1, CH_3OH). ^1H NMR (400 MHz,

CD₃OD): δ 4.76 (1H, d, H_{Glc-1}, J 4.8 Hz), 4.35 (1H, d, H_{Gal-1}, J 7.6 Hz), 3.75 – 3.88 (5H, m), 3.68 – 3.72 (3H, m), 3.53 – 3.60 (3H, m), 3.42 – 3.51 (3H, m), 3.27 (2H, t, J 6.9 Hz), 1.55 – 1.65 (4H, m), 1.29 – 1.40 (16H, m, -(CH₂)₈). ¹³C NMR (100 MHz, CD₃OD): δ 105.1 (CH, C_{Gal-1}), 99.9 (CH, C_{Glc-1}), 81.1 (CH), 77.1 (CH), 76.4 (CH), 74.9 (CH), 73.5 (CH), 73.3 (CH), 72.6 (CH), 70.3 (CH), 69.3 (-CH₂O-), 62.5 (CH₂, C_{Gal-6}), 61.9 (CH₂, C_{Glc-6}), 52.5 (-CH₂-N₃), 30.7, 30.7, 30.6, 30.6, 30.6, 30.3, 29.9, 27.8, 27.3 (9 x CH₂). HRMS: m/z 536.2811, calculated for C₂₃H₄₃N₃O₁₁ ([M-H]⁻) 536.2814.

2,3,4,6-tetra-*O*-acetyl- β -D-galactopyranosyl-(1 \rightarrow 4)-1-(11-azido-undecanyl)-2,3,6-tri-*O*-acetyl- β -D-glucopyranoside (11). ¹H NMR (400 MHz, CDCl₃): δ 5.34 (1H, dd, H_{Gal-4}, J = 3.30 and 0.76 Hz), 5.18 (1H, t, H_{Glc-3}, J = 9.32 Hz), 5.10 (1H, dd, H_{Gal-2}, J = 10.36 and 7.88 Hz), 4.95 (1H, dd, H_{Gal-3}, J = 10.40 and 3.44 Hz), 4.87 (1H, dd, H_{Glc-2}, J = 9.52 and 7.96 Hz), 4.48-4.43 (3H, m, H_{Gal-1}, H_{Glc-6a}, H_{Glc-1}), 4.15-4.05 (3H, m, H_{Gal-6}, H_{Glc-6b}), 3.88-3.76 (3H, m, H_{Gal-5}, -OCH_aH_b-(CH₂)₁₀N₃, H_{Glc-4}), 3.62-3.56 (1H, m, H_{Glc-5}), 3.47-3.41 (1H, m, -OCH_aH_b-(CH₂)₁₀N₃), 3.24 (2H, t, -CH₂N₃, J = 6.96 Hz), 2.14 (3H, s, -OC(O)CH₃), 2.11 (3H, s, -OC(O)CH₃), 2.05 (3H, s, -OC(O)CH₃), 2.03 (6H, s, -OC(O)CH₃), 2.02 (3H, s, -OC(O)CH₃), 1.95 (3H, s, -OC(O)CH₃), 1.64-1.48 (4H, m, CH₂-tail), 1.39-1.25 (14H, m, CH₂-tail). ¹³C NMR (100 MHz, CDCl₃): δ 170.3, 170.3, 170.1, 170.0, 170.0, 170.0, 169.0 (7 x C=O), 101.0 (CH, C_{Gal-1}), 100.6 (CH, C_{Glc-1}), 76.3 (CH, C_{Glc-4}), 72.8 (CH, C_{Glc-3}), 72.6 (CH, C_{Glc-5}), 71.7 (CH, C_{Glc-2}), 71.0 (CH, C_{Gal-3}), 71.0 (CH, C_{Gal-5}), 70.2 (OCH₂-(CH₂)₁₀N₃), 69.1 (CH, C_{Gal-2}), 66.6 (CH, C_{Gal-4}), 62.1 (CH₂, C_{Glc-6}), 60.8 (CH₂, C_{Gal-6}), 51.5 (CH₂N₃), 29.5, 29.4, 29.4, 29.4, 29.3, 29.1, 28.8, 26.7, 25.8 (9 x CH₂), 20.8, 20.8, 20.6, 20.6, 20.6, 20.6, 20.5 (7 x CH₃). MS m/z 831 [M]⁺; HRMS calcd. for C₃₇H₅₇N₃O₁₈ ([M-H]⁺) 830.3553, found 830.3556.

β -D-galactopyranosyl-(1 \rightarrow 4)-1-(11-azido-undecanyl)- β -D-glucopyranoside (12). $[\alpha]^{20}_D$ - 8.2° (c 1.1, CH₃OH), *lit.* $[\alpha]^{23}_D$ -7.9° (c 1.0, CH₃OH). ²H NMR (400 MHz, CD₃OD): δ 4.27 (1H, d, H_{Gal-1}, J 7.5 Hz), 4.18 (1H, d, H_{Glc-1}, J 7.8 Hz), 3.75 – 3.82 (2H, m), 3.71 – 3.73 (1H, m), 3.66 – 3.69 (1H, m), 3.58 – 3.62 (1H, m), 3.37 – 3.50 (6H, m), 3.28 – 3.32 (1H, m), 3.12 – 3.19 (2H, m), 1.45 – 1.54 (4H, m), 1.19 – 1.34 (16H, m, -(CH₂)₈). ¹³C NMR (100 MHz, CD₃OD): δ 105.1 (CH, C_{Gal-1}), 104.2 (CH, C_{Glc-1}), 80.8 (CH), 77.1 (CH), 76.5 (CH), 76.4 (CH), 74.9 (CH), 74.8 (CH), 72.6 (CH), 71.0 (CH), 70.3 (-CH₂O-), 62.5 (CH₂, C_{Gal-6}), 62.0

(CH₂, C_{Glc-6}), 52.5 (-CH₂-N₃), 30.8, 30.7, 30.7, 30.6, 30.6, 30.3, 29.9, 27.8, 27.1 (9 × CH₂). HRMS: *m/z* 536.2824, calculated for C₂₃H₄₃N₃O₁₁ ([M-H]⁻): 536.2814.

2 XPS spectra of NHS terminated monolayer S3 on Si₃N₄ surfaces

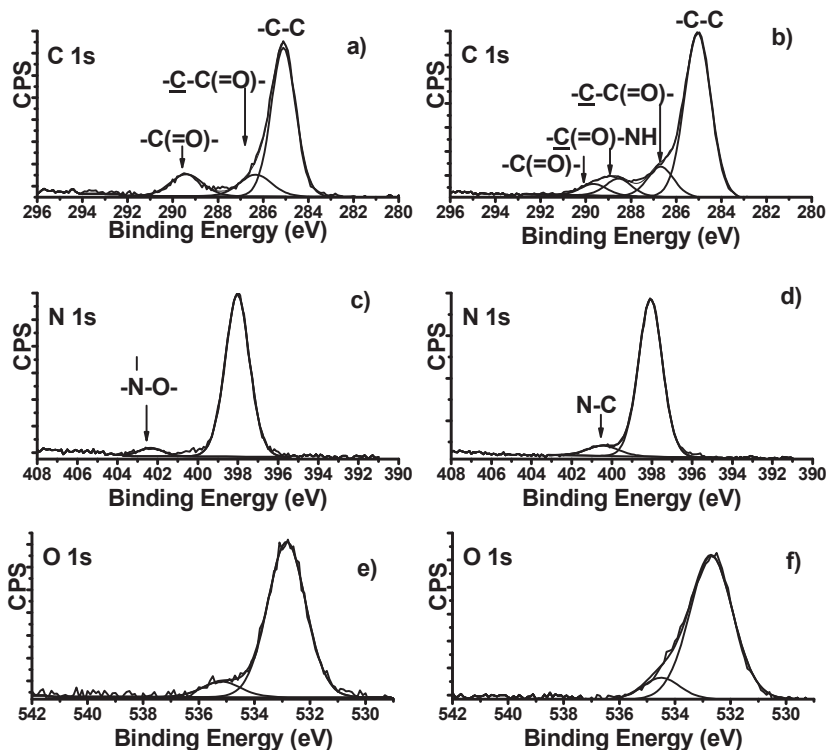


Figure S1: XPS characterization of NHS ester on Si₃N₄ surfaces. High resolution spectra of (a) C 1s, (c) N 1s and (e) O 1s after stepwise formation of NHS on the surface and high resolution (b) C 1s, (d) N 1s and (f) O 1s after direct attachment of NHS-UA spectra.

3 Thickness calculation by XPS

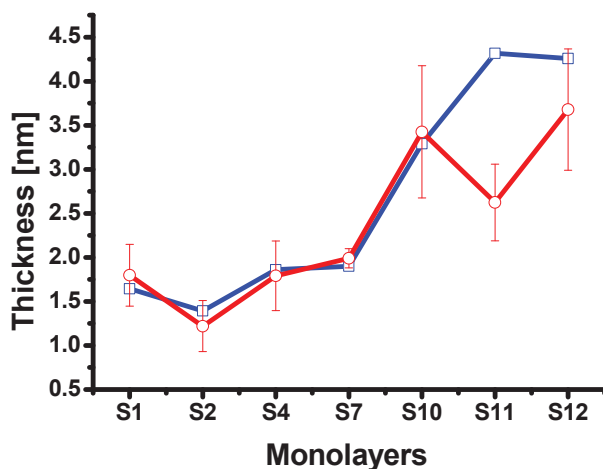


Figure S2: Experimental thickness of monolayer S1-S3, S7, S10-S12 calculated from XPS data (red line; open circles) and the predicted thickness of the same layers as calculated by *Chem3D* (blue line, open squares).

For the purpose of thickness calculation of the organic adlayers after each consecutive reaction, we used the average attenuation length for organic films, following the example by Seah and Spencer³

$$L = 0.00837 \cdot E^{0.842} \quad (1)$$

where L is the attenuation length in nm and E is the electron kinetic energy, E , in eV.

Due to the fact that most organic materials have similar densities and other physical properties, according to reference 75 equation (1) can give useful results with an RMS deviation of 20% for different organic overlayers. The equation (1) might provide additional information for analysis of organic films of uncertain identity. This could be the case in our work where after each consecutive reaction step the mixtures of moieties from previous steps are present. Thus the equation (1) was employed for XPS thickness calculation.

Assuming that the films are uniform, the film thickness was determined using the standard uniform overlay model according to equation (2):

$$I = I^0 \cdot \exp\left[\frac{-t}{L \cdot \cos\theta}\right] \quad (2)$$

where I is the measured intensity of Si 2p with a carbon overlayer with a thickness t, I⁰ is the peak intensity of Si 2p of an unmodified, cleaned substrate, t = the thickness of the adsorbed layer, L = the attenuation length of Si 2p electrons in the hydrocarbon layer, derived from equation (1) and θ is the photoelectron emission takeoff angle relative to the surface normal (θ=10°).

The expected theoretical thickness was estimated by applying *Chem3D* to models of the SAMs **S1**, **S2**, **S4**, **S7**, **S10**, **S11** and **S12**, in an orientation normal to the substrate. The geometries were optimized with B3LYP/6-311G(d,p), using the Gaussian 09 package.¹³

In **Figure S2** the average thicknesses (n=8) calculated by XPS for monolayers **S1**, **S2**, **S4** and average thicknesses for **S7**, **S10**, **S11**, **S12** (n=3) are shown. The experimental values for SAMs **S1**, **S2**, **S4**, **S7**, **S10** and **S12** agree well with the predicted values. The thickness for **S11** (after SPAAC reaction with the protected lactoside **11** on **S7**) gives a lower thickness than expected. It might be due to the lower efficiency of the surface reaction, hindered by the bulky protecting acetyl groups. This low conversion can be also related with a low intensity of carbonyl emission in the narrow scan of the C 1s spectrum relative to the CH₂ contribution.

4 Electronic core level calculations for **S1**, TFE terminated monolayer

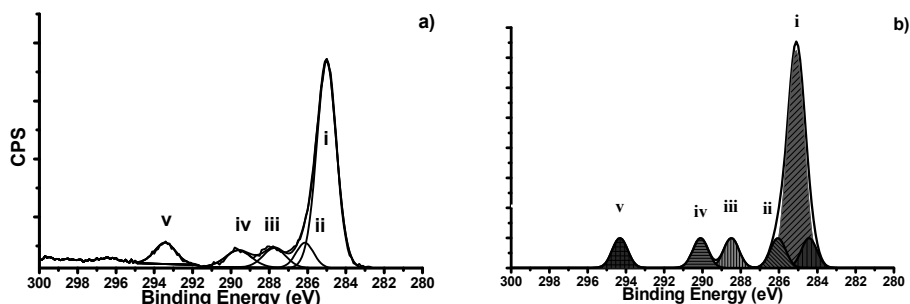


Figure S3: Experimental (a) and simulated (b) core level C 1s XPS-spectra for monolayer **S1**; simulation based on DFT-calculations of the C 1s core level energies for

the TFE capped with a $(\text{NH}_2)_3\text{Si}$ - group. The spectra can be divided according to the assignment **i-v** giving the open black curves for the simulation. On basis of the calculation these can be subsequently be splitted into the filled colour curves following the assignment in Table S1.

Table S1: Calculated ΔBE of carbon atoms in TFE terminated monolayer (S1)

Carbon type	Atom No.	ΔBE (eV)	Structure
CH2	1	0.47	
CH2- (alfa)	2	1.06	
C=O	3	5.11	
CH2 (O-)	6	3.50	
CH2	7	0.34	
CH2	8	0.19	
CH2	9	0.12	
CH2	10	0.06	
CH2	11	0.00	
CH2	12	-0.08	
CH2	13	-0.05	
CH2 (-Si)	14	-0.57	
CF3	19	9.31	

Table S2: Analysis of the simulated C 1s spectra and comparison with the experimental data (relative to 285 eV) for TFE terminated (S1) monolayer.

XPS peak	v	iv	iii	ii	i		
assigned carbons	19	3	6	2	1	7-13	14
calculated (average) ΔBE (eV)	9.31	5.11	3.50	1.06	0.4	0.08	-0.60
experimental BE (eV)	293.37	289.68	287.99	286.22	285.00		
experimental ΔBE (eV)	8.37	4.68	2.99	1.22	0.00		

5 Electronic core level calculations for S2, undecanoic acid terminated surface

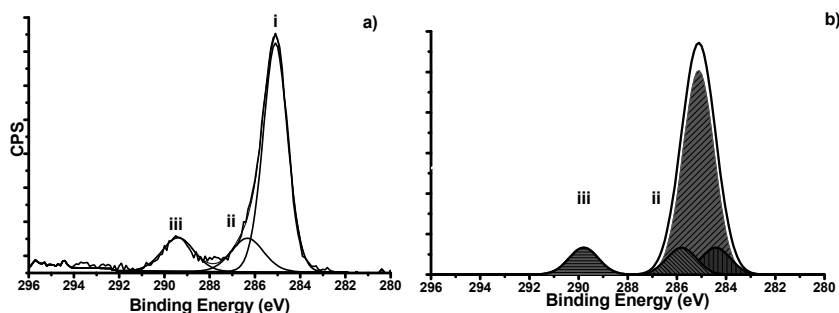


Figure S4: Experimental (a) and simulated (b) core level C1s XPS spectra for the undecanoic acid monolayer (S2) monolayer, simulation based on DFT-calculations of the C1s core level energies for the acid capped with a $(\text{NH}_2)_3\text{Si}$ - group. The spectra can be divided according to the assignment i-v giving the open black curves for the simulation. On basis of the calculation these can be subsequently be splitted into the filled color curves following the assignment in Table S3.

Table S3: Calculated ΔBE of carbon atoms in undecanoic acid terminated monolayer (S2)

Carbon type	Atom No.	ΔBE (eV)	Structure
C=O	2	4.79	
CH ₂ (alfa)	3	0.81	
CH ₂	4	0.56	
CH ₂	5	0.30	
CH ₂	6	0.18	
CH ₂	7	0.11	
CH ₂	8	0.05	
CH ₂	9	-0.02	
CH ₂	10	-0.09	
CH ₂	11	-0.06	
CH ₂ (-Si)	12	-0.58	

Table S4: Analysis of the simulated C 1s spectra and comparison with the experimental data (relative to 285 eV) for monolayer **S2**.

XPS peak	iii	ii	i		
assigned carbons	2	3	4-5	6-11	12
calculated (average) Δ BE (eV)	4.79	0.81	0.43	0.03	-0.58
experimental BE (eV)	289.51	286.31	285.00		
experimental Δ BE (eV)	4.51	1.31	0.0		

6 Electronic core level calculations for S3, NHS ester terminated surface

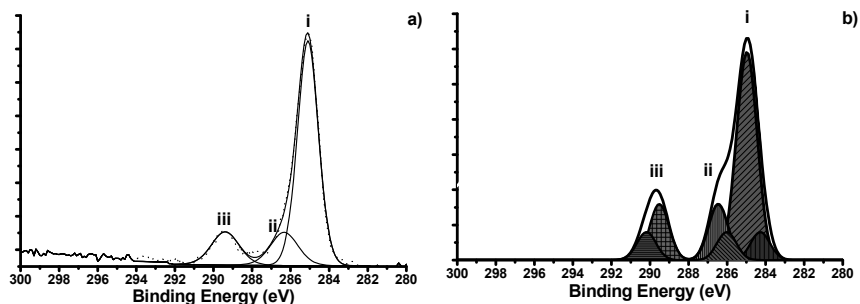


Figure S5: Experimental (a) and simulated (b) core level C1s XPS-spectra for the NHS terminated monolayer (**S3**), simulation based on DFT-calculations of the C1s core level energies for the NHS ester of undecanoic acid capped with a $(\text{NH}_2)_3\text{Si}$ -group. The spectra can be divided according to the assignment **i-iii** giving the open black curves for the simulation. On basis of the calculation these can be subsequently be splitted into the filled colour curves following the assignment in Table S5.

Table S5: Calculated ΔBE of carbon atoms in overlayer **S3**

Carbon type	Atom No.	ΔBE (eV)	Structure
CH2	1	0.38	
CH2 (alfa)	2	1.02	
C=O	3	5.18	
CH2	7	0.20	
CH2	8	0.04	
CH2	9	-0.04	
CH2	10	-0.10	
CH2	11	-0.16	
CH2	12	-0.24	
CH2	13	-0.21	
CH2	14	-0.72	
C=O	19	4.51	
CH2	20	1.46	
CH2	21	1.46	
C=O	22	4.51	

Table S6: Analysis of the simulated C 1s spectra and comparison with the experimental data (relative to 285 eV) for overlayer **S3**.

XPS peak	iii	ii	i	
assigned carbons	3, 19,22	2, 20-21	1, 7-13	14
calculated (average) Δ BE (eV)	4.74	1.31	-0.01	-0.72
experimental BE (eV)	289.34	286.37	285.00	
experimental Δ BE (eV)	4.34	1.37	0.00	

7 Electronic core level calculations for **S4**, PFP ester terminated surface

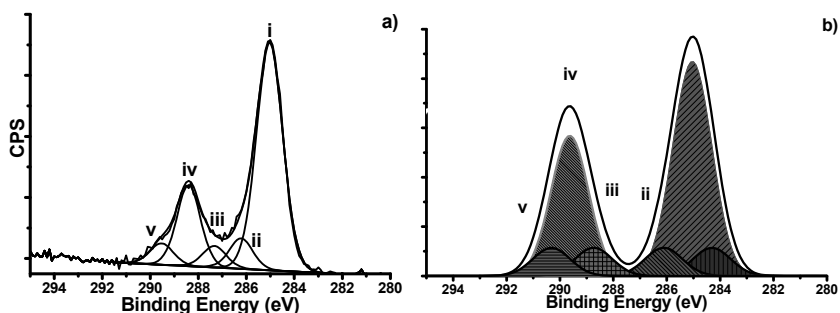


Figure S6: Experimental (a) and simulated (b) core level C 1s XPS-spectra for the **PFP** active ester monolayer **S4**, simulation based on DFT-calculations of the C 1s core level energies for the pentafluorophenol ester of undecanoic acid capped with a $(\text{NH}_2)_3\text{Si}$ -group. The spectra can be divided according to the assignment **i-v** giving the open black curves for the simulation. On basis of the calculation these can subsequently be splitted into the filled colour curves following the assignment in Table S7.

Table S7: Calculated Δ BE of carbon atoms in overlayer S4

Carbon type	Atom No.	Δ BE (eV)	Structure
CH2	1	0.47	
CH2 (alfa)	2	1.11	
C=O	3	5.32	
O-C (-Ar)	6	3.74	
Ar-F	7	4.57	
Ar-F	8	4.64	
Ar-F	9	4.73	
Ar-F	10	4.64	
Ar-F	11	4.57	
CH2	17	0.29	
CH2	18	0.12	
CH2	19	0.03	
CH2	20	-0.04	
CH2	21	-0.11	
CH2	22	-0.20	
CH2 (-Si)	24	-0.69	

Table S8: Analysis of the simulated C 1s spectra and comparison with the experimental data (relative to 285 eV) for overlayer S4.

XPS peak	v	iv	iii	ii	i		
assigned carbons	3	7-11	6	2	1	17-23	24
calculated (average) Δ BE (eV)	5.32	4.63	3.74	1.11	0.47	-0.01	-0.69
experimental BE (eV)	289.50	288.37	287.30	286.19	285.00		
experimental Δ BE (eV)	4.50	3.37	2.30	1.19	0.00		

8 Electronic core level calculations for S7, cyclooctyne terminated surface

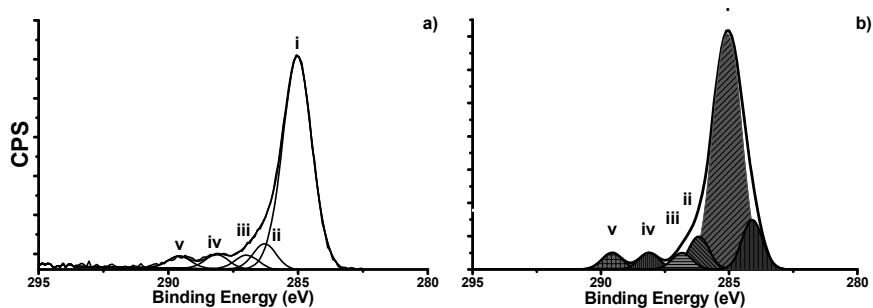


Figure S7: Experimental (a) and simulated (b) core level C 1s XPS-spectra for the bicyclononyne (**7**) terminated monolayer (**S7**), simulation based on DFT-calculations of the C 1s core level energies for the bicyclononyne capped with a $(\text{NH}_2)_3\text{Si}$ - group. The spectra can be divided according to the assignment i-v giving the open black curves for the simulation. On basis of the calculation these can be subsequently be splitted into the filled colour curves following the assignment in Table S9.

Table S9: Calculated ΔBE of carbon atoms in overlayer S7

Carbon type	Atom No.	ΔBE (eV)	Structure
CH2 (TFE)	1	-0.19	
CH2 (alfa TFE)	2	0.26	
C=O (TFE)	3	3.12	
CH2 (TFE)	4	-0.29	
CH2 (BCN)	5	1.16	
CH2 (BCN)	6	0.08	
CH2 (BCN)	7	0.12	
CH2 (BCN)	8	0.10	
CH2 (BCN)	9	1.21	
CH2 (TFE)	10	-0.29	
C=O (-O BCN)	11	4.56	
CH2 (TFE)	12	-0.31	
CH2 (-O BCN)	13	1.83	
CH (Ring BCN)	14	0.34	
CH (Ring BCN)	15	0.39	
CH (Ring BCN)	16	0.48	
CH2 (BCN)	17	0.29	
CH2 (BCN)	18	0.55	
C \equiv C	19	-0.89	
C \equiv C	20	-0.88	
CH2 (BCN)	21	0.56	
CH2 (BCN)	22	0.32	
CH2 (TFE)	23	-0.31	
CH2 (TFE)	24	-0.37	
CH2 (TFE)	25	-0.18	
CH2 (Si-C)	26	-0.94	
CH2 (TFE)	27	-0.20	

Table S10: Analysis of the simulated C 1s spectra and comparison with the experimental data (relative to 285 eV) for **S7** monolayer.

XPS peak	v	iv	iii	ii	i	
assigned carbons	11	3	13	5, 9	1,2,4,6-8, 10,12,14- 18,21- 25,27	19, 20, 26
assigned carbons	4.56	3.12	1.83	1.18	0.07	-0.90
calculated (average) Δ BE (eV)	289.53	288.12	286.99	286.04	285.00	
experimental BE (eV)	4.53	3.12	1.99	1.04	0.00	

9 Electronic core level calculations for S8

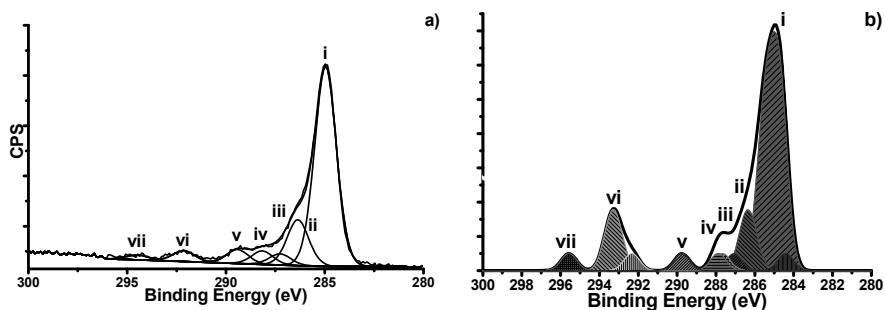
**Figure S8:** Experimental (a) and simulated (b) core level C1s XPS-spectra for the monolayer **S8**, simulation based on DFT-calculations of the C1s core level energies for the polyfluorinated triazole product capped with a $(\text{NH}_2)_3\text{Si}$ - group. The spectra can be divided according to the assignment **i-vii** giving the open black curves for the simulation. On basis of the calculation these can be subsequently be splitted into the filled colour curves following the assignment in Table S11.

Table S11: Calculated Δ BE of carbon atoms in overlayer S8

Carbon type	Atom No.	Δ BE (eV)	Structure
CH2 (TFE)	1	-0.34	
CH2 (alfa TFE)	2	0.18	
C=O (TFE)	3	2.80	
CH2 (BCN)	5	1.22	
CH2 (BCN)	6	0.43	
CH2 (BCN)	7	0.38	
CH2 (BCN)	8	0.50	
CH2 (BCN)	9	1.44	
C=O (BCN)	11	4.67	
CH2 (BCN)	13	1.99	
CH (Ring BCN)	14	0.65	
CH (Ring BCN)	15	0.56	
CH (Ring BCN)	16	0.51	
CH2 (Ring BCN)	17	0.23	
CH2 (Ring BCN)	18	0.26	
C= (Ring BCN)	19	-0.23	
C= (Ring BCN)	20	-0.31	
CH2 (Ring BCN)	21	-0.03	
CH2 (Ring BCN)	22	0.09	
CH2 (N-CH2 PF)	28	2.58	
CH2 (PF)	29	0.95	
CH2 (-CF2 PF)	30	1.43	
CF2 (-CH2 PF)	31	7.25	
CF2 (-CF2 PF)	32	7.92	
CF2 (-CF2 PF)	33	8.13	
CF2 (-CF2 PF)	34	8.29	
CF2 (-CF2 PF)	35	8.43	
CF3 (-CF2 PF)	36	10.49	
CH2 (TFE)	52	-0.37	
CH2 (TFE)	53	-0.43	
CH2 (TFE)	54	-0.42	
CH2 (TFE)	55	-0.43	
CH2 (TFE)	56	-0.43	
CH2 (TFE)	57	-0.41	
CH2 (TFE)	58	-0.24	
CH2 (Si-C)	59	-0.67	

Table S12: Analysis of the simulated C1s spectra and comparison with the experimental data (relative to 285 eV) for overlayer **S8**.

XPS peak	vi	v	iv	iii	iii	ii	i	
assigned carbons	36	31-35	11	3, 28	13	5,9,30,29	1,2, 6-8, 14-22, 52-58	59
assigned carbons	10.49	8.00	4.67	2.69	1.99	1.27	-0.02	-0.67
calculated (average) Δ BE (eV)	294.50	292.18	289.27	288.20	287.30	286.38	285.00	
experimental BE (eV)	9.50	7.18	4.45	3.20	2.30	1.38	0.00	

10 Electronic core level calculations for S12

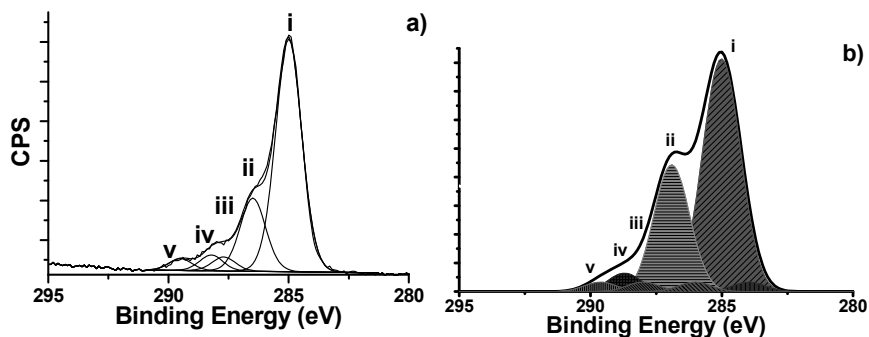


Figure S9: Experimental (a) and simulated (b) core level C 1s XPS-spectra for monolayer **S12**, simulation based on DFT-calculations of the C 1s core level energies for the triazole product after clicking azide **12** on surface **S7**. The spectra can be divided according to the assignment **i-v** giving the open black curves for the simulation. On basis of the calculation these can be subsequently be splitted into the filled colour curves following the assignment in Table S13.

Table S13: Calculated ΔBE carbon atoms in overlayer S12.

Carbon type	Atom No.	ΔBE (eV)	Structure
CH2 (sugar)	2	-0.04	
CH2 (sugar)	3	-0.01	
CH2 (sugar)	4	-0.14	
CH2 (sugar)	5	-0.17	
CH2 (sugar)	6	-0.18	
CH2 (sugar)	7	-0.14	
CH2 (sugar)	8	-0.07	
CH2 (sugar)	9	0.10	
CH2 (sugar)	10	0.22	
CH2 (-N-)	11	1.51	
C=O (TFE)	12	2.91	
CH2 (NH- BCN)	14	1.32	
CH2 (BCN)	15	0.27	
CH2 (BCN)	16	0.21	
CH2 (BCN)	17	0.09	
CH2 (NH-BCN)	18	1.26	
C=O (BCN)	20	4.54	
CH2 (BCN)	22	1.80	
CH (Ring BCN)	23	0.28	
CH (Ring BCN)	24	0.44	
CH (Ring BCN)	25	0.45	
CH2 (Ring BCN)	26	0.36	
CH2 (Ring BCN)	27	0.53	
C= (Ring BCN)	28	0.93	
C= (Ring BCN)	29	0.35	
CH2 (Ring BCN)	30	-0.12	
CH2 (Ring BCN)	31	0.00	
CH2 (alfa)	39	0.02	
CH2 (TFE)	40	-0.53	

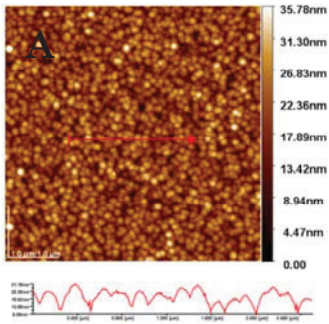
CH2 (TFE)	41	-0.48
CH2 (TFE)	42	-0.57
CH2 (TFE)	43	-0.57
CH2 (TFE)	44	-0.60
CH2 (TFE)	45	-0.64
CH2 (TFE)	46	-0.69
CH2 (TFE)	47	-0.65
CH2 (TFE)	48	-1.16
CH (-OH)	53	1.91
CH (-OH)	54	1.97
CH (-OH)	55	1.75
O-CH-O	56	3.68
CH (-O-)	58	2.07
CH2 (-OH)	61	1.46
CH (-OH)	64	1.70
CH (-O-)	65	2.06
CH (-O-)	66	2.28
O-CH-O	68	3.53
CH (-OH)	69	1.72
CH2 (-OH)	72	2.28

Table S14: Analysis of the simulated C 1s spectra and comparison with the experimental data (relative to 285 eV) for overlayer **S12**.

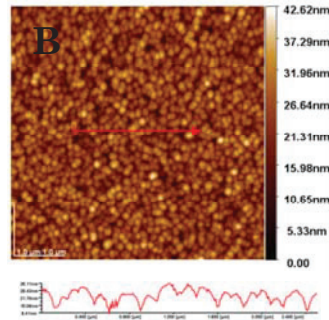
XPS peak	v	iv	iii	ii	i	
assigned carbons	20	56, 68	12	53- 55,61,64,65,69; 58,66,1,22,72, 11; 18,14,28	2-10; 15-17, 23-27, 29-31, 39-47	48
assigned carbons	4.54	3.61	2.91	1.74	-0.08	-1.16
calculated (average) Δ BE (eV)	289.50	288.22	287.70	286.49	285.00	
experimental BE (eV)	4.50	3.22	2.70	1.49	0.0	

11 Atomic Force Microscopy (AFM)

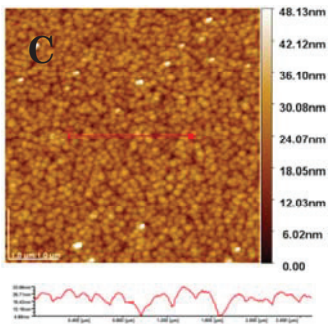
Atomic force microscopy imaging were performed using a JEOL JSPM-5400 scanning probe microscope (JEOL , Tokyo, Japan). The AFM head is mounted on an optical microscope (CCD, TM-24041, JEOL). Scanning was performed in tapping mode in air, using NSC35/AIBS noncontact tetrahedral-shaped n-type silicon cantilever with a nominal spring constant of 14 N/m purchased from MikroMasch Europe. AFM were performed in a $5\ \mu\text{m} \times 5\ \mu\text{m}^2$ region, with a 512 scan line and scan rate of 0.3 Hz. Results were analysed with WinspaceII Data Processing (version 1.01.46) software. The topographic height difference was represented by a yellow-orange colour scale in which bright colour denoted higher height and dark colour denoted lower height for all images.



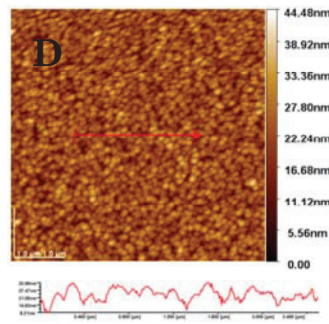
SB Si₃N₄ after washing with acetone
Ra = 4.0 nm



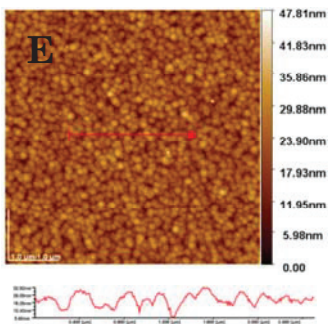
S0 Si₃N₄ plasma and HF-etching
Ra = 4.4 nm



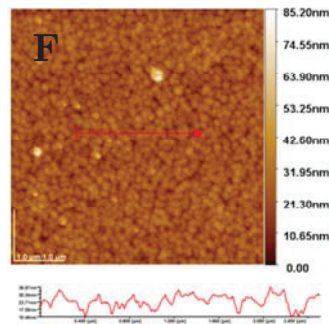
S1 TFE; Ra = 4.3 nm



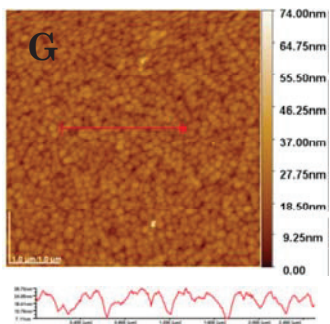
S2 COOH; Ra = 4.2 nm



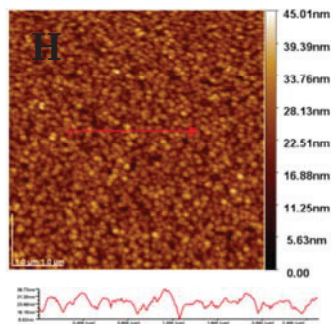
S3 NHS; Ra = 4.2 nm



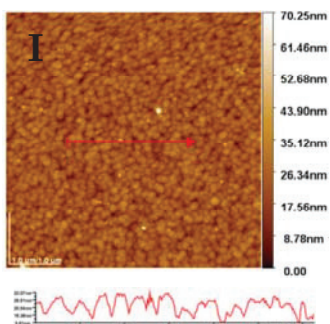
S4 PFP; Ra = 4.4 nm



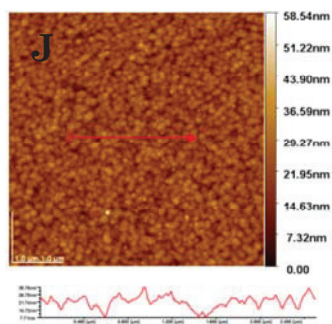
S5; Ra = 4.2 nm



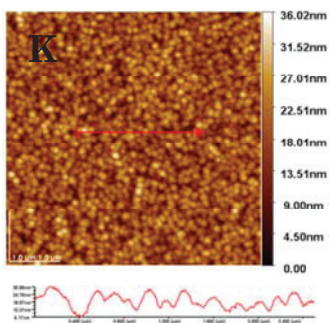
S7 BCN; Ra = 4.1 nm



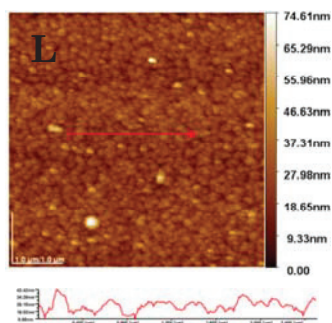
S8; Ra = 4.4 nm



S10 α -lactoside; Ra = 4.2 nm



S11 Acetyl β -lactoside; Ra = 4.5 nm



S12 β -lactoside; Ra = 4.7 nm

Figure S10. AFM topography images of (A) **SB** - Si₃N₄ after washing with acetone (Ra = 4.0 nm), (B) **S0** - Si₃N₄ after plasma treatment and HF-etching (Ra = 4.4 nm), (C) monolayer **S1** (Ra = 4.3 nm) (D) **S2** COOH (Ra = 4.2 nm), (E) **S3** (Ra = 4.2 nm), (F) **S4** (Ra = 4.4 nm), (G) **S5** (Ra = 4.2 nm), (H) **S7** (Ra = 4.1 nm), (I) **S8** (Ra = 4.4 nm), (J) **S10** (Ra = 4.2 nm), (K) **S11** (Ra = 4.5 nm), (L) **S12** (Ra = 4.7 nm)

12 References

1. Mukhopadhyay, B.; Kartha, K. P. R.; Russell, D. A.; Field, R. A. Streamlined Synthesis of Per-O-acetylated Sugars, Glycosyl Iodides, or Thioglycosides from Unprotected Reducing Sugars1. *J. Org. Chem.* **2004**, *69* (22), 7758-7760.
2. Andersen, S. M.; Ling, C.-C.; Zhang, P.; Townson, K.; Willison, H. J.; Bundle, D. R. Synthesis of Ganglioside Epitopes for Oligosaccharide Specific Immunoabsorption Therapy of Guillian-Barre Syndrome. *Org. Biomol. Chem.* **2004**, *2* (8), 1199-1212.
3. Seah, M. P.; Spencer, S. J. Attenuation lengths in organic materials. *Surf. Interface Anal.* **2011**, *43* (3), 744-751.

Appendix 2

Information supplementing Chapter 4

Contents

1 Mass spectra of monolayers S1, S3-S6, S10, S11, S _{mix}	146
1.1 Mass spectrum of S1	146
1.2 Mass spectrum of S3	147
1.3 Mass spectrum of S4	147
1.4 Mass spectrum of S5	148
1.5 Mass spectrum of S6	149
1.6 Mass spectrum of S10.....	149
1.7 Mass spectrum of S11.....	150
1.8 Mass spectrum of S _{mix}	151
2 XPS analysis of monolayers S1-S6, S10, S11, S _{mix}	152

1 Mass spectra of monolayers S1, S3-S6, S10, S11, Smix

1.1 Mass spectrum of S1

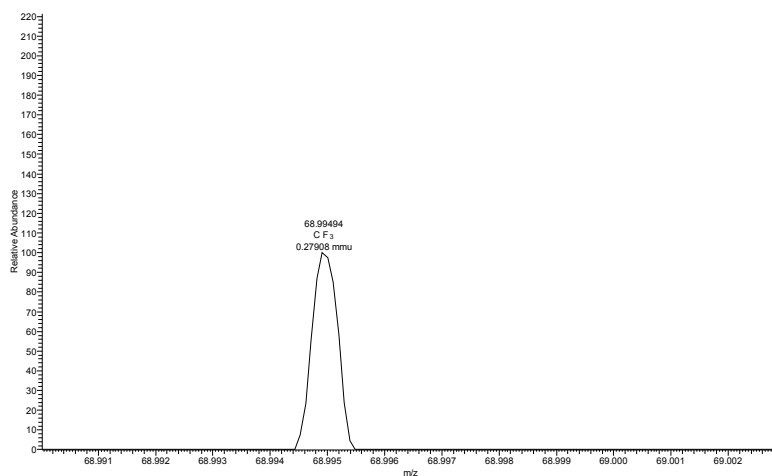


Figure S1: Negative mode DART-Orbitrap mass spectrum from m/z 68.990-69.003 of S1. Peak at m/z 68.99494 is $[\text{CF}_3]^-$.

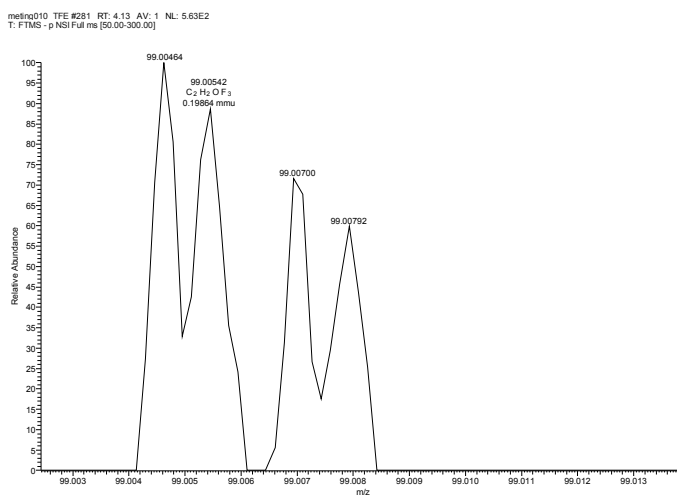


Figure S2: Negative mode DART-Orbitrap mass spectrum from m/z 99.002-99.014 of S1. Peak at m/z 99.00542 is $[\text{M}-\text{H}]^-$, where M is $\text{CF}_3\text{CH}_2\text{OH}$.

1.2 Mass spectrum of S3

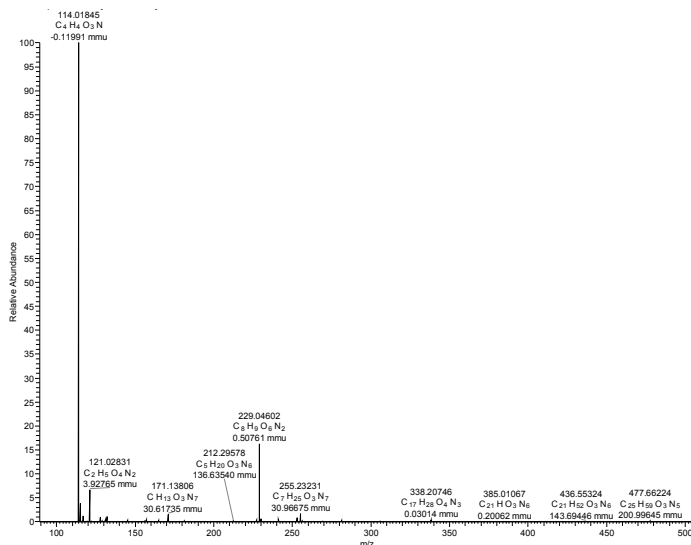


Figure S3: Negative mode DART-Orbitrap mass spectrum from m/z 90-500 of **S3**. Peak at m/z 114.01845 is $[M-H]^-$ and peak at m/z 229.04602 is $[2M-H]^-$, where M is **3** (N-hydroxysuccinimide, NHS).

1.3 Mass spectrum of S4

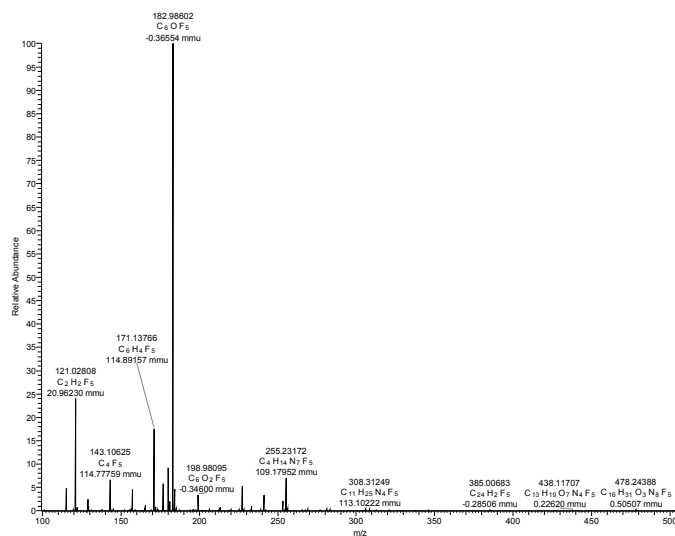


Figure S4: Negative mode DART-Orbitrap mass spectrum from m/z 100-500 of **S4**. Peak at m/z 182.98602 is $[M-H]^-$, where M is **4** (pentafluorophenol, PFP).

1.4 Mass spectrum of S5

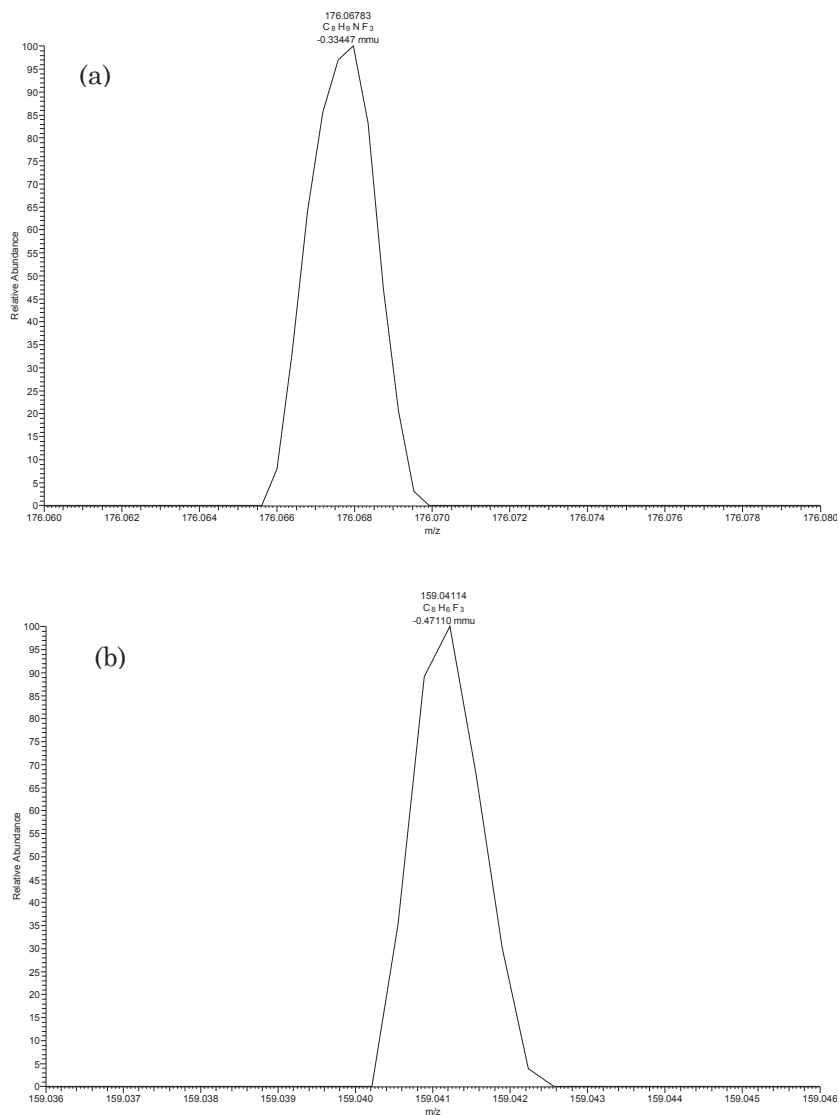


Figure S5: Positive mode DART-Orbitrap mass spectrum of **S5**; (a) from m/z 176.06-176.08; peak at m/z 176.06783 is $[M+H]^+$, where M is **5** (4-(trifluoromethyl)benzylamine); (b) from m/z 159.036-159.046; peak at m/z 159.04114 is $[M+H-NH_3]^+$, where M is **5** (4-(trifluoromethyl)benzylamine).

1.5 Mass spectrum of S6

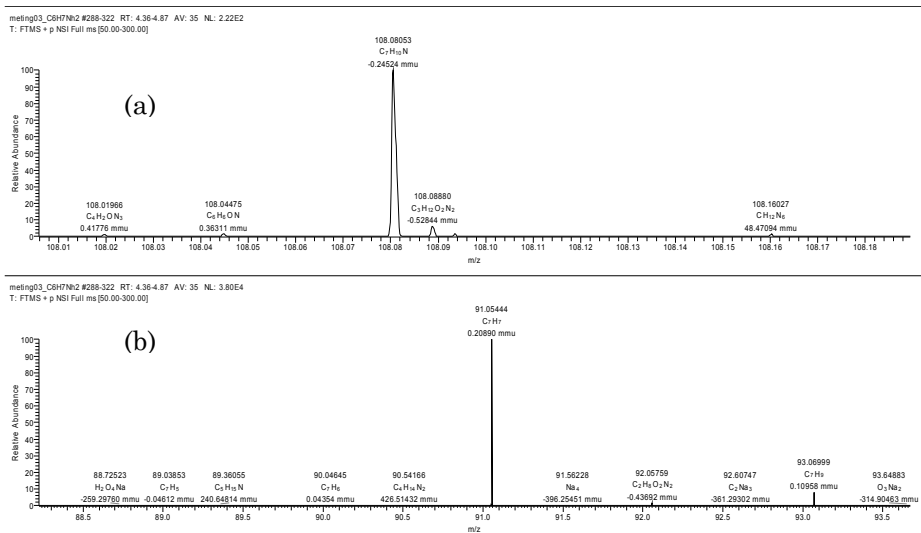


Figure S6: Positive mode DART-Orbitrap mass spectrum of **S6**: (a) from (m/z 108.0-108.19); peak at m/z 108.08053 is $[M+H]^+$, (b) from m/z 88.2-93.6; peak at m/z 91.05444 is $[M+H-NH_3]^+$, where M is **6** (benzylamine).

1.6 Mass spectrum of S10

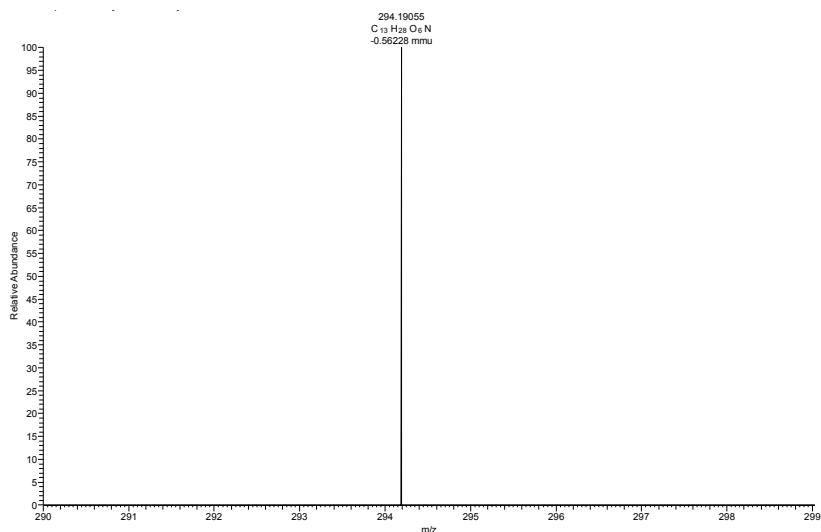


Figure S7: Positive mode DART-Orbitrap mass spectrum of **S10** from (m/z 290.0-299.0); peak at m/z 294.19055 is $[M+H]^+$, where M is **10** (2-aminomethyl-18-crown-6).

1.7 Mass spectrum of S11

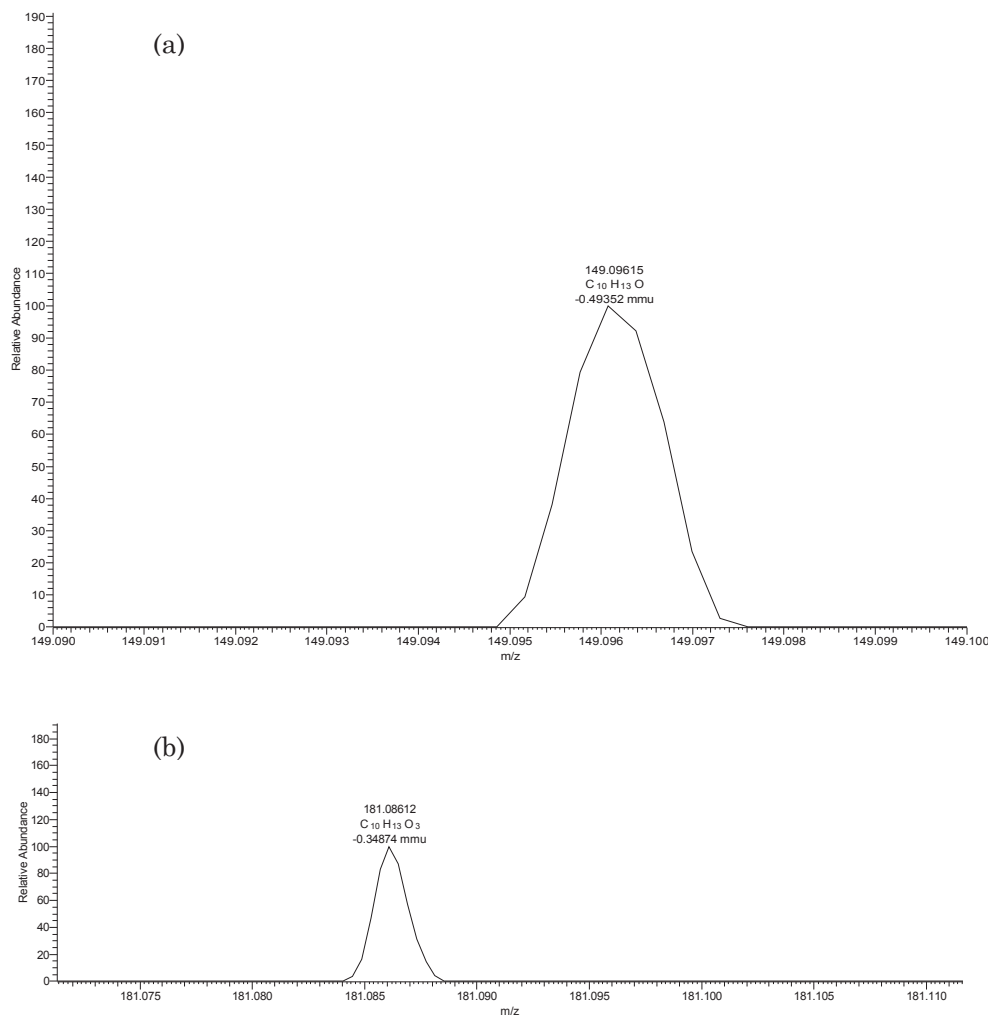


Figure S8: Negative mode DART-Orbitrap mass spectrum of **S11**, (a) from m/z 149.09–149.10; peak at m/z 149.09615 is $[M-H]^-$. (b) m/z 181.07–181.11; peak at m/z 181.08612 is $[M+2O-3H]^-$, where **M** is **12** (1R,8S,9s)-bicyclo[6.1.0]non-4-yn-9-ylmethanol).

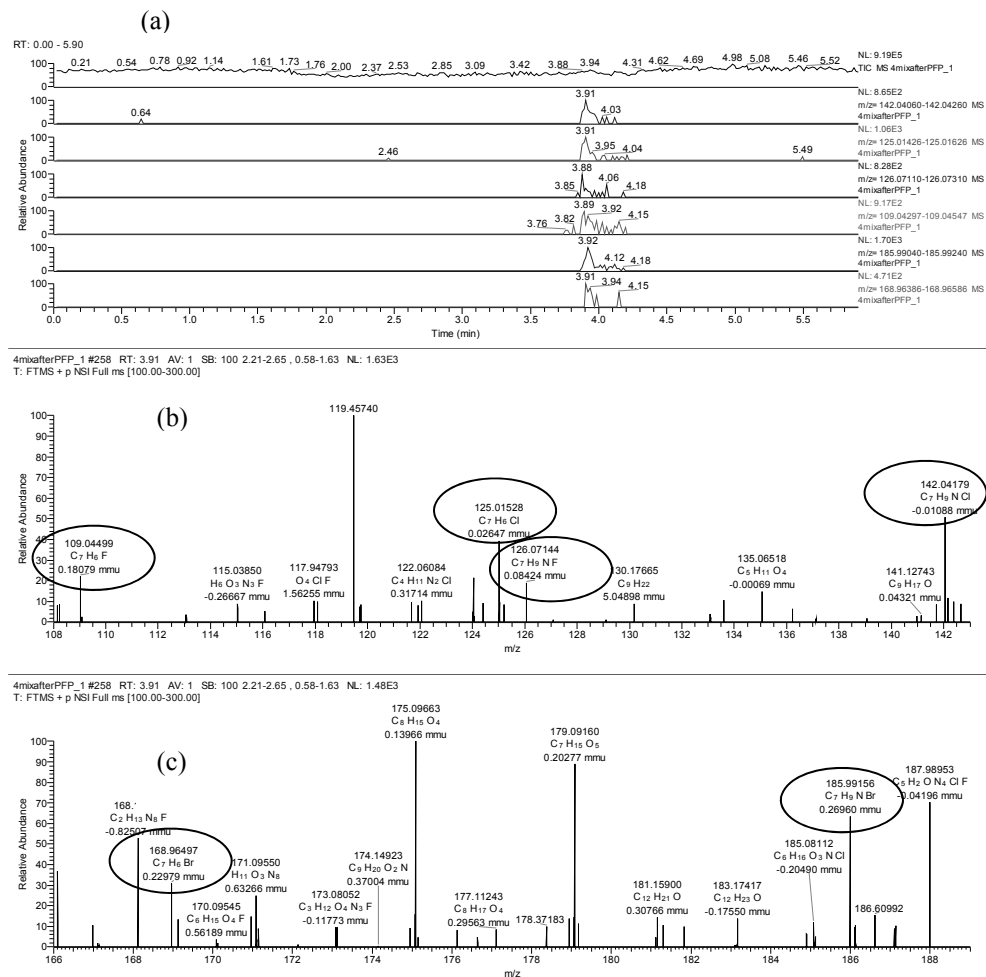
1.8 Mass spectrum of S_{mix} 

Figure S9: Positive mode DART-Orbitrap mass spectrum of S_{mix} . (a) Chronograms of mixed monolayer S_{mix} from top to bottom: TIC; EIC of m/z 142.0418 for $[M+H]^+$ of **8**; EIC of m/z 125.0153, for $[M+H-NH_3]^+$ of **8**; EIC of m/z 126.0714 for $[M+H]^+$ of **7**; EIC of m/z 109.0449 for $[M+H-NH_3]^+$ of **7**; EIC of m/z 185.9915 for $[M+H]^+$ of **9**; EIC of m/z 168.9649 for $[M+H-NH_3]^+$ of **9**; (b) mass spectrum of S_{mix} from m/z 108.0-143.0 from left to the right: m/z 109.0449 for $[M+H-NH_3]^+$ of **7**; m/z 125.0153 for $[M+H-NH_3]^+$ of **8**; m/z 126.0714 for $[M+H]^+$ of **7**; and of m/z 142.0418 for $[M+H]^+$ of **8**; (c) mass spectrum of S_{mix} from m/z 166.0-188.0 from left to the right: m/z 168.9650 for $[M+H-NH_3]^+$ of **9** and m/z 185.9916 for $[M+H]^+$ of **9**.

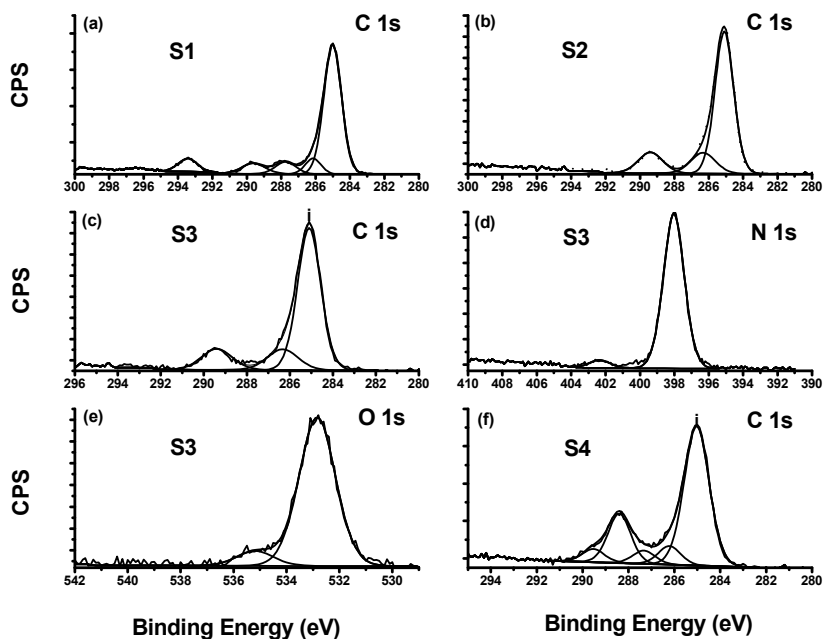
2 XPS analysis of monolayers S1-S6, S10, S11, S_{mix}

Figure S10: XPS high resolution C 1s spectra for (a) S1; (b) S2; (c) S3; (f) S4; and (d), (e) XPS high resolution spectra of N1s and O1s for S3.

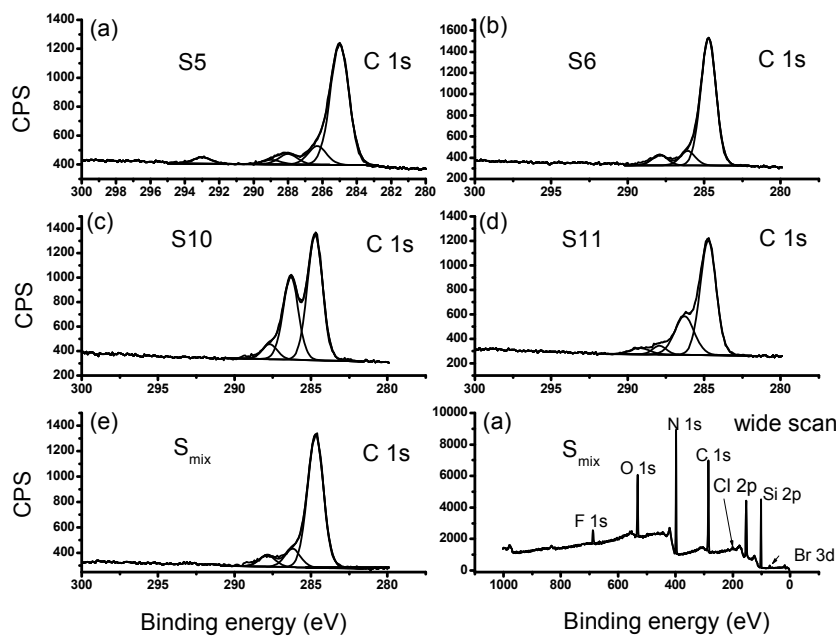


Figure S11: XPS high resolution C 1s spectra for a) S5; b) S6; c) S10; d) S11; and e) S_{mix}. f) XPS wide scan of S_{mix}.

Appendix 3

Information supplementing Chapter 5: XPS spectra

Contents

1 Chemicals and materials	156
2 Synthesis of azidoundecanyl carbohydrates (1, 4 and 7)	156
2.1 Synthesis of β -D-galactopyranosyl-(1 \rightarrow 4)-1-(11-azido-undecanyl)- α -D-glucopyranoside (1).....	156
2.2 Synthesis of 1-(11-azidoundecanyl)- α -d-mannopyranoside (4)	157
2.3 Synthesis of 1-(11-azidoundecanyl)- β -D-fucopyranoside (7).....	157
2.4 NMR spectra	159
3 Preparation of monolayers with different head and tail groups	161
3.1 Preparation of monolayers on gold	161
3.2 Preparation of monolayers on silicon nitride (Si_3N_4).....	161
3.3 Preparation of monolayers on glass (SiO_2).....	163
3.4 Preparation of monolayers on alumina (Al_2O_3).....	164
3.5 Preparation of monolayers on silicon Si(111).....	164
4 X-ray Photoelectron Spectroscopy (XPS).....	166
4.1 XPS spectra of monolayers on Al_2O_3	166
4.2 XPS spectra of monolayers on Si(111).....	170
4.3 XPS spectra of monolayers on Si_3N_4	171
4.4 XPS spectra of monolayers on SiO_2	173
4.5 XPS spectra of monolayers on Au	174
5 DART-HRMS of SPR chip.....	175

1 Chemicals and materials

All chemicals and solvents (analytical grade) were obtained from Sigma Aldrich and used without purification, unless stated otherwise. Dichloromethane and 1,2-epoxydecene (Alfa Aesar, Karlsruhe, Germany) were distilled before use. Tris(2-aminoethyl)amine, perfluorononanoyl chloride, 2-[[methoxypoly(ethyleneoxy)₆₋₉]-propyl]trimethoxysilane were purchased from ABCR (Karlsruhe, Germany); 10-undecynylphosphonic acid was obtained from SiKÉMIA (Clapiers, France). Substrates to be investigated by DART-HRMS were typically 1 × 1 cm, unless noted otherwise. The gold substrates (200 nm of Au sputtered on glass) were purchased from SSens (Enschede, The Netherlands). Silicon nitride (Si₃N₄, 120 nm on Si) and glass (SiO₂) substrates were obtained from Lionix B.V. (Enschede, The Netherlands); the SiO₂ substrates were obtained from a 95.1 nm thick tetraethylorthosilicate (TEOS) layer, deposited on a Si surface and annealed at 1150 °C. Porous aluminum oxide (PAO) substrates (3.6 × 0.8 cm; average pore size 200 nm) were purchased from MicroDish BV (Utrecht, Netherlands). Single-side polished Si(111) (n-type, 475 - 550 μm thick, resistivity 1.0 - 5.0 Ω·cm) was purchased from Siltronix (Archamps, France). Microarray glass slides with 3D-NHS (N-hydroxy-succinimide ester groups), and PEGs were purchased from PolyAn GmbH (Berlin, Germany). Surface plasmon resonance (SPR) chips with carboxymethyl-polyethylene-glycol coating were ordered from XanTec bioanalytics (Duesseldorf, Germany). Sonication steps were performed in an Elmasonic P 30 H ultrasonic unit at a frequency of 80 kHz. Optical rotation was measured at 589 nm on a Perkin-Elmer 241 polarimeter.

2 Synthesis of azidoundecanyl carbohydrates (1, 4 and 7)

2.1 Synthesis of β-D-galactopyranosyl-(1→4)-1-(11-azido-undecanyl)-α-D-glucopyranoside (1)

The β-D-galactopyranosyl-(1→4)-1-(11-azidoundecanyl)-α-D-glucopyranoside (1) was synthesized as previously reported.^{1,2}

2.2 Synthesis of 1-(11-azidoundecanyl)- α -D-mannopyranoside (4).

A solution of peracetylated mannose iodide³ (2) (0.86 g, 1.9 mmol), 11-azido-1-undecanol (0.80 g, 3.75 mmol), and activated molecular sieves (1.15 g, 4 Å) in acetonitrile (12 mL) was cooled to 0 °C under an argon atmosphere. Iodine (0.95 g, 3.75 mmol) was added and the mixture was stirred for 4 h and allowed to warm up to room temperature. The dark brown suspension was diluted with ethyl acetate (90 mL) and filtered. The filtrate was washed with 1 M Na₂S₂O₃ (2x 70 mL) and saturated NaCl solution (30 mL), dried over Na₂SO₄, filtered, and concentrated under reduced pressure. The crude product was purified by column chromatography (eluent petroleum ether/ethyl acetate, 80:20) to yield 2,3,4,6-tetra-*O*-acetyl-1-(11-azidoundecanyl)- α -D-mannopyranoside (3) as a yellowish syrup. Intermediate 3 (0.30 g, 0.55 mmol) was then dissolved in dry methanol (3 mL) and a solution of sodium methoxide in methanol (0.5 M, 60 μ L) was added. The mixture was stirred for 16 h and after complete conversion (monitored by TLC, eluent: ethyl acetate), additional methanol (6 mL) was added to fully dissolve the product. Afterwards, Dowex 50 (H⁺ form) was added to the solution until the pH was 7 and the mixture was filtered over a Celite layer. The solution was concentrated under reduced pressure to yield 1-(11-azidoundecanyl)- α -D-mannopyranoside (4) as a cream-colored solid (0.15 g, 0.4 mmol, 22%). $[\alpha]_D^{20} +40.7$ (*c* 1.0, MeOH). ¹H NMR (400 MHz, MeOD): δ 5.54 (1H, s, OH), 4.78 (1H, d, H-1, *J* = 1.8 Hz), 3.86 (1H, dd, H-6a, *J* = 2.1 Hz, 11.8 Hz), 3.80 (1H, m, -OCHa-), 3.76 – 3.70 (3H, m, H-2, H-3, H-6b), 3.66 (1H, t, H-4, *J* = 9.4 Hz), 3.57 (1H, m, H-5), 3.45 (1H, m, -OCHb-), 3.32 (2H, t, -CH₂-N₃, *J* = 6.8 Hz), 1.68 – 1.59 (4H, m, -CH₂CH₂N₃, -OCH₂CH₂-), 1.49 – 1.32 (14H, m, -(CH₂)₇-). ¹³C NMR (100 MHz, MeOD): δ 101.6 (CH, C-1), 74.6 (CH, C-5), 72.7, 72.3 (2 x CH, C-2, C-3), 68.7 (CH, C-4), 68.6 (CH₂, -CH₂O-), 62.9 (CH₂, C-6), 52.5 (CH₂, -CH₂N₃), 30.7, 30.6, 30.6, 30.6, 30.5, 30.2, 29.9, 27.8, 27.3 (9 x CH₂, -(CH₂)₉-, overlap of three peaks). HRMS: *m/z* 374.2291; calcd for C₁₇H₃₂N₃O₆ ([M - H]⁻), 374.2286.

2.3 Synthesis of 1-(11-azidoundecanyl)- β -D-fucopyranoside (7).

Peracetylated fucose iodide (5) was prepared according to a method previously described in the literature.³ A solution of 5 (2.19 g, 5.5 mmol), 11-azido-1-undecanol (2.33 g, 10.9 mmol), and activated molecular sieves (1.05 g, 4

Å) in acetonitrile (50 mL) was cooled to 0 °C under an argon atmosphere. Iodine (2.77 g, 10.9 mmol) was added and the mixture was stirred for 16 h, slowly warming up to room temperature. The dark brown suspension was diluted with ethyl acetate (60 mL) and filtered. The filtrate was washed with 1 M Na₂S₂O₃ (2x 35 mL) and saturated NaCl solution (35 mL), dried over Na₂SO₄, filtered, and concentrated under reduced pressure. The crude product was purified by column chromatography (eluent petroleum ether/ethyl acetate, 10:90 to 80:20) to yield 2,3,4-tri-*O*-acetyl-1-(11-azidoundecanyl)-β-D-fucopyranoside (6) as a yellowish syrup. Intermediate 6 (0.50 g, 1 mmol) was then dissolved in dry methanol (5 mL) and a solution of sodium methoxide in methanol (0.5 M, 100 μL) was added. The mixture was stirred for 16 h and after complete conversion (monitored by TLC, eluent: ethyl acetate), additional methanol (10 mL) was added to fully dissolve the product. Afterwards, Dowex 50 (H⁺ form) was added to the solution until the pH was 7 and the mixture was filtered over a Celite layer. The solution was concentrated under reduced pressure to yield 1-(11-azidoundecanyl)-β-D-fucopyranoside (7) as a colorless syrup (0.36 g, 0.9 mmol, 46%). [α]_D²⁰ +12.2 (*c* 1.0, MeOH). ¹H NMR (400 MHz, MeOD): δ 4.80 (1H, s, OH), 4.17 (1H, d, H-1, *J* = 7.6 Hz), 3.83 (1H, dt, -OCHa-, *J* = 6.8, 9.4 Hz), 3.62 (1H, m, H-5), 3.59 (1H, m, H-4), 3.53 (1H, ddd, -OCHb-, *J* = 3.5, 6.7, 9.5 Hz), 3.46 (1H, m, H-3), 3.45 (1H, m, H-2), 3.27 (2H, t, -CH₂-N₃, *J* = 6.9 Hz), 1.64 – 1.55 (4H, m, -CH₂CH₂N₃, -OCH₂CH₂-), 1.42 – 1.29 (14H, m, -(CH₂)₇-), 1.26 (3H, d, H-6, *J* = 6.4 Hz). ¹³C NMR (100 MHz, MeOD): δ 104.8 (CH, C-1), 75.2, 73.0, 72.3, 71.8 (4x CH, C-2, C-3, C-4, C-5), 70.8 (CH₂, -CH₂O-), 63.0 (CH₂, -CH₂N₃), 30.8, 30.7, 30.6, 30.6, 30.5, 30.2, 29.9, 27.8, 27.1 (9 x CH₂, -(CH₂)₉-, overlap of two peaks). HRMS: *m/z* 358.2343; calcd for C₁₇H₃₂N₃O₅ ([M - H]⁻), 358.2336.

Synthesis of methoxy-tri(ethylene oxide) undec-1-ene, methoxy-hexa(ethylene oxide) undec-1-ene, and methoxy-nona(ethylene oxide) undec-1-ene. Methoxy-tri(ethylene oxide) undec-1-ene (CH₃O(CH₂CH₂O)₃(CH₂)₉CH=CH₂; EO3), methoxy-hexa(ethylene oxide) undec-1-ene (CH₃O(CH₂CH₂O)₆(CH₂)₉CH=CH₂; EO6), and methoxy-nona(ethylene oxide) undec-1-ene (CH₃O(CH₂CH₂O)₉(CH₂)₉CH=CH₂; EO9) were synthesized according to the literature.⁴ The compounds EO3, EO6 and EO9 were purified

before use with preparative HPLC (column C18; isocratic separation in MeCN/H₂O 90:10, UV (195 nm and 220 nm) and ELSD detection).

2.4 NMR spectra

Nuclear magnetic resonance (NMR) spectra were recorded on a Bruker 400 MHz spectrometer. NMR peak assignments were made based on COSY and HSQC experiments.

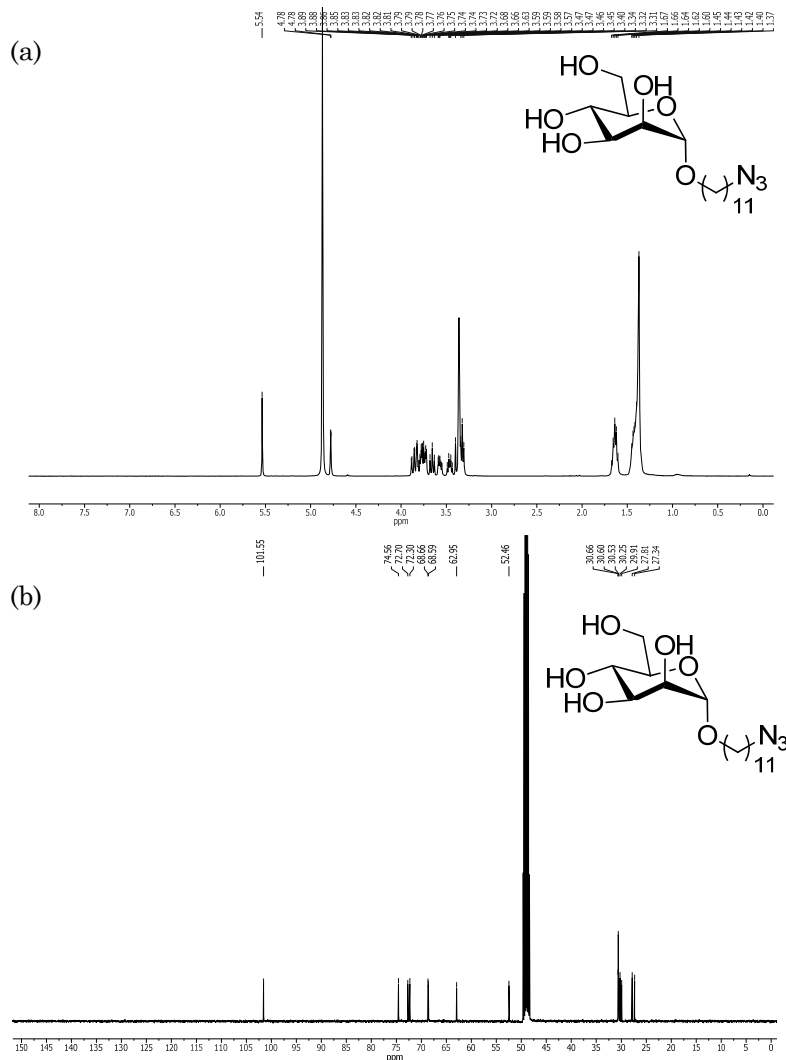


Figure S1: NMR spectra of 1-(11-azidoundecyl)-α-D-mannopyranoside (4); (a) ¹H NMR spectrum and (b) ¹³C NMR spectrum.

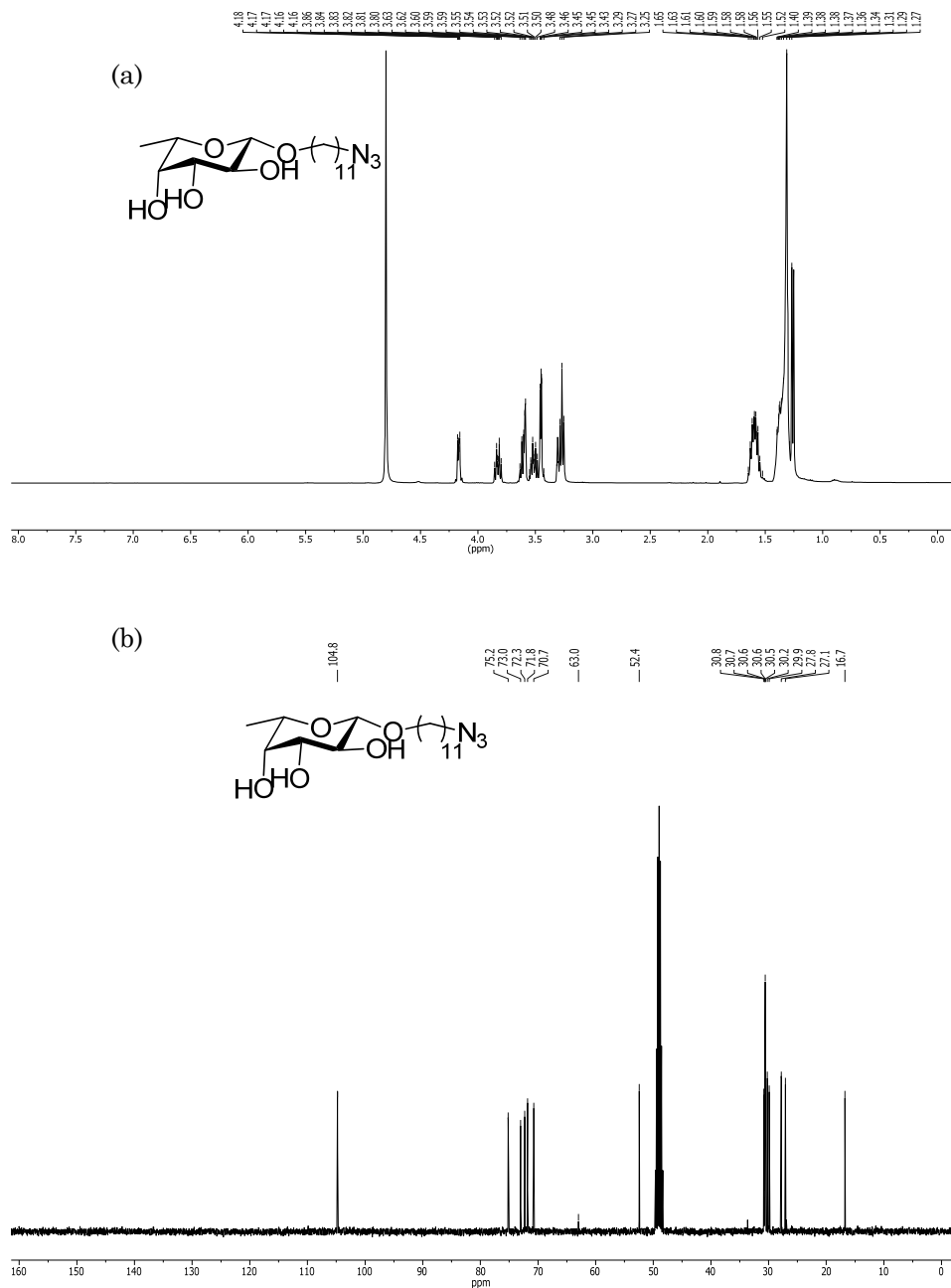


Figure S2: NMR spectra of 1-(11-azidoundecanyl)- β -D-fucopyranoside **7**; (a) ^1H NMR spectrum of **7** and (b) ^{13}C NMR spectrum of **7**.

3 Preparation of monolayers with different head and tail groups.

3.1 Preparation of monolayers on gold

Prior to modification, the gold substrates were rinsed with ethanol and water followed by drying under nitrogen. The specimens were immersed in a 1 mM solution of the 16-mercaptohexadecanoic acid (MHDA) in ethanol for 24 h. The MHDA-modified surfaces (M_{Au}^1 , Table 1) were then removed and rinsed with ethanol and water, sonicated in ethanol, and dried under nitrogen. The acid terminated substrates (M_{Au}^1) were activated using 2,3,4,5,6-pentafluorophenol (PFP) and *N,N'*-dicyclohexylcarbodiimide (DCC) as reported earlier.² The PFP-terminated substrates (M_{Au}^2) were then immersed in a 1 mg/ml solution of either $\text{NH}_2\text{-(CH}_2\text{CH}_2\text{O)}_{22}\text{-COOH}$ (1 kDa) or $\text{NH}_2\text{-(CH}_2\text{CH}_2\text{O)}_{77}\text{-COOH}$ (3.5 kDa) in dichloromethane for 24 h, resulting in layers M_{Au}^3 and M_{Au}^4 , respectively. The PEG-modified surfaces were removed and rinsed with dichloromethane, sonicated in the same solvent, and dried under nitrogen. The monolayer M_{Au}^5 was prepared as described above using 1-decanethiol instead of MHDA.

3.2 Preparation of monolayers on silicon nitride (Si_3N_4)

3.2.1 Preparation of the epoxy- terminated monolayer $M_{\text{Si}_3\text{N}_4}^1$ (primary modification).

Silicon nitride substrates were cleaned by rinsing and sonication in acetone for 3 min and dried in a stream of argon. Thereafter, the substrates were exposed to an O_2 -plasma for 5 min. The resulting oxidized surfaces were etched in 2.5% HF solution for 2 min, properly rinsed with water and finally dried with argon. The prepared samples were immediately used for modification. For preparation of the epoxy- terminated monolayer $M_{\text{Si}_3\text{N}_4}^1$ an 1,2-epoxy-9-decene was transferred into a clean, dry, and degassed, flat bottom quartz flask, followed by three consecutive freeze-pump-thaw cycles to remove trace amounts of oxygen and water. Finally, the flask was backfilled with argon and the alkene was frozen again and freshly cleaned samples were transferred in the flask. The grafting of Si_3N_4 samples was carried out following the UV-assisted method described elsewhere⁵. Two UV pen lamps (254 nm, 9 $\text{mW}\cdot\text{cm}^{-2}$, low pressure mercury vapor, double bore lamps from Jelight

Company Inc., California) were aligned at a distance of ~5 mm from the flat bottom of the flask and the samples were irradiated for 10 h in argon atmosphere at ambient temperature. After the formation of $M_{Si_3N_4}^1$, the samples were removed from the flask and cleaned by rinsing and sonication in DCM for 3 min to remove physisorbed molecules and dried under argon.

3.2.2 Preparation of amine-terminated monolayer $M_{Si_3N_4}^2$ (secondary modification).

The epoxide-terminated silicon nitride surfaces $M_{Si_3N_4}^1$ were transferred into neat, argon saturated tris(2-aminoethyl)amine in a flat-bottom flask. The flask was closed under argon and the reaction mixture was kept for 16 h at 40 °C. Subsequently, the samples were rinsed several times with ethanol, sonicated in ethanol for 3 min rinsed with DCM and finally dried with an argon flow.

3.2.3 Preparation of reversed amide monolayer $M_{Si_3N_4}^3$ (tertiary modification).

Amine-terminated silicon nitride surfaces were transferred into 5 ml degassed, freshly prepared 0.1 M solution of perfluorononanoyl chloride in $C_2H_2Cl_2$ in a flat bottom flask. Thereafter, 70 μ l triethylamine (one equivalent pertaining to the perfluorononanoyl chloride) were added to the reaction mixture under argon. The flask was closed under argon and kept for 16 h at 60 °C. Subsequently, the samples were rinsed several times with ethanol and DCM, sonicated in DCM for 3 min and finally dried under argon.

3.2.4 Preparation of oligo(ethylene glycol)-terminated monolayers.

Preceding the modification, Si_3N_4 samples were cleaned and etched (2.5 % HF, 2.5 min) as described elsewhere.² Afterwards, the UV-induced formation of oligoethylene glycol monolayers on Si_3N_4 was carried out following a procedure as reported.⁴ The methoxy-hexa(ethylene oxide) undec-1-ene ($CH_3O(CH_2CH_2O)_6(CH_2)_9CH=CH_2$; EO6) and methoxy-nona(ethylene oxide) undec-1-ene ($CH_3O(CH_2CH_2O)_9(CH_2)_9CH=CH_2$; EO9) were used for the preparation of monolayers $M_{Si_3N_4}^{EO6}$ and $M_{Si_3N_4}^{EO9}$, respectively.

3.3 Preparation of monolayers on glass (SiO₂)

3.3.1 Formation of octadecyl-monolayer and mixed oligo(ethylene glycol)-terminated monolayer

Silicon oxide samples were cleaned by rinsing and sonication in acetone for 3 min, dried with argon and treated with O₂-plasma for 5 min. Hereafter, the substrates were activated in a freshly made 1:1 (v:v) mixture of hydrochloric acid (37%) and methanol for at least 30 min, rinsed with water and methanol and dried with argon. The prepared samples were immediately used for modification as follows. Dry toluene (3 ml) and 30 µl of the silane were transferred into a dry, argon filled, flat bottom flask which was backfilled with argon. The clean SiO₂ surfaces were transferred into this solution and left overnight at ambient temperature. The samples were removed from the flask, rinsed and sonicated in toluene to remove physisorbed molecules and dried with argon. Subsequently, the samples were cured at 130 °C at reduced pressure for at least 4 hours. Afterwards, the samples were again rinsed and sonicated in toluene and dried under argon. Trichloro(octadecyl)silane was used to obtain octadecyl monolayer on SiO₂ ($M_{SiO_2}^1$), while 2-[[methoxypoly(ethyleneoxy)₆₋₉]-propyl]trimethoxysilane was employed to obtain oligo(ethylene glycol)-terminated monolayer ($M_{SiO_2}^2$), containing 6 to 9 ethylene oxide units.

3.3.2 Preparation of oligo(ethylene glycol)-terminated monolayers on SiO₂

Preceding the modification, SiO₂ substrates were cleaned and etched in a freshly prepared 1:1 (v:v) mixture of hydrochloric acid (37%) and methanol as described above. The substrates were, then, rinsed with water and methanol, dried with argon and transferred in a quartz reactor to carry out UV-induced monolayer formation as reported.⁵ The samples were irradiated for 10 h in the presence of methoxy-poly(ethylene oxide) undec-1-ene. For instance, methoxy-tri(ethylene oxide) undec-1-ene (CH₃O(CH₂CH₂O)₃(CH₂)₉CH=CH₂; EO3), methoxy-hexa(ethylene oxide) undec-1-ene (CH₃O(CH₂CH₂O)₆(CH₂)₉CH=CH₂; EO6), and methoxy-nona(ethylene oxide) undec-1-ene

(CH₃O(CH₂CH₂O)₉(CH₂)₉CH=CH₂; EO9) were utilized for the formation of monolayers $M_{SiO_2}^{EO3}$, $M_{SiO_2}^{EO6}$ and $M_{SiO_2}^{EO9}$, respectively.

3.4 Preparation of monolayers on alumina (Al₂O₃)

The monolayer preparation was done according to the literature.¹ Briefly, PAO substrates were rinsed and sonicated in acetone (5 min) and ultrapure water (5 min). After this the PAO surfaces were immersed in a fresh mixture of 37% hydrochloric acid and methanol (1:1, v/v) for 30 min. Then, the substrates were rinsed and sonicated with ultrapure water and absolute ethanol and finally were immersed in a 1 mM solution of 10-undecynylphosphonic acid in absolute ethanol (room temperature, 16 h). Hereafter, the substrates were washed with absolute ethanol, heated at 140 °C under vacuum for 6 h. After the curing step, the samples were rinsed and sonicated in ethanol and dichloromethane (5 min each), and dried in air. Afterwards, a copper-catalyzed azide–alkyne cycloaddition (CuAAC) reaction on the alkyne-terminated PAO surfaces was done in a reaction tube using a solution of azidoundecanyl carbohydrate (0.1 mM), copper (I) sulfate (0.2 mM), and sodium ascorbate (0.2 mM). The reaction tube was equipped with a stirring bar and a platform to protect the fragile surface from the stirring bar. The alkyne-terminated PAO surfaces were immersed in the solution and heated in a microwave oven (CEM Discover) for 30 min at 70 °C under stirring. After the reaction, the substrate was thoroughly washed and sonicated in water, ethanol, and dichloromethane (5 min per solvent) and dried in air. In this way, utilizing 1, 4, and 7, three types of sugar-terminated monolayers were prepared on PAO substrates: lactose-, mannose- and fucose-terminated monolayers ($M_{Al_2O_3}^{lac}$, $M_{Al_2O_3}^{man}$, $M_{Al_2O_3}^{fuc}$, accordingly).

3.5 Preparation of monolayers on silicon Si(111)

The modification of Si (111) was performed according to a procedure described in the literature.⁶ Briefly, an alkyne-terminated monolayer M_{Si}^1 was formed on Si(111) using 1,15-hexadecadiyne and heating at 80 °C, under oxygen free and water free conditions for 16 h. The resultant alkyne-terminated monolayers were further modified via a thiol-yne click reaction with freshly prepared mixture of a thiol and 2,2-dimethoxy-2-phenylacetophenone

(DMPA) as photoinitiator in a 5 : 1 molar ratio. A few drops of freshly prepared reaction mixture (thiol and initiator) were transferred onto an alkyne-terminated monolayer on Si(111) substrates. The thiol-yne click reaction was initiated by irradiating with 365 nm light ($800 \mu\text{W}/\text{cm}^2$, Spectroline, Westbury, NY) for 1.5 h. Afterwards, the modified Si substrates were rinsed with THF and dichloromethane and sonicated for 10 min in these solvents. The reactions were performed either with 2-mercaptoethanol or butanethiol to obtain monolayers M_{Si}^2 and M_{Si}^3 , respectively.

Similarly, alkene-terminated monolayers M_{Si}^4 were prepared on Si(111) wafers using 1,13-tetradecadiene.⁶ The alkene-terminated monolayers were further modified via a thiol-ene click reaction with freshly prepared mixture of a thiol and DMPA as described above. A few drops of it were transferred onto an alkene-terminated monolayer on Si(111) substrates and subsequently the substrates were irradiated with the same source of UV light (365 nm, $800 \mu\text{W}/\text{cm}^2$, Spectroline, Westbury, NY) for 1.5 h. Afterwards, the modified Si substrates were rinsed with THF and dichloromethane, and sonicated for 10 min in the same solvents. The a thiol-ene click reactions were done either with 2-mercaptoethanol or butanethiol to obtain monolayers M_{Si}^5 and M_{Si}^6 , correspondingly. X-ray Photoelectron Spectroscopy (XPS). Prior to DART-HRMS analysis, the monolayer formation and quality were first assessed by XPS. Before the analysis with XPS, all substrates were extensively cleaned by sonication in appropriate solvents, dried under a stream of argon and stored under oxygen-free and water-free conditions (in a glovebox MBraun MB200G, under an argon atmosphere and a content of H_2O and O_2 each below 0.1 ppm) till the XPS measurement. XPS analyses were performed using a JPS-9200 photoelectron spectrometer (JEOL). The spectra were obtained under ultrahigh vacuum (UHV) conditions using monochromatic Al K α X-ray radiation at 12 kV and 20 mA, and an analyzer pass energy of 10 eV. The X-ray incidence angle and the electron acceptance angle were 80° and 10° to the surface normal, respectively. In case of electrostatic charging in the positive direction on the surface, a charge compensation was used during the XPS scans with an accelerating voltage of 2.8 eV and a filament current of 5.00 A. Afterwards, the spectra were reprocessed with the CASA XPS peak fit program (version 2.3.15) using the alkyl C 1s component calibrated at 285.0 eV. For the curve fitting of

C 1s spectra, linear background subtraction and a Gaussian/Lorentzian peak shape model GL(30) were used. The full widths at half maximum (FWHM) were constrained to be equal for all peaks within one spectrum, resulting in FWHM values ranging from 0.9 to 1.4 eV. After successful confirmation of the resultant monolayers, the samples were subjected to DART-HRMS analysis.

4 X-ray Photoelectron Spectroscopy (XPS)

4.1 XPS spectra of monolayers on Al₂O₃

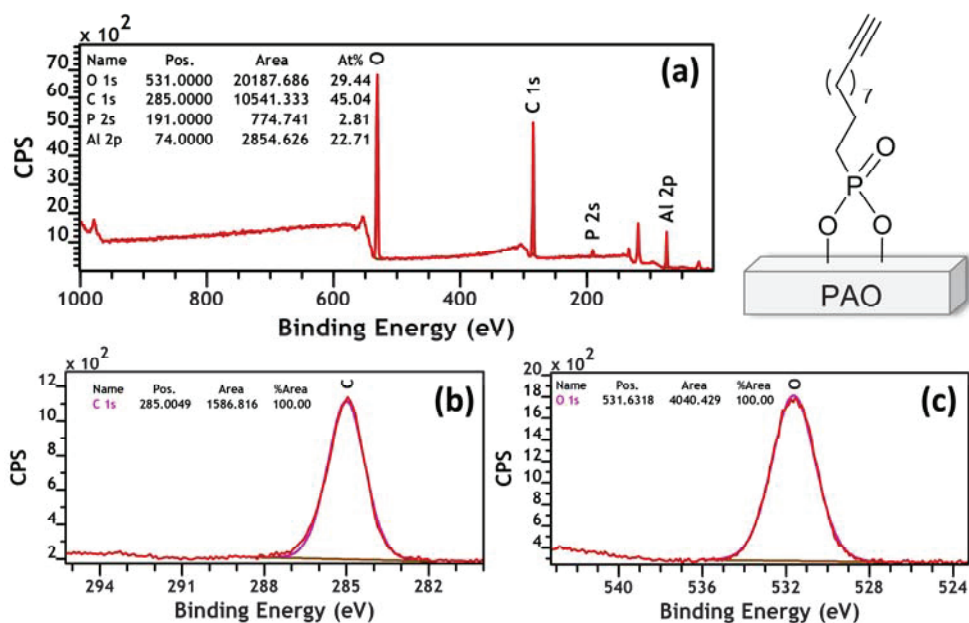


Figure S3: XPS spectra of alkyne-terminated monolayer on alumina before “click reactions” with **1**, **4** or **7** (before formation of lactose-, mannose- or fucose-terminated monolayers). (a) survey spectrum lacking a N 1s peak; (b) C 1s narrow scan (c) O 1s narrow scan.

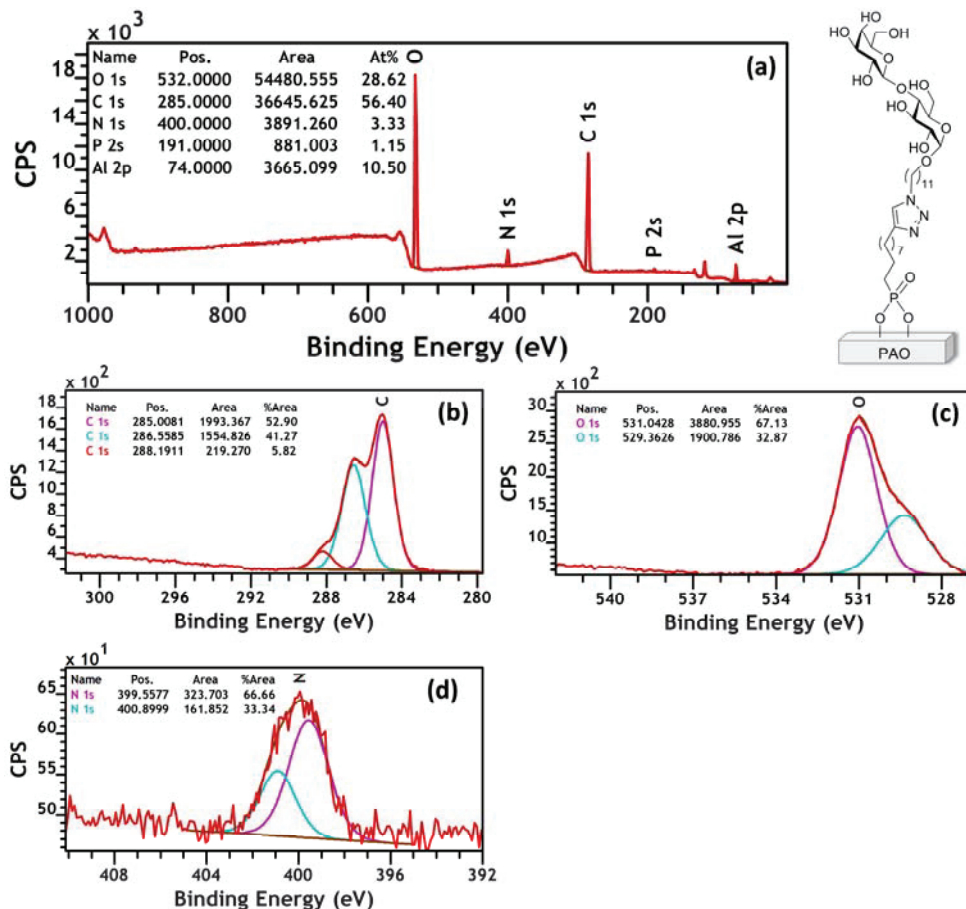


Figure S4: XPS spectra of lactose-terminated monolayer $M_{Al_2O_3}^{lac}$ (after “click reaction” with 1). (a) survey spectrum with presence of N 1s peak; (b) C 1s narrow scan and a clear contribution of C-O bonds introduced by the attachment of 1 on the surface (c) O 1s narrow scan (d) N 1s narrow scan indicating formation of triazole ring and lack of azide group at 404 eV Binding Energy (BE).

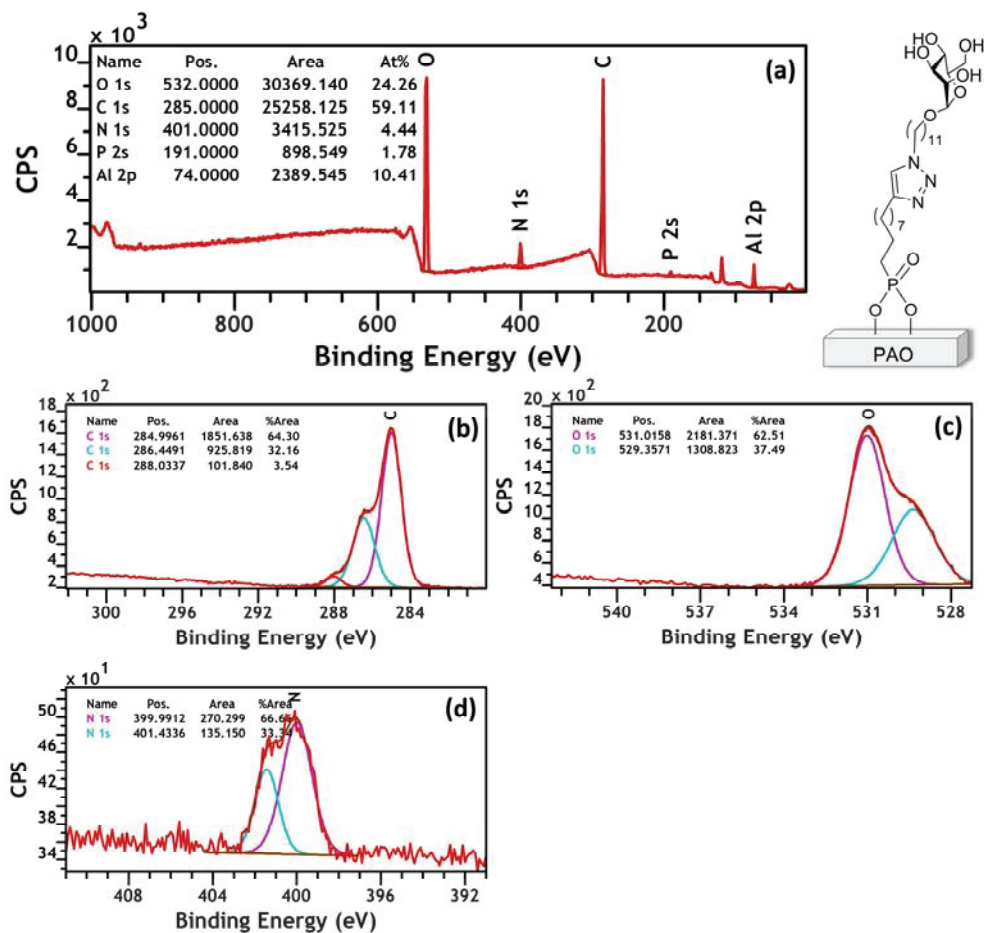


Figure S5: XPS spectra of manose-terminated monolayer $M_{Al_2O_3}^{man}$ (after “click reaction” with 4). (a) survey spectra with N 1s peak; (b) C 1s narrow scan with a clear contribution of C-O bonds introduced with the attachment of the sugar on the surface (c) O 1s narrow scan (d) N 1s narrow scan indicating formation of triazole ring and lacking peak for an azide group at 404 eV (BE).

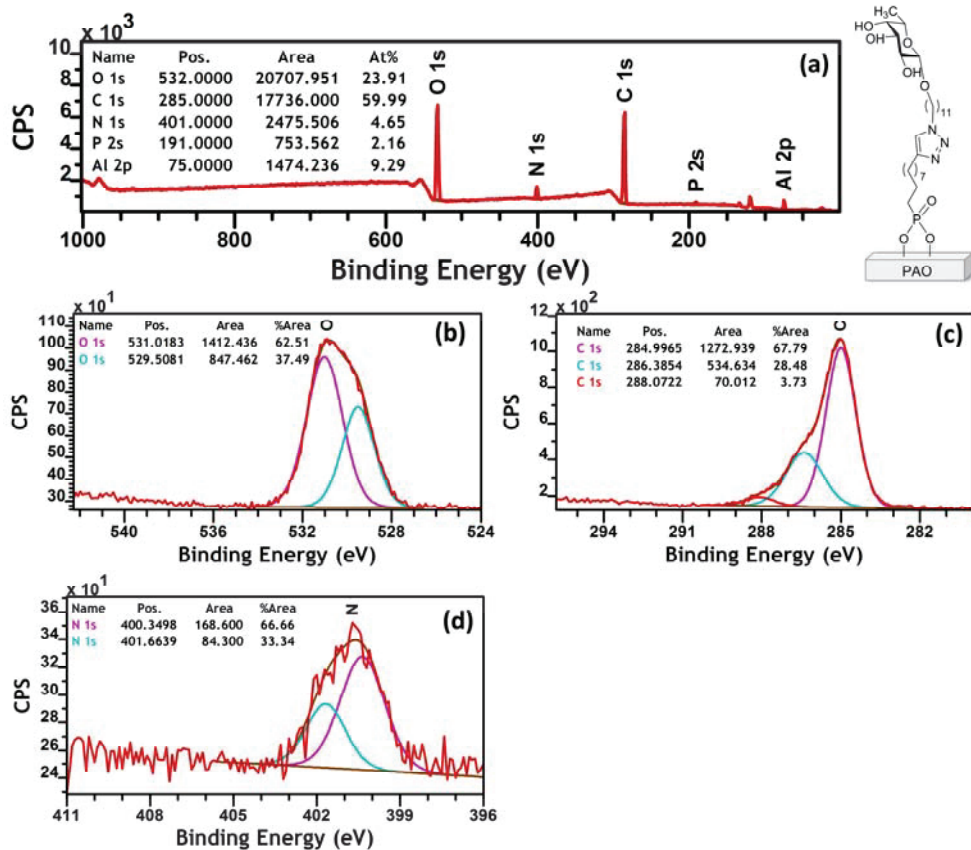


Figure S6: XPS spectra of fucose-terminated monolayer $M_{Al_2O_3}^{fuc}$ (after "click reaction" with 7). (a) survey spectra with N 1s peak; (b) C 1s narrow scan with a clear contribution of C-O bonds introduced with the attachment of the sugar on the surface (c) O 1s narrow scan (d) N 1s narrow scan indicating formation of triazole ring and the lack of an azide group at 404 eV (BE).

4.2 XPS spectra of monolayers on Si(111)

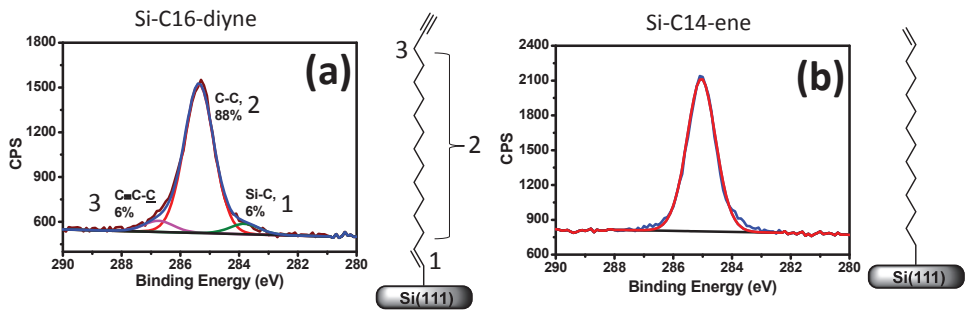


Figure S7: XPS spectra⁶ of monolayer (a) M_{Si}^1 and (b) M_{Si}^4 .

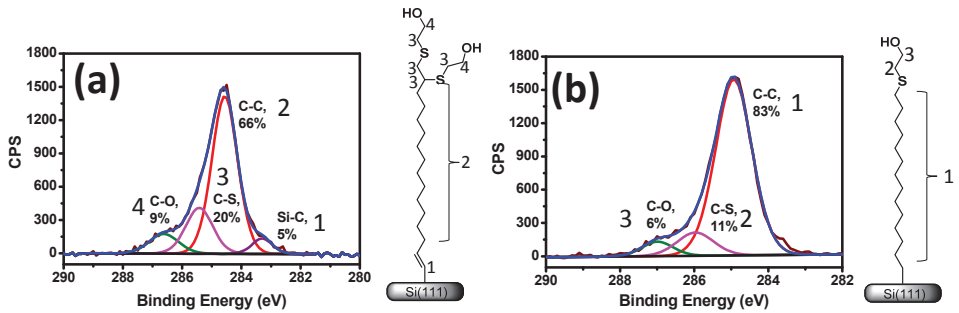


Figure S8: XPS spectra⁶ of monolayer (a) M_{Si}^2 and (b) M_{Si}^5 .

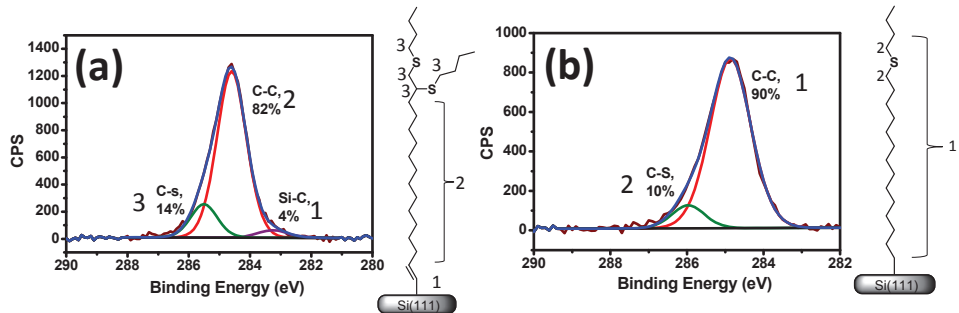


Figure S9: XPS spectra of monolayer (a) M_{Si}^3 and (b) M_{Si}^6 .

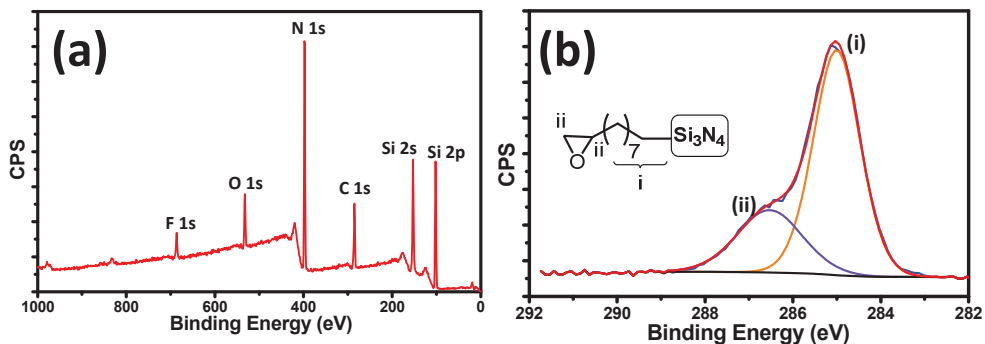
4.3 XPS spectra of monolayers on Si_3N_4


Figure S10: XPS spectra of monolayer $M^1_{\text{Si}_3\text{N}_4}$ (a) survey spectra and (b) C 1s narrow scan

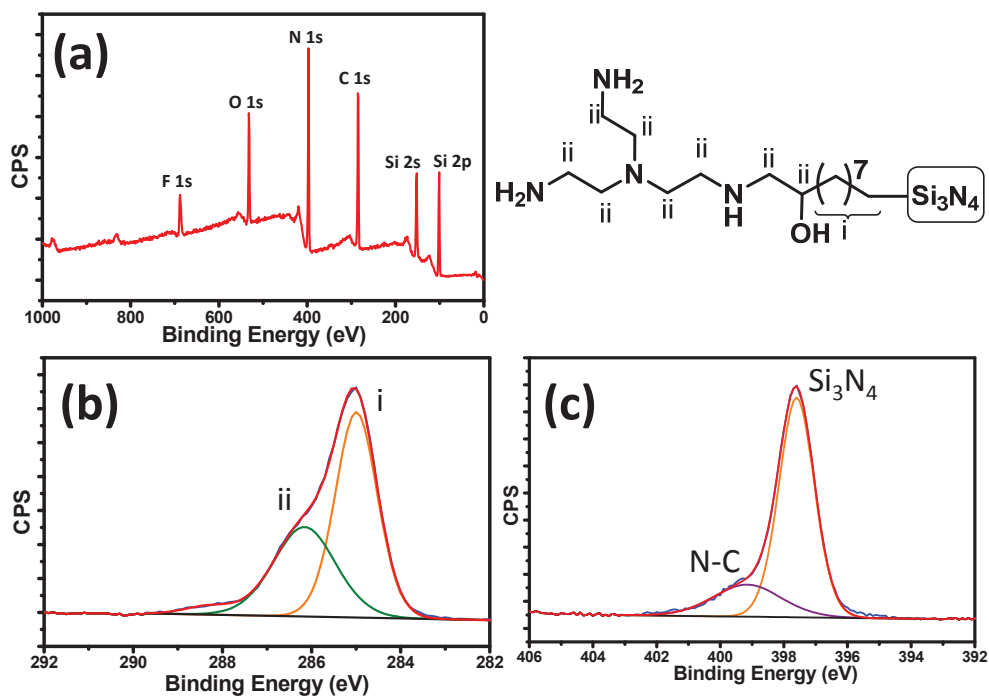


Figure S11: XPS spectra of monolayer $M^2_{\text{Si}_3\text{N}_4}$ (a) survey spectra and (b) C 1s narrow scan (c) N 1s spectra with a new contribution indicating formation of N-C bonds.

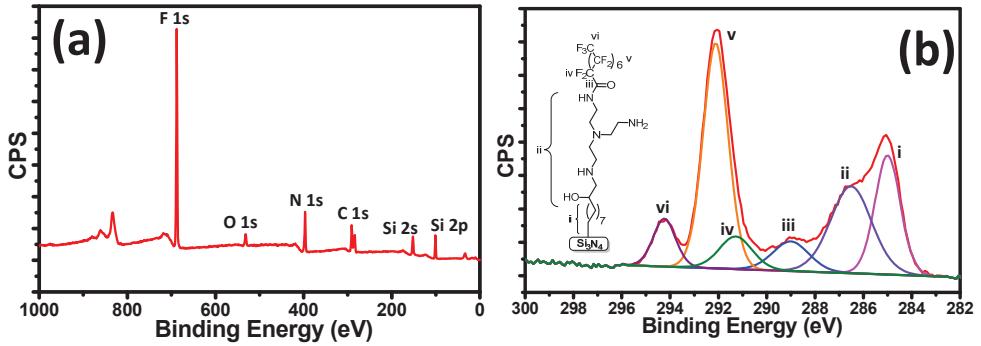


Figure S12: XPS spectra of monolayer $M^3_{Si_3N_4}$ (a) survey spectra and (b) C 1s narrow scan.

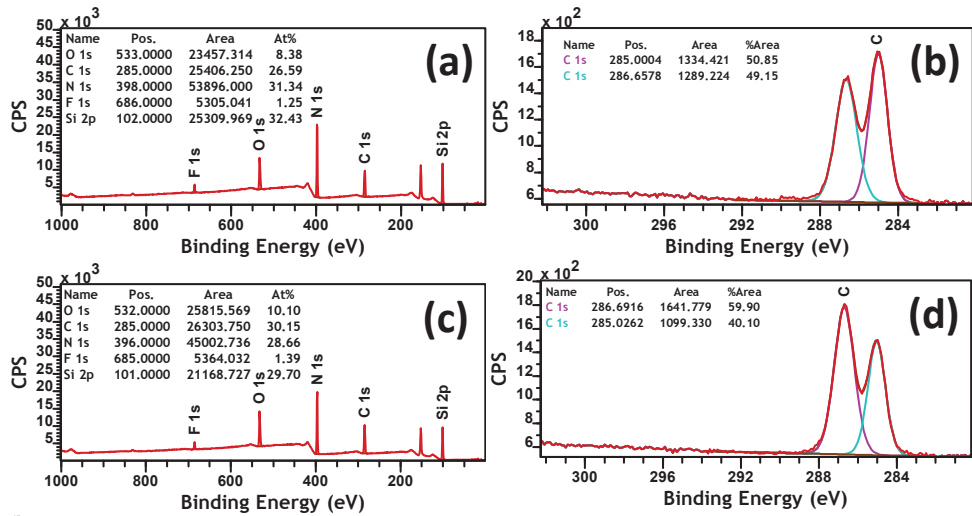


Figure S13: XPS spectra of monolayers $M^{EO6}_{Si_3N_4}$ and $M^{EO9}_{Si_3N_4}$ (a) survey spectra of $M^{EO6}_{Si_3N_4}$; (b) C narrow scan of $M^{EO6}_{Si_3N_4}$ (c) survey spectra of $M^{EO9}_{Si_3N_4}$ (d) C narrow scan of $M^{EO9}_{Si_3N_4}$

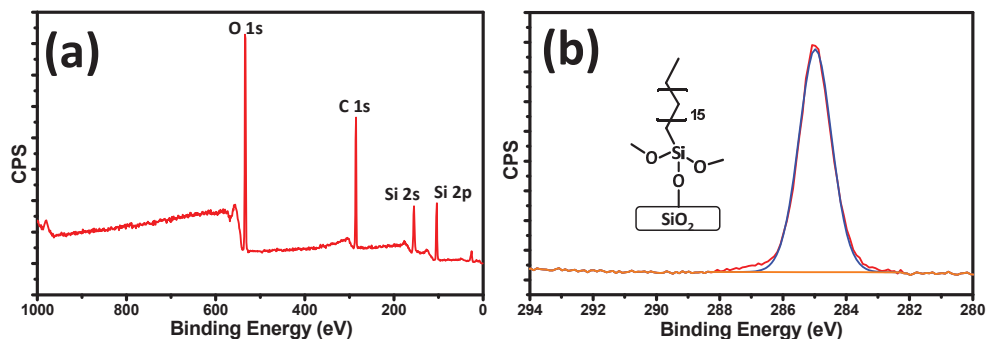
4.4 XPS spectra of monolayers on SiO₂


Figure S14: XPS spectra of monolayer $M^1_{SiO_2}$ (a) survey spectra and (b) C 1s narrow scan

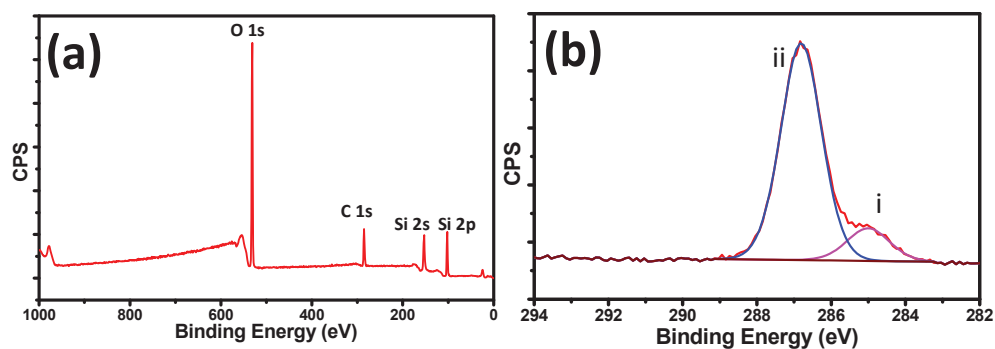


Figure S15: XPS spectra of monolayer $M^2_{SiO_2}$ (a) survey spectra and (b) C 1s narrow scan

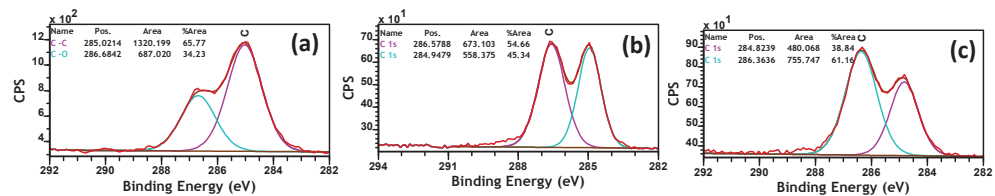


Figure S16: XPS spectra C 1s narrow scan of monolayers (a) $M^{EO3}_{SiO_2}$ (b) $M^{EO6}_{SiO_2}$ and (c) $M^{EO9}_{SiO_2}$

4.5 XPS spectra of monolayers on Au

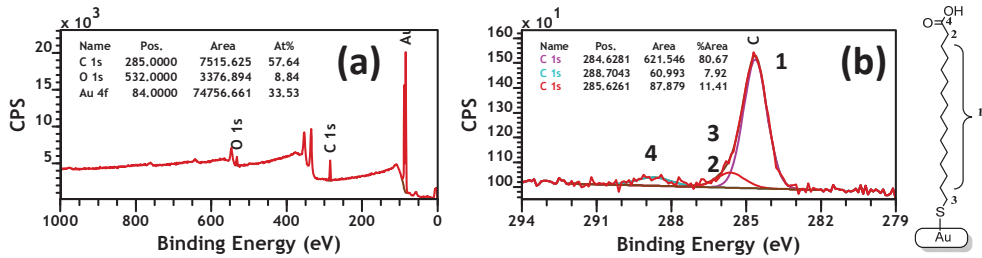


Figure S17: XPS spectra of monolayer M_{Au}^1 (a) survey spectra (b) C 1s narrow scan

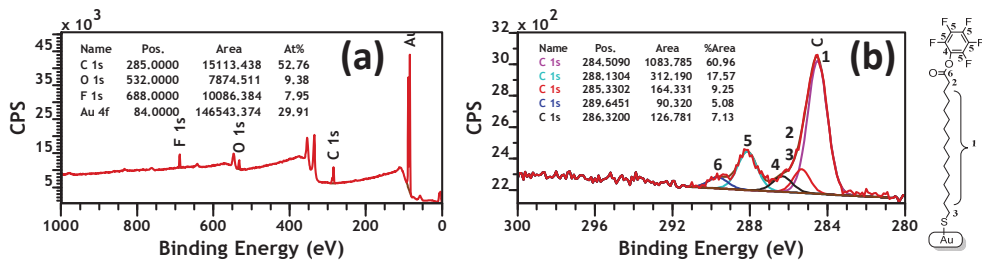


Figure S18: XPS spectra of monolayer M_{Au}^2 (a) survey spectra (b) C 1s narrow scan

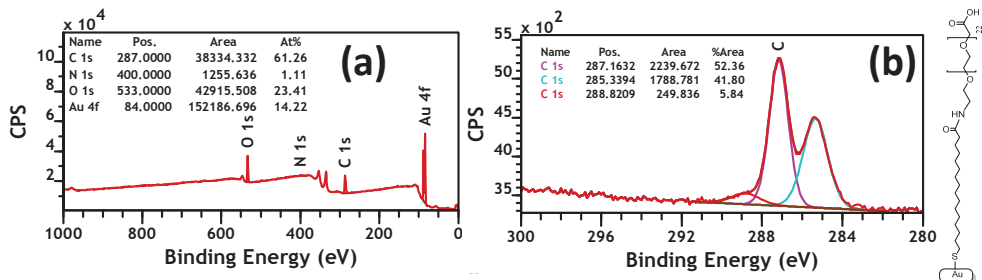


Figure S19: XPS spectra of monolayer M_{Au}^3 (a) survey spectra (b) C 1s narrow scan

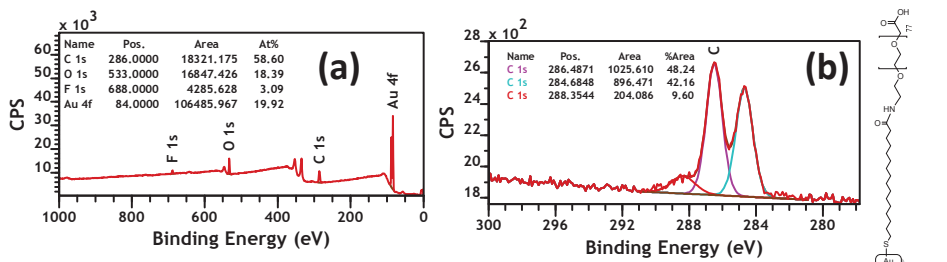


Figure S20: XPS spectra of monolayer M_{Au}^4 (a) survey spectra (b) C 1s narrow scan

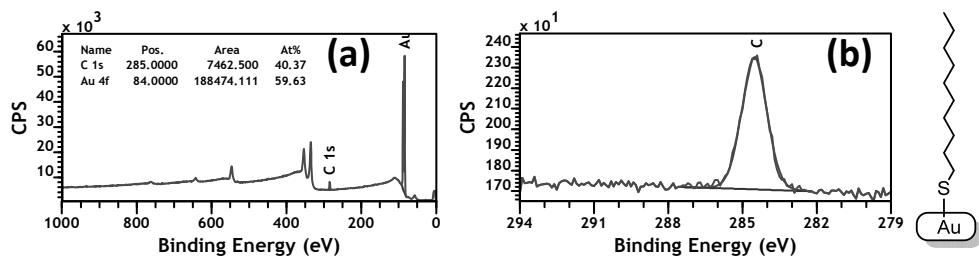


Figure S21: XPS spectra of monolayer M_{Au}^5 (a) survey spectra (b) C 1s narrow scan

5 DART-HRMS of SPR chip

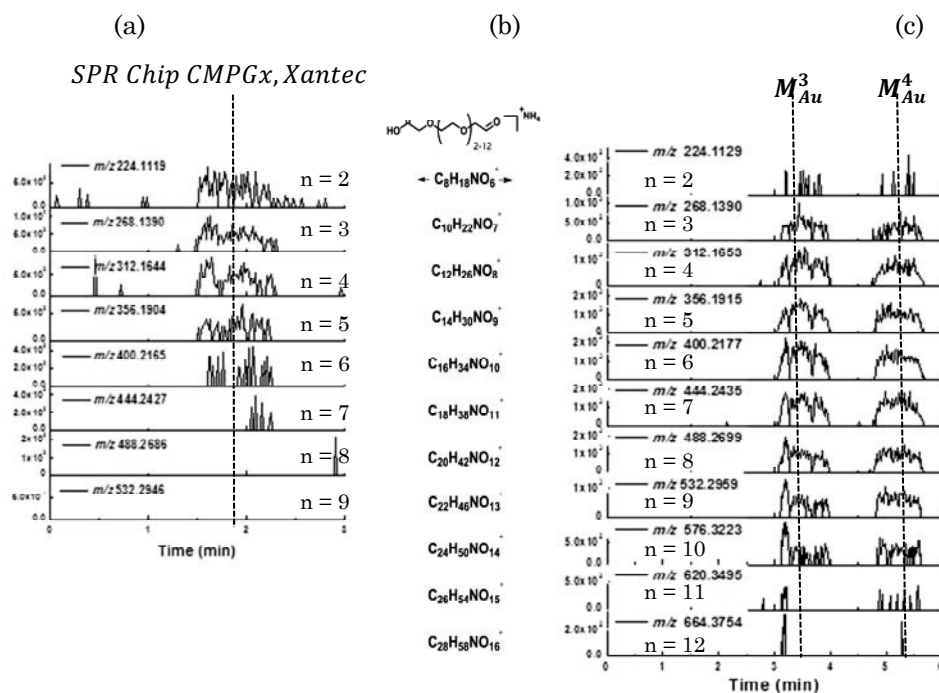


Figure S2: DART-HRMS of monolayers with carboxymethyl-PEG coatings: (a) commercially available gold SPR chip CMPGx with attached carboxymethyl-PEG (6 kDa) analyzed between 1.5 - 2.7 min; (b) the most intense ions observed for carboxymethyl-PEG, and (c) in-house prepared monolayers M_{Au}^3 - carboxymethyl-PEG (1 kDa), measured between 3.0 - 4.0 min, and M_{Au}^4 - carboxymethyl-PEG (3.5 kDa), measured between 5.0 - 6.0 min.

References

1. ter Maat, J.; Regeling, R.; Ingham, C. J.; Weijers, C. A. G. M.; Giesbers, M.; de Vos, W. M.; Zuilhof, H. Organic Modification and Subsequent Biofunctionalization of Porous Anodic Alumina Using Terminal Alkynes. *Langmuir* **2011**, *27* (22), 13606-13617.
2. Manova, R. K.; Pujari, S. P.; Weijers, C. A. G. M.; Zuilhof, H.; van Beek, T. A. Copper-Free Click Biofunctionalization of Silicon Nitride Surfaces via Strain-Promoted Alkyne–Azide Cycloaddition Reactions. *Langmuir* **2012**, *28* (23), 8651-8663.
3. Mukhopadhyay, B.; Kartha, K. P. R.; Russell, D. A.; Field, R. A. Streamlined Synthesis of Per-O-acetylated Sugars, Glycosyl Iodides, or Thioglycosides from Unprotected Reducing Sugars. *J. Org. Chem.* **2004**, *69* (22), 7758-7760.
4. Rosso, M.; Nguyen, A. T.; de Jong, E.; Baggerman, J.; Paulusse, J. M. J.; Giesbers, M.; Fokink, R. G.; Norde, W.; Schroën, K.; Rijn, C. J. M. v.; Zuilhof, H. Protein-Repellent Silicon Nitride Surfaces: UV-Induced Formation of Oligoethylene Oxide Monolayers. *ACS Applied Materials & Interfaces* **2011**, *3* (3), 697-704.
5. ter Maat, J.; Regeling, R.; Yang, M.; Mullings, M. N.; Bent, S. F.; Zuilhof, H. Photochemical Covalent Attachment of Alkene-Derived Monolayers onto Hydroxyl-Terminated Silica. *Langmuir* **2009**, *25* (19), 11592-11597.
6. Bhairamadgi, N. S.; Gangarapu, S.; Caipa Campos, M. A.; Paulusse, J. M. J.; van Rijn, C. J. M.; Zuilhof, H. Efficient Functionalization of Oxide-Free Silicon(111) Surfaces: Thiol–yne versus Thiol–ene Click Chemistry. *Langmuir* **2013**, *29* (14), 4535-4542.

Appendix 4

Information supplementing Chapter 5: MS Spectra

Contents

1	DART-HRMS of $M_{Si_3N_4}^3$ in (+)-mode.....	178
2	DART-HRMS of M_{Au}^5 in (-)-mode	179
3	DART-HRMS of M_{Au}^1 in (-)-mode	180
4	DART-HRMS of M_{Au}^1 in (+)-mode	181
5	DART-HRMS of M_{Au}^2 in (+)-mode	182
6	DART-HRMS of carboxymethyl-PEG coating M_{Au}^3 in (+)-mode	182
7	DART-HRMS of oligo(ethylene glycol)-terminated monolayers in (+)-mode.....	183
8	DART-HRMS of M_{Si}^2 in (-)-mode	185
9	DART-HRMS of M_{Si}^5 in (-)-mode	186
10	DART-HRMS of M_{Si}^3 in (-)-mode	187
11	DART-HRMS of M_{Si}^6 in (-)-mode	188
12	DART-HRMS of M_{Si}^1 in (-)-mode	188
13	DART-HRMS of M_{Si}^1 in (+)-mode	189
14	DART-HRMS of M_{Si}^4 in (-)-mode	189
15	DART-HRMS of M_{Si}^4 in (+)-mode	190
16	DART-HRMS of $M_{Si_3N_4}^1$ in (-)-mode.....	190
17	DART-HRMS of $M_{Si_3N_4}^1$ in (+)-mode.....	191
18	DART-HRMS of $M_{Si_3N_4}^2$ in (+)-mode.....	191
19	DART-HRMS of $M_{Si_3N_4}^2$ in (-)-mode.....	192
20	DART-HRMS of $M_{SiO_2}^1$ in (+)-mode	192
21	DART-HRMS of $M_{SiO_2}^1$ in (-)-mode	193
22	DART-HRMS of $M_{Al_2O_3}^{lac}$ in (+)-mode	194
23	DART-HRMS of $M_{Al_2O_3}^{man}$ in (+) mode.....	196
24	DART-HRMS of $M_{Al_2O_3}^{man}$ in (+) mode.....	198

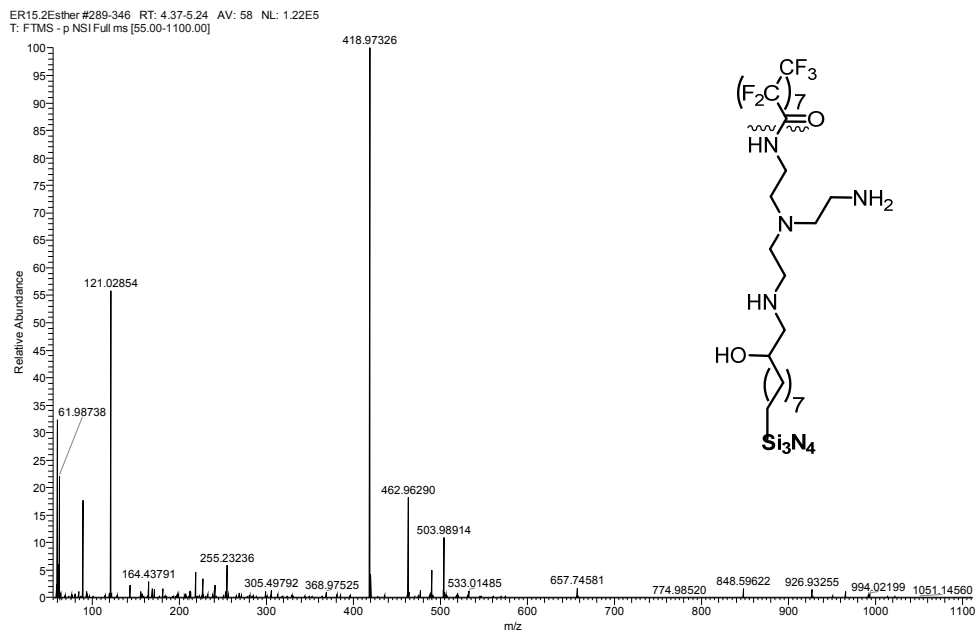
1 DART-HRMS of $M_{Si_3N_4}^3$ in (+)-mode

Figure S1: DART-HRMS of $M_{Si_3N_4}^3$ in (+)-mode from m/z 55 to m/z 1110.

Characteristic ions of this monolayer are:

1. Ion at m/z 418.9732 (0.3877 mDa*) is $[CF_3(CF_2)_7COO - CO_2]^-$; (C_8F_{17})
2. Ion at m/z 462.9629 is (0.1577 mDa) is $[CF_3(CF_2)_7COO]^-$; ($C_9O_2F_{17}$)

* difference in mDa (Δ) between calculated accurate mass and measured mass.

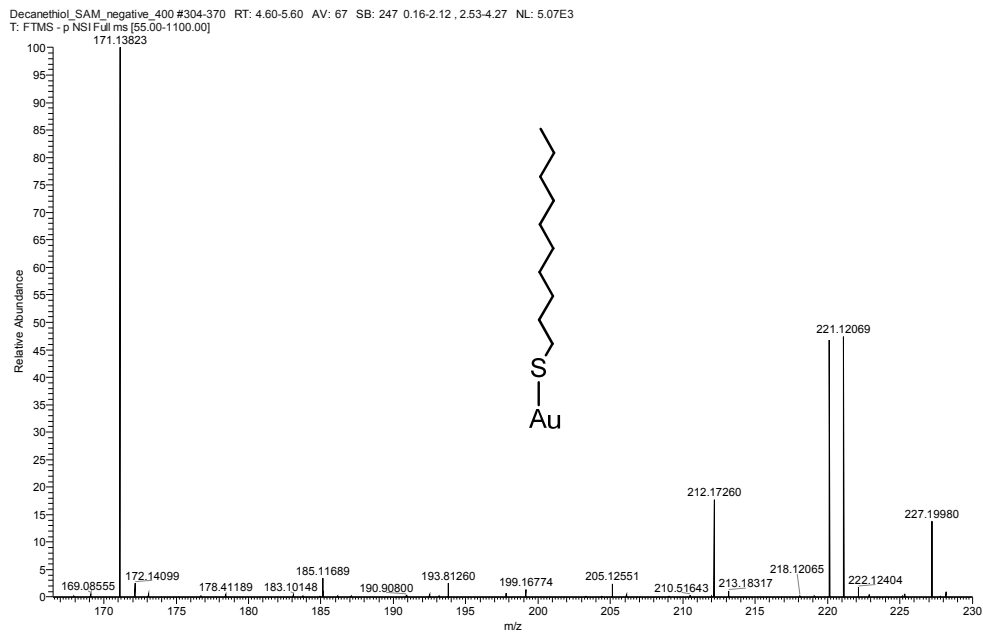
2 DART-HRMS of M_{Au}^5 in (-)-mode

Figure S2: DART-HRMS of M_{Au}^5 in (-)-mode from m/z 167 to m/z 230.

Characteristic ions of this monolayer are:

1. Ion at m/z 221.1207 (0.1097 mDa) is $[\text{CH}_3(\text{CH}_2)_9\text{SO}_3]^-$; $\text{C}_{10}\text{H}_{21}\text{O}_3\text{S}$
2. Ion at m/z 205.1255 (-0.1630 mDa) is $[\text{CH}_3(\text{CH}_2)_9\text{SO}_2]^-$; $\text{C}_{13}\text{H}_{21}\text{O}_2\text{S}$
3. Ion at m/z 171.1382 (0.28619 mDa) is $[\text{CH}_3(\text{CH}_2)_9\text{SO}_2 - \text{H}_2\text{S}]^-$; $\text{C}_{10}\text{H}_{19}\text{O}_2$

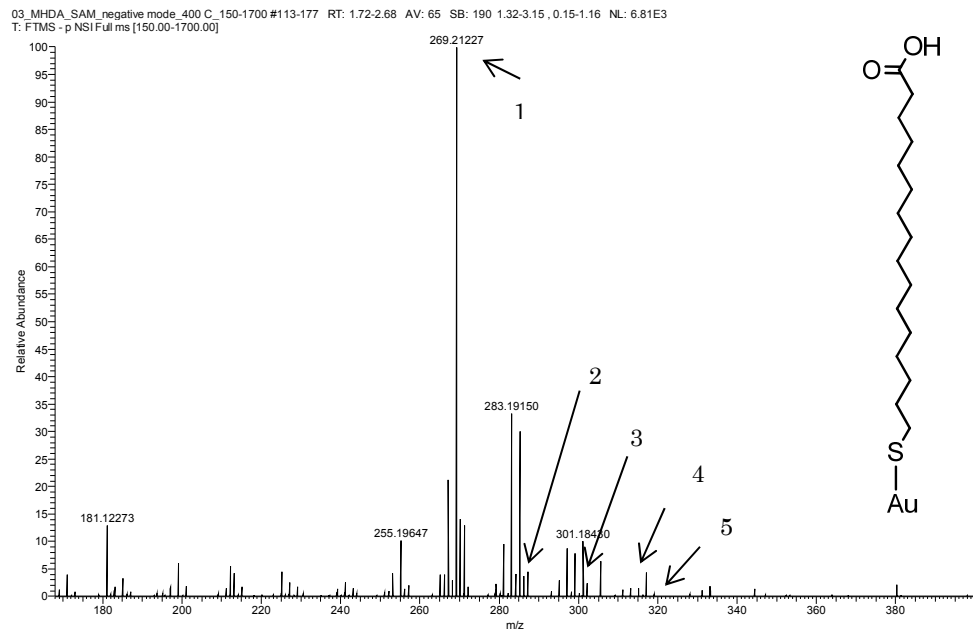
3 DART-HRMS of M_{Au}^1 in (-)-mode

Figure S3. DART-HRMS of M_{Au}^1 in (-)-mode from m/z 168 to m/z 400.

Characteristic ions of this monolayer are:

1. Ion at m/z 269.2123 (0.5856 mDa) is $C_{16}H_{29}O_3$
2. Ion at m/z 287.2050 (0.8274 mDa) is $C_{16}H_{31}O_2S$
3. Ion at m/z 301.1872 (0.5474 mDa) is $C_{16}H_{29}O_3S$
4. Ion at m/z 317.1791 (0.5279 mDa) is $C_{16}H_{29}O_4S$
5. Ion at m/z 319.1949 (0.6073 mDa) is $C_{16}H_{31}O_4S$

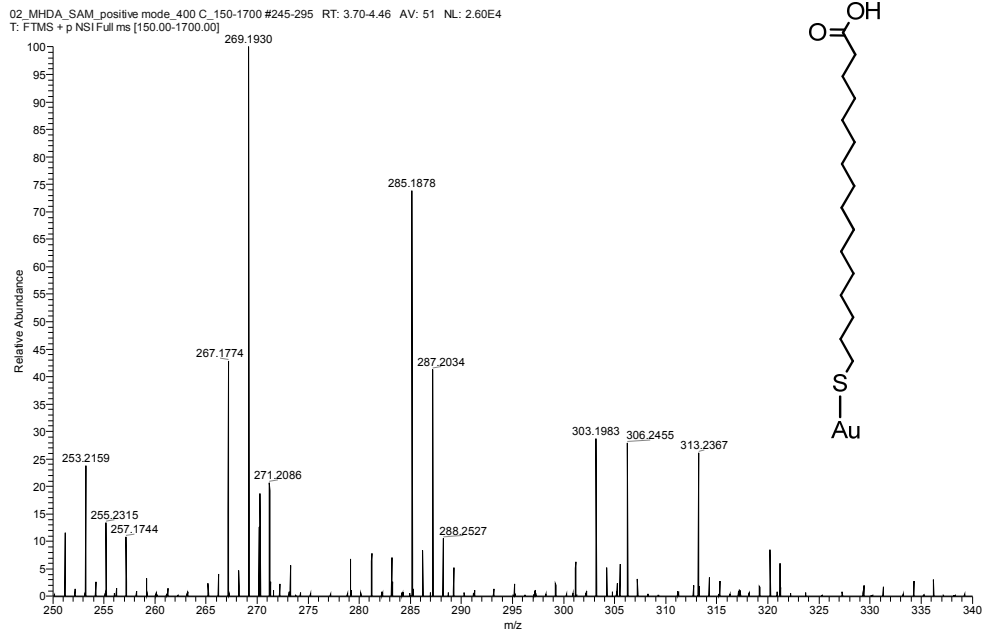
4 DART-HRMS of M_{Au}^1 in (+)-mode

Figure S4: DART-HRMS of M_{Au}^1 in (+)-mode from m/z 250 to m/z 340.

Characteristic ions for this monolayer are:

1. Ion at m/z 269.1930 (-0.8589 mDa) is $C_{16}H_{29}OS$
2. Ion at m/z 287.2034 (-1.0735 mDa) is $C_{16}H_{31}O_2S$
3. Ion at m/z 285.1878 (-0.9960 mDa) is $C_{16}H_{29}O_2S$
4. Ion at m/z 253.2159 (-0.3074 mDa) is $C_{16}H_{29}O_2$

(for details see Chapter 5).

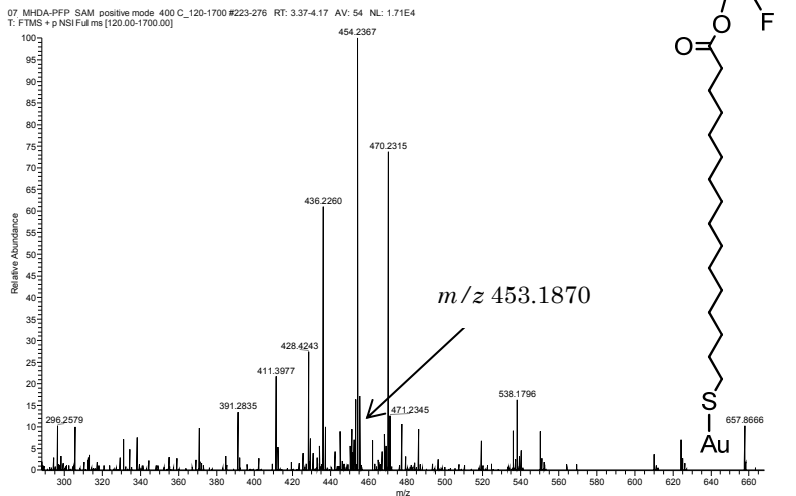
5 DART-HRMS of M_{Au}^2 in (+)-mode

Figure S5: DART-HRMS of M_{Au}^2 in (+)-mode from m/z 288 to m/z 667. Characteristic ion at m/z 453.1870 (-1.1221 mDa) for $[C_6F_5OC(=O)(CH_2)_{15}S]^+$, $(C_{22}H_{30}O_2F_5S)$.

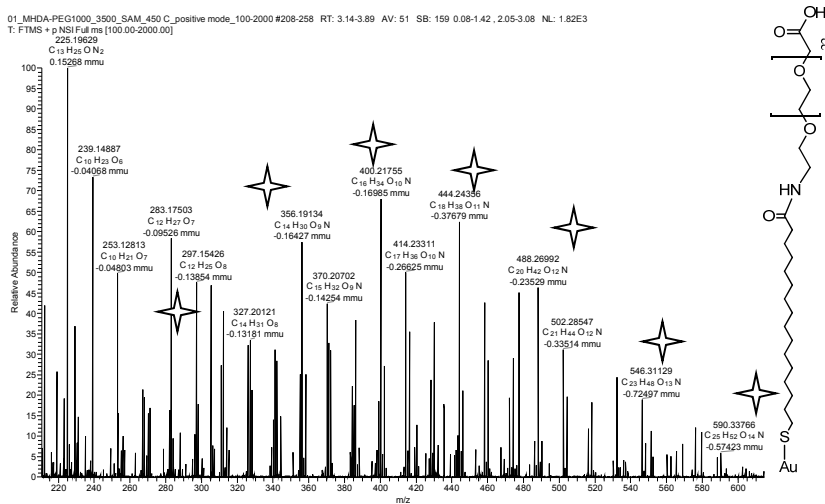
6 DART-HRMS of carboxymethyl-PEG coating M_{Au}^3 in (+)-mode

Figure S6: DART-HRMS of carboxymethyl-PEG coating M_{Au}^3 in (+)-mode from m/z 210 to m/z 615. Characteristic ions are labeled with 4-pointed stars and belong to the homologous series of ions with general formula $[HOOC-CH_2O(CH_2CH_2O)_nCH_2CHO + NH_4]^+$. For details see the main text.

7 DART-HRMS of oligo(ethylene glycol)-terminated monolayers in (+)-mode

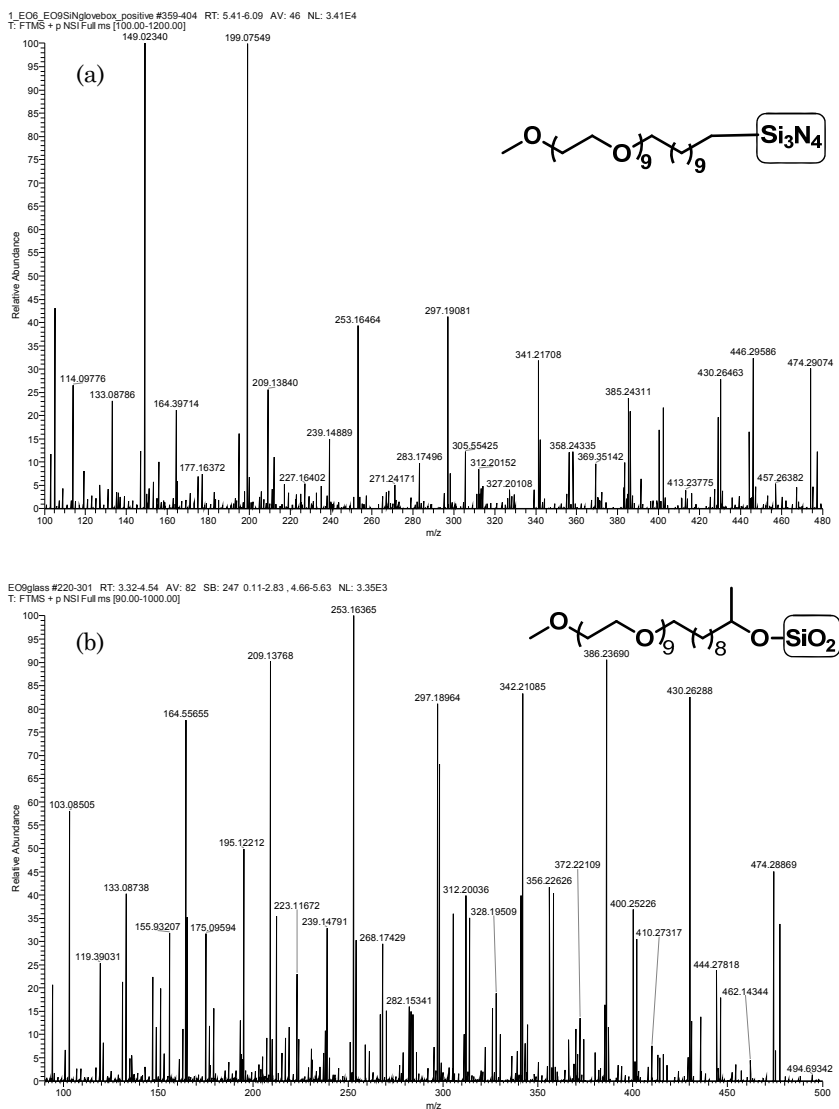


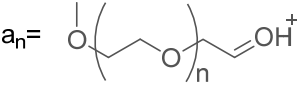
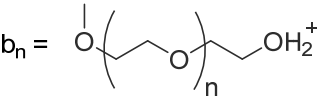
Figure S7: DART-HRMS of oligo(ethylene glycol)-terminated monolayers in (+)-mode:

(a) $M_{Si_3N_4}^{EO9}$ from m/z 100 to m/z 480 and (b) $M_{SiO_2}^{EO9}$ from m/z 90 to m/z 500.

Characteristic ions for these monolayers are described in Table S1.

Appendix 4

Table S1: Characteristic ions for monolayers $M_{Si_3N_4}^{EO9}$ and $M_{SiO_2}^{EO9}$

$a_n =$ 	from a_n series:
<hr/>	
m/z 163.0963, $C_7H_{15}O_4$ (-0.1842 mDa)	
m/z 207.1169, $C_9H_{19}O_5$ (-0.6915 mDa)	
m/z 251.1486, $C_{11}H_{23}O_6$ (0.2591 mDa)	
m/z 295.1748, $C_{13}H_{27}O_7$ (-0.2591 mDa)	
m/z 339.2011, $C_{15}H_{31}O_8$ (-0.1842 mDa)	
m/z 383.2272, $C_{17}H_{35}O_9$ (-0.3206 mDa)	
m/z 427.2535, $C_{19}H_{39}O_{10}$ (-0.2604 mDa)	
<hr/>	
$b_n =$ 	from b_n series
<hr/>	
m/z 165.1120, $C_5H_{17}O_4$ (-0.0543 mDa)	
m/z 209.1384, $C_9H_{21}O_5$ (0.0454 mDa)	
m/z 253.1646, $C_{11}H_{25}O_6$ (0.0614 mDa)	
m/z 297.1908, $C_{13}H_{29}O_7$ (0.0577 mDa)	
m/z 341.2170, $C_{15}H_{33}O_8$ (-0.0543 mDa)	
m/z 385.2431, $C_{17}H_{37}O_9$ (-0.1039 mDa)	
m/z 429.2693, $C_{19}H_{41}O_{10}$ (-0.074 mDa)	

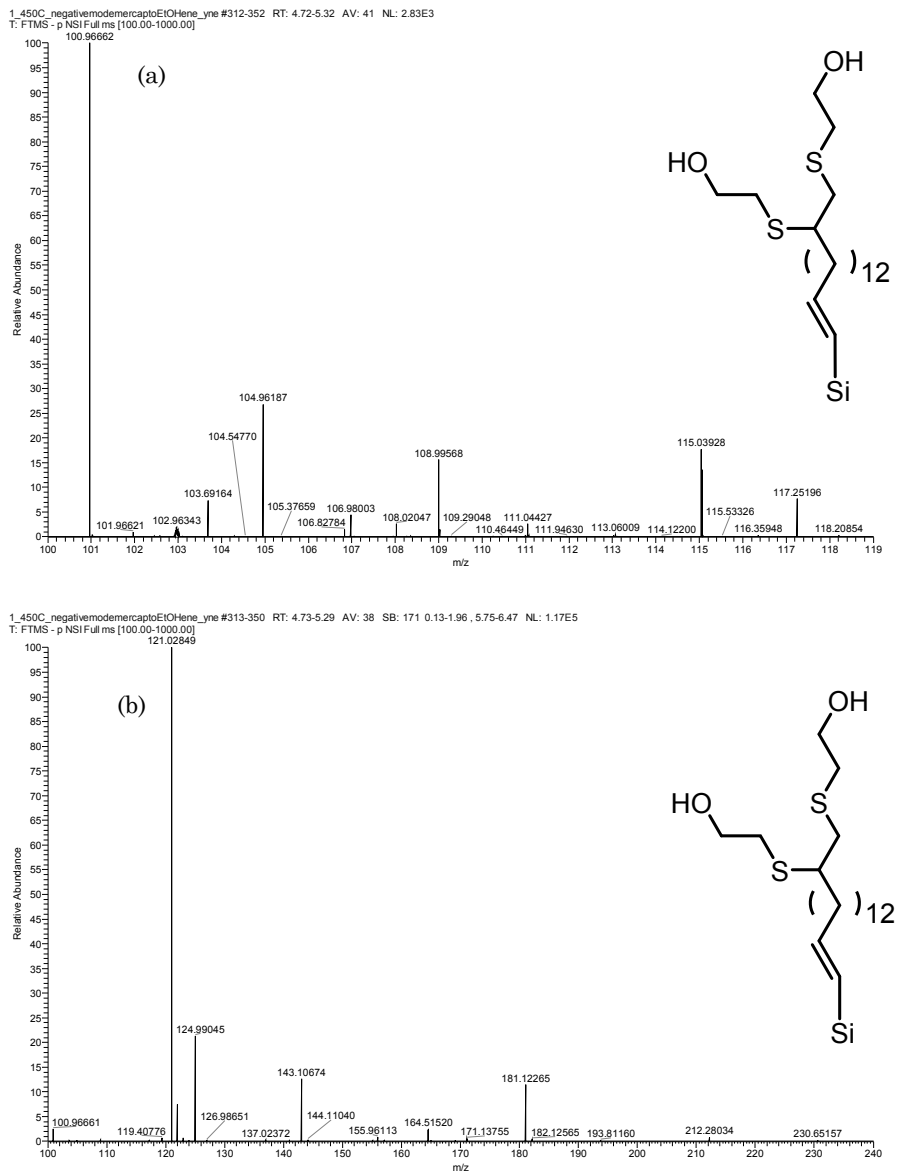
8 DART-HRMS of M_{Si}^2 in (-)-mode

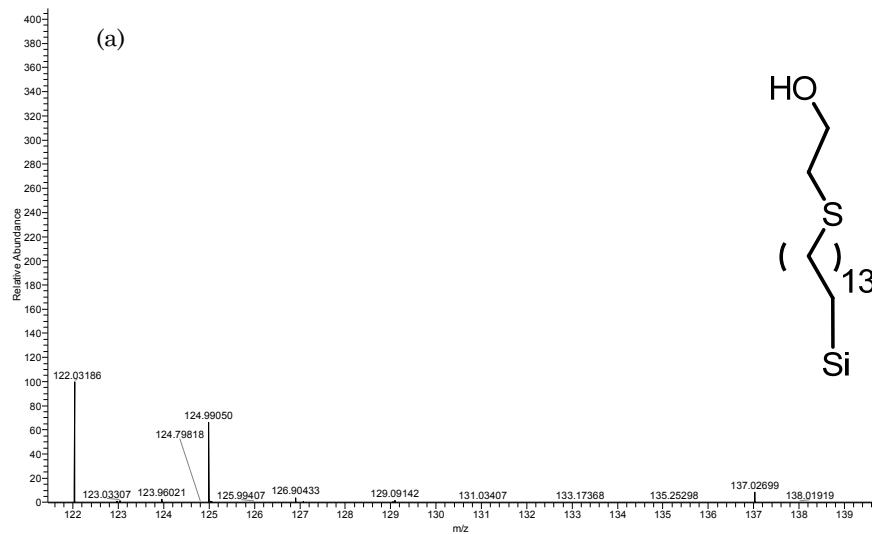
Figure S8: DART-HRMS of M_{Si}^2 in (-)-mode (a) from m/z 100.0 to m/z 119.0 and (b) from m/z 100 to m/z 240. Characteristic ions for this monolayer are:

m/z 124.9904 (-0.4086 mDa) for $[\text{HO}(\text{CH}_2)_2\text{SO}_3]^-$; ($\text{C}_2\text{H}_5\text{O}_4\text{S}$)

m/z 108.9956 (-0.2550 mDa) for $[\text{HO}(\text{CH}_2)_2\text{SO}_2]^-$; ($\text{C}_2\text{H}_3\text{O}_3\text{S}$)

9 DART-HRMS of M_{Si}^5 in (-)-mode

1_450C_negativeodemercaptoEtOHene_yne#208-250 RT: 3.15-3.78 AV: 43 SB: 171 0.13-1.96 , 5.75-6.47 NL: 5.79E3
T: FTMS - p NSI Full ms [100.00-1000.00]



1_450C_negativeodemercaptoEtOHene_yne#202-248 RT: 3.06-3.75 AV: 47 NL: 6.82E2
T: FTMS - p NSI Full ms [100.00-1000.00]

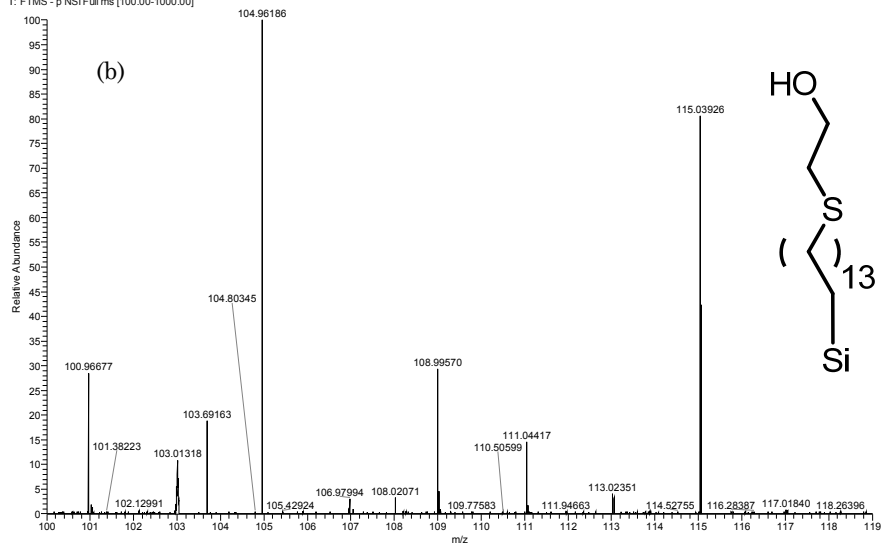


Figure S9: DART-HRMS of M_{Si}^5 in (-)-mode (a) from m/z 121 to m/z 140 a and (b) from m/z 100.0 to m/z 119.0. Characteristic ions for these monolayers are:

m/z 124.9905 (-0.3524 mDa) for $[\text{HO}(\text{CH}_2)_2\text{SO}_3]^-$; $(\text{C}_2\text{H}_5\text{O}_4\text{S})$

m/z 108.9957 (-0.2530 mDa) for $[\text{HO}(\text{CH}_2)_2\text{SO}_2]^-$; $(\text{C}_2\text{H}_3\text{O}_3\text{S})$

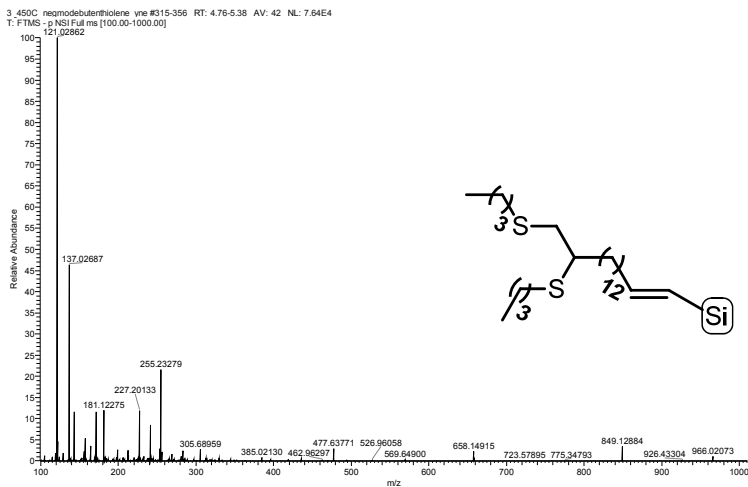
10 DART-HRMS of M_{Si}^3 in (-)-mode

Figure S10: DART-HRMS of M_{Si}^3 in (-)-mode from m/z 100 to m/z 1000.

A characteristic ion for these monolayers is:

m/z 137.0268 (-0.3687 mDa) for $[\text{CH}_3(\text{CH}_2)_3\text{SO}_3]^-$; $(\text{C}_4\text{H}_9\text{O}_3\text{S})$

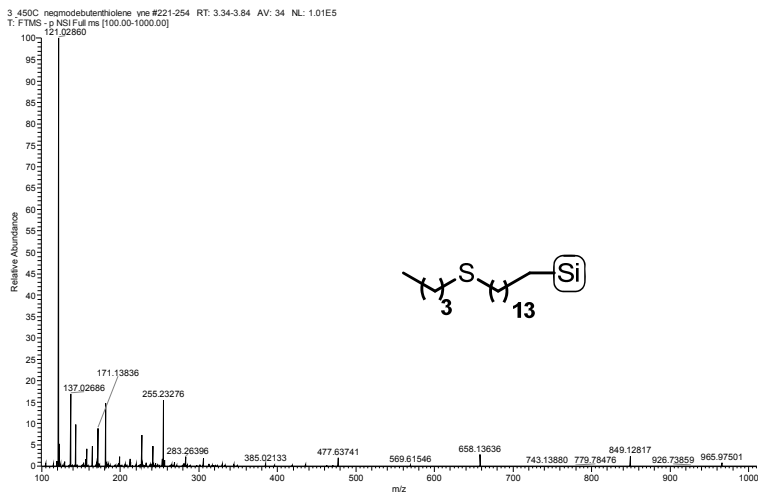
11 DART-HRMS of M_{Si}^6 in (-)-mode

Figure S11: DART-HRMS of M_{Si}^6 in (-)-mode from m/z 100 to m/z 1000.

A characteristic ion for these monolayers is: m/z 137.0268 (-0.3687 mDa) for $[\text{CH}_3(\text{CH}_2)_3\text{SO}_3]^-$; $(\text{C}_4\text{H}_9\text{O}_3\text{S})$

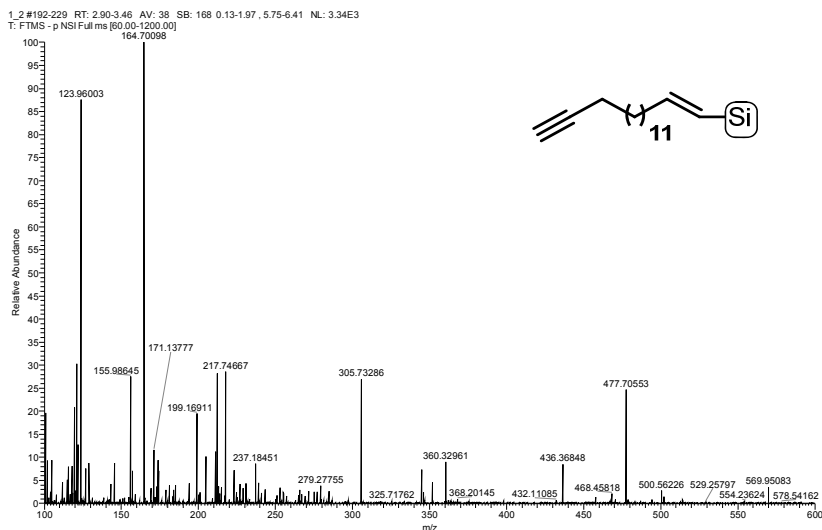
12 DART-HRMS of M_{Si}^1 in (-)-mode

Figure S12: DART-HRMS of M_{Si}^1 in (-)-mode from m/z 100 to m/z 600. For this monolayer no characteristic ions were found.

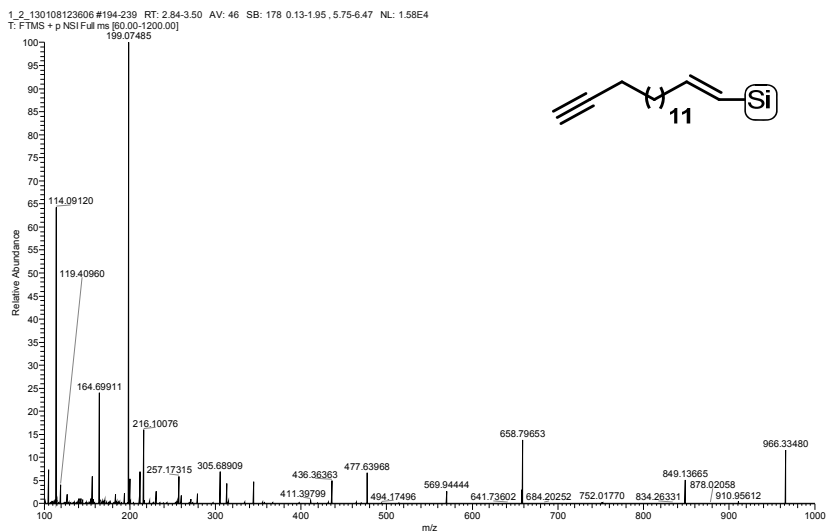
13 DART-HRMS of M_{Si}^1 in (+)-mode

Figure S13: DART-HRMS of M_{Si}^1 in (+)-mode from m/z 100 to m/z 1000. For this monolayer no characteristic ions were found.

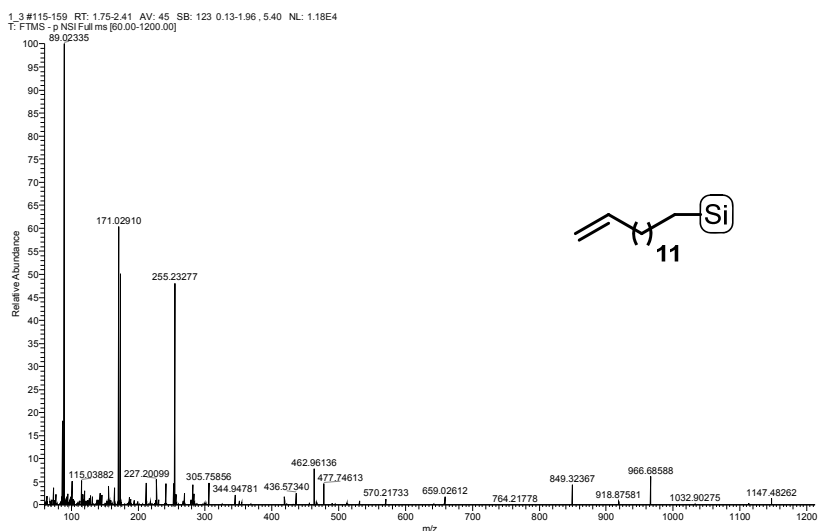
14 DART-HRMS of M_{Si}^4 in (-)-mode

Figure S14: DART-HRMS of M_{Si}^4 in (-)-mode from m/z 60 to m/z 1200. For this monolayer no characteristic ions were found.

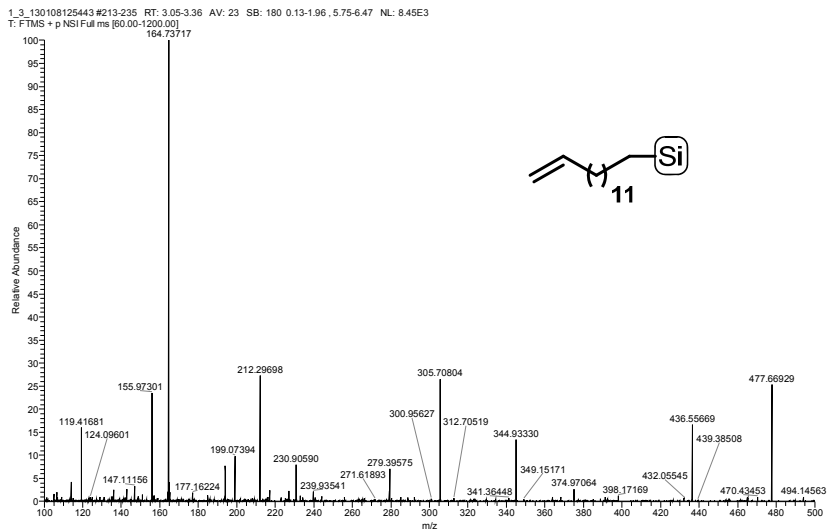
15 DART-HRMS of M_{Si}^4 in (+)-mode

Figure S15: DART-HRMS of M_{Si}^4 in (+)-mode from m/z 100 to m/z 500
For this monolayer no characteristic ions were found.

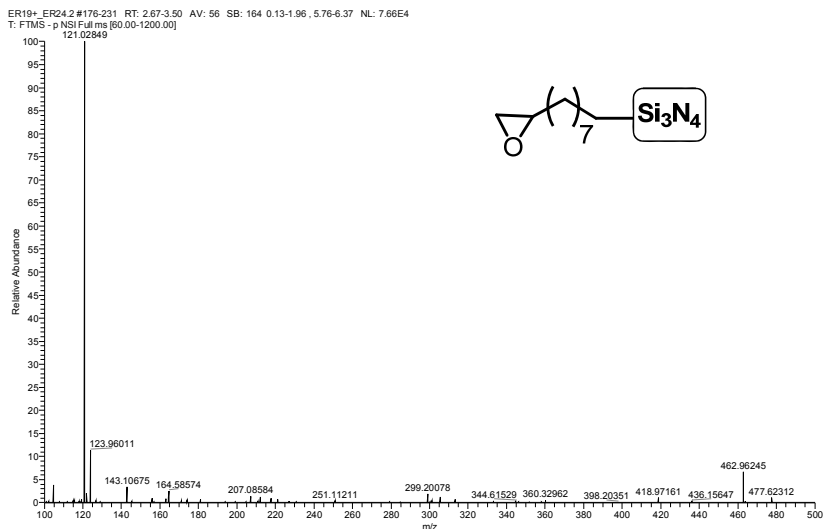
16 DART-HRMS of $M_{Si_3N_4}^1$ in (-)-mode

Figure S16: DART-HRMS of $M_{Si_3N_4}^1$ in (-)-mode from m/z 100 to m/z 500. For this monolayer no characteristic ions were found.

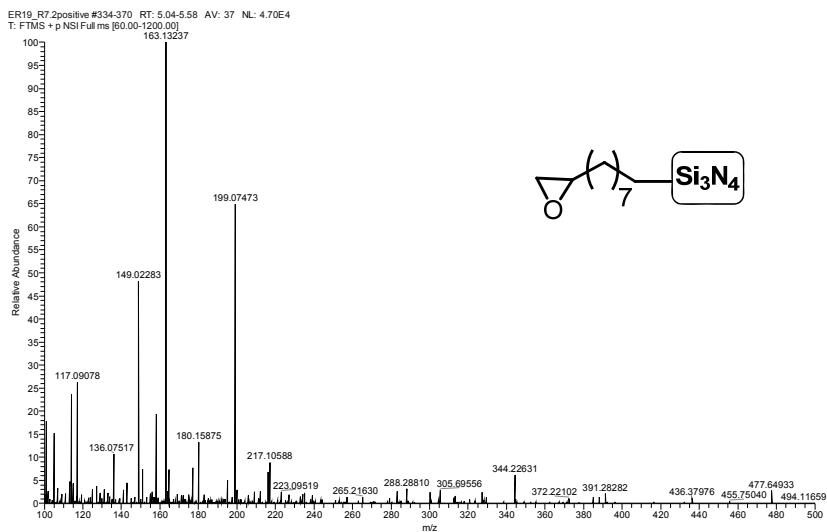
17 DART-HRMS of $M_{Si_3N_4}^1$ in (+)-mode

Figure S17: DART-HRMS of $M_{Si_3N_4}^1$ in (+)-mode from m/z 100 to m/z 500. For this monolayer no characteristic ions were found.

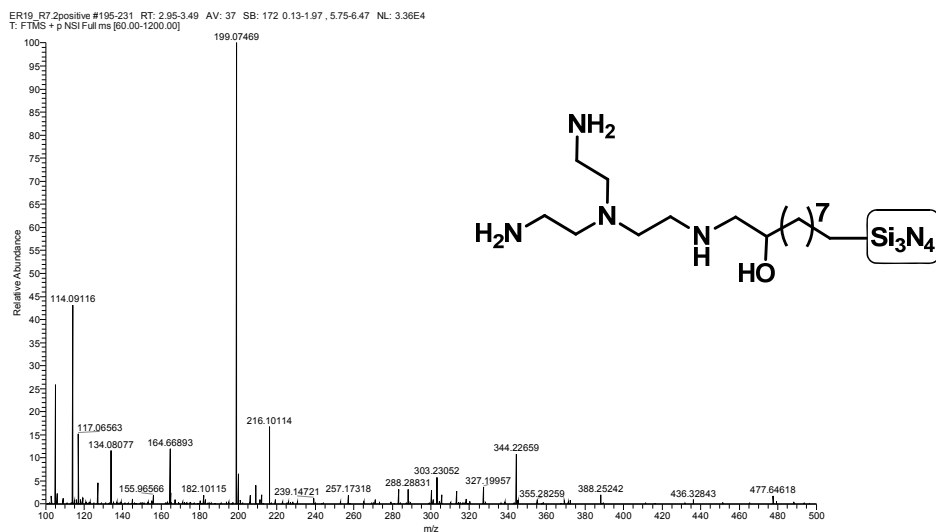
18 DART-HRMS of $M_{Si_3N_4}^2$ in (+)-mode

Figure S18: DART-HRMS of $M_{Si_3N_4}^2$ in (+)-mode from m/z 100 to m/z 500. For this monolayer no characteristic ions were found.

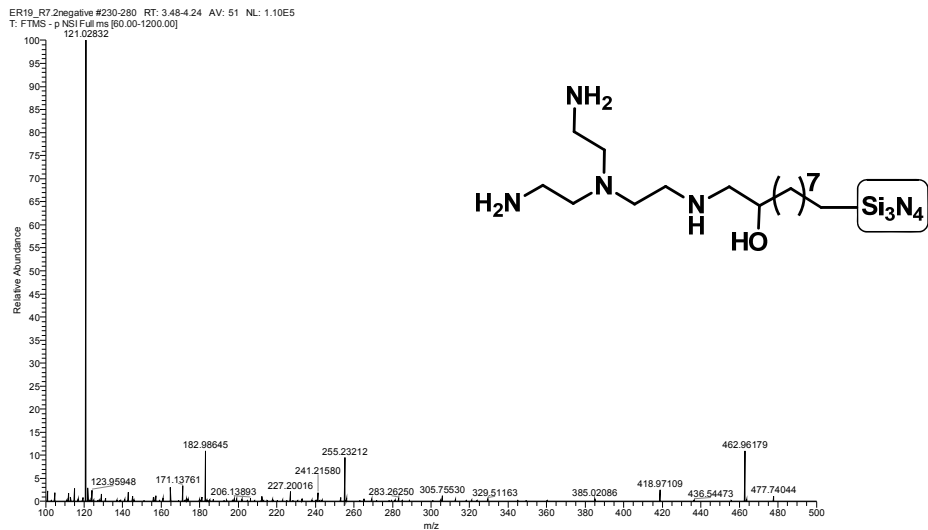
19 DART-HRMS of $M_{Si_3N_4}^2$ in (-)-mode

Figure S19: DART-HRMS of $M_{Si_3N_4}^2$ in (-)-mode from m/z 100 to m/z 500. For this monolayer no characteristic ions were found.

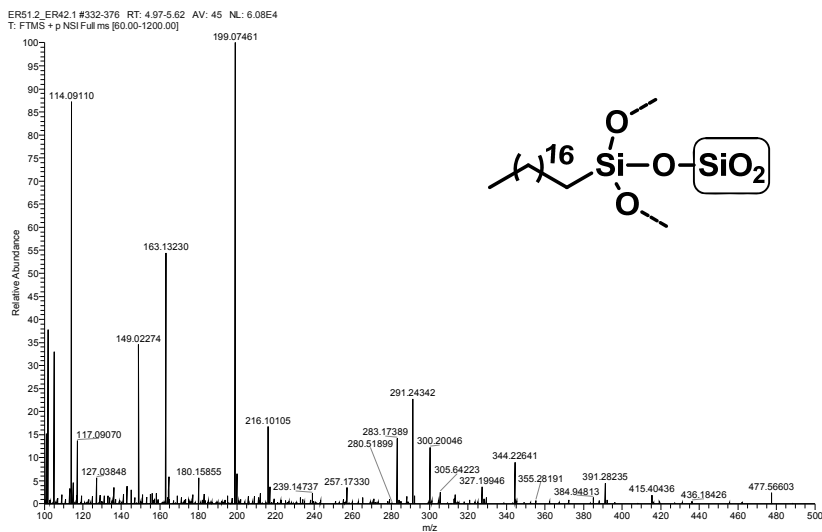
20 DART-HRMS of $M_{SiO_2}^1$ in (+)-mode

Figure S20: DART-HRMS of $M_{SiO_2}^1$ in (+)-mode from m/z 100 to m/z 500. For this monolayer no characteristic ions were found.

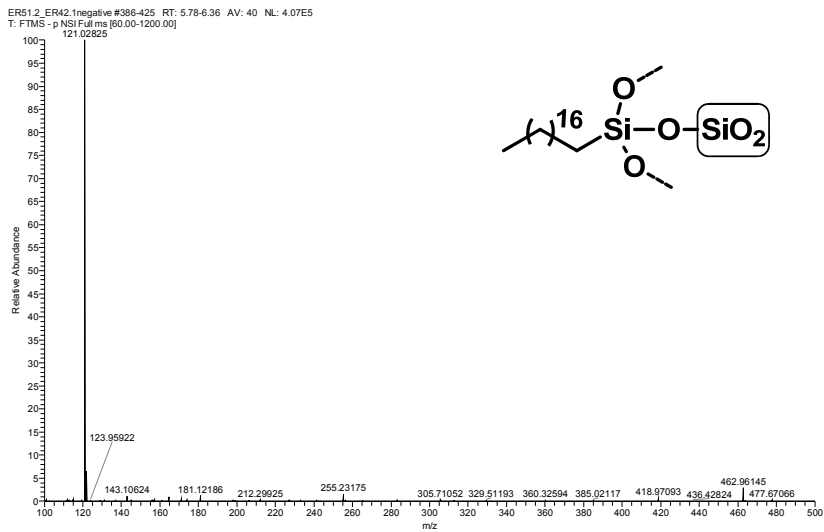
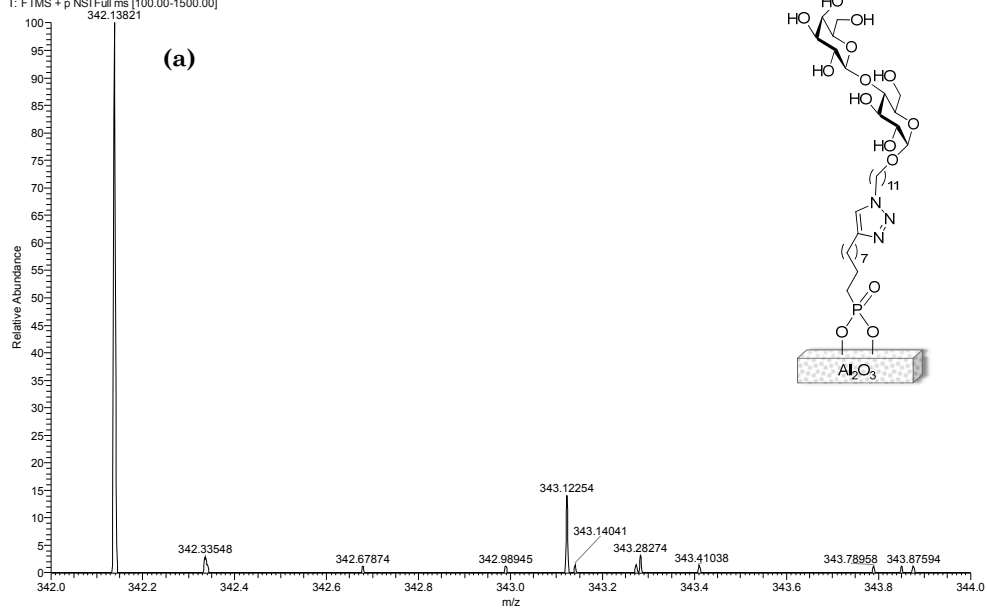
21 DART-HRMS of $M_{SiO_2}^1$ in (-)-mode

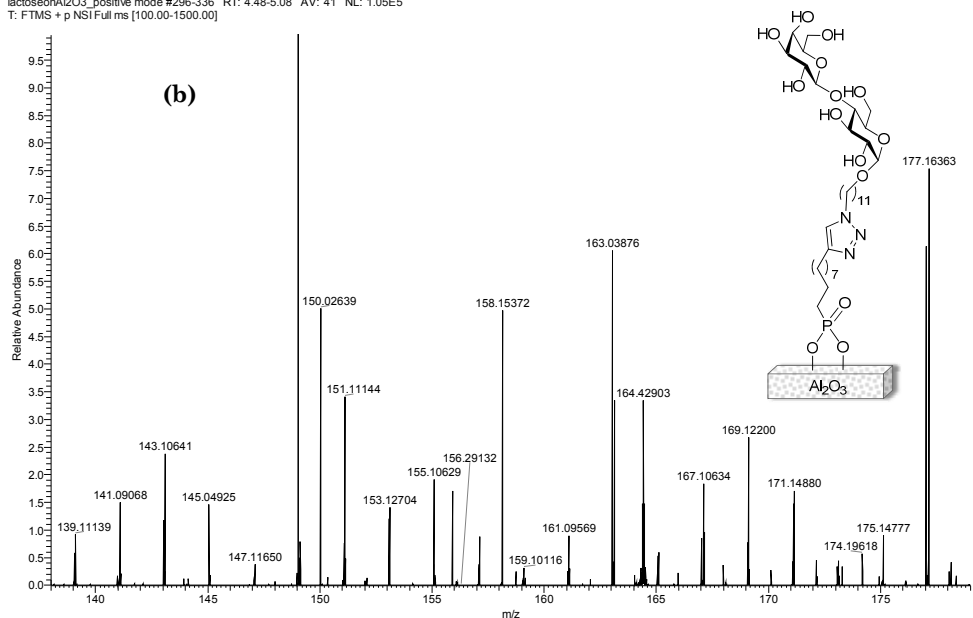
Figure S21: DART-HRMS of $M_{SiO_2}^1$ in (-)-mode from m/z 100 to m/z 500. For this monolayer no characteristic ions were found.

22 DART-HRMS of $M_{Al_2O_3}^{lac}$ in (+)-mode

lactoseonAl2O3_positive mode #298-333 RT: 4.51-5.04 AV: 36 NL: 3.55E2
T: FTMS + p NSIFull ms [100.00-1500.00]



lactoseonAl2O3_positive mode #296-336 RT: 4.48-5.08 AV: 41 NL: 1.05E5
T: FTMS + p NSIFull ms [100.00-1500.00]



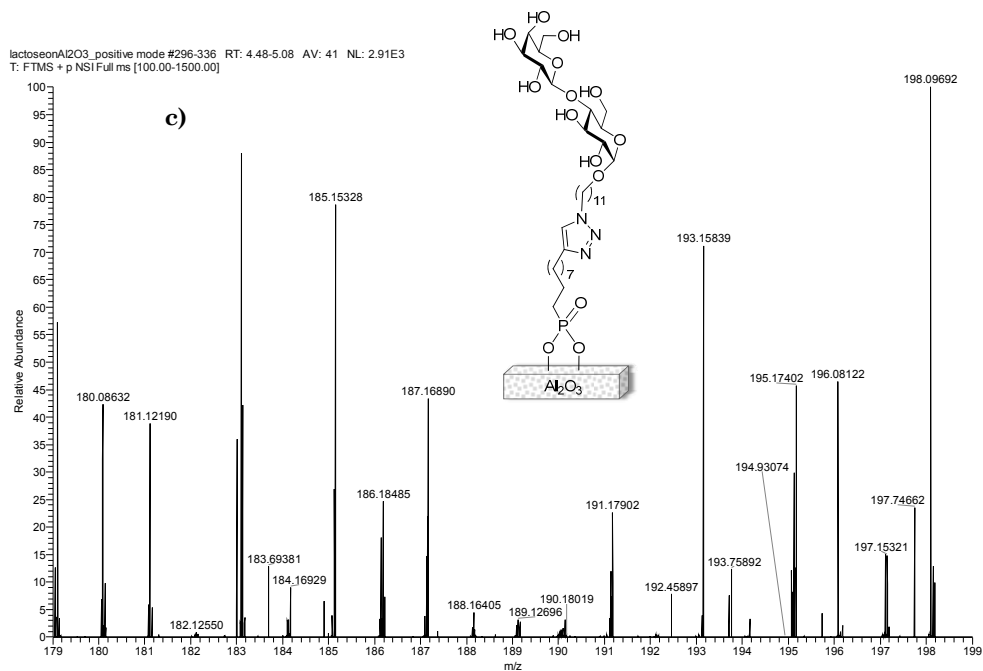


Figure S22: DART-HRMS of $M_{Al_2O_3}^{lac}$ in (+)-mode (a) from m/z 342.0 to m/z 344.0. (b) from m/z 138.0 to m/z 179.0 and (c) from m/z 179.0 to m/z 199.0.

Characteristic ions for this monolayer are:

m/z 198.0978 (−0.8457 mDa) for $[C_6H_{12}O_6 + NH_4]^+$; $C_6H_{16}O_6N$

m/z 180.0863 (−0.8814 mDa) for $[C_6H_{12}O_6 + NH_4 - H_2O]^+$; $C_6H_{14}O_5N$

m/z at 163.0597 (−0.8630 mDa) for $[C_6H_{12}O_6 + NH_4 - H_2O - NH_3]^+$; $C_6H_{11}O_5$

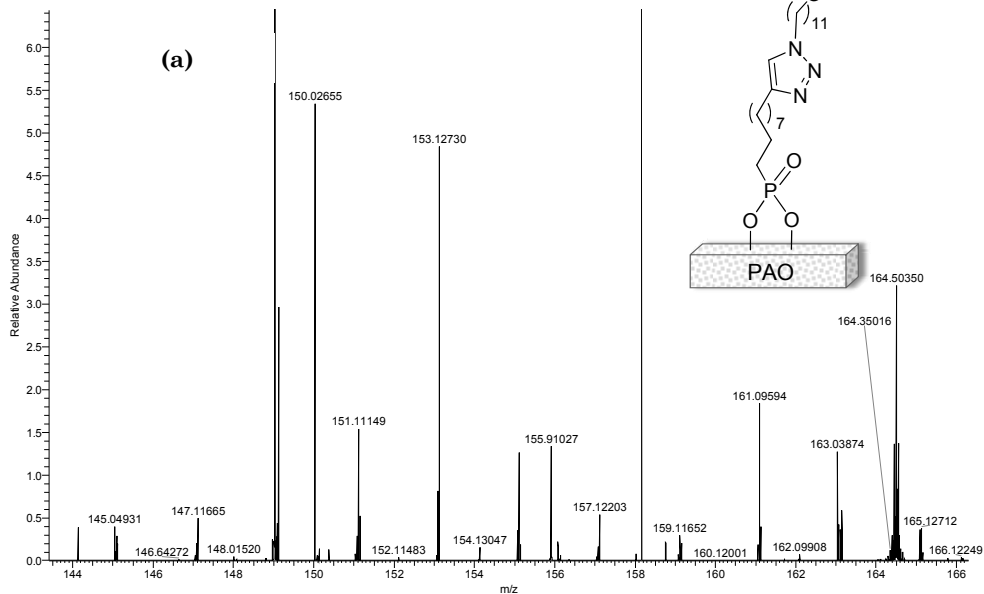
m/z at 145.0492 (−0.8321 mDa) for $[C_6H_{12}O_6 + NH_4 - 2H_2O - NH_3]^+$; $C_6H_9O_4$

m/z at 343.1225 (−1.4983 mDa) for $[C_{12}H_{22}O_{11} + NH_4 - NH_3]^+$; $C_{12}H_{23}O_{11}$

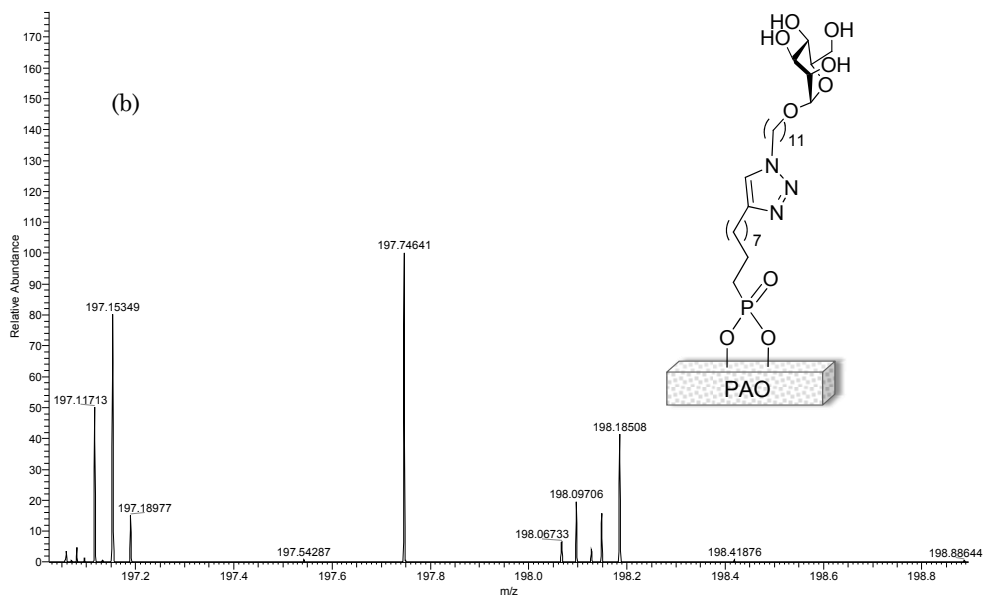
m/z at 342.1382 (−1.8065 mDa) for $[C_{12}H_{22}O_{11} + NH_4 - H_2O]^+$; $C_{12}H_{24}O_{10}N$

23 DART-HRMS of $M_{Al_2O_3}^{man}$ in (+) mode

positivmannose #279-329 RT: 4.22-4.98 AV: 51 NL: 1.32E5
T: FTMS + p NSI Full ms [100.00-1500.00]



positivmannose #296-336 RT: 4.48-5.08 AV: 41 NL: 7.44E2
T: FTMS + p NSI Full ms [100.00-1500.00]



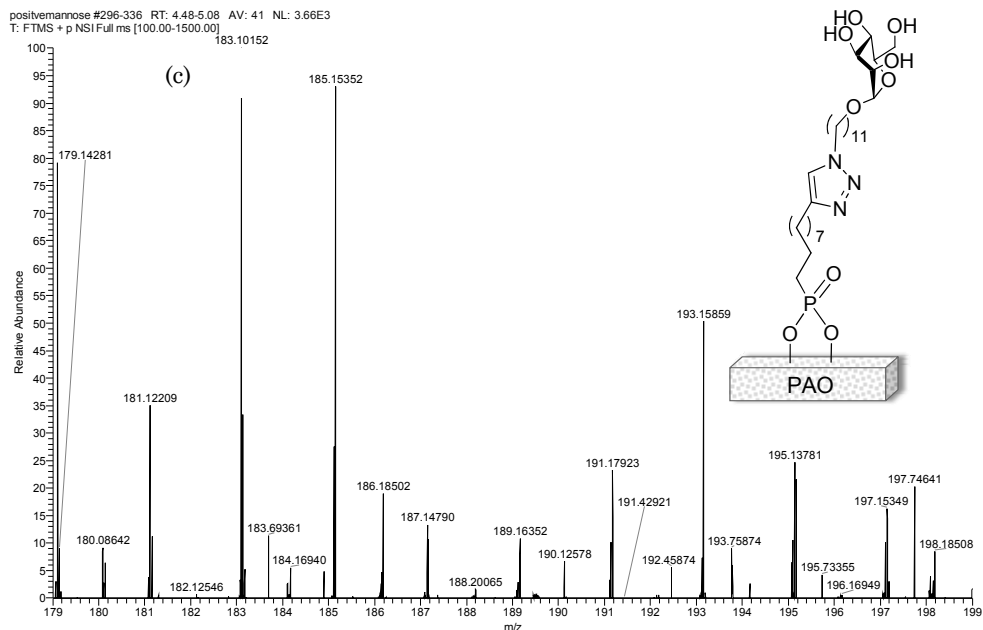


Figure S23: DART-HRMS of $M_{Al_2O_3}^{man}$ in (+) mode (a) from m/z 143 to m/z 166. (b) from m/z 197.0 to m/z 199.0 and (c) from m/z m/z 179.0 to m/z 199.0.

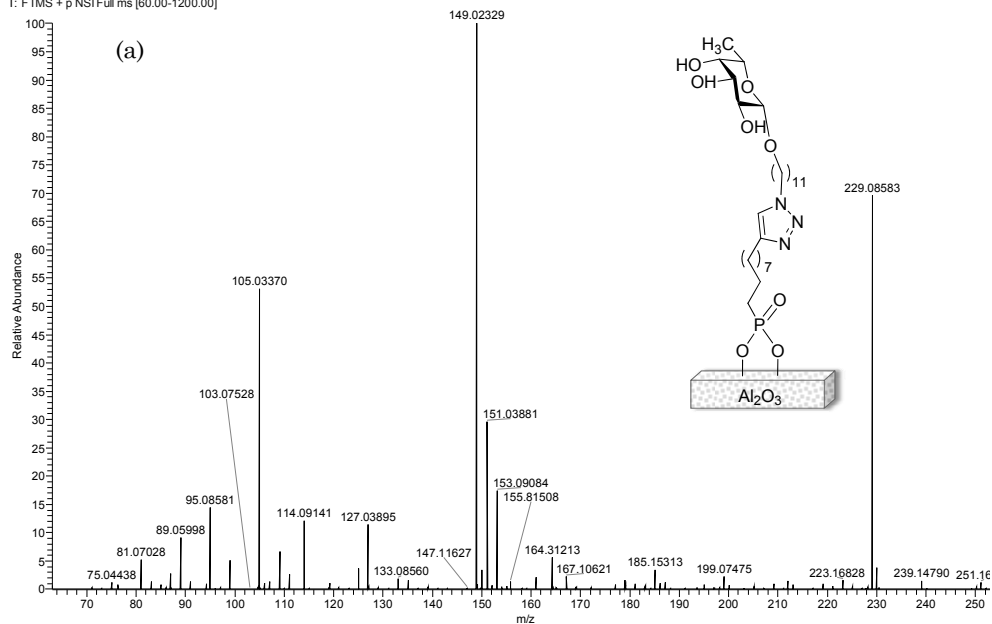
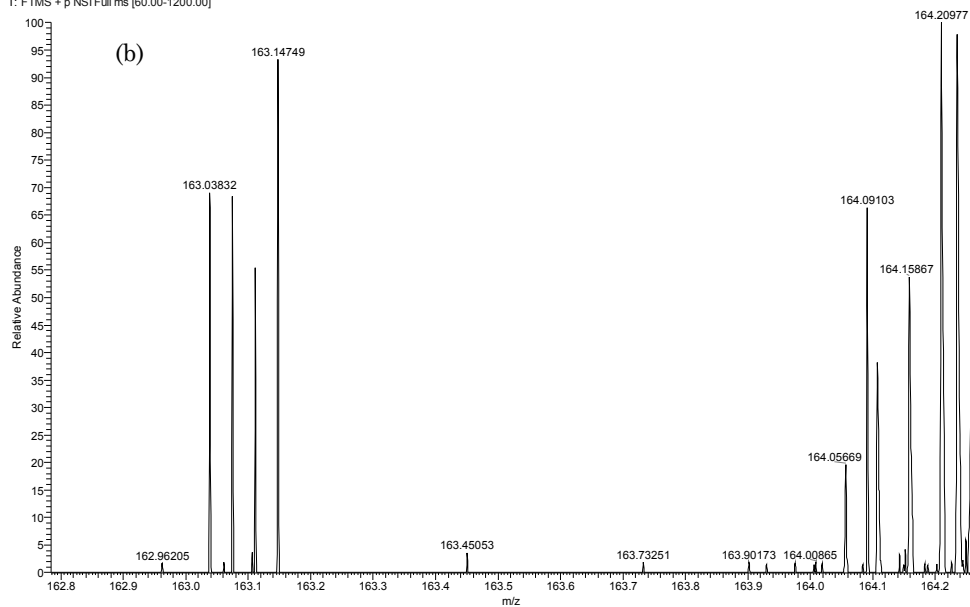
Characteristic ions for this monolayer are:

m/z 198.0970 (-0.7048 mDa) for of $[C_6H_{12}O_6 + NH_4]^+$; $C_6H_{16}O_6N$

m/z 180.0864 (-0.7744 mDa) for $[C_6H_{12}O_6 + NH_4 - H_2O]^+$; $C_6H_{14}O_5N$

m/z at 163.0597 (-0.8630 mDa) for $[C_6H_{12}O_6 + NH_4 - H_2O - NH_3]^+$; $C_6H_{11}O_5$

m/z at 145.0493 (-0.8321 mDa) for $[C_6H_{12}O_6 + NH_4 - 2H_2O - NH_3]^+$; $C_6H_9O_4$

24 DART-HRMS of $M^{fuc}_{Al_2O_3}$ in (+) modeFICOSE&ALKYNEPOSITIVE #213-246 RT: 3.23-3.72 AV: 34 SB: 436 0.16-3.05 , 4.12-7.79 NL: 7.18E4
T: FTMS + p NSI Full ms [60.00-1200.00]FICOSE&ALKYNEPOSITIVE #211-248 RT: 3.20-3.75 AV: 38 NL: 2.28E2
T: FTMS + p NSI Full ms [60.00-1200.00]

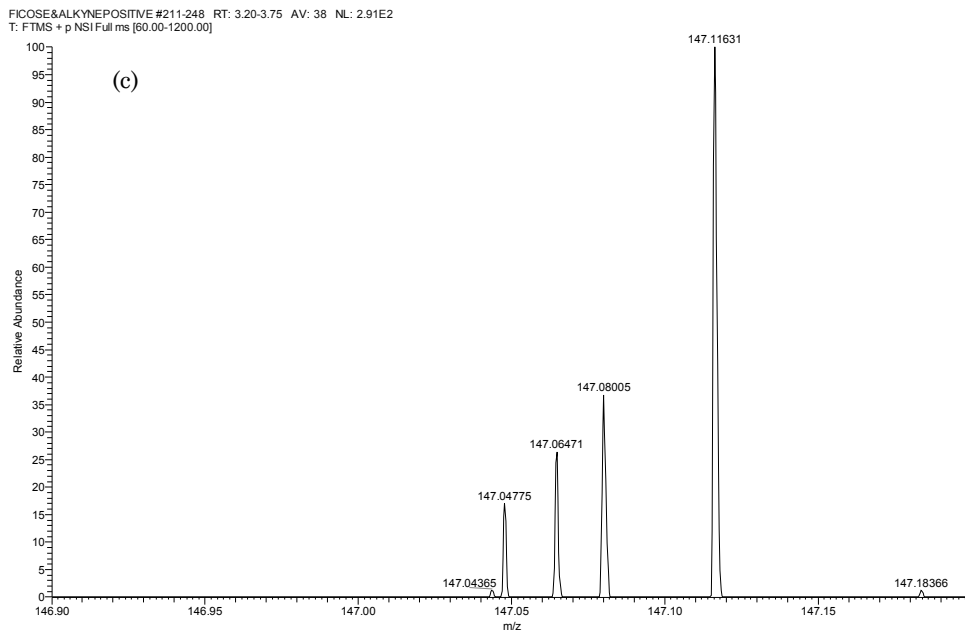


Figure S24: DART-HRMS of $M_{Al_2O_3}^{fuc}$ in (+) mode from (a) m/z 63 to m/z 253. (b) from m/z 162.8 to m/z 164.2 and (c) from m/z m/z 146.9 to m/z 147.2.

Characteristic ions for this monolayer are:

m/z at 164.0910 (−1.2479 mDa) for of $[C_6H_{12}O_5 + NH_4 - H_2O]^+$; $C_6H_{14}O_4N$

m/z at 147.0647 (−1.0874 mDa) for $[C_6H_{12}O_5 + NH_4 - 2H_2O - NH_3]^+$; $C_6H_{11}O_4$

Summary

From the overview given in **Chapter 1**, it follows that a Si_3N_4 – based sensor has the potential to be used in point-of-care tests or – in a clinical setting – as a biosensor with a broad application. In order to achieve this goal, attachment of monolayers bearing ligand molecules is necessary. Additionally, a good characterization of the resulting monolayers is a *sine qua non* for proper quality control.

Chapter 2 deals with strain-promoted Cu-free click reactions (SPAAC) and their role in surface modification. In the chapter current applications of these reactions are discussed, which forms the incentive of this thesis to explore them as attachment reaction for a new biosensor.

Chapter 3 experimentally explores the potential of these reactions for the attachment of biomolecules onto the surface while preserving their biological function. Additionally, the chapter proposes a surface modification method for Si_3N_4 – based sensors. Following this approach, a surface coating can be customized with desirable functional groups, and by the use of SPAAC reactions ligand molecules can be tethered on the surface in order to screen biomolecular interactions. In addition, an analytical approach with X-ray photoelectron spectroscopy was established for characterization of surface-bound reactions and their products.

Although that is sufficient to characterize the monolayers prepared in this work, the development of a novel analytical method that can support our findings with molecular information derived from these ultra-thin layers was pursued. The tool, consisting of a Direct Analysis in Real Time (DART) ion source combined with a high-resolution mass spectrometer (DART-HRMS), is described in **Chapter 4**. Two types of monolayers, e.g., ester- and amide-terminated layers were investigated with DART-HRMS.

Chapter 5 expands the applications of DART-HRMS for the analysis and characterization of different monolayers grafted on a variety of substrates. The study deepens the understanding how monolayers fragment upon DART analysis, and formulates general interpretation rules for identification of monolayers. The studied monolayers are widely used in engineered surfaces and coatings for biosensor platforms and bioassays.

The final **Chapter 6** discusses the major findings of this work giving further perspectives and potential applications.

Samenvatting

Uit een literatuuroverzicht gegeven in **Hoofdstuk 1** volgt dat er goede perspectieven zijn om sensoren gebaseerd op silicium nitride (Si_3N_4) te gebruiken in point-of-care testen of – in een meer klinische omgeving – als breed toepasbare biosensoren. Om dit mogelijk te maken dienen monolagen met daaraan vast specifieke biomoleculen op de sensor aangebracht te worden. Voor een goede kwaliteitscontrole van de sensor is een uitvoerige analyse van de aangebrachte monolaag een absolute vereiste.

Hoofdstuk 2 gaat in op kopervrije door ringspanning geactiveerde “klik”-reacties, ook wel SPAAC genoemd, en hun rol in de chemische modificatie van oppervlakken. De toepassingen van deze reacties worden samengevat en besproken hetgeen er mede toe geleid heeft dat deze “klik”-reacties daadwerkelijk toegepast zijn bij de modificatie van de sensoren in dit onderzoek.

In **Hoofdstuk 3** wordt de ontwikkeling van een reproduceerbare generieke methode voor de chemische modificatie van op Si_3N_4 gebaseerde sensoren beschreven. Deze methode maakt het mogelijk om verschillende geactiveerde functionele groepen in een goede opbrengst aan te brengen. Daarna kunnen door middel van de eerder beschreven “klik”-reacties, diverse soorten biomoleculen onder milde omstandigheden aangebracht worden. Deze sensoroppervlakken kunnen dan gebruikt worden om biomoleculaire interacties aan te tonen. Voor het volgen van de diverse oppervlaktereacties en hun producten is een methode gebaseerd op X-ray fotoelectron spectroscopie (XPS) ontwikkeld.

Hoewel de diverse monolagen goed met XPS gekarakteriseerd konden worden, is in het kader van dit project toch een geheel nieuwe analyse methode ontwikkeld. Deze methode, zoals beschreven in **Hoofdstuk 4**, maakt het mogelijk om gedetailleerde complementaire moleculaire informatie te

verkrijgen van de uiterst dunne monolagen. De methode is gebaseerd op de “Direct Analysis in Real Time” (DART) techniek. Hierbij wordt op het gemodificeerde oppervlak een hete bundel van aangeslagen neutrale helium atomen gericht die vervolgens delen van de organische monolaag kunnen afsplitsen en ioniseren. De gevormde ionen kunnen geanalyseerd worden met hoge-resolutie massaspectrometrie (HRMS). Dit bleek goed te werken voor ester- en amide-getermineerde monolagen.

Hoofdstuk 5 gaat dieper in op de nieuwe DART-HRMS oppervlakte-analyse techniek. Om een beter beeld te krijgen van de (on)mogelijkheden werd een groot scala van organische monolagen op verschillende substraten gesynthetiseerd en onderzocht. Diverse van deze monolagen worden commercieel toegepast in coatings, biosensoren en bioassays. Dit onderzoek leidde tot meer inzicht hoe de monolagen fragmenteren zodat het uiteindelijk mogelijk bleek een set van algemene regels te formuleren die kunnen helpen bij toekomstige analyses van organische monolagen met behulp van DART-HRMS.

Hoofdstuk 6 tenslotte integreert de resultaten van de eerdere hoofdstukken en schetst een perspectief voor mogelijke toekomstige toepassingen.

Acknowledgment

The four-year journey of this work would not have been possible without many passers-by, friends and fellow travelers. All of them, in one or another way, contributed to and fed my research. And I am glad to have this opportunity to express my appreciation and gratitude to them.

“The journey of a thousand miles begins with one step.” And this step was made with my former manager and supervisor associate professor Rositsa Mladenova. Thank you, Rossi, for your kind support; the work with you on mycotoxins analysis was an incentive to pursue a second master degree in Chemistry, followed by a PhD in Chemistry. Without you the transition from Biotechnology to Chemistry would not have been achievable.

Another person without whom this thesis would not have existed is my co-promoter. Teris, first of all, thank you for giving me the opportunity to complete this research work under your supervision. I will never forget our first dinner after the final job interview at ORC. You were concerned about my family situation. The warm hospitality at social gatherings in your house, the dinners and Jeux de boules contests are some of the most memorable moments during my stay in the Netherlands. Thank you for your valuable suggestions, your unflagging optimism, guidance and assistance. I am honored to have found in you a good teacher, who not only inspired but also supported me in difficult situations, like one said “What the teacher is, is more important than what he teaches.”

I would like to express my gratitude to my promoter Prof. Dr. Han Zuilhof. Thank you for accepting me in the Laboratory of Organic Chemistry. Besides your guidance and support, you always offered me challenging tasks that stimulated me to evolve into an independent researcher.

Acknowledgment

Frank, it was a great pleasure to work with you. I enjoyed not only our scientific discussions but also all our short breaks in which you shared your experience in parenting. With an infinite patience, you answered all my questions such as: “How to select the best day-care for your child in Wageningen?”, “How to select a good school for your child in Wageningen?”, “How to organize a birthday for your child, preferably not in Wageningen?”, and etc. You are my survival guide in Wageningen. And of course, my biggest success in this research project was achieved together with you. During the DART-MS analysis of flat surfaces, you were standing next to me, supporting and encouraging me, when I was initially frightened to waste my precious specimens and to damage the monolayer under the plasma. We cherished those moments when we found exciting and surprising results.

I am grateful to all my co-authors - Aline, Sweccha, Nagendra and Carel for willing to work together and for your trust in me. No matter how busy you were with your own research projects, you were right on time to supply me with specimens and experimental data. With you, I experienced how gratifying collaboration can be.

I wish to thank other few former colleagues at the Laboratory of Organic Chemistry: Dr. Mabel Campos, Dr. Jos Paulusse, and Umesh for their support, encouragement, and warm friendship. Umesh, you are an example of patience and persistence, an unbeatable combination for success.

I send my appreciation to my office roommates - Tuha, Jacinthe, Alexandre, Wilco, Sweccha, Florine, to other colleagues - Satish, Sourav, Willem, Jacob, Ai, Jaime, Bas, Elbert, Anke, Elly, Aleida, Tom Wennekes, and to all staff at ORC.

I wish to express my gratitude to my dear friends Sonja and Serge, who took care of Angie and supported me through the years. Thank you for being compassionate, for being a huge support, and most of all for being YOU.

I wish to thank my dear friend Sidharam who showed me that fun and academic work can go hand in hand. Although, we worked on different projects, we teamed up for a research paper. We also shared our struggles to finish our dissertations on time. Sidhu, your defense was about a year ago and your

support was of great help for me at this last stage. Additionally, you are the best friend of my son, Angie. The three of us, we had a wonderful time together. We often worked on the weekends; we took turns in looking after Angie, while taking care of surface chemistry reactions, storage of the specimens, etc. Finally, Angie grew up surrounded by hardworking students, and this is where a good role model steps in a child's life. At the age of 4, Angie was able to handle and fix our specimens on the XPS sample stage holder!

I wish to thank my mother for her unwavering support and her courage to move to the Netherlands for taking care of my son during the first two years of my PhD. Благодаря ти, майко, за обичта и помощта!

Thank you, Angie, for your deep love, patience, and will to help me in everything.

About the author

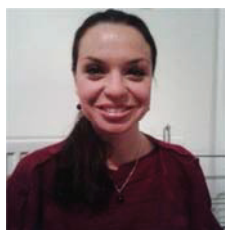


Curriculum vitae

List of Publications

Completed training activities

About the author



Radostina Koleva Manova was born on the 4th of May, 1978 in Varna, Bulgaria. She studied MSc in Biotechnology at Sofia University, Bulgaria. As part of her MSc, she carried out a research project of six months at Biosystems and Process Engineering Laboratory, INSA, Toulouse, France. In this project, she worked on food natural colorant obtainable by fermentation of fungus culture and elimination of toxic co-products e.g. mycotoxins. She finished her MSc study successfully in 2002 and soon afterwards she started working in the Laboratory of Toxicology at the Plant Protection Institute, Bulgaria. There, she developed methods for the analysis of *Fusarium* mycotoxins, and she simultaneously completed her second MSc degree in Chemistry. During her MSc in Chemistry, she completed an internship of 6 months at IFA - Tulln, Austria, and worked in a private research company, Biopure GmbH. As part of this internship, she carried out a research project on the synthesis of mycotoxin-conjugates and analysis of mycotoxins in agricultural commodities. After completing her MSc study in Chemistry, she began her PhD under the supervision of Teris van Beek and Han Zuilhof, at the Laboratory of Organic Chemistry, Wageningen University. The results of her PhD are presented and described in this thesis. Currently, Radostina Manova works as a scientist, Research and Development, at the Netherlands Food and Consumer Product Safety Authority.

List of publications

1. Manova, R. K.; and Mladenova, R. *Food Control*. **2009**, *20*, 362-365.
2. Manova, R. K.; van Beek, T. A.; and Zuilhof, H. *Angew. Chem. Int. Ed.* **2011**, *50*, 5428-5430.
3. Manova, R. K.; Pujari S. P.; Weijers, C. A. G. M.; Zuilhof, H.; and van Beek, T. A. *Langmuir*. **2012**, *28*, 8651-8663.
4. Manova, R. K.; Claassen, F. W.; Nielen, M. W. F.; Zuilhof, H.; and van Beek, T. A. Ambient Mass Spectrometry of Covalently Bound Organic Monolayers. *Chem. Commun.* **2013**, *49*, 922-924.
5. Manova, R. K.; Joshi, S.; Debrassi, A.; Bhairamadgi, N. S.; Roeven, E.; Gagnon, J.; Tahir, M. N.; Claassen, F. W.; Scheres, L. M. W.; Wennekes, T.; Schroën, K.; van Beek, T. A.; Zuilhof, H.; and Nielen, M. W. F. *Anal. Chem.* **2014**, *86*, 2403-2411.

Completed training activities

Discipline specific activities

Courses

- Advanced Organic Chemistry 1&2, Wageningen University, 2009-2011
- Advanced food analysis, VLAG, Wageningen University, 2010
- ANAC Separation Science, University of Amsterdam, 2012
- Advanced proteomics, VLAG, Wageningen University, 2013
- Microscopy and Spectroscopy in Food and Plant Sciences, VLAG, 2013

Conferences and Meetings

- Annual NWO Conference, Analytical Chemistry, Lunteren, 2009-2010
- Annual NWO Conference, Organic Chemistry, Lunteren, 2009-2010
- CHAINS (Chemistry as Innovating Science), Maarsen, 2011
- Advances in Biodetection and Biosensors, Hamburg, Germany, 2011
- Meeting of the NWO/CW & COAST, Analytical Chemistry, Lunteren, 2012
- Organic Chemistry Symposium, KNCV & NOW, Wageningen, 2013
- Thermo Fischer Scientific, User meeting, 2013
- 7th Inter Symposium on hormone & veterinary drug residue analysis, Ghent, Belgium, 2014

General courses

- Techniques for writing and presenting a scientific paper, WUR, 2012
- Advanced course Guide to Scientific Artwork, WUR, 2011
- Introduction in CorelDraw, Sofia University, 2010
- Effective behavior in your professional surroundings, WUR, 2013
- Career perspectives, Wageningen Graduate Schools, 2013

Optionals

- Preparation of PhD proposal
- PhD trip, Scotland, 2013
- Group meetings, ORC, Wageningen University 2009-2013
- Colloquia, ORC, Wageningen University 2009-2013

Project meetings, Nijmegen University, WUR, Germany 2009-2014

The research described in this thesis was financially supported by the INTERREG IV A Germany-Netherlands program through EU funding from the European Regional Development Fund, the MWEBWV Ministry of North-Rhine Westphalia, the Dutch Ministry of Economic Affairs, Province of Gelderland, and the program management Euregio Rhein-Waal.

Financial support from Wageningen University for printing this thesis is gratefully acknowledged.

Cover design: Radostina K. Manova

Printed by: Gildeprint – The Netherlands